EXPLORING THE POTENTIAL OF NANOFLUIDS TO ENHANCE THE PRODUCTIVITY OF SOLAR STILLS

Deepti Charitar

Thesis presented for the Degree of Doctor of Philosophy in Sustainable Energy Engineering in the Department of Mechanical Engineering

UNIVERSITY OF CAPE TOWN

December 2019

Supervisor: Dr. Amos Madhlopa

PLAGIARISM DECLARATION

1. I know the meaning of plagiarism and declare that all the work in this document, save for that which is properly acknowledged, is my own.
2. I know that plagiarism is wrong. Plagiarism is to use another's work and to pretend that it is one's own.
3. I have used the prescribed Harvard UCT referencing style for citation and referencing. Each significant contribution to, and quotation in this thesis from the work, or works, of other people has been attributed, and has been cited and referenced.
4. This thesis is my own work.
5. I have not allowed, and will not allow, anyone to copy my work with the intention of passing it off as his or her own work.

Signature: Signed by candidate

Date handed in: 05 December 2019

ABSTRACT

Desalination technologies are being used to augment access to safe drinking water around the world. Nonetheless, most of these technologies are energy-intensive and driven by fossil fuels which emit greenhouse gases into the atmosphere, thereby contributing to climate change. Additionally, fossil fuels are non-renewable sources of energy and the exhaustion of such reserves can cause a threat to energy security. Consequently, exploitation of sustainable sources of energy for the desalination process has attracted a lot of attention. One such strategy is the use of a solar still which utilises solar energy to produce fresh water from saline or brackish water. However, the major drawback of a solar still lies in its low productivity. Many studies have investigated means of increasing the productivity of a solar still. One such technique which has recently been studied is to disperse nanoparticles into the impure water inside the basin of a solar still in order to obtain a nanofluid with enhanced optical and heat transfer characteristics.

Since this is a relatively new topic, very few numerical studies on solar stills with nanofluids are available. Moreover, based on a literature review, no study examining the effect of nanoparticle size on the productivity of solar stills, and on the economic and environmental performance of solar stills was found. Additionally, the few available numerical studies on solar stills with nanofluids have not taken into account the view factor in the computation of the internal radiative heat transfer coefficient. Therefore, the aim of this study was to investigate both numerically and experimentally the effect of nanoparticle size on the performance of solar stills.

Mathematical models with the view factor (Model 1) and without the view factor (Model 2) were developed for single slope solar stills, and a code was written in MATLAB software to solve a system of equations iteratively. Calculations were performed using climatic data from Stellenbosch (latitude 33.93°S, longitude 18.86°E) and University of Cape Town (latitude 33.96°S, longitude 18.46°E), South Africa, in order to evaluate the performance of solar stills with varying nanoparticle sizes. For the experimental phase, four identical solar stills were designed and built, and they were first tested with water only (base fluid) in all of them to test their performance and for calibration purposes. An Analysis of Variance (ANOVA) test was conducted on the experimental data collected from this first test. Subsequently, nanofluids containing aluminium oxide (Al_2O_3) nanoparticles of size 10 nm, 50 nm and 100 nm were

used in three of the solar stills, with the other solar still containing the base fluid only. All the experiments were conducted at the University of Cape Town. The mathematical models were then validated using experimental data.

Simulations in MATLAB based on Stellenbosch climatic data showed that for the month of January, which is a summer month in South Africa, the productivity of the solar still with the 10 nm, 50 nm and 100 nm Al_2O_3 nanoparticles was 9.01%, 8.94% and 8.89%, respectively higher than the productivity of the solar still with the base fluid only. On the other hand, for the month of July, which is a winter month in South Africa, the average productivity of the solar still with the 10 nm, 50 nm and 100 nm Al_2O_3 nanoparticles was 1.31%, 1.23% and 1.19%, respectively higher than the productivity of the solar still with base fluid only.

In terms of the economic analysis, the simulations in MATLAB based on annual climatic data from Stellenbosch revealed that the cost of distilled water obtained from the solar still with the 10 nm, 50 nm and 100 nm Al_2O_3 nanoparticles was 10.42%, 6.21% and 3.51%, respectively higher than the cost of water obtained from the solar still with the base fluid only. Additionally, the payback period for the solar still with the 10 nm, 50 nm and 100 nm Al_2O_3 nanoparticles was 13.32%, 7.86% and 4.37%, respectively higher than the payback period for the solar still with the base fluid only. In terms of the environmental performance, the amount of carbon dioxide equivalent (CO_2 equivalent) mitigated by the solar still with the 10 nm, 50 nm and 100 nm Al_2O_3 nanoparticles was 6.18%, 6.11% and 6.06%, respectively higher than the amount of CO_2 equivalent mitigated by the solar still with the base fluid only.

For the experimental phase, the ANOVA test based on the first set of experimental data (with base fluid only in all four solar stills) gave a probability-value (P-value) of 1.00. Moreover, experimental data collected from solar stills with base fluid and nanofluids revealed that the productivity of the solar still with nanoparticles of size 10 nm and 50 nm was 26.46% and 1.46%, respectively higher than the productivity of the solar still with base fluid only. On the other hand, the productivity of the solar still with nanoparticles of size 100 nm was 9.38% lower than that of the solar still with base fluid only. Furthermore, the root mean square error (RMSE) for the solar stills with nanofluids for Model 1 and Model 2 was 22.02% and 36.03%, respectively.

It was confirmed that the performance of the calibrated solar stills was not significantly different. Moreover, the enhancement in the productivity of a solar still with nanofluids is much more distinct in summer than in winter. It was also demonstrated that the productivity

of a solar still decreases with increasing nanoparticle size. Additionally, it was established that the cost of distilled water, the payback period and the amount of mitigated CO_2 equivalent decrease with increasing nanoparticle size. Theoretically, the distillate yield and environmental performance of a solar still with nanofluids were marginally sensitive to the nanoparticle size while the cost of distilled water and payback period were significantly affected by the nanoparticle size. The effect of nanoparticle size on distillate yield was experimentally significant. Finally, it was demonstrated that the inclusion of the view factor improves the accuracy of modelling of solar stills with nanofluids.

ACKNOWLEDGEMENTS

I would like to acknowledge the National Research Foundation in South Africa for funding this project; and the following people who have assisted me during this research:

- My supervisor, Dr Amos Madhlopa, for his insightful advice, crucial feedback, encouragement and patience throughout this research.
- My mother, Ouma Charitar, for her daily encouragement and moral support, despite being in another country. Her moral support has been of paramount importance in helping me complete this dissertation. I would also like to thank my father Jagdish Charitar, my sister Hemlata; and my friends David, Melissa and Vikram.
- Mr Dominic De Maar from the Electrical Engineering Department at the University of Cape (UCT), for providing his support and various electronic pieces of equipment which were crucial for recording the data during the experiments conducted in this study.
- Mr Peter Jacobs from the Mechanical Engineering Workshop at UCT, for building the solar stills needed in this research, and Mr Pierre Smith, Dillon, Gavin, Richard and other members from the Mechanical Engineering Workshop.
- Dr Peter Johnston, from the Environmental and Geographical Sciences Department, Portia Johnston, Shilpa Rumjeet and Chantal Le Roux from the Chemical Engineering Department at UCT for allowing me to borrow equipment and use the laboratories in their Department.

TABLE OF CONTENTS

LIST OF FIGURES

LIST OF TABLES

LIST OF ACRONYMS

AD	Adsorption Desalination
CNT	Carbon Nanotube
ED	Electrodialysis
ETSAP	Energy Technology Systems Analysis Programme
FAO	Food and Agriculture Organisation
FD	Freeze Desalination
FO	Forward Osmosis
FRP	Fibre Reinforced Plastic
GHG	Greenhouse Gas
HDH	Humidification-Dehumidification
IDA	International Desalination Association
IEA	International Energy Agency
IRENA	International Renewable Energy Agency
MD	Membrane Distillation
MED	Multi Effect Distillation
MSF	Multi Stage Flash
MVC	Mechanical Vapour Compression
NF	Nanofiltration
PCM	Phase Change Material
RO	Reverse Osmosis
SDBS	Sodium Dodecyl Benzene Sulfonate
SS	Solar Still
TVC	Thermal Vapour Compression
UN	United Nations
UNICEF	United Nations Children's Fund
VC	Vapour Compression
VD	Vacuum Desalination
WHO	World Health Organisation

NOMENCLATURE

Symbol	Definition	Unit
A_{bl}	Surface area of basin liner	m^2
$A_{bw,p}$	Projected area of back wall	m^2
A_f	Surface area of fluid	m^2
$A_{f,di}$	Surface area of fluid receiving beam radiation directly	m^2
A_g	Surface area of glass cover	m^2
A_{sw}	Area of side walls in contact with fluid	m^2
$c_{p,air}$	Specific heat capacity of air	$Jkg^{-1}K^{-1}$
$c_{p,bl}$	Specific heat capacity of basin liner	$Jkg^{-1}K^{-1}$
$c_{p,f}$	Specific heat capacity of fluid	$Jkg^{-1}K^{-1}$
$c_{p,g}$	Specific heat capacity of glass cover	$Jkg^{-1}K^{-1}$
$c_{p,np}$	Specific heat capacity of Al_2O_3 nanoparticles	$Jkg^{-1}K^{-1}$
g	Acceleration due to gravity	ms^{-2}
Gr	Grashof Number	Dimensionless
$h_{co,bl-atm}$	Conductive heat transfer coefficient between basin liner and atmosphere	$Wm^{-2}K^{-1}$
$h_{cv,bl-f}$	Convective heat transfer coefficient between basin liner and fluid	$Wm^{-2}K^{-1}$
$h_{cv,f-g}$	Convective heat transfer coefficient between fluid and glass cover	$Wm^{-2}K^{-1}$
$h_{cv,g-atm}$	Convective heat transfer coefficient between glass cover and atmosphere	$Wm^{-2}K^{-1}$
$h_{e,f-g}$	Evaporative heat transfer coefficient between fluid and glass cover	$Wm^{-2}K^{-1}$
$h_{r,f-g}$	Radiative heat transfer coefficient between fluid and glass cover	$Wm^{-2}K^{-1}$
$h_{r,g-s}$	Radiative heat transfer coefficient between glass cover and sky	$Wm^{-2}K^{-1}$
$h_{t,f-g}$	Total heat transfer coefficient between fluid and glass cover	$Wm^{-2}K^{-1}$
h_v	Latent heat of vaporisation	Jkg^{-1}
H_{bw}	Height of back wall of solar still	m
H_{ew}	Height of east wall of solar still	m
H_{fw}	Height of front wall of solar still	m
H_{ww}	Height of west wall of solar still	m
$I_{b,eff}$	Effective beam radiation inside solar still	Wm^{-2}
$I_{b,h}$	Beam radiation on a horizontal surface	Wm^{-2}
I_{bl}	Amount of solar radiation absorbed by basin liner	Wm^{-2}
$I_{d,eff}$	Effective diffuse radiation inside solar still	Wm^{-2}
$I_{d,h}$	Diffuse radiation on a horizontal surface	Wm^{-2}
I_f	Amount of solar radiation absorbed by fluid	Wm^{-2}

$I_{g,eff}$	Effective global radiation inside solar still	Wm^{-2}
$I_{g,h}$	Global radiation on a horizontal surface	Wm^{-2}
$I_{g,i}$	Global radiation on an inclined surface	Wm^{-2}
I_{glass}	Amount of solar radiation absorbed by glass cover	Wm^{-2}
I_o	Extraterrestrial radiation	Wm^{-2}
I_{sc}	Solar constant	Wm^{-2}
k_D	Diffuse Fraction	Dimensionless
k_f	Thermal conductivity of fluid	$Wm^{-1}K^{-1}$
$k_{ins,1}$	Thermal conductivity of polystyrene	$Wm^{-1}K^{-1}$
$k_{ins,2}$	Thermal conductivity of plywood	$Wm^{-1}K^{-1}$
k_{mix}	Thermal conductivity of binary mixture of air and water vapour	$Wm^{-1}K^{-1}$
k_{np}	Thermal conductivity of nanoparticles	$Wm^{-1}K^{-1}$
k_T	Clearness index	Dimensionless
K_{ec}	Extinction coefficient of glass	m^{-1}
L	Characteristic length	m
L_b	Length of basin	m
$L_{ins,1}$	Thickness of insulation of polystyrene	m
$L_{ins,2}$	Thickness of insulation of plywood	m
M_a	Molecular weight of air	$kgkmol^{-1}$
MBE	Mean Bias Error	%
M_v	Molecular weight of water vapour	$kgkmol^{-1}$
Nu	Nusselt number	Dimensionless
P_o	Atmospheric Pressure	Pa
Pr	Prandtl Number	Dimensionless
$P_{v,f}$	Saturated Vapour Pressure at fluid temperature	Pa
$P_{v,g}$	Saturated Vapour Pressure at glass cover temperature	Pa
q_{evap}	Evaporative heat flux	Wm^{-2}
r	Correlation Coefficient	Dimensionless
$r_{\parallel}$	Parallel component of unpolarized radiation	Dimensionless
$r_{\perp}$	Perpendicular component of unpolarized radiation	Dimensionless
R_a	Gas constant for air	$Jkg^{-1}K^{-1}$
Ra	Rayleigh Number	Dimensionless
R_b	Ratio of beam radiation on an inclined surface to that on a horizontal surface	Dimensionless
RMSE	Root Mean Square Error	%
R_v	Gas constant for water vapour	$Jkg^{-1}K^{-1}$
T_{bl}	Temperature of basin liner	K
T_f	Temperature of fluid	K
T_g	Temperature of glass cover	K
T_s	Sky temperature	K
U_{sw}	Conductive heat transfer coefficient between fluid and atmosphere, through plywood side walls	$Wm^{-2}K^{-1}$

V	Wind speed	ms^{-1}
$V_{f\text{-}bw}$	View factor from fluid to back wall of solar still	Dimensionless
$V_{f\text{-}ew}$	View factor from fluid to east wall of solar still	Dimensionless
$V_{f\text{-}fw}$	View factor from fluid to front wall of solar still	Dimensionless
$V_{f\text{-}g}$	View factor from fluid to glass cover	Dimensionless
$V_{f\text{-}ww}$	View factor from fluid to west wall of solar still	Dimensionless
W_b	Width of basin	m
Y	Productivity/yield of distillate	kgm^{-2}
z_{glass}	Thickness of glass cover	m

Greek symbol	**Definition**	**Unit**
$\alpha_{\parallel}$	Absorptance for parallel component of polarization	Dimensionless
$\alpha_{\perp}$	Absorptance for perpendicular component of polarization	Dimensionless
α_{bl}	Absorptivity of basin liner	Dimensionless
α'_{bl}	Fractional solar flux absorbed by basin liner	Dimensionless
α_f	Absorptivity of fluid	Dimensionless
α'_f	Fractional solar flux absorbed by fluid	Dimensionless
α_{gc}	Absorptivity of glass cover	Dimensionless
α'_{gc}	Fractional solar flux absorbed by glass cover	Dimensionless
α_{solar}	Solar altitude angle	Radians
$\alpha_{t,f}$	Thermal diffusivity of fluid	m^2s^{-1}
$\alpha_{t,np}$	Thermal diffusivity of nanoparticles	m^2s^{-1}
β	Angle of inclination of glass cover	Radians
β_{vol}	Coefficient of volumetric expansion	K^{-1}
γ	Surface azimuth angle	Radians
γ_s	Solar azimuth angle	Radians
δ	Declination angle	Radians
ΔT	Temperature difference	K
ε	Emissivity	Dimensionless
η	Efficiency of solar stills	%
θ_1	Angle of incidence	Radians
θ_2	Angle of refraction	Radians
θ_z	Zenith angle	Radians
μ_f	Dynamic viscosity of fluid	Pa.s
μ_{mix}	Dynamic viscosity of binary mixture of air and water vapour	Pa.s
ν	Kinematic viscosity	m^2s^{-1}
$\rho_{\parallel}$	Reflectance for parallel component of polarization	Dimensionless
$\rho_{\perp}$	Reflectance for perpendicular component of polarization	Dimensionless
ρ_f	Density of fluid	kgm^{-3}
ρ_{gc}	Reflectivity of glass cover	Dimensionless

ρ_{gr}	Ground reflectance	Dimensionless
ρ_{mix}	Density of binary mixture of air and water vapour	kgm^{-3}
ρ_{np}	Density of nanoparticles	kgm^{-3}
σ	Stefan-Boltzmann constant	$Wm^{-2}K^{-4}$
$\tau_{\parallel}$	Transmittance for parallel component of polarization	Dimensionless
$\tau_{\perp}$	Transmittance for perpendicular component of polarization	Dimensionless
τ_a	Transmittance due to absorption losses	Dimensionless
τ_{gc}	Transmissivity of glass cover	Dimensionless
φ_m	Mass concentration of nanoparticles	%
φ_v	Volume concentration of nanoparticles	%
ϕ	Latitude of location	Radians
ω	Hour angle	Radians

Subscript	**Definition**
atm	Atmospheric
bf	Base fluid (water only)
bl	Basin liner
co	Conductive
cv	Convective
e	Evaporative
f	Fluid (either the base fluid or the nanofluid, depending on the context)
g, gc	Glass cover
ins, ply	Plywood insulation
ins, pol	Polystyrene insulation
mix	Mixture of air and water vapour
nf	Nanofluid (mixture of base fluid and nanoparticles)
np	Nanoparticles
r	Radiative
s	Sky
sw	Side Walls

CHAPTER 1
INTRODUCTION

Access to safe drinking water is a major issue in many parts of the world. It is estimated that nearly 50% of the global population will be living in water-stressed regions by the year 2025 (WHO, 2019). Desalination is increasingly becoming a crucial method of generating potable water. However, desalination processes are most often driven by fossil fuels. The combustion of fossil fuels releases greenhouse gases into the atmosphere, in turn contributing to climate change. The other major drawback of fossil fuels is that they are non-renewable. Consequently, the use of solar energy represents an attractive means of driving the desalination process and a solar still can be used for this purpose.

Chapter 1 starts with an overview on global water scarcity, depicting the decline in fresh water resources per capita over the years, followed by a section on the need for safe drinking water. The topic of desalination is then discussed, and a short description of the various types of desalination technologies are subsequently given, as well as their energy requirements. The carbon footprint of the most commonly used desalination technologies is then presented, followed by a discussion on the need to switch to renewable sources of energy for desalination processes. Thereafter, an explanation is given on the working principle of a solar still. The problem statement, scope of the study, aim and objectives are then outlined, followed by a section on the novelty of this investigation. Lastly, a thesis structure is included at the end of Chapter 1.

1.1. Global water scarcity

Water is the basis of life. Human beings, animals and plants cannot survive without water. It is needed daily for domestic, agricultural and industrial purposes. Water can typically be categorised into 5 groups, namely (i) fresh water which can have a maximum salt concentration of 0.5 g/L, (ii) brackish water having a salt concentration ranging from 0.5 to 30 g/L, (iii) saline water with a salt concentration of 30 to 50 g/L, (iv) sea water having a salt concentration of 35 g/L and (v) brine water with a salt concentration of at least 50 g/L (Ghalavand, Hatamipour & Rahimi, 2015).

Although more than 71% of the surface of the Earth is covered with water (Yadav & Sudhakar, 2015), only a small percentage is available as fresh water which can be used for daily activities. It is estimated that the total amount of water on Earth is around 1.5 billion km^3, constituting mainly of sea water which is approximately 1.4 billion km^3, water trapped in land ice and glaciers amounting to nearly 29 million km^3 and groundwater having a volume of around 15 million km^3 (Bengtsson, 2010). The mechanism responsible for the presence and movement of water within, and on the Earth's surface, is known as the water cycle which consists of evaporation and precipitation (Esteve-Calvo & Lloret-Clement, 2007).

Although the water cycle is an ongoing process, the global amount of fresh water per capita has been declining over the years. Figure 1.1 illustrates the decline in the global renewable internal fresh water resources (consisting of groundwater from rainfall and internal river flows) per capita, decreasing from 10 836.957 m^3 per capita in 1972 to 5925.665 m^3 per capita in 2014, corresponding to a decrease of approximately 45% (World Bank, 2016).

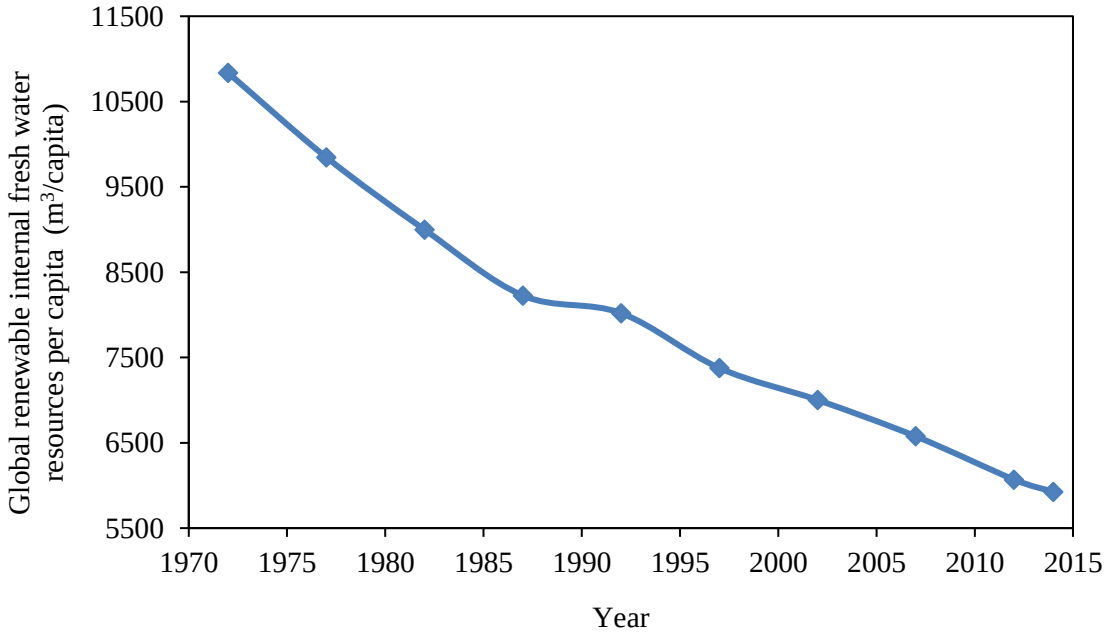

Figure 1.1: Declining global renewable internal fresh water resources per capita.
Source: Compiled from data obtained from World Bank (2016).

The decline in fresh water resources can be associated with non-climatic factors such as demographic, socioeconomic, technological and lifestyle changes as well as climatic factors such as precipitation (Cisneros et al., 2014). In fact, changes in the distribution of

precipitation over space and time are projected to occur due to climate change, subsequently causing arid and semi-arid regions to become drier and wet regions to become wetter.

Furthermore, it is claimed that water scarcity occurs as a result of numerous factors which can be categorised into three main dimensions, namely (i) physical water scarcity, due to a water shortage in a specific region; (ii) economic water scarcity, occurring when there is inadequate infrastructure due to technical, financial or other limitations, irrespective of the amount of available water resources and (iii) institutional scarcity, due to the ineffectiveness of institutions to ensure a consistent, secure and equitable supply of water to consumers (FAO, 2012).

1.2. The need for safe drinking water

It is estimated that each person requires approximately 20 L of fresh water per day to ensure that basic hygiene needs are met (WHO, 2017). However, many countries around the world are unable to meet the water demands of their inhabitants. In 2010, the UN General Assembly recognised "the right to safe and clean drinking water and sanitation as a human right" (UN, 2012). Nevertheless, more than 2 billion people around the world still have to use a source of drinking water which is contaminated with faecal matter (WHO, 2019).

Furthermore, it is estimated that 663 million people did not have access to improved sources of drinking water in 2015 (UNICEF & WHO, 2015). Improved drinking water sources are defined as those which are protected from external contamination, particularly from faecal matter, by virtue of the construction or intervention associated with such water sources, for instance, protected springs, boreholes and piped water into dwellings (UNICEF, 2009).

Approximately 50% of all people who are constrained to use unimproved sources of drinking water live in Sub-Saharan Africa and around 20% live in Southern Asia (UNICEF & WHO, 2015). Consequently, it can be noted that these two regions are in dire need of improved quality of drinking water. A lack of access to safe drinking water has disastrous effects on the health of human beings. It is estimated that around 829 000 people die each year from diarrhoea due to a lack of safe drinking water, improper sanitation and inadequate hygiene (WHO, 2019). One way of increasing access and the quality of water for human consumption is through the desalination process.

1.3. Desalination

Desalination is a process whereby saline or brackish water is converted into potable water, using some source of energy. Desalination is increasingly becoming a crucial method of generating fresh water as only 0.5% of the global water resources consist of directly accessible potable water (Skiborowski et al., 2012) and the demand for fresh water is escalating in many parts of the world due to a rise in population and economic growth (Khan, Rehman & Al-Sulaiman, 2018).

It is estimated that the global demand for fresh water is growing by 640 billion litres annually (Johnston, 2015). Consequently, desalination is an important technique which is being used worldwide to increase access to potable water. As from 30th June 2015, there were 18 426 desalination plants worldwide, with a global capacity of more than 86.8 million m^3 per day (IDA, 2017).

1.3.1. Classification of desalination technologies

Desalination technologies can generally be categorised into a) thermal processes, which involve a phase change, and b) membrane technologies, which do not entail any phase change (Kumar et al., 2015). A phase change is a process whereby the feed water (impure water) is heated to the boiling point to produce steam at the operating pressure and the steam is in turn condensed to produce fresh water (or the feed water is converted into ice which is then melted to obtain fresh water) while a non-phase change is a process whereby the dissolved salts are separated from the feed water mechanically, chemically or electrically by means of a membrane barrier between the feed water and the potable water (Gude, Nirmalakhandan & Deng, 2010). Figure 1.2 illustrates the various types of desalination technologies.

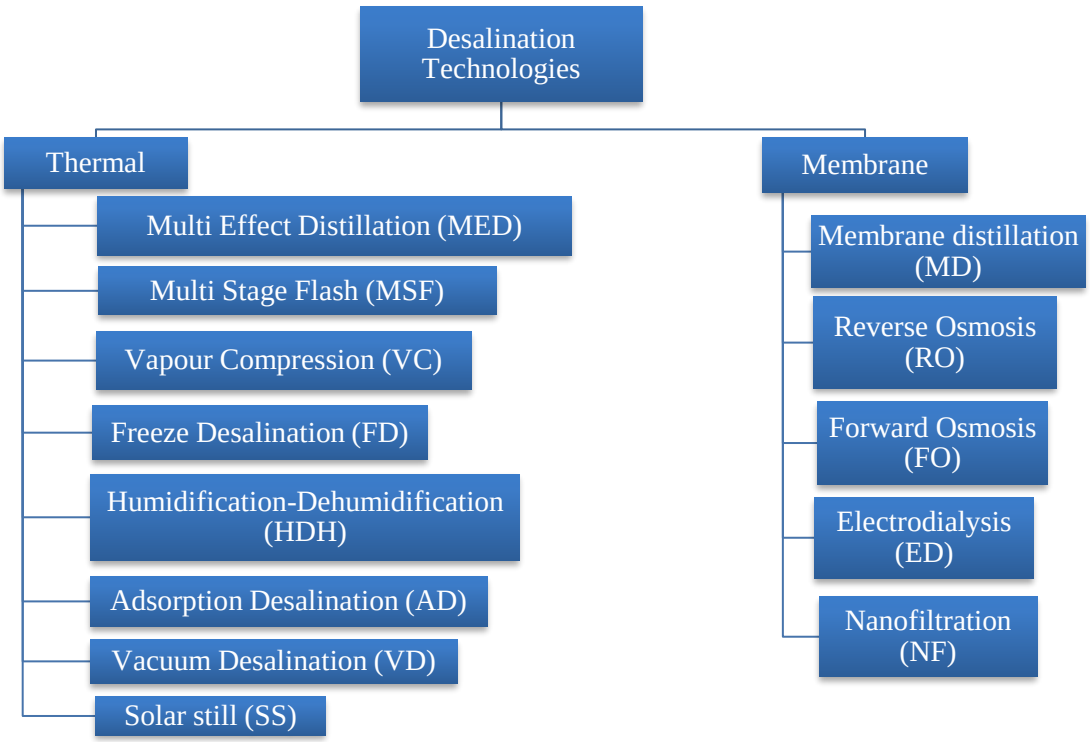

Figure 1.2: Classification of desalination technologies.

Source: Compiled from Kumar et al. (2015); Sharon & Reddy (2015); Pugsley et al. (2016).

1.3.1.1. Description of various types of desalination technologies

Table 1.1 gives a brief description of each type of desalination technique listed in Figure 1.2.

Table 1.1: Brief description of desalination technologies.

Desalination Technology	Brief description of desalination technology
MED	In MED, saline water is sprayed in each of several vessels which are arranged in series. These vessels are also known as effects, with decreasing pressure maintained in each subsequent vessel (Sharon & Reddy, 2015). An external heat source is used to increase the temperature of the feed water in the first effect to bring about the evaporation process, subsequently generating water vapour, which then moves to the second effect and this process repeats itself such that the heat generated in one effect is used in the next effect and so on (Al-Karaghouli & Kazmerski, 2013).
MSF	In MSF, a heat source is used for heating the inlet feed water and this heated feed water then goes through a series of flash units which are kept successively at lower temperatures and pressures. In each unit, some of the hot feed water is allowed to flash, resulting in the generation of water vapour, while the remaining feed water goes to the next stage for additional flashing until it is discharged at the end of the process. The water vapour from each flash unit is allowed to condense and subsequently collected as fresh water (Al-Karaghouli & Kazmerski, 2013).
VC	The working principle of a VC system is as follows: (i) an external heat source is used to increase the temperature of the feed water; (ii) the heated feed water is allowed to flash; (iii) the generated water vapour is compressed and used as heat input to the same stage where it was produced or to other stages (Sharon & Reddy, 2015). There are two types of VC systems, namely thermo VC and mechanical VC, employing steam and electricity respectively for the vapour compression process (Al-Karaghouli & Kazmerski, 2013).

FD	It is a process whereby seawater is cooled below its freezing point, leading to the formation of pure ice crystals, which are then melted to produce fresh water (Sharon & Reddy, 2015).
HDH	The working principle of an HDH system is as follows: (i) the temperature of dry air is increased by means of a heater; (ii) this warm air is then made to pass through a humidifier where water vapour is generated; (iii) the water vapour leaves the humidifier and is condensed in a dehumidifier by exchanging heat with the incoming seawater which gets preheated before going into the humidifier; (iv) the condensed water vapour leaving the dehumidifier is collected as the distillate while excess brine is discharged from the humidifier (Bourouni, Chaibi & Tadrist, 2001).
AD	Saline water which is fed into an evaporator, vaporises and flows to the adsorption bed (kept at a low temperature by the circulation of cold water), where an adsorbent is used for adsorption of the vapour. The vapour is then recovered in the desorption bed by circulating hot water and is then condensed in the condenser, hence obtaining fresh water (Sharon & Reddy, 2015).
VD	It is a process whereby seawater is made to evaporate at a lower temperature using vacuum to decrease its boiling point (Tay, Low & Jeyaseelan, 1996). The water vapour is then condensed to obtain fresh water.
SS	It is a device which uses solar energy for the conversion of saline or brackish water into potable water (Sivakumar & Sundaram, 2013).
MD	It is a technology which utilises a hydrophobic membrane, allowing the permeation of water vapour while preventing the passage of liquid water and consequently, rejecting dissolved solutes and suspended particles (Duong et al., 2015). The driving force for the movement of water vapour through the membrane is the partial vapour pressure gradient which is generated by the temperature difference between the feed side and the permeate side of the membrane (Hitsov et al., 2015).

	There are four basic types of MD technologies, namely (i) direct contact MD, where the liquid is directly in contact with the membrane at the permeate section; (ii) air gap MD, where an air gap acts as a condensing surface at the permeate section; (iii) sweeping gas MD, where a gas is allowed to pass through the gap at the permeate section to help the evaporation of more stable constituents and (iv) vacuum MD, where vacuum is applied to a gap channel (Ashoor et al., 2016).
RO	It is a process whereby the feed water is pressurized so as to make the hydrostatic pressure higher than the osmotic pressure of the solution. This positive pressure difference in turn causes a concentration gradient across the membrane, subsequently allowing the permeation of water molecules through the membrane, while retaining salt molecules on the other side of the membrane (Greenlee et al., 2009).
FO	It is a process driven by the osmotic pressure difference across a semi-permeable membrane, allowing only water molecules to be transported from the feed solution section which is at low osmotic pressure, to the draw solution section which is at a high osmotic pressure (Qasim et al., 2015).
ED	It entails the application of a potential difference between 2 ion-exchange membranes which are in contact with the feed water, thereby allowing the migration of the positively charged sodium ions to a negatively charged chamber and the migration of the negatively charged chloride ions to a positively charged chamber, leaving behind fresh water while the oppositely charged ions get accumulated in their respective chambers (Reif & Alhalabi, 2015).
NF	It is a pressure driven membrane separation technique which depends on the interfacial and micro-hydrodynamic activities taking place at the surface of the membrane and within the nanopores of the membrane (Oatley-Radcliffe et al., 2014). NF has predominantly been used for the removal of low amounts of contaminants from already fairly clean water (Baker, 2012).

1.3.2. Energy requirements of desalination processes

A major drawback of conventional desalination processes is that they are energy-intensive and most often this energy is derived from fossil fuels (IRENA, 2012; Kumar et al., 2012; Gude, 2016). Kalogirou (2005) claimed that the production of 1000 m^3 of fresh water per day from desalination processes consume about 10 000 tons of oil per year. Due to the energy intensiveness of desalination processes, most of the desalination plants around the world have been set up in regions where energy is available abundantly at a low cost; and it is also estimated that only 1% of the total water obtained from desalination is derived from renewable sources of energy (IEA-ETSAP & IRENA, 2012). Table 1.2 gives the thermal and electrical energy requirements of various desalination processes.

Table 1.2: Thermal and electrical energy requirements (in kWh per m^3 of desalinated water) for various desalination processes.

Technology	Thermal energy requirements (kWh/m^3)	Electrical energy requirements (kWh/m^3)	References
MED	80.6	1.5 – 2.5	(IEA-ETSAP & IRENA, 2012)
MSF	80.6	2.5 – 3.5	(IEA-ETSAP & IRENA, 2012)
TVC	14.5	1.6-1.8	(Al-Karaghouli & Kazmerski, 2013)
MVC	-	10 – 14	(Ettouney, 2009)
FD	-	11.9	(Youssef, Al-Dadah & Mahmoud, 2014)
HDH	120	3	(Youssef, Al-Dadah & Mahmoud, 2014)
AD	-	1.38	(Youssef, Al-Dadah & Mahmoud, 2014)
VD	417	< 1 (Natural VD, double stage configuration)	(Gude et al., 2012)
SS	Solar Passive	Solar Passive	(IEA-ETSAP & IRENA, 2012)
MD	120 – 1700	2	(Camacho et al., 2013)
RO	-	4 – 13	(European Union, 2008)
FO	-	< 1	(Ghalavand, Hatamipour & Rahimi, 2015)
ED	-	1 – 4	(Baker, 2012)
NF	-	3.35	(Zhou et al., 2015)

As can be observed from Table 1.2, natural VD and MD have the highest thermal energy requirements, followed by HDH, MED, MSF and TVC. In terms of electrical energy requirements, FD, MVC and RO have the highest requirements.

1.3.3. Carbon footprint of desalination processes

As mentioned earlier, the energy used in desalination processes is predominantly derived from the combustion of fossil fuels, resulting in the emission of greenhouse gases (GHGs). Figure 1.3 illustrates the GHG emissions for the most commonly used desalination techniques, namely RO, MSF, MED and ED, with market shares of 63%, 23%, 8% and 3% respectively, with the remaining 3% representing the market share of other desalination processes (Gude, 2016).

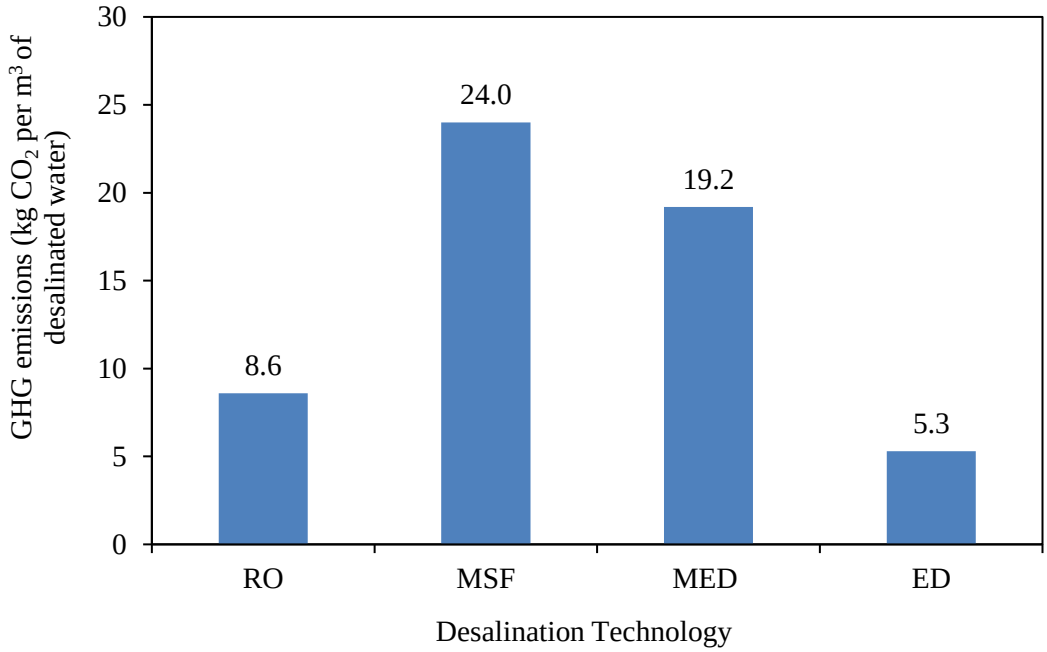

Figure 1.3: GHG emissions from commonly used desalination technologies.

Source: Compiled from data given in Gude, Nirmalakhandan & Deng (2010).

MSF and MED have the largest GHG emissions, of approximately 24.0 and 19.2 kg CO_2 per m^3 of desalinated water produced, as depicted in Figure 1.3. The emission of GHGs into the atmosphere leads to climate change, which in turn has disastrous impacts on the environment. Furthermore, fossil fuels are non-renewable sources of energy and thus, the dependence on such sources of energy causes a threat to energy security. Consequently, it is crucial to shift to renewable sources of energy in desalination technologies in an attempt to minimize the impact of climate change and to minimize the threat associated with energy security.

One such strategy is to make use of solar energy for driving the desalination process. It has been stated by Elango, Gunasekaran and Sampathkumar (2015) that solar desalination is amongst the most promising sustainable technologies for obtaining fresh water for human

consumption. In areas where there is an abundant supply of solar radiation, solar desalination can be used to obtain potable water and a solar still is used for this purpose (El-Sebaii & El-Bialy, 2015).

1.3.4. Solar Stills

A solar still is a device which uses solar energy for the conversion of saline or brackish water into potable water (Sivakumar & Sundaram, 2013). A conventional solar still consists of an insulated basin, a transparent cover and has a distillate collector for collecting the fresh water produced, as illustrated in Figure 1.4.

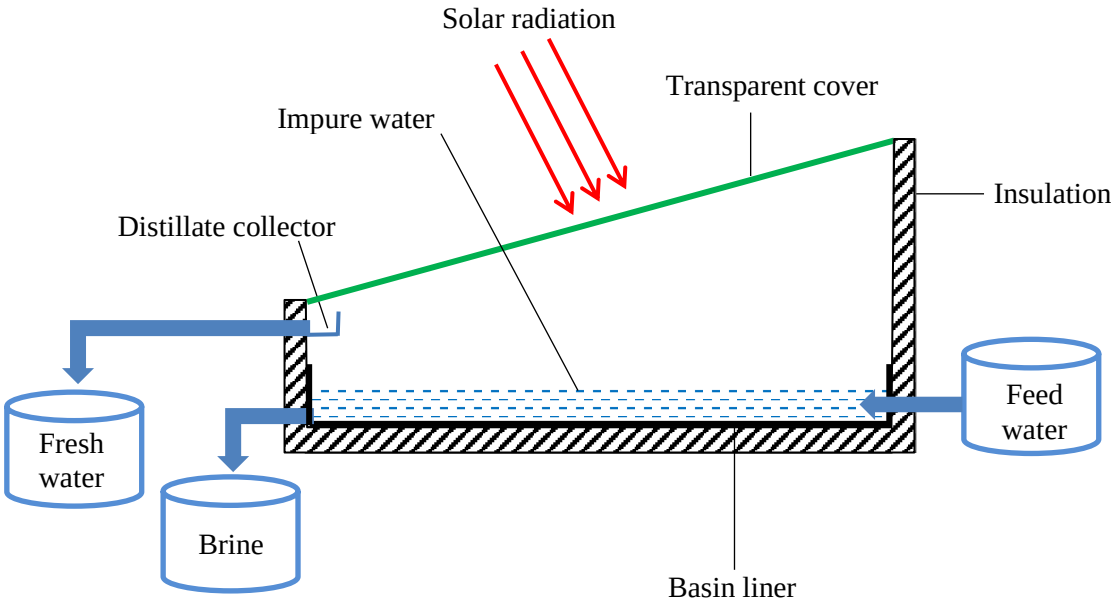

Figure 1.4: Schematic of a conventional solar still.

The basin of a solar still is typically black in colour and the transparent cover is inclined so as to enhance the transmission of solar radiation (Sharon & Reddy, 2015). Solar radiation is captured by the basin liner in the form of thermal energy which in turn heats up the impure water in the basin. As the temperature of the water increases, evaporation occurs and thus, water vapour is produced. Convection currents are subsequently induced between the water surface and the transparent cover since the air-vapour mixture has a higher temperature and a lower density at the water surface as compared to the air-vapour mixture at the inner surface of the transparent cover. Due to this temperature and density difference, the air-vapour mixture at the water surface rises, and as it comes into contact with the colder surface of the

inner transparent cover, it condenses. This distillate then flows along the lower side of the glass cover and is subsequently collected (Elango, Gunasekaran & Sampathkumar, 2015).

1.4. Problem Statement

A major drawback of a conventional solar still is that it has a very low productivity (Park et al., 2015, Prakash & Velmurugan, 2015; Kaviti, Yadav & Shukla, 2016). Consequently, many studies have been carried out in order to improve the distillate yield from solar stills, including the: (i) incorporation of flat or concentrating solar collectors (Chaichan & Kazem, 2015; Morad, El-Maghawry & Wasfy, 2015; Srithar et al., 2016); (ii) integration of internal and external reflectors (Matrawy, Alosaimy & Mahrous, 2015; Omara et al., 2016; Estahbanati et al., 2016); (iii) addition of Phase Change Materials (PCM) (Dashtban & Tabrizi, 2011; Arunkumar et al., 2013; Kabeel & Abdelgaied, 2016); (iv) inclusion of external condenser (Madhlopa & Johnstone, 2009a; Ibrahim & Elshamarka, 2015; Kumar, Esakkimuthu & Murugavel, 2016); (v) coupling of solar stills with solar ponds (El-Sebaii et al., 2008; Velmurugan et al., 2009; Appadurai & Velmurugan, 2015); and (vi) integration of waste heat (Elminshawy, Siddiqui & Sultan, 2015; Maheswari, Murugavel & Esakkimuthu, 2015; Park et al., 2016).

Recently, the use of nanofluids in solar stills has also been investigated. The main research areas have been on comparing the productivity obtained with and without nanofluids, comparison between different types of nanoparticles and the use of nanofluids in conjunction with other techniques of increasing the productivity of a solar still. The first work on the use of nanofluids in solar stills was published by Gnanadason et al. (2012). They investigated experimentally the performance of a single basin solar still operating under vacuum, with and without nanofluids. They used carbon nanotube (CNT) based nanofluids in their experiments which were conducted under the climatic conditions of Tamil Nadu in India. Singh and Singh (2015) compared experimentally the performance of a single slope solar still with and without Al_2O_3 (Aluminium Oxide) nanoparticles under the meteorological conditions of Jaipur in India.

Elango, Kannan and Muragavel (2015) compared experimentally the performance of solar stills with different types of nanoparticles, namely Al_2O_3, SnO_2 (Tin Oxide) and ZnO (Zinc Oxide). They performed the experiments on single basin single slope solar stills under the climatic conditions of Tamil Nadu in India. Kabeel, Omara and Essa (2014a, 2014b) carried

out an experimental investigation on a solar still with nanofluids and operating under vacuum by means of a vacuum fan which was connected to an external condenser at Kafrelsheikh University in Egypt. Photovoltaic panels were used to run an electric DC motor which in turn ran the vacuum fan. They tested two nanoparticles, namely Cu_2O (Cuprous Oxide) and Al_2O_3.

Sahota and Tiwari (2016a, 2016b) conducted a numerical study on the performance of a double slope solar still with nanofluids based on the climatic conditions of New Delhi in India. In the first study, Sahota and Tiwari (2016a) compared three different nanoparticles, namely Al_2O_3, TiO_2 (Titanium oxide) and CuO (Copper Oxide). In the second study, they investigated the effect of varying the concentration of Al_2O_3 nanoparticles on the productivity of a double slope solar still (Sahota & Tiwari, 2016b).

Sahota and Tiwari (2016a) claimed that very little work has been done on the utilisation of nanofluids in solar stills. Moreover, most of the studies conducted on solar stills with nanofluids were experimental only and limited work has been done numerically. Furthermore, based on an extensive literature review, no study examining the effect of nanoparticle size on the productivity of solar stills, and on the economic and environmental performance of solar stills was found. Additionally, the few previous mathematical models of solar stills with nanofluids have not accounted for the view factor in the computation of the internal radiative heat transfer coefficient.

The view factor between two surfaces, A and B, is defined as the fraction of energy leaving surface A that is intercepted by surface B (Maor & Appelbaum, 2012). It is an important parameter in calculating radiative heat transfer coefficients between different surfaces. In the context of a solar still, the internal radiative heat transfer is between the impure water in the basin and the transparent cover. It has been found in previous studies that the inclusion of the view factor in the computation of the internal radiative heat transfer coefficient improves the model accuracy of a conventional solar still (Madhlopa, 2014; El-Maghlany, El-Samadony & Kabeel, 2016).

Nonetheless, the few numerical studies conducted on solar stills with nanofluids have ignored the view factor and they assumed that all of the radiation leaving the surface of the impure fluid in the basin reaches the transparent cover. It is thus desirable to develop a mathematical model incorporating the view factor for solar stills with nanofluids, and to investigate the

effects of nanoparticle size on productivity, and on the economic and environmental performance of solar stills.

1.5. Scope of study

Mathematical models were developed for single slope solar stills. Identical solar stills were designed and built; and experiments were conducted at the University of Cape Town (latitude 33.96°S, longitude 18.46°E), South Africa. The mathematical models were validated with experimental data. This study was limited to single slope solar stills under South African climatic conditions and only one type of nanomaterial (Al_2O_3) was investigated, with three different sizes, namely 10 nm, 50 nm and 100 nm.

1.6. Aim and objectives

The aim of this study was to investigate both numerically and experimentally the effect of nanoparticle size on the productivity of solar stills. The specific objectives of this study were to:

a) Develop mathematical models for single slope solar stills.
b) Design, build and test solar stills under identical climatic conditions.
c) Determine the productivity of the solar stills with and without Al_2O_3 nanoparticles.
d) Explore the effect of nanoparticle size on the productivity, and on the economic and environmental performance of solar stills.
e) Validate the mathematical models by comparing numerical results with experimental results.

1.7. Novelty

It has been observed that numerous attempts have been made in previous studies to increase the productivity of solar stills using various methods such as the use of external energy from solar collectors, solar concentrators, solar pond or waste heat, the incorporation of internal and external reflectors, Phase Change Materials, the addition of external condensers and wick materials, and recently, the use of nanofluids has also been investigated. Nevertheless, as mentioned earlier, the few studies carried out on solar stills with nanofluids have mostly been experimental only, and the few available numerical studies did not account for the view factor in the computation of the internal radiative heat transfer coefficient in the mathematical models.

Moreover, based on a comprehensive literature review, it was found that no study focused on how the particle size of the nanoparticles dispersed into the impure fluid affects the productivity of the solar still. Additionally, the effects of nanoparticle size on the economic and environmental performance of solar stills have not been reported in any study from the extensive literature review conducted. Consequently, this research has achieved the following contributions to knowledge:

(i) A mathematical model incorporating the view factor in the calculation of the internal radiative heat transfer coefficient has been developed for solar stills with nanofluids.

(ii) The effect of nanoparticle size on the productivity of solar stills has been investigated both numerically and experimentally.

(iii) The effects of nanoparticle size on the economic and environmental performance of solar stills have been studied numerically.

1.8. Thesis structure

This thesis is structured as follows:

1) Chapter 1: The global water scarcity and the various types of desalination techniques are discussed, as well as the problem statement, scope, aim and objectives of this investigation. The contributions to knowledge achieved by this study are also stated in Chapter 1.
2) Chapter 2: This chapter is the literature review, entailing a discussion on topics relevant to this study, namely the principles of solar radiation, mechanisms of heat and mass transfer and a comprehensive review of previous studies conducted on solar stills with nanofluids.
3) Chapter 3: This chapter comprises a design section which describes how design parameters were chosen for this study, a mathematical modelling section which gives a thorough explanation on how the mathematical models for the solar stills were developed, an experimentation section which describes the procedures which have been followed in order to generate the experimental data and a model validation section which indicates the statistical tools which were used to compare numerical results with experimental results.
4) Chapter 4: The numerical and experimental results are presented in this chapter, as well as a discussion on these results. The model validation results are also presented and discussed in this chapter.
5) Chapter 5: This chapter gives the conclusions and recommendations which were made based on the discussion of the results. After Chapter 5, the references and appendices are given.

CHAPTER 2
LITERATURE REVIEW

This chapter discusses the need for solar stills, as well as the fundamentals of solar radiation and solar geometry which are essential in the design and operation of such devices. The mechanisms of heat transfer including conduction, convection and radiation are then presented. The concept of the view factor is subsequently explained, followed by the analogy between heat and mass transfer. The various climatic factors and design parameters affecting the productivity of solar stills are then presented. Thereafter, a detailed review of solar stills with nanofluids is given, including the laws of thermodynamics applicable to solar stills, as well as the thermodynamic, economic and environmental analysis of solar stills with nanofluids. The techniques used in the preparation of nanofluids are then discussed, in conjunction with the methods of improving the stability of nanofluids. Lastly, the quality of the distillate produced from solar stills with nanofluids is discussed.

2.1. The need for solar stills

2.1.1. Minimal environmental impact

Desalination has become a common technique for the production of potable water in many parts of the world, particularly in the Middle East, Spain, Australia and China. However, most of the existing desalination plants run on electricity which is often generated from the burning of fossil fuels, which in turn releases GHGs in the environment, thereby contributing to climate change. Additionally, fossil fuels are non-renewable sources of energy and the depletion of such energy sources can cause a threat to energy security. A solar still has the advantage of being driven by solar energy which is a non-polluting and renewable source of energy.

Moreover, one of the major issues associated with desalination is the disposal of the brine concentrate which is generated as a by-product. Commonly used desalination techniques such as Reverse Osmosis, Multi Effect Distillation and Multi Stage Flash require pre-treatment of the feed water such as the addition of chemicals to prevent scaling and corrosion. Thus, the brine concentrate which is generated can contain small amounts of such chemicals which pose a threat for marine habitats and other water environments which receive the brine

concentrate (Younos, 2005 : 12). On the other hand, it has been claimed that the brine generated from solar stills do not contain any antiscalants or chemicals; and therefore, may cause less harm to the environment as compared to the brine generated from other desalination processes (Ayoub & Malaeb, 2012: 2102).

In the context of a solar still with nanoparticles, the latter provide a means of enhancing heat transfer and increasing the yield of fresh water. The nanoparticles remain inside the basin water during the continuous processes of evaporation and condensation. Based on the extensive literature review conducted, no study focusing on the brine disposal from solar stills with nanoparticles was found as the use of nanoparticles in solar stills is a relatively new research area. Nevertheless, the use of nanoparticles in solar stills is justified as a review study conducted by Bait (2020) showed that there is a scope for improvement in the performance of solar desalination systems by employing the use of nanoparticles in a base fluid.

2.1.2. Ease of operation and convenience in remote locations

A conventional solar still is easy to construct, maintain and operate. The major operation and maintenance aspects include cleaning of the basin, removal of brine deposit and cleaning of the glass cover. Additionally, a conventional solar still does not consist of any moving parts and consequently, it does not cause any noise pollution. On the other hand, for other desalination processes, the construction phase is time-consuming and disruptive to the surroundings (Younos, 2005).

Additionally, in rural areas, access to safe drinking water is a daily challenge for many people. In such locations, people often have to travel long distances just to get their daily potable water requirements. Sathyamurthy et al. (2015) claimed that the transport of potable water in remote locations is very expensive and solar stills are very advantageous in such places as they can be easily constructed with low cost materials.

2.2. Fundamentals of solar radiation

The Sun is made up of approximately 74% hydrogen and 25% helium, with the remaining 1% consisting of infinitesimal amounts of heavier elements (Kalogirou, 2009). Solar energy is a free and inexhaustible energy source and it arises due to the fusion of hydrogen nuclei into helium nuclei, whereby a tiny quantity of mass is converted into energy (Mackay, 2015). The centre of the Sun has a temperature of about 20 million K and its outer surface is at a temperature of approximately 5760 K, with energy being emitted at a rate of 3.8×10^{23} kW and around 1.7×10^{14} kW of energy being captured by the Earth (Goswami, 2015).

Solar radiation can either be converted directly into electricity via the photovoltaic effect as used in photovoltaic panels or captured as heat for solar thermal applications such as in Concentrated Solar Power (CSP) plants. Solar stills also fall under the category of solar thermal applications as the radiation from the Sun is captured in the form of heat which is then used to drive the desalination process. Some fundamental concepts associated with the application of solar energy in solar stills and relevant to this investigation are presented in the following section.

2.2.1. Components of solar radiation on a tilted surface

The total radiation on a tilted surface is the sum of the beam radiation, diffuse radiation and ground-reflected radiation. Beam radiation, also commonly known as direct radiation, is the radiation that comes directly from the Sun and strikes a given surface without undergoing any scattering from the atmosphere while diffuse radiation is the radiation that strikes a surface after it is scattered by the atmosphere (Duffie & Beckman, 2013).

On the other hand, ground-reflected radiation is that component of solar radiation which is reflected from the ground or from intercepting objects such as buildings and trees onto a given surface (Shukla, Rangnekar & Sudhakar, 2015). Figure 2.1 illustrates the components of solar radiation on a tilted surface.

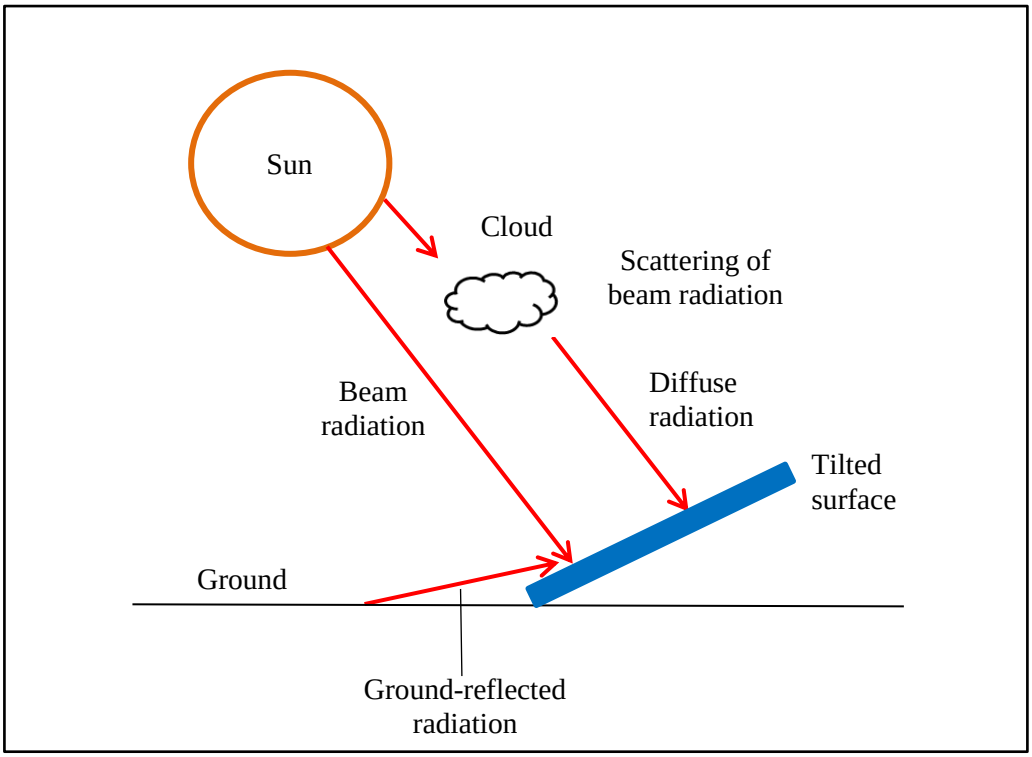

Figure 2.1: Components of solar radiation on a tilted surface.

Adapted from Charitar (2015).

2.2.2. Solar geometry

The amount of solar radiation captured by a particular object is largely influenced by its location on the surface of the Earth, as well as the position of the Earth with respect to the Sun. In this study, various geographical and astronomical parameters were used in the mathematical modelling of solar stills and these parameters play a crucial role in determining how much solar radiation can be captured by the solar stills. These geographical and astronomical concepts are defined below.

a) Latitude and longitude

Any location on the surface of the Earth can be given in terms of its latitude and longitude. The latitude is the angle which is measured north or south of the equatorial plane, ranging from 0° at the equator and 90° at the poles while the longitude is measured east or west of the Greenwich Meridian line. The convention for latitudes and longitudes is as follows: a location north of the equator has a positive latitude while a location south of the equator has a negative latitude and a location east of the Greenwich Meridian is positive while a location west of the Greenwich Meridian has a negative value.

b) Declination angle

The declination angle is defined as the angle between the rays of the Sun and the equatorial plane of the Earth. On a given day, the declination angle is constant, and it only changes on the following day, mainly due to the Earth's rotation about an axis (Tiwari & Dubey, 2010). The declination angle ranges between -23.45°C to 23.45°C throughout the year (Duffie & Beckman, 2013).

c) Solar time

In solar engineering calculations, it is essential to differentiate between solar time and clock time. The latter is the time which is shown on a clock while solar time is based on the concept that it is noon (solar noon) only when the Sun crosses the meridian of the observer (Tiwari & Dubey, 2010).

d) Hour angle

The hour angle is defined as the angle through which the Earth must rotate in order to make the observer's meridian directly in line with the rays of the Sun (Garg & Prakash, 2000). The hour angle is zero at solar noon, positive in the afternoon and negative in the morning, with maximum positive occurring at sunset and maximum negative at sunrise.

e) Zenith angle

The zenith angle is the angle between the line to the Sun and the vertical (Duffie & Beckman, 2013).

f) Angle of incidence

The angle of incidence is defined as the angle between the normal to a surface and the beam radiation striking the surface (Tiwari & Dubey, 2010).

g) Solar azimuth angle and solar altitude angle

The solar azimuth angle is the angle between the projection of the Sun's beam rays on a horizontal surface and the south direction, while the solar altitude angle is the angle between the line to the Sun and the horizontal (Duffie & Beckman, 2013).

2.3. Heat transfer mechanisms

In order to study the processes which take place in a solar still, it is essential to understand the heat transfer mechanisms occurring within such a system. Heat transfer is said to occur when there exists a temperature gradient within a system or between systems which are in thermal contact with one another (Böckh & Wetzel, 2012). There are three modes by which heat transfer can occur, namely conduction, convection and radiation. Both conduction and convection require a medium for heat transfer to occur while radiation occurs even in vacuum.

2.3.1. Conduction

All types of matter are made up of molecules which are in random motion and the energy possessed by these molecules can primarily be categorised either as macroscopic energy, namely potential and kinetic energy, or microscopic energy, for example vibrational and rotational energy (Rao, 2001). As these molecules interact with one another, the molecule which is at a higher temperature imparts energy to the molecule which is at a lower temperature.

Conduction can thus be defined as the transfer of energy, in the form of heat, from a region of higher temperature to a region of lower temperature, within a solid, liquid or gas, or between these different mediums which are in physical contact with one another, due to molecules having different energy levels (Ganji, Sabzehmeidani & Sedighiamiri, 2018). The rate of energy transferred during the conduction process can be expressed as given in Equation (2.1) which is the Fourier rate equation (Bergman et al., 2011).

$$\frac{q_x}{A} = -k\frac{dT}{dx} \tag{2.1}$$

In Equation (2.1), q_x represents the heat flux in the x direction, in Wm^{-2}, A is the area over which heat transfer is taking place, in m^2, k denotes the thermal conductivity (in $Wm^{-1}K^{-1}$) of the material within which conduction is taking place and $\frac{dT}{dx}$ is the temperature gradient within the system, computed as follows:

$$\frac{dT}{dx} = \frac{T_1 - T_2}{L} \tag{2.2}$$

These parameters are given in Figure 2.2, where T_1 and T_2 represent two points at a distance L apart, at different temperatures, with T_1 being greater than T_2.

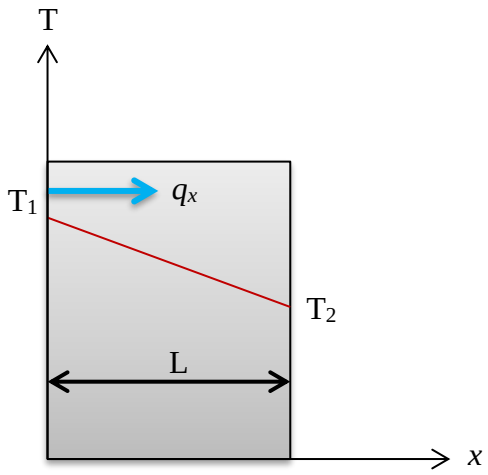

Figure 2.2: Temperature gradient for heat transfer by conduction.

2.3.2. Convection

Convective heat transfer occurs due to a temperature gradient existing between a surface and a fluid which are in contact with each other. There are two types of convection, namely natural and forced convection. In natural convection, also known as free convection, the motion of the fluid past the surface is induced by density gradients within the fluid which occur as a result of temperature differences arising as the fluid is heated or cooled. On the other hand, under forced convection, the motion of the fluid past the surface is driven by an external force (Nellis & Klein, 2009).

Figure 2.3 illustrates the motion of a fluid from a heated flat plate which is at a higher temperature ($T_{surface}$) than that of the bulk temperature of the fluid (T_{bulk}). The fluid molecules near the hot plate get heated up and their temperature increases, thus causing a decrease in their density. These molecules thus move in the upwards direction, due to the density gradient.

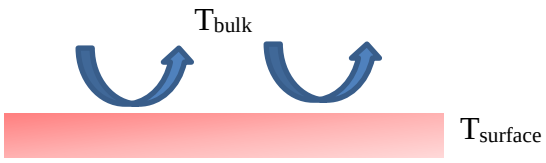

Figure 2.3: Natural convection from a hot plate.

The rate of heat transferred (q), in W, can be expressed by Newton's Law of cooling as given in Equation (2.3), where A represents the surface area of the hot surface (in m^2), h is the convective heat transfer coefficient in $Wm^{-2}K^{-1}$ and ΔT is the temperature difference between the surface and the fluid. The convective heat transfer coefficient is a parameter which depends on the geometry of the surface, the type of flow occurring within the fluid and the thermophysical properties of the fluid (Bergman et al., 2011).

$$\frac{q}{A} = h\,\Delta T \tag{2.3}$$

2.3.3. Radiation

Radiation can be defined as electromagnetic energy which is emitted by a body by virtue of its temperature, either in the form of electromagnetic waves or in the form of discrete photons (Rathore & Kapuno, 2011). When the atoms, molecules or electrons of a body are raised to excited states due to the body's temperature, these atoms, molecules or electrons revert spontaneously to lower energy levels by emitting electromagnetic radiation (Duffie & Beckman, 2013). No medium is required for radiative heat transfer between two surfaces and in fact, maximum radiative heat can be transferred between two surfaces if they are separated by a perfect vacuum (Welty, Rorrer & Foster, 2015).

The rate of radiative heat emitted by a body per unit area (E in Wm^{-2}) is given by the Stefan-Boltzmann Law, as given in Equation (2.4), where σ is the Stefan-Boltzmann constant (5.67×10^{-8} $Wm^{-2}K^{-4}$) and T represents the temperature of the body in K (Bergman et al., 2011).

$$E = \sigma T^4 \tag{2.4}$$

When considering two given surfaces, A and B, with surface A being at a higher temperature than surface B, surface A will radiate heat towards surface B but not all the radiative heat

leaving surface A will strike surface B. In order to compute the amount of radiation incident on surface B, it is crucial to introduce a term known as the view factor.

2.3.3.1. View Factor

The view factor between two surfaces, A and B, denoted by V_{A-B}, can be defined as the fraction of energy leaving surface A that is intercepted by surface B (Maor & Appelbaum, 2012). The view factor is also known as the angle factor, shape factor, interchange factor, exchange factor or configuration factor (Howell, Mengüç & Siegel, 2016) and can be expressed as given in Equation (2.5).

$$V_{A-B} = \frac{\text{Amount of radiation striking surface B}}{\text{Amount of radiation leaving surface A}} \tag{2.5}$$

With regards to surfaces within an enclosure, as illustrated in Figure 2.4, the sum of the view factors is equal to 1, that is, $V_{A-B} + V_{A-C} + V_{A-D} + V_{A-E} = 1$.

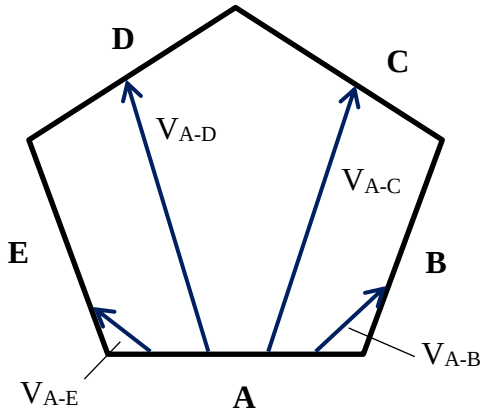

Figure 2.4: View Factor within an enclosure.

The correlations for the computation of the view factor are dependent on the geometry of the enclosure. In the context of this research, the correlation for a 3-dimensional geometry entailing perpendicular rectangles with a common edge was required in the computation of the view factor for the internal radiative heat transfer coefficient. This correlation is given in Equation (2.6) with the geometry given in Figure 2.5 (Bergman et al., 2011).

$$V_{A-B} = \frac{1}{\pi W}\left(W\tan^{-1}\left(\frac{1}{W}\right) + H_1\tan^{-1}\left(\frac{1}{H}\right) - (H^2+W^2)^{\frac{1}{2}}\tan^{-1}\left(\frac{1}{(H^2+W^2)^{\frac{1}{2}}}\right) + \frac{1}{4}\ln\left\{\frac{(1+W^2)(1+H^2)}{(1+W^2+H^2)}\left[\frac{W^2(1+W^2+H^2)}{(1+W^2)(W^2+H^2)}\right]^{W^2}\left[\frac{H^2(1+H^2+W^2)}{(1+H^2)(H^2+W^2)}\right]^{H^2}\right\}\right) \quad (2.6)$$

$$W = \frac{Y}{X} \quad (2.7)$$

$$H = \frac{Z}{X} \quad (2.8)$$

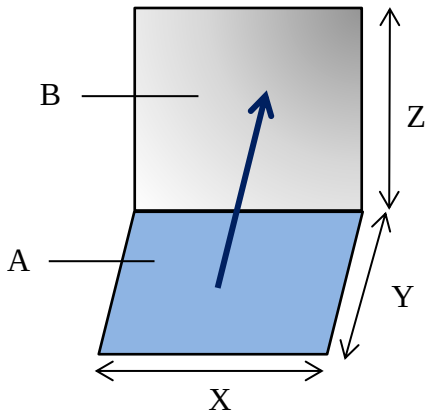

Figure 2.5: Perpendicular rectangles with a common edge.

2.4. Analogy between heat and mass transfer

In engineering applications such as desalination or drying processes, evaporation of water into an air stream is encountered, resulting in the co-existence of heat and mass transfer (Gu, Min & Tang, 2018). Mass transfer entails the transport of a substance from a region of high concentration to a region of low concentration. In the context of this research which deals with desalination, it is crucial to understand the concept of evaporation as it determines the productivity of the solar still.

Evaporation is an isothermal process which takes place at the liquid-vapour interface when the vapour pressure is lower than the saturation pressure of the liquid and in the context of a solar still, this process occurs at the water and water-vapour interface (Elango, Gunasekaran & Sampathkumar, 2015).

2.5. Solar Stills

As mentioned earlier, a solar still is a device driven by solar energy which is used to convert brackish or saline water into potable water through the continuous process of evaporation and condensation. There are two types of solar stills, namely passive and active solar stills (Abad et al., 2013). In a passive solar still, the only source of energy is solar energy and evaporation occurs naturally without the assistance of any external source of energy. On the other hand, in an active solar still, additional thermal energy is added to the system by an external source in order to increase the temperature of water in the basin of the solar still so as to increase the evaporation rate and the yield of clean water (Singh et al., 2016).

There are various designs of passive solar stills which have been studied, with the single slope single basin type being the conventional design. In the case of active solar stills, various methods of providing additional energy have been investigated and these are illustrated in Figure 2.6.

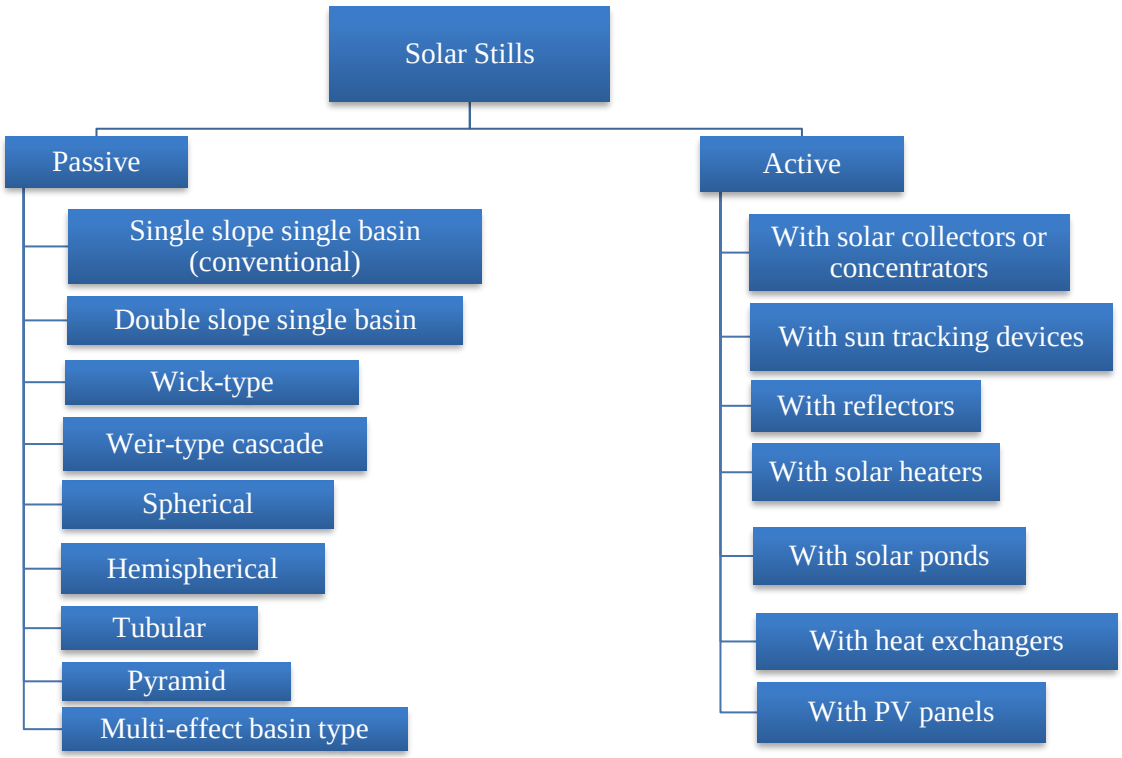

Figure 2.6: Types of solar stills (Sathyamurthy et al., 2015; Kumar et al., 2015; Durkaieswaran & Murugavel, 2015).

2.5.1. Factors affecting the productivity of a solar still

The productivity of a passive solar still depends on numerous factors such as environmental conditions, design parameters and operational conditions. Climatic conditions cannot be controlled and include solar radiation, wind velocity and ambient temperature. On the other hand, design parameters entail the various physical components of the solar still which can be controlled and improved in order to achieve an optimum productivity. The major design parameters include the thickness and the inclination angle of the transparent cover, the water depth in the basin of the solar still, the surface area of water and insulation. Operational conditions relate to the maintenance of the solar stills, such as regular cleaning of the glass cover to prevent accumulation of dust particles which can hinder the transmission of solar radiation through the transparent cover to the basin liner.

2.5.1.1. Environmental conditions

2.5.1.1.1. Solar radiation

The productivity of a solar still is highly dependent on the intensity of solar radiation. In fact, it has been claimed that solar radiation is the most dominating factor which affects the yield of a solar still (Nafey et al., 2000). Many studies have shown that the productivity of a solar still increases with an increase in solar radiation (Rahbar & Esfahani, 2012; Muftah et al., 2014; Abujazar et al., 2016).

When the intensity of solar radiation increases, a higher amount of solar radiation gets transmitted through the transparent cover and captured by the basin liner, which in turn transfers more heat to the fluid. As the temperature of the fluid increases, the convective and evaporative heat transfer coefficients from the fluid to the transparent cover increases, resulting in an increase in the productivity of the solar still.

2.5.1.1.2. Wind speed

Conflicting results have been found in previous studies with regards to the effect of wind speed on the productivity of solar stills. Some studies have revealed that the productivity increases with increasing wind speed while some studies have indicated a decrease in productivity with increasing wind speed. El-Sebaii (2000) conducted a numerical analysis and the results showed that (i) the productivity increases between midday till sunset when the wind velocity increases due to an increase in the temperature difference between the basin fluid and the glass cover and (ii) the productivity decreases after sunset with an increase in wind speed as the temperature difference between the fluid and the glass cover decreases after sunset with increasing wind speed. Zurigat and Abu-Arabi (2004) also investigated numerically the effect of wind speed on the productivity of a solar still and they found that the productivity can increase by more than 50% when the wind velocity increases from 0 to 10 ms^{-1}. It has been further claimed by Sharshir et al. (2016) that an increase in the wind speed leads to an increase in the productivity as the convective heat transfer from the glass cover to the atmosphere increases with wind speed. This in turn causes the temperature difference between the basin fluid and the glass cover to increase, leading to higher rates of evaporation and condensation.

On the other hand, the mathematical investigation conducted by Nafey et al. (2000) revealed that the productivity decreases by 13% when wind speed is increased from 1 to 9 ms^{-1}. They

claimed that the ratio between the evaporative heat transfer coefficient and the convective heat transfer coefficient from the glass cover to the atmosphere decreases when the wind speed increases, thus leading to a decrease in the productivity. Al-Garni (2012) carried out an experimental analysis on a solar still under the climatic conditions of Saudi Arabia and the results showed a decrease in productivity with increasing wind speed. The productivity decreased by 4% and 8% when the wind speed was increased to 7 ms^{-1} and 9 ms^{-1}, respectively. Danish et al. (2019) conducted both a numerical and experimental investigation and they found that the productivity of the solar still decreases with an increase in the wind speed, which was attributed to an increase in heat loss with increasing wind speed.

2.5.1.1.3. Ambient temperature

Previous studies have shown that the productivity of a solar still increases with increasing ambient temperature. Nafey et al. (2000) reported an increase of 3% in the productivity of a solar still when ambient temperature increased by 5°C. Al-Hinai, Al-Nassri and Jubran (2002) reported an increase of 8.2% in the productivity when ambient temperature increased by 10°C. Additionally, Danish et al. (2019) found that the productivity increases by 17% when ambient temperature increases by 25°C. A higher ambient temperature causes the fluid temperature to be higher; and a higher fluid temperature enhances the evaporation process (Xiao et al., 2013), thus resulting in a higher productivity.

2.5.1.2. Design parameters

2.5.1.2.1. Thickness of transparent cover

Panchal and Shah (2011) conducted an experimental analysis on the effect of glass thickness on the productivity of a solar still. They found that the solar still with the smallest glass cover thickness (4 mm) could achieve a higher yield than those with thicker glass covers (8 mm and 10 mm). Morad, El-Maghawry and Wasfy (2015) carried out an experimental investigation using glass cover thickness of 3, 4 and 5 mm and they also reported a higher productivity with decreasing thickness of the glass cover. They claimed that when the thickness of the glass cover increases, a lower amount of solar radiation gets transmitted to the basin fluid, causing the solar still efficiency to decrease, in turn resulting in a lower productivity.

Panchal (2016) investigated both theoretically and experimentally the effect of three different glass thicknesses, namely 4 mm, 5 mm and 6 mm on productivity. The results revealed that

the productivities of the 4 mm and 5 mm glass cover were respectively 27% and 12% higher than that of the 6 mm glass cover.

2.5.1.2.2. Inclination angle of transparent cover

Muftah et al. (2014) claimed that the angle of inclination of the glass cover greatly affects the productivity of a solar still. Singh and Tiwari (2004) conducted a numerical analysis on the performance of solar stills under various climatic conditions. They claimed that the annual productivity of the solar still is optimal when the glass cover tilt angle is equal to the latitude of the location. Khalifa (2011) conducted a comprehensive literature review on the effect of tilt angle of the glass cover on the productivity of solar stills, and the observed trend in the research suggested that the optimum inclination angle is close to the latitude of the location. Kabeel and El-Agouz (2011) claimed that a glass cover whose tilt angle is equal to the latitude is optimised with regards to the solar azimuth angle and solar intensity of the location, thereby obtaining Sun rays nearly at normal incidence throughout the year, hence maximising productivity.

2.5.1.2.3. Depth of fluid in the basin

Khalifa and Hamood (2009a) conducted an experimental analysis on the effect of water depth (1, 4, 6, 8 and 10 cm) on the productivity of a single slope solar still under the climatic conditions of Baghdad in Iraq. They found that the daytime productivity of the solar still increases with decreasing water depth while the nocturnal productivity decreases with decreasing water depth. They further claimed that the water depth could influence the productivity of a solar still by up to 48%. A similar trend was observed by Elango and Murgavel (2015) who investigated experimentally both single and double slope solar stills under the climatic conditions of Tamil Nadu in India. They investigated water depths ranging from 1 to 5 cm and they found that the productivities of the solar stills were highest at a water depth of 1 cm.

Nonetheless, keeping the water depth in the basin to a minimum can cause the formation of dry spots which can in turn affect the productivity (Prakash & Velmurugan, 2015). It is thus crucial not to maintain the water level in the basin too low in order to prevent the formation of dry spots.

2.5.1.2.4. Insulation

Al-Hinai, Al-Nassri and Jubran (2002) carried out a numerical analysis on a double slope solar still under the climatic conditions of Oman. They revealed that increasing the thickness of the insulation on the base and the sides to 0.13 m considerably increased the productivity. They further claimed that the optimum insulation thickness under the climatic conditions of Oman is 0.1 m as any additional increase in the productivity obtained with thicker insulation does not justify the extra cost of insulation.

Khalifa and Hamood (2009b) conducted an experimental investigation on the effect of using insulation on the sides and the base of a single slope solar still. They investigated insulation thicknesses of 30, 60 and 100 mm and they found that increasing the insulation thickness up to 60 mm could increase the productivity by 80%. They attributed this to the fact that the insulation led to higher operating temperatures within the solar still.

2.5.1.2.5. Internal and external reflectors

Tanaka (2009) carried out an experimental and theoretical study on the use of internal and external reflectors in a basin type solar still under the climatic conditions of Kurume in Japan. The results showed that the reflectors could increase the daily productivity of a basin type solar still by 70% to 100%. Matrawy, Alosaimy and Mahrous (2015) investigated numerically and experimentally the effect of using a wick type solar still with an external reflector. Their results showed that the productivity of the wick type solar still with the reflector could be improved by nearly 34% compared to a simple basin type solar still. Omara et al. (2016) performed an experimental investigation on a wick type solar still with internal reflectors under Egyptian climatic conditions. They claimed that the productivity of the wick type solar still with reflectors was approximately 145.5% higher than that of a conventional solar still.

2.5.1.2.6. Solar collectors and solar concentrators

Badran et al. (2005) investigated experimentally the effect of integrating a flat plate collector into a single stage basin-type solar still under the climatic conditions of Jordan. They found that the mass of water produced when a flat plate collector was integrated into the system increased by 231% when tap water was used as the feed and by 52% when salt water was used as the feed.

Rajaseenivasan, Raja and Srithar (2014) carried out experiments on a single slope single basin solar still and on a single slope solar still with a flat plate collector under the climatic conditions of Tamil Nadu in India. Their research showed that the solar still with the flat plate collector had approximately 60% higher distillate than the solar still without the flat plate collector. The maximum daily productivities for the solar stills with and without the flat plate collector were 5.82 kg/m^2 and 3.62 kg/m^2 respectively.

Srithar et al. (2016) performed an experimental investigation on a triple basin solar desalination system with a parabolic dish concentrator under the climatic conditions of Madurai in India. The system was also equipped with a cover cooling arrangement and a photovoltaic panel. They claimed that the solar still with the parabolic dish concentrator could increase the temperature of water in the lower basin up to 85 °C while the solar still without the concentrator could only increase the water temperature to 59 °C. They also stated that the solar still with the parabolic concentrator could produce approximately 2.61 times higher amount of distillate than the conventional triple basin solar still.

2.5.1.2.7. External condenser

Madhlopa and Johnstone (2009a) carried out a numerical analysis of a single-slope solar still with an external condenser based upon the climatic conditions of Chileka in Malawi. Their results showed that the productivity of the distillate is 62% higher when an external condenser is used, as compared to a conventional solar still with no condenser. Ibrahim and Elshamarka (2015) performed numerical and experimental investigations on a basin type solar still with an external air-cooled condenser under the climatic conditions of Cairo in Egypt. They found that the productivity of the solar still with the condenser is approximately 16.2% higher than the conventional solar still.

2.5.1.2.8. Phase Change Material

A Phase Change Material (PCM) can be added beneath the basin liner of a solar still in order to act as a storage material for additional heat during periods of high solar radiation instead of the heat being wasted to the environment (El-Sebaii et al., 2009). El-Sebaii et al. (2009) developed transient mathematical models for a single slope single basin solar still with and without PCM under the climatic conditions of Saudia Arabia. They used stearic acid as the PCM and they found that in summer, the daily productivity of water was only 4.998 kg/m^2 without the PCM but 9.005 kg/m^2 with the PCM. Tabrizi, Dashtban and Moghaddam (2010)

investigated experimentally the productivities of a cascade solar still, with and without PCM under the Iranian climate. Their study showed that on partly cloudy days, the solar still with the paraffin wax as PCM could achieve a productivity of 3.4 kg/m^2 as compared to only 2.1 kg/m^2 by the solar still with no PCM. Arunkumar et al. (2013) carried out experiments on single-slope solar stills with and without PCM and their study revealed that the productivity is 26% higher when the PCM is used. In their investigation, they used paraffin as the PCM.

2.5.2. Mechanisms of heat and mass transfer in a solar still

Heat and mass transfer processes in a conventional solar still can be categorised into (i) internal processes consisting of convection, radiation and evaporation and (ii) external processes which include conduction, convection and radiation (Sampathkumar et al., 2010). Figure 2.7 illustrates the various heat and mass transfer processes which occur in a solar still.

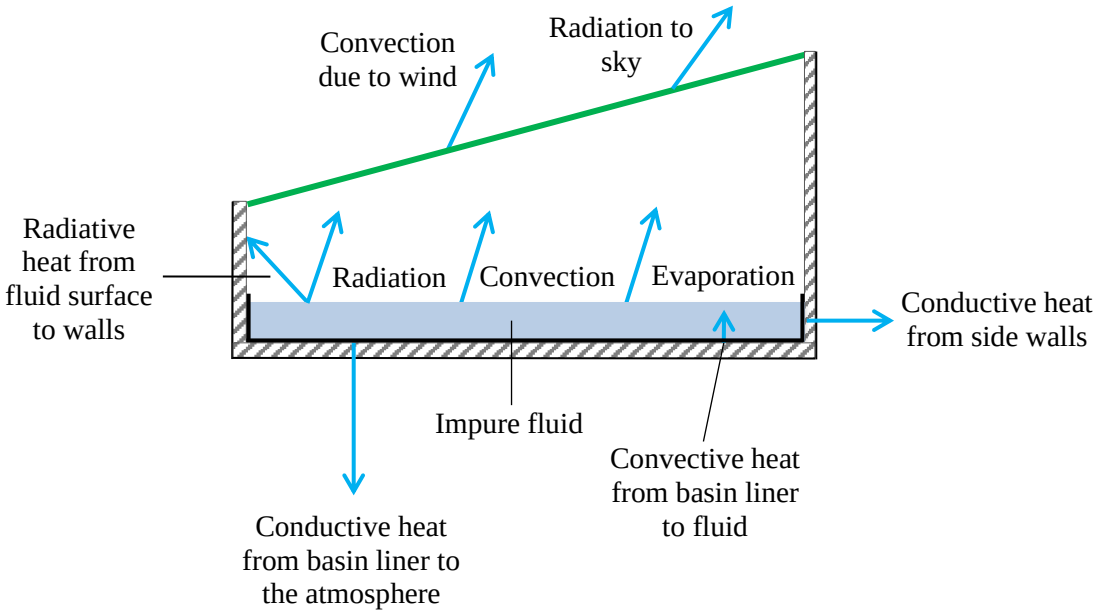

Figure 2.7: Heat transfer processes within a conventional solar still.

2.5.2.1. Internal heat and mass transfer processes

2.5.2.1.1. Convection

In a solar still, there are two cases of internal convective heat transfer; (i) between the impure fluid inside the basin and the glass cover and (ii) between the basin liner and the impure fluid. In the first instance, the rate of convective heat transfer between the fluid in the basin and the glass cover ($q_{cv,f-g}$) is given as a function of the surface area of the fluid (A_f), the convective heat transfer coefficient between the fluid and the glass cover ($h_{cv,f-g}$) and the temperature difference between the fluid and the glass cover (T_f – T_g). This can be expressed mathematically as given in Equation (2.9), according to Newton's Law of Cooling.

$$q_{cv,f-g} = A_f h_{cv,f-g}(T_f - T_g) \quad (2.9)$$

A similar equation can be written for the rate of convective heat transfer between the basin liner and the fluid, as given in Equation (2.10).

$$q_{cv,bl-f} = A_{bl} h_{cv,bl-f}(T_{bl} - T_f) \quad (2.10)$$

2.5.2.1.2. Radiation

The radiative heat transfer that occurs inside a solar still is between the basin fluid and the glass cover. The rate at which this radiative heat transfer occurs ($q_{r,f-g}$) is given as a function of the radiative heat transfer coefficient between the fluid and the glass cover ($h_{r,f-g}$), the surface area of the basin fluid and the temperature difference between the fluid and the glass cover, as expressed in Equation (2.11).

$$q_{r,f-g} = A_f h_{r,f-g}(T_f - T_g) \quad (2.11)$$

2.5.2.1.3. Evaporation

The rate of evaporative heat transfer between the fluid and the glass cover ($q_{e,f-g}$) is given as a function of the evaporative heat transfer coefficient between the fluid and glass cover ($h_{e,f-g}$), the surface area of the fluid and the temperature difference between the fluid in the basin and the glass cover, as given in Equation (2.12).

$$q_{e,f-g} = A_f h_{e,f-g}(T_f - T_g) \quad (2.12)$$

2.5.2.2. External heat transfer processes

External heat transfer processes are considered as the heat losses from the solar still, consisting of radiation, convection and conduction which are independent of each other (Elango, Gunasekaran & Sampathkumar, 2015).

2.5.2.2.1. Radiation

Heat is lost from the outer surface of the glass cover via radiation to the sky. The rate of energy loss to the sky due to radiation ($q_{r,g\text{-}s}$) is dependent on the area of the glass cover (A_g), the radiative heat transfer coefficient from the glass cover to the sky ($h_{r,g\text{-}s}$) and the temperature difference between the glass cover and the sky ($T_g - T_s$) as given in Equation (2.13).

$$q_{r,g-s} = A_g h_{r,g-s}(T_g - T_s) \tag{2.13}$$

2.5.2.2.2. Convection

The rate of heat loss from the surface of the glass cover to the atmosphere due to the effects of the wind ($q_{cv,g\text{-}atm}$) is a function of the area of the glass cover, the convective heat transfer coefficient between the glass cover and the atmosphere ($h_{cv,g\text{-}atm}$) and the temperature difference between the glass cover and the atmosphere ($T_g - T_{atm}$). This can be expressed mathematically as given by Equation (2.14).

$$q_{cv,g-atm} = A_g h_{cv,g-atm}(T_g - T_{atm}) \tag{2.14}$$

2.5.2.2.3. Conduction

Heat is lost via conduction both from the basin liner and from the side walls of the basin to the atmosphere. The rate of conductive heat lost from the basin liner to the atmosphere ($q_{co,bl\text{-}atm}$) can be expressed as given in Equation (2.15). It is dependent on the area of the basin liner (A_{bl}), the conductive heat transfer coefficient between the basin liner and the atmosphere ($h_{co,bl\text{-}atm}$) and the temperature difference between the basin liner and the atmosphere ($T_{bl} - T_{atm}$).

$$q_{co,bl-atm} = A_{bl} h_{co,bl-atm}(T_{bl} - T_{atm}) \tag{2.15}$$

A similar mathematical expression, given in Equation (2.16) can be used to express the rate of conductive heat lost from the side walls of the basin to the atmosphere ($q_{co,sw\text{-}atm}$).

$$q_{co,sw-atm} = A_{sw} h_{co,sw-atm} (T_f - T_{atm}) \quad (2.16)$$

2.6. Solar stills with nanofluids

The use of nanofluids in solar stills is a relatively new method of enhancing the distillate output. A nanofluid is a fluid containing a base fluid (such as water, ethylene glycol or oil) and nanometre-size particles, called nanoparticles, suspended in the fluid. Choi and Eastman (1995) first proposed the concept of adding metallic nanoparticles to conventional heat transfer fluids to obtain a nanofluid. There is a wide spectrum of solid materials available for the production of nanoparticles. These nanoparticles can be made from (i) metals, for example, aluminium, copper, titanium, silver, tin; (ii) oxides, for instance, copper oxide, aluminium oxide, titanium oxide; or (iii) carbonic structures, for example, carbon nanotubes. Different ranges of nanoparticle size have been reported in literature.

Hu et al. (2007) investigated packed beds of alumina nanoparticles of diameter range 11-500 nm. Pinto and Fiorelli (2016) reported that nanoparticles have an average size of less than 100 nm. This specification of nanometre size is consistent with the approximate range (1-100 nm) given by the International Organization for Standardization (2015). Nanoparticles can be exploited either to reduce or augment the transfer of heat from one point to another. Nanoparticles with low thermal conductivities are used in insulation applications (Elsahati & Richards, 2017). On the other hand, nanomaterials with high thermal conductivities assist in raising the rate of heat transfer, and this is the context in which nanofluids are exploited in solar stills.

2.6.1. Heat transfer characteristics of nanofluids

A nanofluid exhibits better heat transfer and optical characteristics compared to a base fluid (Gorji, Ranjbar & Mirzababaei, 2015), attributed to the presence of nanoparticles with high thermal conductivities. Sahota and Tiwari (2016a) stated that the thermal conductivity of a nanofluid is the most crucial characteristic which is responsible for improving heat transfer. The degree of enhancement in the thermal conductivity of a nanofluid is dependent on the size, shape, concentration and thermal characteristics of the nanoparticles (Xuan & Roetzel, 2000).

Keblinski et al. (2002) postulated that there are four main factors which contribute to the enhancement of thermal conductivity in nanofluids, namely:

(i) Brownian motion of the nanoparticles, resulting in the movement of the nanoparticles through the base fluid and the possible collision amongst one another, thus contributing to the increase in thermal conductivity by the direct transport of heat from one nanoparticle to another.

(ii) Liquid layering at the liquid and nanoparticle interface, causing the atomic structure of the liquid layer to be considerably more ordered than that of the base fluid. Since crystalline solids, in which the constituents are arranged in an orderly structure, exhibit higher thermal characteristics than liquids, the liquid layering at the liquid – nanoparticle interface is expected to increase the thermal conductivity of the nanofluid.

(iii) The nature of heat transport in nanoparticles, whereby heat is transferred by phonons which are quanta of energy associated with the crystalline lattice vibrations of the nanoparticles. A considerable increase in thermal conductivity could occur as a result of ballistic phonon effects, for instance if the ballistic phonon initiated in one nanoparticle reaches another nanoparticle within proximity in the liquid.

(iv) Nanoparticle clustering, whereby the nanoparticles become agglomerated into percolating patterns, leading to the generation of lower thermal resistance paths. Moreover, these percolating patterns are separated by liquid layers which are thin enough to allow rapid heat transfer between the nanoparticles, thereby resulting in higher thermal conductivity of the nanofluid. Nevertheless, clustering may also lead to a reduction in thermal conductivity due to sedimentation of nanoparticles, thus generating bigger nanoparticle-free regions within the liquid having high thermal resistance.

2.6.2. Mechanisms of heat transfer in a solar still with nanofluids

The heat transfer mechanisms which occur in a solar still with a nanofluid include the following:

(i) convection and radiation from the surface of the glass cover to the atmosphere,

(ii) convection, radiation and evaporation from the surface of the nanofluid in the basin to the glass cover,

(iii) convection from nanoparticles to the base fluid,

(iv) convection from the basin liner to the nanofluid,

(v) conduction from the basin liner to the nanoparticles and molecules of the base fluid which are in direct contact with the basin liner at the boundary between the basin liner and the nanofluid,

(vi) conduction from the basin liner to the outer surface of the bottom insulation, and

(vii) conduction from the side walls of the basin to the atmosphere.

The internal and external heat transfer mechanisms for a solar still with nanofluids are illustrated in Figure 2.8.

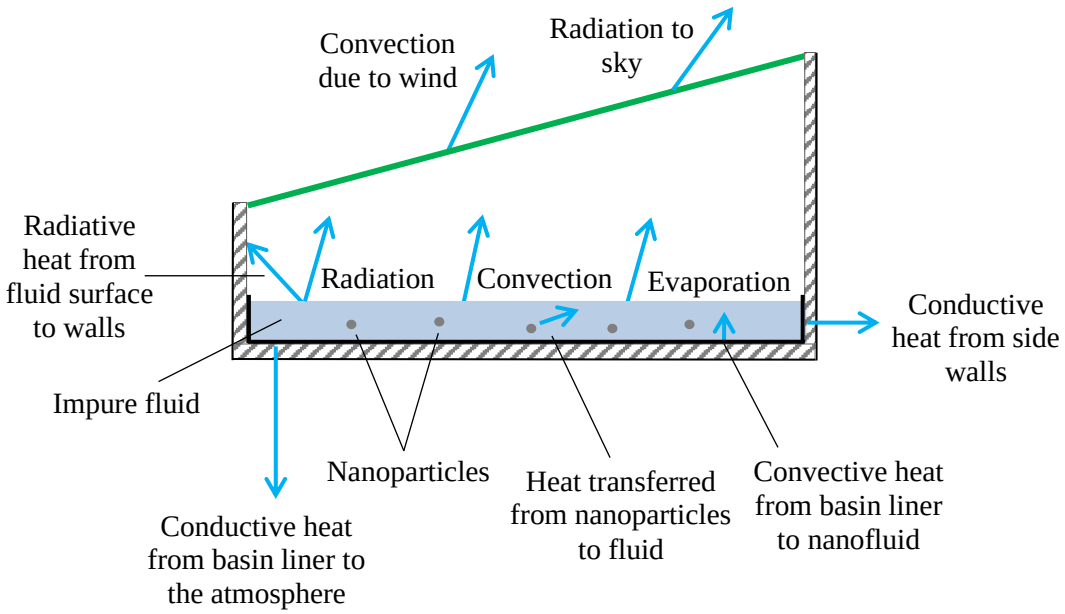

Figure 2.8: Internal and external heat transfer processes in a solar still with nanofluids.

The purpose of adding nanoparticles in solar stills is to obtain a higher yield of fresh water. It is to be noted that the nanoparticles remain inside the basin of the solar still during the continuous processes of evaporation and condensation. Nanoparticles enhance the thermal conductivity of the nanofluid due to the reasons mentioned in the above section. Sahota and Tiwari (2016a) claimed that the addition of nanoparticles in the basin of a solar still also leads to the improvement of the optical characteristics of the fluid. They claimed that this occurs as a result of the ascension of the plasmon resonance absorption bands in the visible and infrared spectrum, causing the optical absorption spectrum of the nanoparticles to match that of the solar radiation spectrum, thereby allowing the nanoparticles to absorb solar radiation directly into the base fluid. The temperature of each distinct nanoparticle thus increases and subsequently, both the temperature and the thermal conductivity of the nanofluid also increase. In addition to the heat transferred from the basin liner to the nanofluid, heat is also transferred directly from the nanoparticles to the fluid, as shown in Figure 2.8.

2.7. Performance of solar stills with nanofluids

2.7.1. Application of the Laws of Thermodynamics in mathematical modelling of solar stills

Thermodynamics can be described as the study of energy, its different forms and its transformation from one form into another, and its synergy with matter (Rathakrishnan, 2006). This concept is essential in engineering and science because it gives an insight into the type and magnitude of energy transformations which occur, so that they can be interpreted and applied accordingly (Annamalai, Puri & Jog, 2011). The thermodynamic performance of a solar still is most often assessed based on the principle of conservation of energy, which constitutes the First Law of Thermodynamics. According to the First Law of Thermodynamics, energy can neither be created nor destroyed. It can only be converted from one form to another, with the overall energy of the system remaining constant (Zohuri, 2018).

Mathematical models for solar stills based on the First Law of Thermodynamics have been reviewed in previous studies. Kaushal and Varun (2010) provided a review on different types of solar stills with their energy balance equations. They claimed that for a specific water requirement, there is a need to select the appropriate solar still based on local and operating conditions. Sampathkumar et al. (2010) gave a review on thermal modelling of active solar stills based on energy balance equations. They claimed that various factors such as capital,

operating and maintenance costs, as well as solar radiation availability, water requirements, saline water availability, improved use of available hot waste water and life of the solar still need to be considered for the successful implementation of solar stills in remote areas.

Elango, Kannan and Murugavel (2015) provided a comprehensive review on thermal modelling of active and passive solar stills, as well as on innovative designs of solar stills. They observed that in each investigation, the energy balances were adapted to suit the structure of the solar still which was studied. Moreover, they found that most of the studies were limited to laboratory conditions while only a few investigations were conducted under actual outdoor conditions. They further claimed that all the developed models have their own pros and cons but additional research is needed concerning real time applications of solar stills.

Edalatpour et al. (2016) gave a review on the numerical studies conducted on various types of solar stills. They presented the mathematical models of solar stills based on energy balance equations, as well as the Computational Fluid Dynamics (CFD) formulation used for modelling solar stills. They claimed that studies employing CFD simulations could be carried out on solar still designs where different techniques such as the use of reflectors or fins have been used for enhancing the productivity of solar stills.

Some studies on solar stills have also been conducted based on an exergy analysis, derived from the Second Law of Thermodynamics, aimed at finding the sources of thermodynamic inefficiencies, their locations and magnitudes (Singh et al., 2016). Ranjan and Kaushik (2013) presented a review on the thermodynamic models for both exergy and energy analysis of solar stills. They found that the exergy efficiencies range between 19% and 26% for a triple effect solar still, 17% to 20% for a double effect solar still and below 5% for a single effect solar still. On the other hand, they found that the energy efficiency of a conventional solar still could vary between 20% and 46%. They further claimed that most of the studies conducted on solar stills have been based on the First Law of Thermodynamics and there is limited research on the exergy analysis of solar stills but it is important to analyse a solar still based on the concept of exergy. Sharshir et al. (2017a) provided a review of the studies carried out on solar stills based on both exergy and energy. It was found that the productivity of a solar still is dependent on both external and internal operating conditions, as well as the design features and technical advancements of the solar still.

2.7.2. Thermodynamic performance of solar stills with nanofluids

The first study conducted on the use of nanofluids in solar stills was only published recently, in the year 2012. Gnanadason et al. (2012) investigated experimentally the effect of using carbon nanotube (CNT) based nanofluids in a single basin solar still under vacuum at Tamil Nadu in India. They claimed that the productivity of the solar still with nanofluids was higher as compared to the solar still without nanofluids. They attributed this to the presence of CNT in the basin of the solar still which resulted in an increase in the temperature of the basin fluid, in turn improving the rate of evaporation. They further stated that the average daily productivity of the solar still with nanofluids and operating under vacuum was 4 L for a basin area of 0.36 m^2. Gnanadason et al. (2013) conducted an experimental investigation on a single basin solar still with CNT based nanofluids and they found that for a basin area of 1 m^2, the average daily productivity of the solar still with nanofluids was around 6 litres, as compared to only 3 L in the case of the solar still without nanofluids, hence an increase in approximately 50% could be achieved when using nanofluids.

Panitapu et al. (2014) conducted an experimental analysis on a single slope solar still containing Titanium Oxide (TiO_2) nanoparticles under the climatic conditions of Hyderabad in India. Their results indicated that the temperatures of the basin, water, inner and outer surface of the glass cover were higher when using the TiO_2-water nanofluid as compared to using water only. They further stated that TiO_2 is a promising nanoparticle which can be used in improving the productivity of a solar still. Kabeel, Omara and Essa (2014a, 2014b) carried out an experimental investigation on a solar still with nanofluids and operating under vacuum by means of a vacuum fan which was connected to an external condenser at Kafrelsheikh University in Egypt. Photovoltaic panels were used to run an electric DC motor which in turn ran the vacuum fan. They claimed that the use of an external condenser without nanofluids caused the productivity to increase by approximately 53.2%. They tested two nanoparticles, namely cuprous oxide (Cu_2O) and aluminium oxide (Al_2O_3), at weight concentrations ranging from 0.02% to 0.2% and with an average particle size of 10 to 14 nm. They found that the highest productivity was achieved by the solar still operating under the vacuum fan and with Cu_2O nanoparticles, at a concentration of 0.2%. They further claimed that the solar still with the Cu_2O nanoparticles could achieve an increase in productivity of 133.64 % and 93.87%, with and without vacuum, as compared to a conventional solar still. On the other hand, the solar still with the Al_2O_3 nanoparticles could achieve an increase in productivity of 125.0% and 88.97%, with and without vacuum, as compared to a conventional solar still.

Singh and Singh (2015) examined experimentally the performance of a single slope solar still with Al_2O_3-water nanofluid under the meteorological conditions of Jaipur in India. They found that the thermal efficiency of the solar still with the nanofluid was 5% higher than the thermal efficiency of the solar still without the nanofluid. Additionally, they stated that the distillation process occurred faster when nanofluid was used in the solar still.

Rajasekhar and Eswaramoorthy (2015) conducted an experimental study on the performance of a single slope solar still with Al_2O_3 nanoparticles dispersed in paraffin wax which acts as the Phase Change Material (PCM), under the climatic conditions of Bangalore in India. The solar still was made up of two partitions, one to store the impure water and the other one to store the PCM with the Al_2O_3 nanoparticles. Their results revealed that the average daily yield was 2.800 L, 4.195 L and 4.840 L for the solar still without the PCM, with the PCM only and with Al_2O_3 nanoparticles dispersed in the PCM, respectively. An increase of approximately 15.4% in the productivity was achieved when nanoparticles are used in the PCM as compared to the solar still with the PCM only. On the other hand, the use of nanoparticle-based PCM resulted in a productivity increase of around 72.9% over the conventional solar still. Moreover, they also reported that the daily efficiency of the solar still without PCM, with PCM and with nanoparticle-based PCM was 25%, 45% and 66%, respectively.

Shankar et al. (2015) carried out an experimental investigation on a single slope solar still with and without nanofluids. They used Al_2O_3 as nanoparticles and performed the experiments under the climatic conditions of Jabalpur in India. They claimed that the solar still with and without the nanofluid could achieve a daily productivity of 2.605 L/m^2 and 3.258 L/m^2, respectively. Thus, a productivity increase of approximately 25% was achieved when adding Al_2O_3 nanoparticles to the basin water of the solar still.

Elango, Kannan and Muragavel (2015) investigated experimentally the effect of using three different nanoparticles, namely Al_2O_3, SnO_2 (Tin Oxide) and ZnO (Zinc Oxide), at a weight concentration of 0.1%, in a single basin single slope solar still under the climatic conditions of Tamil Nadu in India. Al_2O_3, SnO_2 and ZnO were found to increase the productivity of the solar still by 29.95%, 18.63% and 12.67% respectively. The maximum daily outputs from the solar stills with Al_2O_3, SnO_2 and ZnO were 0.935 L, 0.805 L and 0.750 L respectively while the solar still without nanofluids could only achieve a maximum daily yield of 0.655 L.

Omara, Kabeel and Essa (2015) conducted an experimental investigation on the performance of a corrugated wick solar still with nanofluids at Kafrelsheikh University in Egypt. Their results showed that the productivity of the corrugated wick solar still at a saline water depth of 1cm, with internal mirrors, a vacuum pump operated by photovoltaic panels, external condenser and with Cu_2O nanoparticles, was 7.625 L/day, which is around 285.10% higher than that of a conventional solar still. On the other hand, the productivity of the corrugated wick solar still at a saline water depth of 1cm, with internal mirrors, external condenser and with Al_2O_3 nanoparticles was 7.275 L/day, which is nearly 254.88% higher than a conventional solar still. The particle size of the nanoparticles was in the range of 10 to 14 nm, at a weight concentration of 1.97%.

Navale, Kumbhar and Bhojawani (2016) studied experimentally the performance of a single slope solar still with Al_2O_3 and CuO (Copper Oxide) nanoparticles under the climatic conditions of Pune in India. They found that the productivity of the solar still with Al_2O_3 and CuO, each at 0.3% concentration was 45.19% and 89.42%, respectively higher than that of the solar still without nanofluids. The average hourly yield of the solar still with Al_2O_3 and CuO at 0.3% concentration during hours of peak sunshine was 0.302 L and 0.394 L, respectively.

Gupta et al. (2016) conducted an experimental investigation on a single slope solar still with white painted side walls and CuO nanoparticles at 0.12% weight concentration, under the climatic conditions of Jabalpur in India. Their results indicated that the daily productivity of the solar still at a water depth of 5 cm and 10 cm was 3.445 $Lm^{-2}day^{-1}$ and 3.058 $Lm^{-2}day^{-1}$, respectively. On the other hand, a conventional solar under the same climatic conditions could only achieve a daily productivity of 2.814 $Lm^{-2}day^{-1}$ and 2.351 $Lm^{-2}day^{-1}$ at a water depth of 5 cm and 10 cm, respectively. Therefore, the addition of CuO nanoparticles in the basin water of the solar still resulted in an increase in productivity of 22.42% and 30.07% at a water depth of 5 cm and 10 cm, respectively. Ankoliya and Modi (2016) investigated experimentally the performance of a single slope double basin solar still with and without Al_2O_3 nanoparticles under the climatic conditions of Valsad in India. They indicated that the daily yield of the solar still with the Al_2O_3 nanoparticles was 49% higher than that of the solar still without the Al_2O_3 nanoparticles.

Sahota and Tiwari (2016a, 2016b) carried out a numerical study on the performance of a double slope solar still with nanofluids based on the climatic conditions of New Delhi in

India. In the first study (2016a), they used three different nanoparticles, namely Al_2O_3, TiO_2 and CuO, each having a particle size of 20 nm, at a concentration of 0.25%. Their results revealed that the thermal energy efficiencies were 50.34%, 46.10% and 43.81% for the solar stills with Al_2O_3, TiO_2 and CuO respectively, while the thermal energy efficiency for the solar still with water only was 37.78%. Thus, Al_2O_3 was found to be the most efficient nanoparticle, achieving the highest increase in the thermal energy efficiency. On the other hand, the thermal exergies were 14.10% for Al_2O_3, 12.38% for TiO_2 and 9.75% for CuO compared to only 4.92% for water. Furthermore, they claimed that the productivity of the solar still with Al_2O_3 was higher for all weather conditions, followed by TiO_2 and CuO, in descending order of productivities. The total yield of fresh water obtained for the month of March was 45.23 L, 42.72 L and 39.74 L with Al_2O_3, TiO_2 and CuO respectively. The increase in the yield of fresh water was 19.4%, 12.77% and 4.91% with Al_2O_3, TiO_2 and CuO respectively, as compared to the yield of the solar still without nanofluids. In the second study (2016b), they investigated the effect of varying concentrations of Al_2O_3 nanoparticles on the productivity of the double slope solar still. Their results showed than an increase in the average daily yield of 12.2% and 8.4% could be achieved when 35 kg and 80 kg base fluid mass was used respectively, at a 0.12% concentration of Al_2O_3 nanoparticles, with an average particle size of 20 nm.

Sahota, Shyam and Tiwari (2017a) conducted a numerical analysis on the performance of double slope solar stills with nanofluids under the climatic conditions of New Delhi in India. Three different nanoparticles were studied, namely Al_2O_3, TiO_2 and CuO, each having a diameter of 20 nm. The annual productivity of the double slope solar still with Al_2O_3, TiO_2 and CuO increased by 19.10%, 10.38% and 5.26%, respectively, as compared to a double slope solar still with water only. This represents a total annual yield of 1483.65 kg, 1370.86 kg and 1307.21 kg with Al_2O_3, TiO_2 and CuO respectively. Moreover, both the annual energy and exergy of the solar still with the nanofluids were found to be higher than those of a solar still with water only. The increase in the annual energy of the system with Al_2O_3, TiO_2 and CuO was 26.76%, 19.36% and 12.96%, respectively. On the other hand, the rise in the annual exergy of the solar still with Al_2O_3, TiO_2 and CuO was found to be 37.77%, 25.55% and 11.99%, respectively.

Sahota, Shyam and Tiwari (2017b) developed characteristic equations for a double slope solar still with nanofluids, coupled with 4 photovoltaic thermal flat plate collectors, with and without a heat exchanger inside the basin of the solar still. They studied theoretically three

different nanoparticles, namely CuO, Al_2O_3 and TiO_2, each of diameter 20 nm and at a concentration of 0.25%. The heat exchanger that they modelled was made of copper and was helical in shape. Their calculations were made based on the climatic conditions of New Delhi in India. They concluded that the daily productivity of the solar still without the heat exchanger with CuO, Al_2O_3 and TiO_2 was 6.93 kg, 6.26 kg and 5.59 kg respectively. On the other hand, with the incorporation of the helical heat exchanger, the daily productivity with CuO, Al_2O_3 and TiO_2 was 5.97 kg, 5.74 kg and 4.87 kg respectively. The increase in the daily productivity when using the nanofluids was 32%, 19.23% and 6.47% without the heat exchanger and 31.49%, 26.4% and 7.26% with the heat exchanger, for CuO, Al_2O_3 and TiO_2 respectively, in comparison to the solar still without the nanofluids.

Kabeel, Omara and Essa (2017) studied theoretically the performance of a single slope solar still with nanofluids, fan and external condenser under the meteorological conditions of Kafrelsheikh City in Egypt. The nanoparticles which they considered in their study include Al_2O_3 and Cu_2O, with a weight concentration ranging from 0.02 to 0.3% and an average particle size of 10 to 14 nm. They validated their mathematical model which they developed in FORTRAN by using published experimental data from literature. The results revealed that the daily efficiency of the solar still with the external condenser was 73.85% and 84.16% using Al_2O_3 and Cu_2O, respectively. On the other hand, they claimed that the daily efficiency of a conventional solar still was 34% while that of a solar still with external condenser only was 46.23%. Additionally, they found that the daily productivity of the solar still with the fan operating at a speed of 1350 rpm was 2.875 and 3.620 $Lm^{-2}day^{-1}$ with Al_2O_3 and Cu_2O respectively, at a weight concentration of 0.02%. The enhancement in productivity was 86.08% with Al_2O_3 and 106.86% with Cu_2O as compared to the solar still without nanofluids.

Sharshir et al. (2017b) performed an experimental investigation on a single slope solar still with nanoparticles, PCM and film cooling, under the climatic conditions of Wuhan in China. They used flake graphite nanoparticles (FGN), having a mean lateral size and thickness of approximately 1.3 μm and 100 nm, respectively. They studied the performance of the solar still under four different scenarios, namely (i) the addition of 0.5% mass concentration of FGN to the basin of the solar still; (ii) the incorporation of 0.5% mass concentration of FGN and 20 stainless steel pipes containing PCM, with each pipe having a length of 49 cm and a diameter of 1.6 cm; (iii) the addition of 0.5% mass concentration of FGN and the inclusion of cooling water, at a mass flowrate of approximately 0.03 kgs^{-1} and (iv) the combination of

FGN, PCM and cooling water over the outer glass cover. Their results showed that the productivity of the modified solar still increased by 50.28%, 65%, 56.15% and 73.8% in scenarios (i) to (iv), respectively, in comparison to a conventional solar still.

Mahian et al. (2017) investigated both theoretically and experimentally the performance of a single slope solar still equipped with two solar collectors and a heat exchanger under the climatic conditions of Bangkok in Thailand. They investigated the effect of using water and nanofluids as the working fluid in the heat exchanger. They studied three performance indices for the solar still, namely fresh water yield and energy and exergy efficiencies. The nanofluid was first allowed to pass through the two solar collectors in order to get heated up and it was subsequently made to enter the heat exchanger in the basin of the solar still so as to transfer heat to the impure basin water. The nanofluid was then returned to the nanofluid tank. Two different nanofluids were considered, namely SiO_2 (Silicon Dioxide) in water and Cu (Copper) in water. They claimed that for inlet temperatures of less than 60°C, the heat exchanger with water as the working fluid is not beneficial while the heat exchanger with nanofluids can increase the performance indices of the solar still by approximately 10% at such inlet temperatures. Moreover, they found that for higher temperatures, for instance at 70°C, the use of the heat exchanger is advantageous but using nanofluids instead of water as the working fluid only increase the performance indices by about 1%. Furthermore, they established that at higher temperatures, the SiO_2-water nanofluid can achieve higher performance indices as compared to the Cu-water nanofluid. Additionally, they found that decreasing the nanoparticle size from 100 nm to 7 nm in the heat exchanger causes the performance indices of the solar still to increase by less than 0.1%. It is to be noted that their study explored two different nanoparticle sizes in a context where the nanoparticles were used inside a heat exchanger and not dispersed directly into the basin water of a solar still.

Gupta, Kumar and Baredar (2017) carried out an experimental investigation on a single slope solar still with Cu_2O nanoparticles and with a sprinkler to allow the flow of water across the outer surface of the glass cover under the climatic conditions of Jabalpur in India. Their results revealed that the solar still with the nanoparticles and the sprinkler could achieve a daily yield of 4000 ml/m^2 while a conventional single slope solar still could only achieve a daily yield of 2900 ml/m^2.

Rashidi et al. (2018) conducted a numerical analysis on a stepped solar still, using Al_2O_3 nanoparticles of size 60 nm and employing CFD techniques. They found that the hourly

productivity of the stepped solar still increased by 22% when the solid volume concentration of the Al_2O_3 nanoparticle was increased from 0 to 5%. Nazari, Safarzadeh and Bahiraei (2019) studied both theoretically and experimentally the performance of a single slope solar still with Cu_2O nanoparticles under the climatic conditions of Kermanshah, Iran. The solar still was also fitted with an external thermoelectric condensing channel. The results revealed that the addition of 0.08% volume fraction of Cu_2O nanoparticles (of size 29 nm) in the basin water of the solar still equipped with an external thermoelectric channel could increase the productivity, energy efficiency and exergy efficiency by approximately 82.4%, 81.5% and 92.6%, respectively. Kabeel et al. (2019) investigated experimentally the performance of a pyramid type solar still comprising a basin coated with black paint containing TiO_2 nanoparticles under the meteorological conditions of Chennai, India. Their results showed that the productivity of the pyramid solar still with the basin coated with TiO_2 black paint was 6.1% higher than the productivity of a conventional pyramid solar still without TiO_2 black paint.

Robert et al. (2018) investigated experimentally the performance of a double slope solar still with Al_2O_3 nanoparticles and external reflecting mirrors under the climatic conditions of Oman. They used a black paint coating on the inside of the solar still. Their results showed that the solar still with the nanoparticles could achieve a 15% increase in the productivity as compared to the solar still without nanoparticles.

2.7.3. Economic evaluation of solar stills with nanofluids

An economic analysis is fundamental for evaluating the cost-effectiveness of any technology. The cost of water produced from desalination processes is highly dependent on the capital investment, energy, operational and maintenance costs, with the energy cost accounting for approximately 50% of the desalinated water cost (Al-Karaghouli & Kazmerski, 2013). Table 2.1 gives the overall costs of water produced from various desalination processes.

Table 2.1: Costs of water from desalination processes.

Source: Al-Karaghouli & Kazmerski (2013).

Desalination Technology	**Source of impure water**	**Capacity (m^3/day)**	**Cost of water (USD/m^3)**
ED	Brackish water	-	0.6 – 1.05
MED	Sea water	91 000 – 320 000	0.52 – 1.01
MED	Sea water	12 000 – 55 000	0.95 – 1.5
MED	Sea water	< 100	2.0 – 8.0
MSF	Sea water	23 000 – 58 000	0.56 – 1.75
RO	Brackish water	40 000	0.26 – 0.54
RO	Brackish water	20 – 1200	0.78 – 1.33
RO	Brackish water	Very small capacity (a few m^3day^{-1})	0.56 – 12.99
RO	Sea water	100 000 – 320 000	0.45 – 0.66
RO	Sea water	15 000 – 60 000	0.48 – 1.62
RO	Sea water	1000 – 4800	0.70 – 1.72
VC	Sea water	30 000	0.87 – 0.95
VC	Sea water	1000	2.0 – 2.6

As can be observed from Table 2.1, the cost of desalinated water ranges from 0.6 to 1.05 USD per m^3 for ED, 0.52 to 8 USD per m^3 for MED, 0.56 to 1.75 USD per m^3 for MSF, 0.26 to 12.99 USD per m^3 for RO and 0.87 to 2.6 USD per m^3 for VC. The key economic benefits of a solar still lie in its simple infrastructure, design, installation, operation and maintenance (Fath et al., 2003). Furthermore, there is no energy cost associated with a solar still as it uses thermal energy captured directly from the Sun. A few studies have examined the economics of solar stills with nanofluids. The experimental studies carried out by Gnanadason et al. (2012, 2013) employing the use of CNT based nanofluids in a single basin solar still revealed

that the total cost of the project was 300 USD, with a payback period of 1.5 years (when vacuum was used) while the total cost of the project was 260 USD, with a payback period of less than one year without the use of vacuum.

The experimental study conducted by Kabeel, Omara and Essa (2014a, 2014b) showed that the cost of producing 1 L of distillate using a conventional solar still was 0.048 USD. On the other hand, when using Cu_2O nanoparticles, the costs with and without vacuum were found to be 0.035 USD/L and 0.045 USD/L, while for the solar still with Al_2O_3 nanoparticles, the costs were 0.038 USD/L and 0.051 USD/L, with and without vacuum, respectively.

The experimental analysis on a single basin solar still with Al_2O_3, SnO and ZnO nanoparticles conducted by Elango, Kannan and Muragavel (2015) disclosed that a 22.50% higher investment is required for a solar still with nanofluids as compared to a conventional solar still. Nonetheless, they claimed that the payback period for a solar still with nanofluids is only 2.85 years, which is less than that of a conventional solar still which has a payback period of 3.2 years.

The cost estimates from the experimental study by Singh and Singh (2015) on a single slope solar still with Al_2O_3-water nanofluid showed that the total cost of the project was 205 USD. The experimental study on a single slope solar still with Al_2O_3 nanoparticles dispersed in paraffin wax carried out by Rajasekhar and Eswaramoorthy (2015) revealed that total cost of the still was 41 721 INR, which is equivalent to 647 USD (based on an exchange rate of 1 USD = 64.47 INR).

The experimental investigation by Gupta et al. (2016) on a single slope solar still with and without CuO nanoparticles disclosed that the cost of water for the conventional and modified solar still was 0.61 INR/L (equivalent to 0.0095 USD/L) and 0.53 INR/L (equivalent to 0.0082 USD/L) at a water depth of 10 cm; and 0.51 INR/L (equivalent to 0.0079 USD/L) and 0.40 INR/L (equivalent to 0.0062 USD/L) at a water depth of 5 cm, respectively. By conducting a numerical analysis, Sahota, Shyam and Tiwari (2017a) claimed that the cost of a double slope solar still with Al_2O_3, TiO_2 and CuO nanofluids was 313.17 USD, 357.24 USD and 359.54 USD, respectively while the corresponding cost of the solar still without nanofluids was 250.29 USD. Additionally, the experimental investigation conducted by Kabeel et al. (2019) on a pyramid solar still with a basin coated with TiO_2 black paint revealed that the cost of distilled water was 0.0107 USD/L. The experimental investigation conducted by Gupta, Kumar and Baredar (2017) showed that the cost of distilled water from

the solar still with nanoparticles and the water sprinkler was 0.0152 USD/L (based on an exchange rate of 1 USD = 64.47 INR).

2.7.4. Environmental benefits of using nanofluids in solar stills

The high energy consumption and brine disposal from desalination processes lead to harmful impacts on the environment but switching to desalination techniques powered by renewable energy helps in mitigating these impacts (Al-Karaghouli & Kazmerski, 2013). Solar distillation uses solar energy which has no GHG emissions.

The environmental benefit of using nanofluids in solar stills has only been examined in one study (Sahota, Shyam & Tiwari, 2017a). The results from this numerical investigation revealed that the amount of CO_2 mitigated was 5.91 tonnes per annum for the solar still without nanofluids and 7.49, 7.05 and 6.68 tonnes per annum for the solar stills with Al_2O_3, TiO_2 and CuO, respectively, calculated on the basis of energy and the average amount of CO_2 emitted from the combustion of coal to generate electricity. It is evident from this study that the exploitation of nanoparticles in solar stills increases the quantity of avoided carbon emissions.

2.8. Preparation of nanofluids

The preparation of nanofluids is a crucial step as it greatly affects the stability and the thermophysical properties of the nanofluids (Bhattad, Sarkar & Ghosh, 2018). The stability of a nanofluid can be analysed in terms of its Zeta potential. The latter can be defined as the potential difference between the bulk fluid and the static layer of fluid connected to the nanoparticles, with a higher positive or negative value representing a more stable nanofluid and lower values representing a less stable nanofluid (Choudhary et al., 2017). There are two major techniques by which nanofluids are prepared, namely the single-step method and the two-step method.

2.8.1. Single-step Method

In the single-step method, also known as the one-step method, the production of the nanoparticles and the dispersion of the nanoparticles into the base fluid occurs in a single step (Devendiran & Amirtham, 2016). The single-step method can be further classified into the one-step chemical method whereby reduction of chemicals occur under microwave irradiation (Yu & Xie, 2012) and the one-step physical method which is derived from the VEROS (Vacuum Evaporation onto a Running Oil Substrate) technique, entailing the condensation of nanoparticles from the vapour phase into a running low vapour pressure fluid (Babita, Sharma & Gupta, 2016).

The advantage of the single-step technique is the production of highly stable nanofluids. This occurs as drying, storage, transport and dispersion of nanoparticles are avoided in this method, leading to negligible agglomeration of the nanoparticles and stable nanofluids (Li et al., 2009). On the other hand, some disadvantages of the one-step technique entail the following:

(i) The VEROS technique can only be used with low vapour pressure fluids (Mukherjee & Paria, 2013).

(ii) The one-step physical technique is costly and does not allow the production of nanofluids on a large scale. Moreover, in the one-step chemical method, residual reactants are left behind in the nanofluids due to stabilisation or incomplete reaction and this leads to the formation of impure nanofluids (Yu & Xie, 2012).

2.8.2. Two-step Method

The two-step method is the most commonly used technique for the preparation of nanofluids (Jama et al., 2016; Kong, Sun & Bao, 2017). In this technique, the nanoparticles are first produced via available commercial methods involving chemical, physical or mechanical processes such as grinding and milling and they are then dispersed into the base fluid (Mukherjee & Paria, 2013).

However, one major disadvantage of this method is that the nanoparticles tend to agglomerate and form clusters in the base fluid, leading to sedimentation (Mohammed et al., 2017). Consequently, various dispersion techniques aimed at minimising this issue have been developed, including the addition of a surfactant (or dispersant), sonication and regulating the pH value (Yang et al., 2017).

2.8.2.1. Addition of a surfactant

A surfactant is a chemical compound which is usually added to nanofluids in order to stabilize them. It has been claimed by Dey, Kumar and Samantaray (2017) that the addition of a surfactant to a nanofluid is both a simple and economical technique to improve the stability of a nanofluid.

The role of a surfactant is to reduce the surface tension of the base fluid, thus increasing the immersion of the nanoparticles in the base fluid (Mukherjee & Paria, 2013). Some examples of surfactants which are commonly used in the stabilization of nanofluids include sodium dodecyl benzene sulfonate (SDBS), sodium dodecyl sulphate (SDS), oleic acid (OA), polyvinyl pyrrolidone (PVP), hexadecyl trimethyl ammonium bromide (CTAB) and polyacrylic acid sodium (PAAS) (Kong, Sun & Bao, 2017).

Prasad, Gupta & Deepak (2015) stated that SDBS is the most effective surfactant for Al_2O_3-water nanofluid. They used a mass ratio of nanoparticle to surfactant of 10:1 in their study. Fuskele and Sarviya (2017) conducted a review on the preparation and stability of nanofluids and it was mentioned that SDBS is the most appropriate surfactant for the long-term stability of Al_2O_3-water nanofluids.

2.8.2.2. Sonication

Sonication is the process whereby supersonic waves are used to disintegrate clusters of nanoparticles into smaller fragments by means of either a bath sonicator or a probe sonicator, with the latter having proven to be more effective in the stabilisation of nanofluids (Dey, Kumar & Samantaray, 2017).

The duration of the sonication process influences the stability and thus, the thermal conductivity of the nanofluid. Mahbubul et al. (2015) investigated experimentally the effect of sonication time (0 to 5 hours) on the thermophysical properties of 0.5 vol.% of Al_2O_3-water nanofluid. They found that an increase in sonication time causes better dispersion and results in an increase in the density and thermal conductivity and a decrease in the viscosity. They recommended that the duration of sonication should at least be 2 hours for an improved nanofluid performance.

Lee et al. (2008) conducted an experimental analysis on Al_2O_3-water nanofluid at concentrations ranging from 0.01 to 0.3 vol.% using sonication at a frequency of 30-40 kHz. The nanoparticle size was 30 ± 5 nm. Their results revealed that the Zeta potential for the 0.1 vol.% nanofluid increases with sonication time up to 5 hours, after which a decrease in Zeta potential is observed. Thus, they concluded that the nanofluid is most stable when a sonication period of 5 hours is used. A similar trend was observed in the experimental investigation conducted by Barrett et al. (2013). They prepared Al_2O_3/water nanofluid at 1 vol.%, with the nanoparticle size being less than 50 nm in a sonic bath at 38 kHz. They found that a sonication period of 5 hours leads to a more stable nanofluid.

Gangadevi, Vinayagam and Senthilraja (2018) conducted an experimental investigation on the stability of 0.2 vol.% of Al_2O_3-water and CuO-water nanofluids using different sonication times. They claimed that the best thermal conductivities for both nanofluids were obtained with a sonication period of 4 hours and that the difference between the thermal conductivity of the nanofluids obtained with 4 hours and 5 hours of sonication is negligible.

Sidik et al. (2014) conducted a review on the preparation techniques of nanofluids and they found that the stability of Al_2O_3 nanofluids could last up to a month when sonication was used, irrespective of the type of base fluid used. Furthermore, they also stated that some researchers did not give sufficient information on how they prepared their nanofluids. Ilyas, Pendyala & Marneni (2014) also claimed that excessive sonication leads to negative impact on the stability of nanofluids.

2.8.2.3. Adjustment of pH

When the pH of a base fluid is adjusted, the electrostatic charges on the surface of the nanoparticles change (Dey, Kumar & Samantaray, 2017). Consequently, the electrostatic repulsive force between the nanoparticles increases, thus preventing attraction and collision between them. This increase in electrostatic force also results in a rise in the number of free particles due to the increase in the distance between the nanoparticles, subsequently minimizing agglomeration and improving the heat transport ability of the nanoparticles (Ju & Fang, 2009).

The experimental investigation conducted by Bouguerra et al. (2016) revealed that for an Al_2O_3-water nanofluid at 2 vol.%, an increase in the thermal conductivity of more than 15% can be obtained when the pH of the nanofluid is between 5.3 and 6.1. They further claimed that the optimum pH for the Al_2O_3-water nanofluid is 5.7, with a maximum increase in thermal conductivity of 21% being achieved at this pH value.

2.8.3. Preparation of aluminium oxide-water nanofluid

In this research, aluminium oxide-water nanofluid was used and it is thus essential to examine the various preparation techniques which have been investigated by researchers for this particular nanofluid. Mojarrad et al. (2014) prepared Al_2O_3-water and Al_2O_3-water/ethylene glycol nanofluids by the two-step method. The nanoparticles were in the range of 20 to 30 nm and spherical in shape. The researchers used sodium dodecyl benzene sulfonate (SDBS) as the surfactant, which was added to the base fluid and then sonicated in an ultrasonic bath (model: Elmasonic S80 H) for 2 hours. The amount of SDBS that they used was equal to one tenth the mass of nanoparticles. The Al_2O_3 nanoparticles were then added to the mixture and sonicated for 4 hours. The resulting mixture was then stirred with a magnetic stirrer (model: Stuart SB 162) for 5 hours. They claimed that the nanofluids were still very stable after a period of three days.

Khairul et al. (2016) prepared Al_2O_3-water and CuO-water nanofluids using the two-step method. They used sodium dodecyl benzene sulfonate (SDBS) as the surfactant, with varying weight concentrations from 0.05% to 0.2% for stabilizing the nanoparticles. They found that the optimum weight fraction of SDBS was 0.10% and 0.15% for the Al_2O_3-water and CuO-water nanofluids, respectively. They also claimed that the maximum increase in thermal conductivity was 10% and 14% with Al_2O_3 and CuO, respectively, at a nanoparticle weight

concentration of 0.15%. Furthermore, they stated that in all cases, the stability of the nanofluids lasted for more than a week, with no visual sign of nanoparticle sedimentation.

Das et al. (2017) carried out an experimental study on the use of surfactants in the preparation of Al_2O_3-water nanofluid, using the two-step method. They used three different surfactants, namely sodium dodecyl benzene sulfonate (SDBS), sodium dodecyl sulfate (SDS), and cetyl trimethyl ammonium bromide (CTAB). They first mixed the specific surfactant with distilled water and stirred the mixture with a magnetic stirrer for 1 hour. The Al_2O_3 nanoparticles were then added to this homogeneous mixture and stirred with a magnetic stirrer (Remi, model name 2MLH) for one hour and sonicated for 15 minutes by means of a probe sonicator (PCI Analytics, PKS750FM, at a power input rate of 0.167 J/s). They found that SDBS at a particle to surfactant mass ratio of 2:1 was the most effective, providing the best stabilization for several hours.

2.9. Purity of distillate obtained from solar stills with nanofluids

Riahi et al. (2015) claimed that the distillate obtained from solar stills meet the drinking water standards set by the World Health Organisation (WHO). Kabeel, Omara and Essa (2014b) conducted a water quality analysis on the distillate produced from a solar still with Cu_2O and Al_2O_3 nanoparticles. They reported TDS (total dissolved solids) values of 932 and 82 mg per litre, before and after desalination respectively, and pH values of 8.9 and 7.1, before and after desalination respectively. They further stated that these values are within the WHO drinking water standards.

Omara, Kabeel and Essa (2015) also conducted TDS and pH tests on water samples collected from a solar still with Cu_2O and Al_2O_3 nanoparticles. They reported TDS values of 980 and 90 mg per litre, before and after desalination, and pH values of 8.9 and 7.2, before and after desalination. They also stated that the water quality lies within the acceptable range set by the WHO. Robert et al. (2018) carried out a pH, turbidity and TDS test on the distillate collected from solar stills with and without Al_2O_3 nanoparticles. For the solar still without the Al_2O_3 nanoparticles, the pH, turbidity and TDS were found to be 6.8, 0.01 NTU and 22.56 ppm, respectively. On the other hand, for the solar still with the Al_2O_3 nanoparticles, the pH, turbidity and TDS were found to be 7.1, 0.02 NTU and 23.26 ppm, respectively. They further claimed that these values are within the range of standard values of pH, turbidity and TDS for drinking water.

2.10. Summary

Different concepts relevant to the study of nanofluids in solar stills, including solar radiation components, solar geometry and heat transfer mechanisms were given in this chapter. A comprehensive review of previous studies on the use of nanofluids in solar stills was also conducted. Based on this literature review, the following observations were noted:

a) The use of nanofluids in solar stills is quite a new research area and most of the studies were experimental only.
b) The few available numerical studies on solar stills with nanofluids did not take into account the view factor in the computation of the internal radiative heat transfer coefficient from the fluid to the glass cover in the mathematical models.
c) No study has investigated the effect of particle size of the nanoparticles dispersed in the basin fluid on the productivity of solar stills, and on the economic and environmental performance of solar stills.
d) The degree of enhancement in the productivity of a solar still with nanofluids as compared to a solar still without nanofluids is quite inconsistent, even for the same nanofluid. For instance, the study conducted by Sahota and Tiwari (2016b) revealed an increase in productivity of 8.4% with Al_2O_3 nanoparticles while another revealed an increase of 45.19% in the productivity of a solar still with the same nanoparticles (Navale, Kumbhar & Bhojawani, 2016).
e) Some contradictory results have been found regarding the comparison between different nanofluids in solar stills. For instance, some studies have found that Al_2O_3 nanoparticles can achieve a higher productivity than CuO nanoparticles (Sahota & Tiwari, 2016a; Sahota, Shyam & Tiwari, 2017a) while some studies have found the opposite trend, with CuO nanoparticles achieving a higher productivity than Al_2O_3 nanoparticles (Navale, Kumbhar & Bhojawani, 2016; Sahota, Shyam & Tiwari, 2017b).

Chapter 3 will provide detailed sections on design, modelling and experimentation of solar stills in an attempt to deal with some of the limitations which have been identified in this chapter.

CHAPTER 3

DESIGN, MODELLING AND EXPERIMENTATION OF SOLAR STILLS

In Chapter 1, the concept of a solar still was introduced as a sustainable means of generating potable water from sea water or brackish water. It was stated that the major drawback of a solar still lies in its low productivity and thus, many attempts have been made by researchers in order to enhance the productivity of a solar still, including the integration of solar collectors, reflectors, PCM, condensers, solar ponds, waste heat and nanofluids.

An extensive literature review on the use of nanofluids in solar stills was presented in Chapter 2. It was found that the first study involving the utilisation of nanofluids in solar stills was only conducted recently, in the year 2012, and most of the studies so far have been experimental only. Consequently, there is still a lot of scope for research on this topic. Some of the limitations concerning the use of nanofluids in solar stills which have been noted from the literature review include the following: a) the few available numerical studies did not incorporate the view factor between the fluid and the glass cover in the calculation of the internal radiative heat transfer coefficient; and b) the effect of nanoparticle size on the productivity of solar stills, and on the economic and environmental performance of solar stills have not been explored in any study. Consequently, it is desirable to take into account these aspects while examining the performance of solar stills with nanofluids. This present study is thus contributing to knowledge by investigating these aspects which have not been explored previously.

Chapter 3 deals with the design, modelling and experimentation of solar stills. The first section in Chapter 3 focuses on the design parameters of solar stills used in this study. The second part deals with the mathematical modelling of solar stills. Previous models were adapted in order to develop mathematical models for solar stills with and without nanofluids, taking into account the view factor. The mathematical models were then solved by writing a code in MATLAB, in order to investigate the effect of nanoparticle size on the productivity, and on the economic and environmental performance of solar stills. The third section gives an explanation on how the experiments were conducted on the solar stills with and without nanofluids. The fourth part of Chapter 3 discusses the development of a clearness index

correlation which was needed in order to compute the solar distribution inside the solar stills and the last section describes how the mathematical models were validated using statistical tools.

3.1. Solar still design

3.1.1. Selection of design parameters

In order to select the design parameters for a solar still, it is crucial to understand which parameters influence the productivity. The three factors which affect the productivity of a solar still include (i) environmental conditions such as solar radiation, wind speed and ambient temperature, which cannot be controlled; (ii) design parameters which can be controlled and (iii) operational factors which can be controlled. Consequently, the design parameters need to be selected in such a way that the distillate production is maximised. Operational factors such as cleaning of the transparent cover, are important during the experimental phase.

3.1.1.1. Type of solar still

There exist various types of solar stills such as single slope, double slope, stepped type and pyramid solar stills. A single slope solar still has various advantages over the other types as it is easier and cheaper to construct, operate and maintain (Nayi & Modi, 2018). Rubio, Porta and Fernández (2000) carried out an investigation aimed at comparing single slope and double slope solar stills and they indicated that there is negligible difference between the productivities of these two types of solar stills operating under the same conditions. On the other hand, an experimental analysis conducted by Dwivedi and Tiwari (2009) under the climatic conditions of New Delhi in India revealed that the annual productivity of a single slope solar still is higher than that of a double slope solar still.

Furthermore, Murugavel, Chockalingam and Srithar (2008) claimed that a single slope solar still is a better choice for locations which have latitudes greater than 20°. Otherwise, if a double slope solar still is used in such places, only one side of the transparent cover will obtain solar radiation while the other side will be in the shadow of the Sun. Consequently, in the context of this study, single slope solar stills were chosen as the experiments were conducted in South Africa at the University of Cape Town which has a latitude of 33.96° South.

3.1.1.2. Type of transparent cover material

In a solar still, solar radiation gets transmitted through a transparent cover and gets captured by the basin where it gets converted into heat, which is then transferred to the impure fluid inside the basin (Rajaseenivasan et al., 2013). The higher the amount of solar radiation that reaches the basin, the higher is the distillate output. Consequently, it is crucial for the transparent material to have a high transmissivity and low reflectivity and low absorptivity.

Some common materials which have been used as the transparent cover in a solar still includes glass and plastic. Bhardwaj, Kortenaar and Mudde (2013) claimed that glass is the preferred material as it gives a higher distillate output compared to other materials. Consequently, the type of transparent cover material chosen in this study was clear float glass due to its high transmissivity. This property allows a higher proportion of solar radiation to pass through the glass cover and reach the basin to heat up the basin fluid.

3.1.1.3. Inclination angle of transparent cover

The inclination angle of the glass cover, denoted by β, is the angle that the glass cover makes with the front wall of the solar still, as illustrated in Figure 3.1.

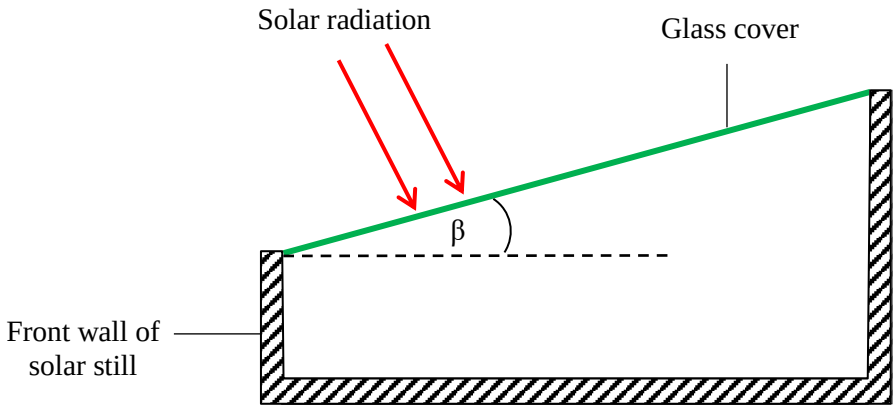

Figure 3.1: Inclination angle of glass cover.

Muftah et al. (2014) claimed that the angle of inclination of the glass cover greatly affects the productivity of a solar still. Singh and Tiwari (2004) conducted a numerical analysis on the performance of solar stills under various climatic conditions. They claimed that the annual productivity of the solar still is optimal when the glass cover tilt angle is equal to the latitude of the location. Khalifa (2011) conducted a comprehensive literature review on the effect of

tilt angle of the glass cover on productivity of solar stills. The observed trend in the research suggested that the optimum inclination cover angle is close to the latitude of the location.

Furthermore, Kabeel and El-Agouz (2011) indicated that a glass cover whose tilt angle is equal to the latitude of the location is optimised with regards to the solar azimuth angle and solar intensity of the location, thereby obtaining Sun rays nearly at normal incidence throughout the year. In this investigation, an inclination angle of 34° was chosen for the glass cover as the site where the experiments were conducted has a latitude of 33.96°.

3.1.1.4. Thickness of transparent cover

Panchal and Shah (2011) conducted an experimental analysis on the effect of glass thickness on the productivity of a solar still. They found that the solar still with the smallest glass cover thickness (4 mm) could achieve a higher yield than those with thicker glass covers (8 mm and 10 mm). Panchal (2016) investigated both theoretically and experimentally the effect of three different glass thicknesses, namely 4 mm, 5 mm and 6 mm on productivity of solar stills. The results revealed that the productivities of the 4 mm and 5 mm glass cover were respectively 27% and 12% higher than that of the 6 mm glass cover.

These studies have shown that the productivity of a solar still increases with decreasing glass cover thickness and that a glass cover of 4 mm thickness has been well established in the investigation of solar stills. Consequently, a 4 mm glass thickness was selected in the present study.

3.1.1.5. Orientation of solar still

It is crucial to position a solar still such that maximum solar radiation can be absorbed. Duffie and Beckman (2013) asserted that the optimum surface azimuth angle for maximum incident solar radiation is 180° if the collector is in the southern hemisphere and 0° if the collector is in the northern hemisphere, which means that the collector needs to be facing the equator.

This rule of thumb has been applied in the context of a solar still, where researchers have indicated that the transparent cover of the solar still should be oriented towards the south for northern latitudes and towards the north for southern latitudes (Murugavel, Chockalingam & Srithar, 2008; Panchal & Patel, 2017). Thus, in this investigation, the orientation chosen for the solar stills was north-facing (towards the equator) since the location where the experiments took place is in the southern hemisphere.

3.1.1.6. Basin of solar still

Fibre Reinforced Plastic (FRP) was chosen as material of construction for the basin as it has proved to be effective in previous studies (Tripathi & Tiwari, 2005; Singh et al., 2013; Sahota & Tiwari, 2016a; Sahota & Tiwari, 2016b, Panchal et al., 2017). FRP is resistant to corrosion and it is a light weight material which makes it ideal to be used in this study as the solar stills had to be mounted on the roof and it allowed for easier transportation and installation. Additionally, the basin was coated with black paint as black surfaces can absorb more solar radiation than light coloured surfaces.

3.1.1.7. Insulation

According to the Fourier rate equation, given in Equation (2.1), the rate of energy transferred during conduction is dependent on the thermal conductivity of the material through which conduction is taking place. Materials having high thermal conductivities are classified as conductors and those having low thermal conductivities are known as insulators. In the context of a solar still, an insulation material is needed to prevent the conduction of heat from the hot basin liner to the atmosphere.

According to Belessiotis, Kalogirou and Delyannis (2016), a suitable insulation material for solar stills should have a low thermal conductivity and be water resistant, lightweight but strong, easily replaceable if needed, able to withstand high temperatures up to approximately 90°C without undergoing any deformation and be able to easily fit to the bottom of the solar still. Since polystyrene possesses all of these characteristics, it was thus chosen in this study. Moreover, polystyrene has the added benefit of being a cost-effective insulating material which has been used in previous studies on solar stills (Cappelletti, 2002; Madhlopa & Johnstone, 2009b; Aboabboud, Mink & Kudish, 2009; Madhlopa & Johnstone, 2011; Heydari & Rahbar, 2016).

Furthermore, Garg and Prakash (2000) claimed that the productivity is higher when the base of a solar still is insulated. Belessiotis, Kalogirou and Delyannis (2016) also asserted that the bottom of a solar still should be insulated to minimize heat loss to the ground or to the surroundings. Consequently, a polystyrene sheet, of thickness 25 mm, was placed at the bottom of the basin of each solar still to increase the productivity by minimising heat losses to the environment.

3.1.1.8. Walls of solar stills

The walls of the solar stills were made of plywood, a material which has frequently been used in previous studies on solar stills (Madhlopa & Johnstone, 2009b; Kannan et al., 2014; Madhlopa, 2014; Rajaseenivasan, Raja & Srithar, 2014; Gupta et al., 2016; Deshmukh & Thombre, 2017). Plywood was chosen as it provides a rigid structure and also acts as an insulator to prevent heat loss from the side walls and bottom of the solar still. Moreover, plywood coated with paints are resistant to environmental conditions such as moisture and rain and are also unaffected by microorganisms and fungi (Sonmez, Budakci & Bayram, 2009). Therefore, all the plywood surfaces were coated with paint.

The 4 inner walls of the solar stills, namely the front wall, the back wall, the east wall and the west wall were coated with white paint, as illustrated in Figure 3.2. The inner walls were painted white as it has been found that the productivity of a solar still with white inner walls is 6.8% more efficient than a conventional solar still (Tenthani, Madhlopa & Kimambo, 2012). This was attributed to the fact that a larger amount of the incoming solar radiation could be reflected to the basin fluid, thereby increasing its temperature and maintaining a low temperature at the condensing surface. Other studies have also used white painted inner walls (Shankar et al., 2015; Gupta et al., 2016; Gupta et al., 2017). According to Gupta et al. (2016), the major benefit of using white coated inner walls is that heat loss from water vapour to the side walls is reduced, hence minimising heat loss to the atmosphere.

On the other hand, the 4 outer walls and the outer base of the solar stills were coated with black paint, as illustrated in Figure 3.2, in order to provide protection against climatic conditions and microorganisms. Additionally, black paint helps to prevent reflection of light from the solar still to the atmosphere, thereby contributing to minimizing heat loss to the environment. Figure 3.3 illustrates the dimensions of the solar stills.

Figure 3.2: White inner walls and black outer walls of north-facing solar stills.

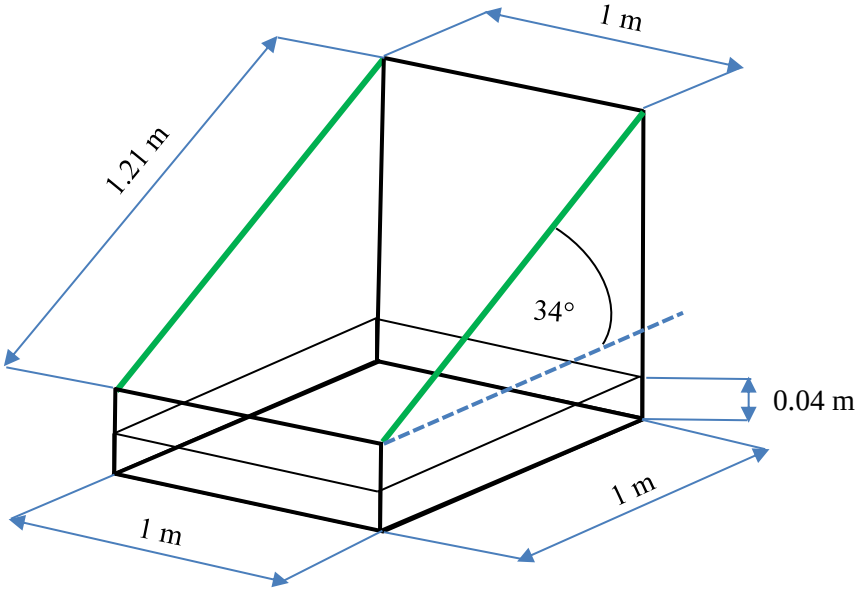

Figure 3.3: Dimensions of solar still.

3.1.1.9. Type of nanoparticle and surfactant

A previous investigation has revealed that aluminium oxide (Al_2O_3) nanoparticles could achieve a higher productivity than other nanoparticles such as SnO_2 and ZnO (Elango, Kannan & Muragavel, 2015). On the other hand, conflicting results have been obtained with regards to the comparison between Al_2O_3 and CuO in solar stills, with some studies revealing a higher productivity with Al_2O_3 nanoparticles (Sahota & Tiwari, 2016a; Sahota, Shyam & Tiwari, 2017a) while some studies indicating that CuO nanoparticles could achieve a higher yield than Al_2O_3 nanoparticles (Navale, Kumbhar & Bhojawani, 2016; Sahota, Shyam & Tiwari, 2017b). Other nanoparticles such as carbon nanotubes were not considered as based on the extensive literature review conducted in Chapter 2, it was found that carbon nanotubes have hardly been used in solar stills. Consequently, in this study, Al_2O_3 nanoparticles were chosen as they have been the most frequently used nanoparticles in solar stills and it has also been found that Al_2O_3 nanoparticles typically give a higher distillate yield as compared to other nanoparticles.

Additionally, sodium dodecyl benzene sulfonate (SDBS), $C_{18}H_{29}NaO_3S$, was used as a surfactant to prevent agglomeration of the nanoparticles as it has proved to be the most effective surfactant for Al_2O_3-water nanofluids (Prasad, Gupta & Deepak, 2015). The various sizes of the nanoparticles considered in this study were 10 nm, 50 nm and 100 nm. As

mentioned earlier, based on the extensive literature review which was conducted, no study examining the effects of nanoparticle size on the productivity of solar stills was found. Therefore, this study seeks to contribute to scientific knowledge by exploring the effect of nanoparticle size on the productivity of a solar still, both theoretically and experimentally.

All the design parameters that were chosen for the control solar still (without the nanofluids) and the solar stills with nanofluids are given in Table 3.1.

Table 3.1: Design parameters of solar stills.

Component	**Design parameter**	**Control solar still (without nanofluids)**	**Solar still with nanofluids**
Number of units	-	1	3
Glass cover	Type of material	Float glass	Float glass
	Angle of inclination	34°	34°
	Orientation	North-facing	North-facing
	Length	1.21 m	1.21 m
	Width	1 m	1 m
	Thickness	0.004 m	0.004 m
Basin, painted with Black Matt Paint	Type of material	FRP	FRP
	Length	1 m	1 m
	Width	1 m	1 m
	Height	0.04 m	0.04 m
Insulation (at the bottom of the basin)	Type of material	Polystyrene	Polystyrene
	Length	1 m	1 m
	Width	1 m	1 m
	Thickness	0.025 m	0.025 m
Distillate collector pipe	Type of material	Polyvinyl Chloride (PVC)	Polyvinyl Chloride (PVC)
Walls of solar still	Type of material	Plywood coated with paint	Plywood coated with paint
Nanoparticles	Type of nanoparticle	None	Al_2O_3
	Nanoparticle size	-	10 nm, 50 nm and 100 nm
	Nanoparticle shape	-	Spherical
	Mass	-	40 g
Surfactant	Type of surfactant	None	SDBS
	Mass	-	4 g

3.2. Mathematical modelling of solar stills

3.2.1. Selection of software package

The three software packages which have previously been used for solving mathematical models of solar stills with nanofluids include MATLAB, FOTRAN and ANSYS-FLUENT, as given in Table 3.2. In this present study, the software MATLAB was used as it excels in performing numerical calculations and it also offers easy access to graphing which is an application that most high-level programs such as C++, JAVA and FORTRAN do not offer (Moore, 2012).

Furthermore, MATLAB consists of a comprehensive library of pre-defined functions which make engineering calculations more efficient and these functions are also very powerful, generating rational outputs for a wide range of inputs while effectively dealing with error conditions (Chapman, 2015). Additionally, it can be noted from Table 3.2 that the most frequently used software for solving mathematical models of solar stills with nanofluids is MATLAB, which means that it is a well-established package which can produce reliable results.

Table 3.2: Software used in previous studies on solar stills with nanofluids.

Numerical Study	Software used	Type of solar still	Type of nanoparticles used
Sahota and Tiwari (2016a)	MATLAB	Double slope	Al_2O_3, TiO_2, CuO
Sahota and Tiwari (2016b)	MATLAB	Double slope	Al_2O_3
Sahota, Shyam and Tiwari (2017a)	MATLAB	Double slope	Al_2O_3, TiO_2, CuO
Sahota, Shyam and Tiwari (2017b)	MATLAB	Double slope	Al_2O_3, TiO_2, CuO
Kabeel, Omara and Essa (2017)	FORTRAN	Single slope, with an external condenser	Al_2O_3, Cu_2O
Mahian et al. (2017)	Not mentioned	Single slope, with solar collectors and nanofluids inside a heat exchanger	SiO_2, Cu
Rashidi et al. (2018)	ANSYS-FLUENT	Stepped solar still	Al_2O_3
Nazari, Safarzadeh and Bahiraei (2019)	MATLAB	Single slope, equipped with an external thermoelectric condensing channel	Cu_2O

3.2.2. Assumptions

The following assumptions were made in developing the mathematical models in this study:

- The solar stills were air-tight and thus, there was no leakage of vapour.
- There was no temperature variation within the fluid inside the basin.
- There was no temperature variation across the basin liner.
- There was no agglomeration of nanoparticles within the nanofluid.
- There was uniform fogging.
- All the vapour from the surface of the basin water condensed on the glass cover, with no condensation occurring on the inner walls of the solar stills.

- There was no drip back and thus, all the water which condensed on the glass cover was collected inside the distillate collector and no water droplets fell into the basin water.

3.2.3. Energy balance equations for solar stills

The major components of the solar still which determine how much solar radiation gets captured within the equipment are the glass cover, the nanofluid (mixture of impure water and nanoparticles) and the basin liner. Energy balance equations on these components are thus crucial to the development of mathematical models for solar stills with nanofluids.

As the Sun rays strike the surface of the glass cover, some of the solar radiation is absorbed by the glass in the form of heat while some of it gets transmitted to the nanofluid and the inner walls of the solar still, and the remainder is reflected off the surface of the glass. The solar radiation which gets transmitted to the nanofluid undergoes absorption, reflection and transmission; and this transmitted solar radiation is subsequently intercepted by the basin liner which absorbs most of the solar radiation and partially reflects some of it. The absorption of solar radiation by the basin liner causes its temperature to increase, thus transferring heat via convection to the nanofluid, in turn generating a temperature gradient between the nanofluid and the glass cover (Sahota & Tiwari, 2016b). Heat is then transferred via radiation, convection and evaporation from the nanofluid surface to the glass cover. Figure 3.4 illustrates the heat transfer mechanisms for the solar still with the nanofluid.

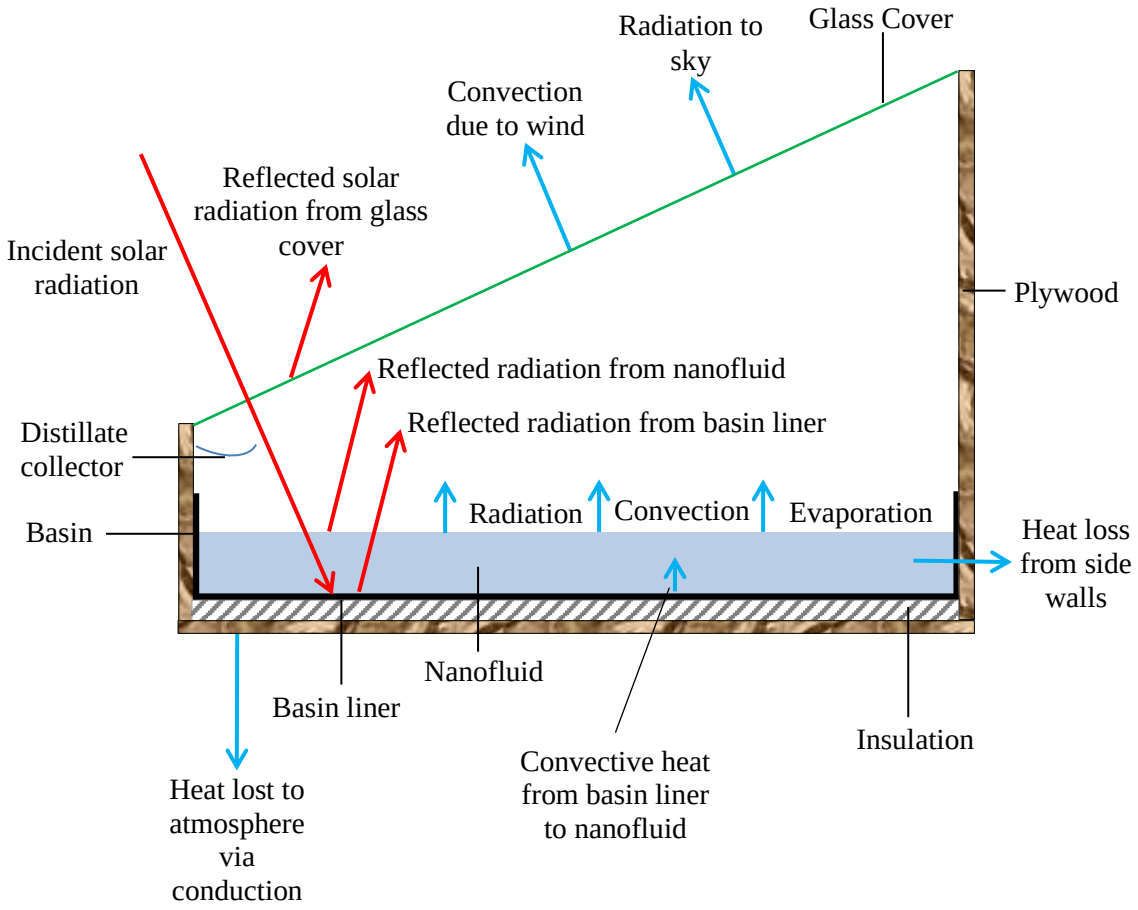

Figure 3.4: Heat transfer mechanisms for the solar still with the nanofluid.

3.2.3.1. Energy balance on glass cover

The glass cover absorbs parts of the incident solar radiation in the form of heat. Moreover, due to a temperature difference which exists between the nanofluid and the glass cover, heat is transferred via convection, radiation and evaporation from the nanofluid to the glass cover, as shown in Figure 3.4. On the other hand, the glass cover loses heat to the atmosphere via convection and radiation. The energy stored in the glass cover is equal to the difference in the sum of energy gained (from solar radiation and from the nanofluid) and the energy lost to the environment and this can be expressed mathematically as given in Equation (3.1).

$$m_g c_{p,g} \frac{dT_g}{dt} = A_g I_{glass} + A_{nf} h_{t,nf-g}(T_{nf} - T_g) - A_g h_{cv,g-atm}(T_g - T_{atm}) - A_g h_{r,g-s}(T_g - T_s) \quad (3.1)$$

3.2.3.2. Energy balance on nanofluid

The heat gained by the nanofluid includes solar radiation transmitted from the glass cover and convective heat from the basin liner. On the other hand, the heat losses from the nanofluid include convective, radiative and evaporative heat to the glass cover and heat loss through the side walls, as illustrated in Figure 3.4. The energy stored in the nanofluid is equal to the difference in the sum of energy gained (from solar radiation and from the basin liner) and the energy lost to the glass cover and through the side walls, as given in Equation (3.2).

$$m_{nf}c_{p,nf}\frac{dT_{nf}}{dt} = A_{nf}I_{nf} + A_{bl}h_{cv,bl-nf}(T_{bl} - T_{nf}) - A_{nf}h_{t,nf-g}\left(T_{nf} - T_{g}\right) - A_{sw}U_{sw}(T_{nf} - T_{atm}) \quad (3.2)$$

3.2.3.3. Energy balance on basin liner

Most of the solar radiation which strikes the surface of the glass cover gets transmitted and absorbed by the basin liner which is painted black for maximum absorption. On the other hand, the heat loss from the basin liner consists of convective heat to the nanofluid, and conductive heat to the environment via the polystyrene insulation and the plywood layer, as shown in Figure 3.4. The energy stored in the basin liner is equal to the difference in the energy gained from solar radiation and the energy lost to the nanofluid and through the bottom insulation. This can be expressed mathematically as given in Equation (3.3).

$$m_{bl}c_{p,bl}\frac{dT_{bl}}{dt} = A_{bl}I_{bl} - A_{bl}h_{cv,bl-nf}(T_{bl} - T_{nf}) - A_{bl}h_{co,bl-atm}(T_{bl} - T_{atm}) \quad (3.3)$$

A similar procedure as above was followed in order to develop equations for the solar stills with the base fluid only (water only) by writing energy balance equations on the glass cover, base fluid and the basin liner, with only the subscript *nf* changed to *bf* in Equations (3.1) to (3.3).

3.2.4. Evaluation of heat transfer coefficients

Equations (3.1) to (3.3) comprise many heat transfer coefficients which had to be calculated. Most of the equations for the base fluid and nanofluid are similar and thus, the subscript f will be used from now on to denote the impure fluid inside the basin of the solar still, which will be either (i) the base fluid in the case of the solar still with the base fluid only, or (ii) the nanofluid in the case of the solar stills with the nanoparticles dispersed into the base fluid.

3.2.4.1. Convective and evaporative heat transfer coefficients from fluid to glass cover

Elango, Gunasekaran and Sampathkumar (2015) conducted a comprehensive review on thermal models for the evaluation of convective and evaporative heat transfer coefficients inside a solar still, namely Dunkle's model (1961), Chen et al.'s model (1984), Clark's model (1990), Adhikari et al.'s model (1990), Kumar and Tiwari's model (1996), Zheng et al.'s model (2001) and Tsilingiris' model (2007). In the context of this investigation, the Tsilingiris' model was used as it is the only model which takes into consideration the thermo-physical properties of the binary mixture of water vapour and dry air which is in equilibrium inside the solar still. Tsilingiris (2007) claimed that the properties of this binary mixture, particularly at saturated conditions and at the higher operating temperatures of a solar still, are very different to the properties of dry air. Therefore, the Tsilingiris' model is the most suitable and accurate model for computing the convective and evaporative heat transfer coefficients inside a solar still and these are given in Equations (3.4) and (3.5), respectively (Tsilingiris, 2007).

M_a and M_v in Equation (3.4) represent the molecular weight of air and water, taken to be 28.97 and 18.02 kgkmol^{-1}, respectively (Bergman et al., 2011). On the other hand, R_a and R_v in Equation (3.5) represent the gas constant for air and water vapour, taken to be 287 Jkg^{-1}K^{-1} and 461.5 Jkg^{-1}K^{-1}, respectively (Tsilingiris, 2009). P_o, the atmospheric pressure was taken to be 101325 Pa.

$$h_{cv,f-g} = 0.075\, k_{mix} \left(\frac{g\rho_{mix}\beta_{vol,mix}}{\mu_{mix}\alpha_{mix}}\right)^{\frac{1}{3}} \left[\left(T_f - T_g\right) + \frac{T_f\left(P_{v,f} - P_{v,g}\right)M_a - M_v}{M_a P_o - P_{v,f}(M_a - M_v)}\right]^{\frac{1}{3}} \tag{3.4}$$

$$h_{evap,f-g} = h_v \left(\frac{h_{cv,f-g}}{c_{p,air}}\right)\left(\frac{R_a}{R_v}\right)\left[\frac{P_o}{\left(P_o - P_{v,f}\right)\left(P_o - P_{v,g}\right)}\right] \tag{3.5}$$

In order to solve Equations (3.4) and (3.5), the thermo-physical properties of the binary mixture of water vapour and air, including the density, viscosity, thermal conductivity and thermal diffusivity were calculated, as given in Equations (3.6), (3.7), (3.8) and (3.9), respectively. The saturated vapour pressure at the fluid temperature and at the glass cover temperature were calculated using Equations (3.10) and (3.11). These equations have been developed by Tsilingiris (2008) and are valid over a temperature range between 273.15 K to 373.15 K. The temperature $T_{m,f\text{-}g}$ in Equations (3.6) to (3.9) was calculated as the mean temperature of the fluid and the glass, given in Equation (3.12). The coefficient of volumetric expansion ($\beta_{vol,mix}$) was calculated using Equation (3.13), given in Tsilingiris (2007).

$$\begin{aligned}\rho_{mix} = {} & 1.293393662 - \left[5.538444326 \times (10^{-3}) \times (T_{m,f-g} - 273.15)\right] \\ & + [3.860201577 \times (10^{-5}) \times (T_{m,f-g} - 273.15)^2] \\ & - [5.2536065 \times (10^{-7}) \times (T_{m,f-g} - 273.15)^3]\end{aligned} \tag{3.6}$$

$$\begin{aligned}\mu_{mix} = {} & [1.715747771 \times (10^{-5})] + \left[4.722402075 \times (10^{-8}) \times (T_{m,f-g} - 273.15)\right] \\ & - \left[3.663027156 \times (10^{-10}) \times (T_{m,f-g} - 273.15)^2\right] \\ & + \left[1.873236686 \times (10^{-12}) \times (T_{m,f-g} - 273.15)^3\right] \\ & - \left[8.050218737 \times (10^{-14}) \times (T_{m,f-g} - 273.15)^4\right]\end{aligned} \tag{3.7}$$

$$\begin{aligned}k_{mix} = {} & [2.40073953 \times (10^{-2})] + \left[7.278410162 \times (10^{-5}) \times (T_{m,f-g} - 273.15)\right] \\ & - \left[1.788037411 \times (10^{-7}) \times (T_{m,f-g} - 273.15)^2\right] \\ & - \left[1.351703529 \times (10^{-9}) \times (T_{m,f-g} - 273.15)^3\right] \\ & - \left[3.322412767 \times (10^{-11}) \times (T_{m,f-g} - 273.15)^4\right]\end{aligned} \tag{3.8}$$

$$\alpha_{mix} = [1.847185729 \times (10^{-5})] + \left[1.161914598 \times (10^{-7}) \times (T_{m,f-g} - 273.15)\right] + \left[2.373056947 \times (10^{-10}) \times (T_{m,f-g} - 273.15)^2\right] - \left[5.769352751 \times (10^{-12}) \times (T_{m,f-g} - 273.15)^3\right] - \left[6.369279936 \times (10^{-14}) \times (T_{m,f-g} - 273.15)^4\right] \quad (3.9)$$

$$P_{v,f} = \{0.7073034146 - [2.703615165 \times (10^{-2}) \times (T_f - 273.15)] + [4.36088211 \times (10^{-3}) \times (T_f - 273.15)^2] - [4.662575642 \times (10^{-5}) \times (T_f - 273.15)^3] + [1.034693708 \times (10^{-6}) \times (T_f - 273.15)^4]\} \times 1000 \quad (3.10)$$

$$P_{v,g} = \left\{0.7073034146 - \left[2.703615165 \times (10^{-2}) \times (T_g - 273.15)\right] + \left[4.36088211 \times (10^{-3}) \times (T_g - 273.15)^2\right] - \left[4.662575642 \times (10^{-5}) \times (T_g - 273.15)^3\right] + \left[1.034693708 \times (10^{-6}) \times (T_g - 273.15)^4\right]\right\} \times 1000 \quad (3.11)$$

$$T_{m,f-g} = \left(\frac{T_f + T_g}{2}\right) \quad (3.12)$$

$$\beta_{vol,mix} = \frac{1}{T_g} \quad (3.13)$$

The correlation for the specific heat capacity of air ($c_{p,air}$) was developed from data given in Welty, Rorrer and Foster (2015), as expressed by Equation (3.14) and the equation for the latent heat of vaporisation (h_v) was obtained from Popiel and Wojtkowiak (1998), given in Equation (3.15).

$$c_{p,air} = \left[-3.6693061774 \times (10^{-7}) \times (T_{m,f-g} + 273.15)^3\right] + \left[8.0958732242 \times (10^{-4}) \times (T_{m,f-g} + 273.15)^2\right] - \left[3.4836762169 \times (10^{-1}) \times (T_{m,f-g} + 273.15)\right] + [1.0477229221 \times (10^3)] \quad (3.14)$$

$$h_v = \left\{2500.304 - \left[2.2521025 \times (T_{m,f-g} - 273.15)\right] - \left[0.021465847 \times \left(T_{m,f-g} - 273.15\right)^{1.5}\right] + \left[3.1750136 \times 10^{-4} \times \left(T_{m,f-g} - 273.15\right)^{2.5}\right] - \left[2.8607959 \times 10^{-5} \times \left(T_{m,f-g} - 273.15\right)^3\right]\right\} \times 1000 \quad (3.15)$$

3.2.4.2. Radiative heat transfer coefficient from fluid to glass cover

The radiative heat transfer coefficient from the fluid to the glass cover was calculated using Equation (3.16), as given by Duffie and Beckman (2013).

$$h_{r,f-g} = \frac{\sigma\left(T_g^2 + T_f^2\right)\left(T_g + T_f\right)}{\left(\frac{1-\varepsilon_f}{\varepsilon_f}\right) + \frac{1}{V_{f-g}} + \frac{\left(1-\varepsilon_g\right)A_f}{\varepsilon_g A_g}} \quad (3.16)$$

The view factor ($V_{f\text{-}g}$) between the fluid and the glass cover was computed using the correlations given by Bergman et al. (2011). In addition to radiating heat to the glass cover, the fluid also radiates heat to the back wall, front wall and west and east walls of the solar still. The view factor between the fluid and each of these 4 walls was computed using Equations (A.1) to (A.11), given in Appendix A. As mentioned earlier, previous mathematical models on solar stills with nanofluids have ignored the view factor in the calculation of the radiative heat transfer coefficient between the fluid and the glass cover.

3.2.4.3. Total heat transfer coefficient from fluid to glass cover

The evaporative heat transfer coefficient in Equation (3.5) is in units ms^{-1}. Thus, it was essential to convert it to $Wm^{-2}K^{-1}$ to make it consistent with the units of convective and radiative heat transfer coefficients in order to compute the total heat transfer coefficient from the fluid to the glass cover. The evaporative heat flux, in Wm^{-2}, was computed using Equation (3.17) given by Tsilingiris (2007). The evaporative heat transfer coefficient, in units

of $Wm^{-2}K^{-1}$, was then calculated using Equation (3.18) and the total heat transfer coefficient from the fluid to the glass cover was subsequently calculated using Equation (3.19).

$$q_{evap} = h_{evap,f-g}(P_{v,f} - P_{v,g}) \quad (3.17)$$

$$h_{e,f-g} = \frac{q_{evap}}{T_f - T_g} \quad (3.18)$$

$$h_{t,f-g} = h_{cv,f-g} + h_{e,f-g} + h_{r,f-g} \quad (3.19)$$

3.2.4.4. Radiative and convective heat transfer coefficients from glass cover to sky and atmosphere

The radiative heat transfer coefficient was computed using Equation (3.20), as given by Duffie and Beckman (2013). It is a function of the sky temperature, which was calculated using the Swinbank Equation, which has been used in previous studies on solar stills (El-Sebaii et al., 2008; Sellami et al., 2017), given in Equation (3.21).

$$h_{r,g-s} = \varepsilon_g \sigma \left(T_g^2 + T_s^2\right)(T_g + T_s) \quad (3.20)$$

$$T_s = 0.0552\, T_{atm}^{1.5} \quad (3.21)$$

The convective heat transfer coefficient from the glass cover to the atmosphere is a function of the wind speed and was evaluated by using the Watmuff correlation, given in Equations (3.22) and (3.23) (El-Sebaii, 2005).

For $V \leq 5$: $h_{cv,g-atm} = 2.8 + 3V$ (3.22)

For $V > 5$: $h_{cv,g-atm} = 6.15\, V^{0.8}$ (3.23)

3.2.4.5. Convective heat transfer coefficient from basin liner to fluid

3.2.4.5.1. Thermophysical properties of base fluid

The major difference between a solar still with base fluid only and a solar still with a nanofluid lies in the thermophysical properties of the base fluid and the nanofluid. In order to compute the convective heat transfer coefficient from the basin liner to the base fluid, the thermophysical properties of the base fluid, namely density, specific heat capacity, dynamic viscosity and thermal conductivity were first calculated using Equations (3.24) to (3.27). Two other parameters, namely the coefficient of volumetric expansion and the Prandtl number were also needed for the calculations and these are given in Equations (3.28) and (3.29), respectively. All these correlations were obtained from Popiel and Wojtkowiak (1998) and they are valid for liquid water for a temperature range of 273.15 K to 423.15 K.

$$\begin{aligned}\rho_{bf} = {} & 999.79684 + \left[0.068317355 \times T_{m,bl-bf}\right] - \left[0.010740248 \times T_{m,bl-bf}^{2}\right] \\ & + \left[0.00082140905 \times T_{m,bl-bf}^{2.5}\right] \\ & - \left[2.3030988 \times (10^{-5}) \times T_{m,bl-bf}^{3}\right]\end{aligned} \tag{3.24}$$

$$\begin{aligned}c_{p,bf} = {} & \left(4.2174356 - \left[0.0056181625 \times T_{m,bl-bf}\right]\right. \\ & + \left[0.0012992528 \times T_{m,bl-bf}^{1.5}\right] - \left[0.00011535353 \times T_{m,bl-bf}^{2}\right] \\ & \left. + \left[4.14964 \times (10^{-6}) \times T_{m,bl-bf}^{2.5}\right]\right) \times 1000\end{aligned} \tag{3.25}$$

$$\begin{aligned}\mu_{bf} = {} & \left[557.82468 + \left[19.408782 \times T_{m,bl-bf}\right] + \left[0.1360459 \times T_{m,bl-bf}^{2}\right]\right. \\ & \left. - \left[3.1160832 \times (10^{-4}) \times T_{m,bl-bf}^{3}\right]\right]^{-1}\end{aligned} \tag{3.26}$$

$$\begin{aligned}k_{bf} = {} & 0.5650285 + \left[0.0026363895 \times T_{m,bl-bf}\right] \\ & - \left[0.00012516934 \times T_{m,bl-bf}^{1.5}\right] \\ & - \left[1.5154918 \times (10^{-6}) \times T_{m,bl-bf}^{2}\right] \\ & - \left[0.0009412945 \times T_{m,bl-bf}^{0.5}\right]\end{aligned} \tag{3.27}$$

$$\beta_{vol,bf} = [-6.8785895 \times 10^{-5}] + [2.1687942 \times 10^{-5} \times T_{m,bl-bf}] - [2.1236686 \times 10^{-6} \times T_{m,bl-bf}^{1.5}] + [7.7200882 \times 10^{-8} \times T_{m,bl-bf}^{2}] \quad (3.28)$$

$$Pr_{bf} = \left[0.074763403 + [0.0029020983 \times T_{m,bl-bf}] + [2.8606181 \times (10^{-5}) \times T_{m,bl-bf}^{2}] - [8.1395537 \times (10^{-8}) \times T_{m,bl-bf}^{3}]\right]^{-1} \quad (3.29)$$

The properties in Equations (3.24) to (3.29) were all evaluated at the mean temperature of the basin liner and the base fluid ($T_{m,bl-bf}$), as expressed by Equation (3.30).

$$T_{m,bl-bf} = \left[\frac{T_{bl} + T_{bf}}{2}\right] \quad (3.30)$$

3.2.4.5.2. Thermophysical properties of nanofluid

The thermophysical properties of the Al_2O_3 nanofluid are responsible for the enhancement in the productivity of the solar still. Consequently, it is essential to use appropriate correlations in computing these physical properties.

(a) Density and specific heat capacity of nanofluid

The density of the nanofluid was calculated using Equation (3.31) which is based on the principle of mass conservation of the base fluid and the nanoparticles in a finite control volume while the specific heat capacity of the nanofluid was calculated using Equation (3.32) which is based on the principle of conservation of thermal energy of the base fluid and the nanoparticles in a finite control volume, obtained from Sharma et al. (2012). These two equations have been used in previous studies on the numerical study of solar stills with nanofluids by Kabeel, Omara and Essa (2017) and Sahota and Tiwari (2016a, 2016b).

$$\rho_{nf} = \varphi_v \rho_{np} + (1 - \varphi_v \rho_{bf}) \quad (3.31)$$

$$c_{p,nf} = \frac{\left[\varphi_v \rho_{cp} c_{p,np} + (1-\varphi_v)\rho_{bf} c_{p,bf}\right]}{\rho_{nf}} \quad (3.32)$$

The symbol φ_v represents the volumetric concentration of the nanoparticles which was computed using Equation (3.33) which is a function of the weight concentration of the nanoparticles and the densities of the nanoparticles and the base fluid (Kabeel, Omara & Essa, 2017).

$$\frac{(1-\varphi_v)}{\varphi_v} = \left[\frac{(1-\varphi_w)}{\varphi_w}\right]\left(\frac{\rho_{np}}{\rho_{bf}}\right) \quad (3.33)$$

(b) Thermal conductivity and viscosity of nanofluid

Many researchers have investigated the viscosity and thermal conductivity of nanofluids. Nevertheless, the experimental data for these thermophysical properties obtained by researchers differ by more than 25% (Sharma et al., 2017). In engineering calculations, the use of correlations derived from such varied data can fail to accurately predict an output. Patel and Sundararajan (2010) claimed that there is no agreement in literature about the extent of thermal conductivity improvement in nanofluids and even for identical nanofluids having the same liquid-nanoparticle combination and concentration, comparison of the results is problematic due to different preparation and stabilisation techniques. Paul et al. (2010) also stated that the inconsistency and the controversy of the thermal conductivity results reported for identical nanofluids across the globe can limit the potential applications of nanofluids. Murshed and Estellé (2017) conducted a review on the viscosity of nanofluids and they found that viscosities of nanofluids are higher than their base fluids but even for the same nanofluid, the results are dispersed and inconsistent.

Correlations which have been developed for thermal conductivity and viscosity of nanofluids are valid for specific ranges of temperatures, volumetric concentration of nanoparticles and nanoparticle size. In the context of this study, the thermal conductivity and viscosity correlations which were used are given in Equation (3.34) (Sharma et al. 2012) and Equation (3.35) (Sekhar & Sharma, 2015), respectively. These correlations were chosen as they have been developed using experimental data from various researchers and they were most suitable in covering the range of temperatures, range of nanoparticle size and the volumetric concentration of nanoparticles in this study. These thermophysical properties were calculated

at mean temperature of the basin liner and the nanofluid, as given in Equation (3.36). The thermal diffusivities present in Equation (3.34) were calculated using Equations (3.37) and (3.38) (Bergman et al., 2011).

$$k_{nf} = k_{bf}\left\{0.8938 \times \left[\left(1 + \frac{\varphi_v}{100}\right)^{1.37}\right] \times \left[\left(1 + \frac{T_{m,bl-nf}}{70}\right)^{0.2777}\right] \times \left[\left(1 + \frac{d_{np}}{150}\right)^{-0.0336}\right] \times \left(\frac{\alpha_{t,np}}{\alpha_{t,bf}}\right)^{0.01737}\right\} \quad (3.34)$$

20 °C ≤ $T_{m,1}$ ≥ 70°C; 20 nm ≤ d_{np} ≥ 150 nm; φ_v ≤ 3.7%

$$\mu_{nf} = \mu_{bf}\left[0.935\left(1 + \frac{T_{m,bl-nf}}{70}\right)^{0.5602}\left(1 + \frac{d_{np}}{80}\right)^{-0.05915}\left(1 + \frac{\varphi_v}{100}\right)^{10.51}\right] \quad (3.35)$$

20 °C ≤ $T_{m,1}$ ≥ 70°C; 13 nm ≤ d_{np} ≥ 100 nm; 0.01% ≤ φ_v ≤ 5.00%

$$T_{m,bl-nf} = \left[\frac{T_{bl} + T_{nf}}{2}\right] - 273.15 \quad (3.36)$$

$$\alpha_{t,np} = \frac{k_{np}}{\rho_{np} c_{p,np}} \quad (3.37)$$

$$\alpha_{t,bf} = \frac{k_{bf}}{\rho_{bf} c_{p,bf}} \quad (3.38)$$

Other correlations have been employed in the few numerical studies on the use of nanofluids in solar stills by other researchers. Kabeel, Omara and Essa (2017) used the Maxwell Model to compute the thermal conductivity and the Einstein Equation for calculating the viscosity of the nanofluid but these equations could not be used in this study as they did not incorporate the nanoparticle size. Correlations from Khanafer and Vafai (2011) were used by Sahota and Tiwari (2016a, 2016b) and Sahota, Shyam and Tiwari (2017a, 2017b). These correlations were not applicable in this investigation as φ_v ranged from 1% to 9% in the viscosity equations that they used (Khanafer & Vafai, 2011) and this range was much above the volumetric concentration used in this study.

Rashidi et al. (2018) used a viscosity correlation developed by Masoumi, Sohrabi and Behzadmehr (2009) and a thermal conductivity correlation developed by Chon and Kihm

(2005). However, the viscosity correlation included a correction factor which was computed using extremely limited data for nanoparticles of size 13 nm and 28 nm only (Masoumi, Sohrabi & Behzadmehr, 2009). Furthermore, the thermal conductivity correlation of Chon and Kihm (2005) was developed using only their own experimental data. Consequently, these correlations were not used in this present study.

3.2.4.5.3. Convective heat transfer coefficient

The equations which were used in computing the convective heat transfer coefficient from the basin liner to the fluid are given in Equations (3.39) to (3.44) (Bergman et al., 2011). In Equation (3.39), L represents the characteristic length and was computed as the ratio of the surface area of the basin liner to the perimeter of the basin liner.

$$h_{cv,bl-f} = \frac{Nu_f k_f}{L} \tag{3.39}$$

For $10^4 \leq Ra_f \leq 10^7$: $Nu_f = 0.54\, Ra_f^{1/4}$ (3.40)

For $10^7 \leq Ra_f \leq 10^{11}$: $Nu_f = 0.15\, Ra_f^{1/3}$ (3.41)

$$Ra_f = Gr_f Pr_f \tag{3.42}$$

$$Gr_f = \frac{g\beta_{vol,f}(T_{bl} - T_f)L^3}{\nu_f^2} \tag{3.43}$$

$$\nu_f = \frac{\mu_f}{\rho_f} \tag{3.44}$$

For the nanofluid, the coefficient of volumetric expansion was computed using Equation (3.45), obtained from Kabeel, Omara and Essa (2017) and the Prandtl number was computed using Equation (3.46), obtained from Bergman et al. (2011). For the base fluid, these were computed using Equations (3.28) and (3.29).

$$\beta_{vol,nf} = \frac{2}{T_{bl} + T_{nf}} \tag{3.45}$$

$$Pr_{nf} = \frac{\mu_{nf} c_{p,nf}}{k_{nf}} \quad (3.46)$$

3.2.4.6. Conductive heat transfer coefficients

Heat is lost from the fluid to the atmosphere, via the side walls made of plywood. The conductive heat transfer coefficient from the fluid to the atmosphere was calculated using Equation (3.47). On the other hand, heat is also lost from the basin liner to the atmosphere, via conduction, through the polystyrene insulation layer and through the plywood. This heat transfer coefficient was computed using Equation (3.48).

$$U_{sw} = \left(\frac{L_{ins,ply}}{k_{ins,ply}}\right)^{-1} \quad (3.47)$$

$$h_{co,bl-atm} = \left(\frac{L_{ins,pol}}{k_{ins,pol}} + \frac{L_{ins,ply}}{k_{ins,ply}}\right)^{-1} \quad (3.48)$$

3.2.5. Computation of solar radiation absorbed by each component

In order to solve the system of equations for the solar still, namely Equations (3.1) to (3.3), the amount of solar radiation absorbed by the glass, the fluid and the basin liner were calculated. These were in turn dependent on geographical and astronomical parameters, optical properties of the glass cover and the effective solar radiation inside the solar still.

3.2.5.1. Geographical and astronomical parameters

3.2.5.1.1. Latitude, Longitude and Standard Meridian

In the context of this research, the simulations in MALTAB were carried out using annual climatic data for Stellenbosch, South Africa. Stellenbosch is situated south of the equator and to the east of the Greenwich Meridian. Consequently, the latitude has a negative value (ϕ = -33.93°) while the longitude has a positive value ($L_{location}$ = 18.86°). The standard meridian for the South African time zone was calculated by multiplying the time difference between South African time and Greenwich Meridian time by 15 (Duffie & Beckman, 2013). Since

there is a two-hour difference between South African time and the Greenwich Meridian time, the standard meridian for the local time zone was 30° ($L_{standard}$ = 30°).

3.2.5.1.2. Equation of time, solar time and Angles

The Equation of time (E_{time}), solar time and various angles, namely the declination angle (δ), initial hour angle (ω_1), final hour angle (ω_2), midpoint of hour angle (ω), zenith angle (θ_z), angle of incidence (θ_1), solar azimuth angle (γ_s) and solar altitude angle (α_{solar}) were calculated using Equations (3.49) to (3.59). These are given in Duffie and Beckman (2013). All the calculations involving the hour angle were performed using the midpoint of the hour angle (ω). $L_{location}$, $L_{standard}$ and ϕ were converted to radians before being used in the equations. The surface azimuth angle (γ) was taken to be π radians as the orientation of the solar stills was north-facing (Duffie & Beckman, 2013).

$$B = \frac{2\pi\,(n-1)}{365} \tag{3.49}$$

n = n^{th} day of the year

$$E_{time} = \frac{1}{60}[229.2\,(0.000075 + 0.001868\cos B - 0.032077\sin B - 0.014615\cos 2B - 0.04089\sin 2B)] \tag{3.50}$$

$$\text{Solar time} = \text{Standard time} + E_{time} + \left[\frac{4\,(L_{standard} - L_{location})}{60}\right] \tag{3.51}$$

$$\delta = [0.006918 - 0.399912\cos B + 0.070257\sin B - 0.006758\cos 2B + 0.000907\sin 2B - 0.002697\cos 3B + 0.00148\sin 3B] \tag{3.52}$$

$$\omega_1 = 15\left(\frac{\pi}{180}\right)(\text{Solar time} - 12) \tag{3.53}$$

$$\omega_2 = \omega_1 + 15\left(\frac{\pi}{180}\right) \tag{3.54}$$

$$\omega = \frac{\omega_1 + \omega_2}{2} \tag{3.55}$$

$$\theta_z = \cos^{-1}[\sin\phi \sin\delta + \cos\phi \cos\delta \cos\omega] \tag{3.56}$$

$$\begin{aligned}\theta_1 = \cos^{-1}[&\sin\delta \sin\phi \cos\beta \\ &- \sin\delta \cos\phi \sin\beta \cos\gamma \\ &+ \cos\delta \cos\phi \cos\beta \cos\omega + \cos\delta \sin\phi \sin\beta \cos\gamma \cos\omega \\ &+ \cos\delta \sin\beta \sin\gamma \sin\omega]\end{aligned} \tag{3.57}$$

$$\gamma_s = \text{sign}(\omega) \left|\cos^{-1}\left(\frac{\cos\theta_z \sin\phi - \sin\delta}{\sin\theta_z \cos\phi}\right)\right| \tag{3.58}$$

sign = +1 if ω is positive and sign = -1 if ω is negative.

$$\alpha_{solar} = \left(\frac{\pi}{2}\right) - \theta_z \tag{3.59}$$

3.2.5.2. Effective solar radiation inside solar still

The approach used by Tripathi and Tiwari (2004), Madhlopa and Johnstone (2009a, 2009b), Madhlopa (2009) and Altarawneh et al. (2017) for evaluating the effective solar radiation inside a solar still has been adopted in this investigation. The fluid inside the basin of the solar still receives energy directly from the Sun and by reflection from the back, front, east and west walls of the solar still.

Tripathi and Tiwari (2004) claimed that the energy received from the east, west and front walls can be neglected. Based on this assumption and by adapting the equations given by Madhlopa (2009a, 2009b), the effective beam radiation and effective diffuse radiation inside the solar still was computed using Equations (3.60) and (3.61) respectively. The effective beam radiation ($I_{b,eff}$) is a function of the surface area of the fluid receiving beam radiation directly ($A_{f,di}$), the reflectance of the inner wall (ρ_{iw}), the view factor from the back wall to the fluid ($V_{bw\text{-}f}$), the projected area of the back wall ($A_{bw,p}$), beam radiation on a horizontal surface ($I_{b,h}$) and the surface area of the fluid (A_f). On the other hand, the effective diffuse radiation ($I_{d,eff}$) is a function of the energy per unit time intercepted by the fluid ($Q_{d,f}$), the view factor from the fluid to the sky ($V_{f\text{-}sky}$), diffuse radiation on a horizontal surface ($I_{d,h}$), the reflectance of the inner wall and the surface area of the fluid.

$$I_{b,eff} = \frac{\left[A_{f,di} + \left(\rho_{iw} V_{bw-f} A_{bw,p}\right)\right] I_{b,h}}{A_f} \tag{3.60}$$

$$I_{d,eff} = \frac{A_f V_{f-sky} I_{d.h} + \rho_{iw} Q_{d.f}}{A_f} \tag{3.61}$$

The area of fluid inside the solar still which receives beam radiation directly was computed using Equation (3.62) and the projected area of the back wall of the solar still was computed using Equation (3.63), obtained from Madhlopa and Johnstone (2009b). The diffuse energy intercepted by the fluid per unit time was calculated using Equation (3.64), obtained from Madhlopa (2009). The reflectance of the inner walls (made of plywood coated with white paint) was assumed to be 0.62 as in a study conducted by Gul et al. (2018), it was found that the reflectance of plywood coated with white paint is approximately 0.62.

$$A_{f,di} = L_b \left(W_b - \left[\frac{H_{fw} \cos(\gamma_s - \gamma)}{\tan \alpha_{solar}}\right]\right) \tag{3.62}$$

$$A_{bw,p} = \frac{L_b H_{bw} \cos(\gamma_s - \gamma)}{\tan \alpha_{solar}} \tag{3.63}$$

$$Q_{d,f} = \left[A_{bw} V_{bw-f} V_{bw-sky}\right] I_{d,h} \tag{3.64}$$

To compute the view factor from the back wall to the fluid, the reciprocity relation given in Bergman et al. (2011) was employed, as given in Equation (3.65). The view factor between the fluid and the back wall ($V_{f\text{-}bw}$) was calculated using Equations (A.1) to (A.3) from Appendix A. The view factor from the back wall to the sky ($V_{bw\text{-}sky}$) was computed using Equation (3.66).

$$V_{bw-f} = \frac{A_f V_{f-bw}}{A_{bw}} \tag{3.65}$$

$$V_{bw-sky} = 1 - (V_{bw-fw} + V_{bw-ew} + V_{bw-ww}) \tag{3.66}$$

In order to determine the view factor from the back wall to the sky, it was first necessary to compute the view factor from the back wall to the front wall ($V_{bw\text{-}fw}$), the view factor from the back wall to the east wall ($V_{bw\text{-}ew}$) and the view factor from the back wall to the west wall ($V_{bw\text{-}ew}$). These were determined using correlations in Bergman et al. (2011). The step-by-step procedure of how these view factors were computed are given in Equations (A.12) to (A.18) from Appendix A. The effective global solar radiation inside the solar still ($I_{g,eff}$) was then calculated by summing the effective beam radiation and the effective diffuse radiation, as given in Equation (3.67).

$$I_{g,eff} = I_{b,eff} + I_{d,eff} \tag{3.67}$$

3.2.5.3. Optical properties of glass cover

The optical properties of the glass cover affect the distillate output from a solar still (Khan & Mustafa, 2019). Consequently, it is essential to model the optical properties accurately. The method outlined in Duffie and Beckman (2013) for calculating absorptance, transmittance and reflectance was employed in this study, as well as the constants such as refractive indices and extinction coefficient. Snell's Law of refraction, given in Equation (3.68), was first applied on the glass cover as solar radiation travels through air and passes through the glass cover. The symbols n_1 and n_2 are the refractive indices of air and glass and were taken to be 1 and 1.526, respectively, and θ_1 is the angle of incidence which was calculated from Equation (3.57) and θ_2 is the angle of refraction.

$$n_1 \sin\theta_1 = n_2 \sin\theta_2 \tag{3.68}$$

The parallel and perpendicular components of unpolarised radiation were then calculated using Equations (3.69) and (3.70), respectively. The extinction coefficient (K_{ec}) for the glass cover was taken to be 18 m^{-1} in Equation (3.71) and the thickness of the glass cover (z_{glass}) was 4 mm. The absorptance, transmittance and reflectance associated with the parallel and perpendicular components of polarised radiation were then computed using Equations (3.72) to (3.77).

$$r_{\parallel} = \frac{\tan^2(\theta_2 - \theta_1)}{\tan^2(\theta_2 + \theta_1)} \tag{3.69}$$

$$r_{\perp} = \frac{\sin^2(\theta_2 - \theta_1)}{\sin^2(\theta_2 + \theta_1)} \tag{3.70}$$

$$\tau_a = \exp\left(-\frac{K_{ec} z_{glass}}{\cos\theta_2}\right) \tag{3.71}$$

$$\alpha_{\parallel} = \frac{(1 - \tau_a)(1 - r_{\parallel})}{(1 - r_{\parallel}\tau_a)} \tag{3.72}$$

$$\tau_{\parallel} = \frac{\tau_a(1 - r_{\parallel})^2}{1 - (r_{\parallel}\tau_a)^2} \tag{3.73}$$

$$\rho_{\parallel} = r_{\parallel}(1 + \tau_a\tau_{\parallel}) \tag{3.74}$$

$$\alpha_{\perp} = \frac{(1 - \tau_a)(1 - r_{\perp})}{(1 - r_{\perp}\tau_a)} \tag{3.75}$$

$$\tau_{\perp} = \frac{\tau_a(1 - r_{\perp})^2}{1 - (r_{\perp}\tau_a)^2} \tag{3.76}$$

$$\rho_{\perp} = r_{\perp}(1 + \tau_a\tau_{\perp}) \tag{3.77}$$

The absorptance (α_g), transmittance (τ_g) and the reflectance (ρ_g) of the glass cover were then computed using Equations (3.78) to (3.80).

$$\alpha_g = \frac{1}{2}(\alpha_{\parallel} + \alpha_{\perp}) \tag{3.78}$$

$$\tau_g = \frac{1}{2}(\tau_{\parallel} + \tau_{\perp}) \tag{3.79}$$

$$\rho_g = 1 - (\alpha_g + \tau_g) \tag{3.80}$$

3.2.5.4. Solar radiation absorbed by each component

The fractional solar flux absorbed by the glass cover, fluid and basin liner were calculated using Equations (3.81) to (3.83), given by Madhlopa and Johnstone (2011). The absorptivity of the fluid (α_f) for the base fluid and nanofluid were taken to be 0.05 and 0.6 respectively (Madhlopa & Johnstone, 2009a; Madhlopa & Johnstone, 2009b; Sahota & Tiwari, 2016a; Sahota & Tiwari, 2016b). The reflectivity of the fluid surface (r_f) and the absorptivity of the basin liner (α_{bl}) were taken to be 0.05 and 0.8 respectively (Tiwari & Tiwari, 2007).

$$\alpha'_g = \alpha_g \tag{3.81}$$

$$\alpha'_f = \alpha_f \tau_g \tag{3.82}$$

$$\alpha'_{bl} = \alpha_{bl} \tau_g (1 - r_f - \alpha_f) \tag{3.83}$$

The amount of solar radiation absorbed by the glass cover (I_{glass}), the fluid (I_f) and the basin liner (I_{bl}) was then computed by multiplying the fractional solar flux of each component by the effective global solar radiation, as given in Equations (3.84) to (3.86).

$$I_{glass} = \alpha'_g \, I_{g,eff} \tag{3.84}$$

$$I_f = \alpha'_f \, I_{g,eff} \tag{3.85}$$

$$I_{bl} = \alpha'_{bl} \, I_{g,eff} \tag{3.86}$$

3.2.6. Computation of the productivity and efficiency of solar stills

The convective and evaporative heat transfer coefficients from the fluid to the glass cover were computed using the Tsilingiris model, as given in Equations (3.4) and (3.5). Consequently, the productivity of the solar stills (Y) was also computed using the equation developed by Tsilingiris (2007), given in Equation (3.87).

$$Y = \frac{h_{cv,f-g}}{c_{p,air}} \frac{R_a}{R_v} \left[\frac{P_o (P_{v,f} - P_{v,g})}{(P_o - P_{v,f})(P_o - P_{v,g})} \right] \tag{3.87}$$

The efficiency of a system is typically given as the ratio of output to input. In the context of this study, the output was the product of the mass of distillate produced and the latent heat of vaporisation while the input was the amount of solar radiation on the tilted glass cover. Thus, the efficiency (η) of the solar stills was computed by dividing the product of the mass of the distillate and the latent heat of vaporisation by the global solar radiation on the inclined glass cover surface, as given in Equation (3.88).

$$\eta = \frac{Y \times h_v}{I_{g,i}} \times 100 \tag{3.88}$$

3.2.7. Numerical method used in solving the mathematical models

The governing equations for the mathematical model for the nanofluid are given in Equations (3.1), (3.2) and (3.3). They represent a set of differential equations which are time-dependent, and they can be discretised in order to generate outputs for small intervals of time (Δt). The process of converting the governing equations into a form which can give discrete values of the solution is known as the discretization process and the discretised equations can either be solved by direct methods or iterative methods (Murthy & Mathur, 1998).

Equations (3.1), (3.2) and (3.3) were discretised and the temperature of the glass cover, the nanofluid and the basin liner was made the subject of formula, respectively, in each equation. The discretised equations are given in Equations (3.89) to (3.91), where the symbol Δt represents the time step, and $T_{g,0}$, $T_{nf,0}$, $T_{bl,0}$ represent the initial temperatures of the glass, nanofluid and basin liner, respectively in each time step, and T_g, T_{nf} and T_{bl} represent the temperatures of the components at the end of each time step. Smaller time steps typically

improve the accuracy of the model and thus, in this study, a time step of 300 seconds was chosen, and this time step has also been used in a previous study on solar stills by Abu-Arabi and Zurigat (2005).

$$T_g = \frac{\left[\frac{m_g c_{p,g} T_{g,0}}{\Delta t} + A_g I_g + h_{t,nf-g} A_{nf} T_{nf,0} + h_{cv,g-atm} A_g T_{atm} + h_{r,g-s} A_g T_s\right]}{\frac{m_g c_{p,g}}{\Delta t} + h_{t,nf-g} A_{bf} + h_{cv,g-atm} A_g + h_{r,g-s} A_g} \quad (3.89)$$

$$T_{nf} = \frac{\left[\frac{m_{nf} c_{p,nf} T_{nf,0}}{\Delta t} + A_{nf} I_{nf} + h_{cv,bl-nf} A_{bl} T_{bl,0} + h_{t,nf-g} A_{nf} T_g + U_{sw} A_{sw} T_{atm}\right]}{\frac{m_{nf} c_{p,nf}}{\Delta t} + h_{cv,bl-nf} A_{bl} + h_{t,nf-g} A_{nf} + U_{sw} A_{sw}} \quad (3.90)$$

$$T_{bl} = \frac{\left[\frac{m_{bl} c_{p,bl} T_{bl,0}}{\Delta t} + A_{bl} I_{bl} + h_{co,bl-atm} A_{bl} T_{atm} + h_{cv,bl-nf} A_{bl} T_{nf}\right]}{\frac{m_{bl} c_{p,bl}}{\Delta t} + h_{co,bl-atm} A_{bl} + h_{cv,bl-nf} A_{bl}} \quad (3.91)$$

An iterative method was chosen for solving Equations (3.89) to (3.91). Iterative methods are based on initial guess values which gradually improve the solution each time the discretised equations are applied (Murthy & Mathur, 1998). The Gauss-Seidel iterative method was chosen as this method allows the estimated solution to be replaced with the new value immediately after it is calculated (Kelley, 1995). Additionally, other numerical studies on solar stills have also employed the use of the Gauss-Seidel iterative method (Singh et al., 2012; Abderachid & Abdenacer, 2013; Mahammed, Kerfah & Bezzina, 2019). The following section gives the algorithm that was used in solving the mathematical models.

3.2.8. Algorithm for solving the mathematical models in MATLAB

Figure 3.5 illustrates the algorithm used in solving the mathematical models for the solar stills with the view factor (Model 1) and without the view factor (Model 2). The hourly climatic data for Stellenbosch (latitude 33.93°S, longitude 18.86°E) included global solar radiation on a horizontal surface ($I_{g,h}$), diffuse solar radiation on a horizontal surface ($I_{d,h}$), ambient temperature (T_{atm}) and wind speed (V). These data were all saved in an m-file in MATLAB. A code was then written in another m-file in MATLAB, where the equations discussed earlier on were written. The data m-file was first run, followed by the code m-file in order to solve the mathematical models. The code m-file is given in Appendix B.

The constants and the design parameters of the solar stills were first written in the code m-file. The geographical and astronomical parameters were then calculated, followed by the various Earth-Sun angles given in Equations (3.52) to (3.59). The effective solar radiation inside the solar still was subsequently computed by using Equations (3.60) to (3.67), followed by the optical properties of the glass cover using Equations (3.68) to (3.80) and the amount of solar radiation absorbed by each component of the solar still by using Equations (3.81) to (3.86).

The thermophysical properties of the fluid and the heat transfer coefficients were then calculated, and the temperatures of the glass, fluid and basin liner were subsequently solved using the Gauss-Seidel iterative method until the solution converged. Thereafter, the mass of distillate was computed, as illustrated in Figure 3.5.

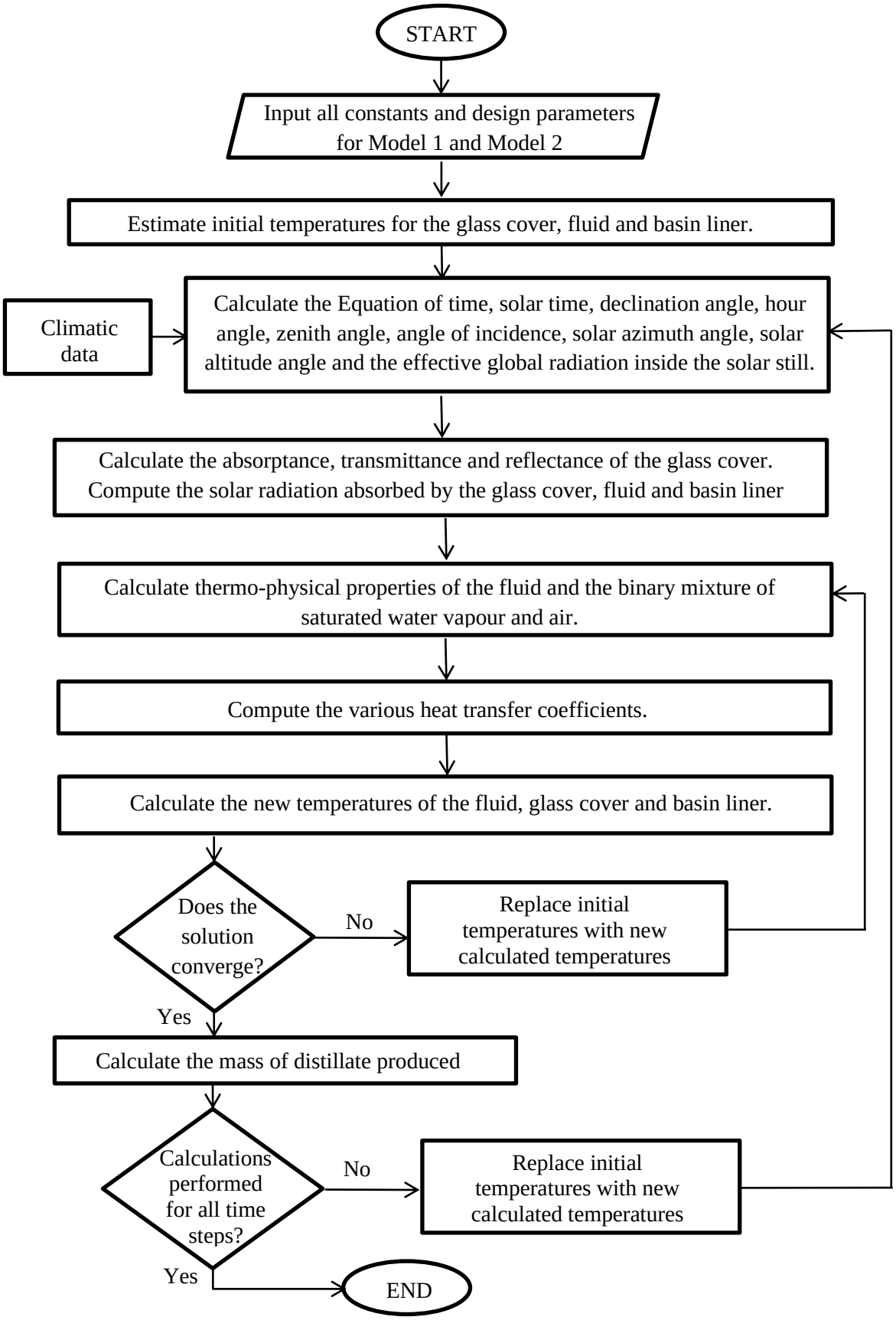

Figure 3.5: Algorithm for solving mathematical models for solar stills with and without nanofluids in MATLAB.

3.2.9. Evaluation of the economic performance of solar stills

The key economic benefits of a solar still lies in its simple design, installation, operation and maintenance, all of which require little infrastructure and can easily be done locally (El-Bialy et al. 2016). The economic analysis of a solar still is dependent on variables such as the initial cost of investment, interest rate, cost of maintenance, annual productivity of the solar still, life of the solar still, cost of distilled water per litre, selling price of distilled water per litre and the salvage value (Kumar & Tiwari, 2009). As mentioned earlier, based on the extensive literature review, it was noted that no study has investigated the effect of nanoparticle size on the economic performance of solar stills.

In this investigation, an economic analysis was conducted on each solar still (with different nanoparticle size), following a similar approach used by Fath et al. (2003), Kumar and Tiwari (2009), Kabeel, Hamed and El-Agouz (2010), El-Bialy et al. (2016) and Bait (2019), as given in Equations (3.92) to (3.100).

$$\mathrm{SFF} = \frac{\mathrm{i_r}}{(1+\mathrm{i_r})^{\mathrm{n}} - 1} \tag{3.92}$$

$$\mathrm{CRF} = \mathrm{SFF}\ (1+\mathrm{i_r})^{\mathrm{n}} \tag{3.93}$$

$$\mathrm{FAC} = \mathrm{P}\ (\mathrm{CRF}) \tag{3.94}$$

$$\mathrm{S} = 0.2\ \mathrm{P} \tag{3.95}$$

$$\mathrm{ASV} = \mathrm{S}\ (\mathrm{SFF}) \tag{3.96}$$

$$\mathrm{AMC} = 0.15\ (\mathrm{FAC}) \tag{3.97}$$

$$\mathrm{AC} = \mathrm{FAC} + \mathrm{AMC} - \mathrm{ASV} \tag{3.98}$$

$$\mathrm{CPL} = \frac{\mathrm{AC}}{\mathrm{M}} \tag{3.99}$$

$$\mathrm{n_{pb}} = \frac{\ln\left[\dfrac{\mathrm{M} \times \mathrm{S_{p,w}}}{(\mathrm{M} \times \mathrm{S_{p,w}}) - (\mathrm{P} \times \mathrm{i_r})}\right]}{\ln(1+\mathrm{i_r})} \tag{3.100}$$

In the above equations, SFF represents the Sinking Fund Factor, i_r is the interest rate, taken to be 10% and n is the life span of the solar still, assumed to be 10 years. CRF represents the Capital Recovery Factor, FAC is the Fixed Annual Cost which is a function of both the Present Capital Cost (P) and the CRF. The Present Capital Cost (P) was calculated by summing the costs of all the raw materials needed to make the solar stills (C_{rm}), labour costs (C_{labour}), the cost of the land required for the layout of the solar stills (C_{land}), and the cost of the feed water ($C_{feedwater}$), as given in Equation (3.101).

$$P = C_{rm} + C_{labour} + C_{land} + C_{feedwater} \quad (3.101)$$

The costs of raw materials used in the calculations are the actual costs which were paid to suppliers when purchasing the materials to construct the solar stills during the experimental phase, given in Table 3.3. It is to be noted that the transport costs of saline water or brackish water to the solar stills have not been taken into consideration as ideally, solar stills would be mounted in regions where there are some nearby sources of saline or brackish water and thus, transportation costs would be negligible.

Table 3.3: Cost of raw materials of solar stills with and without Al_2O_3 nanoparticles.

Item Description	Cost (USD) *			
	Solar still with base fluid only	**Solar still with Al_2O_3 nanoparticles (10 nm)**	**Solar still with Al_2O_3 nanoparticles (50 nm)**	**Solar still with Al_2O_3 nanoparticles (100 nm)**
Glass Cover	21.69	21.69	21.69	21.69
Basin	96.85	96.85	96.85	96.85
Insulation	16.73	16.73	16.73	16.73
Plywood	196.65	196.65	196.65	196.65
Fittings	40.11	40.11	40.11	40.11
Surfactant	0	5.00	5.00	5.00
Nanoparticles	0	97.56	70.05	52.53
Total	**372.03**	**474.59**	**447.08**	**429.56**

*1 USD = 12.40 ZAR

The cost of labour was assumed to be 35% of the total cost of the solar stills (Chaibi, 2000). The cost of land was taken to be USD 206.45 per m^2 (Du Plessis, 2011), based on an exchange rate of 1 USD = 12.40 ZAR, and it was assumed that each solar still would occupy a total area of 1.5 m^2, including the 1 m^2 for the basin area and 0.5 m^2 to account for the distillate collector bottles and storage of feed water. The cost of feed water was taken to be USD 1.99 per kilo litre (Fell & Winter, 2018), based on an exchange rate of 1 USD = 12.40 ZAR and it was assumed that the total amount of feed water needed for each solar still includes: a) the initial 20 L in the basin and b) make up feed water, which was taken to be three times the amount of distillate produced from each solar still (Mehta et al., 2011).

The salvage value (S) is dependent on P while the Annual Salvage Value (ASV) is a function of both the salvage value and the SFF. AMC represents the Annual Maintenance and Operational Costs. The Cost of distilled water Per Litre (CPL) is dependent on the Annual Cost (AC) and the annual distillate yield of the solar still (M). The annual yield was calculated based on annual climatic conditions for Stellenbosch, South Africa. The payback

period is represented by n_{pb} and the selling price of distilled water ($S_{p,w}$) was taken to be 4.01 ZAR per litre (0.3234 per L) based on estimates given in BusinessTech (2018) for the price of distilled water in South Africa.

3.2.10. Evaluation of the environmental performance of solar stills

The main reason driving the use of solar stills for fresh water production is its minimal environmental impact as it uses solar energy as compared to other desalination techniques which commonly use fossil fuels as the source of energy. Previous studies have not looked at the effect of nanoparticle size on the environmental performance of solar stills, as mentioned earlier. In this study, an environmental analysis was conducted on each solar still (with different nanoparticle size) in order to investigate how the nanoparticle size affects the environmental performance.

The environmental performance was conducted in terms of the amount of carbon dioxide equivalent (CO_2 equivalent) mitigated by each solar still annually and the amount of money saved annually by not paying a carbon tax. The approach used by Bait (2019) was adopted in this investigation, as given in Equations (3.102) and (3.103).

$$M_{CO_2} = EF_{CO_2} E_{out} \tag{3.102}$$

$$EC_{CO_2} = P_{CO_2} M_{CO_2} \tag{3.103}$$

In the above equations, M_{CO_2}represents the amount of CO_2 equivalent mitigated per year, EF_{CO_2} is the average CO_2 equivalent emission factor from a coal power plant and E_{out} is the annual energy output from the solar still (the latent heat of vaporisation multiplied by the yield of the solar still) $EC_{CO_2}$is the annual environmental cost which can be avoided by not having to pay a carbon tax on the annual amount of energy generated from the solar still, which would otherwise have to be paid if the energy were to be generated from fossil fuels, and $P_{CO_2}$is the carbon price.

In this investigation, which was based in South Africa, the emission factor and the carbon price were estimated based on local values. The value for the emission factor was taken to be 1.01 kg CO_2 equivalent per kWh (Sanlam, 2016) and the price of carbon was taken to be

USD 9.68 per tonne of CO_2 equivalent emissions (Reuters, 2019), based on an exchange rate of 1 USD = 12.40 ZAR.

3.3. Experimental Approach

3.3.1. Experimental set-up

Four solar stills were constructed corresponding to the design specifications given in Table 3.1. The experiments were conducted outdoors on the roof of the Menzies Building at the University of Cape Town (latitude 33.96°S, longitude 18.46°E). The solar stills were approximately 20 metres above local ground and the orientation of the solar stills was north-facing. This roof was chosen as it could obtain plenty of sunshine, with minimal shadows from other buildings. The arrangement of the four solar stills on the roof during the assembling of the different components is shown in Figure 3.6.

Figure 3.6: Arrangement of solar stills on the roof during assembling of the components.

3.3.2. Measurement of climatic data

Climatic data, including solar radiation, ambient temperature and wind speed were measured during the whole duration of the experiments. For measuring solar radiation, a CM5 pyranometer from Kipp and Zonen was used and it is classified as a first class pyranometer with a response time of less than 1 minute, with an accuracy of ± 5 Wm^{-2}. This accuracy is within the range that has been reported in literature. Arunkumar et al. (2013) used a pyranometer of accuracy ± 30 Wm^{-2}. According to Paulescu et al. (2013), it is essential to record at least 1 sample every minute in order to capture the rapid fluctuations in solar radiation intensities. Moreover, Forgan (2011) claimed that the sampling interval must always be less than the response time Consequently, in this study, the sampling time and logging interval were chosen as 1 second and 10 seconds, respectively.

Two pyranometers are usually used in measuring solar radiation, one for measuring global solar radiation on a horizontal surface and one for measuring diffuse solar radiation on a horizontal surface. Nonetheless, due to the availability of only one pyranometer and due to the high costs associated with buying a new one, the pyranometer in this study was mounted on a wooden structure inclined at the same tilt angle as the glass cover in order to obtain the global solar radiation on an inclined surface, as shown in Figure 3.7.

Iqbal (1983) stated that a pyranometer which is placed in an inclined position also receives ground reflected radiation, in combination with diffuse and direct radiation. Thus, it should be noted that the solar radiation data recorded at the University of Cape Town was slightly different to the available solar radiation data from the Stellenbosch location. The slight adjustments which were made in the mathematical models when running the simulations in MATLAB using climatic data from the University of Cape is discussed in Section 3.4.

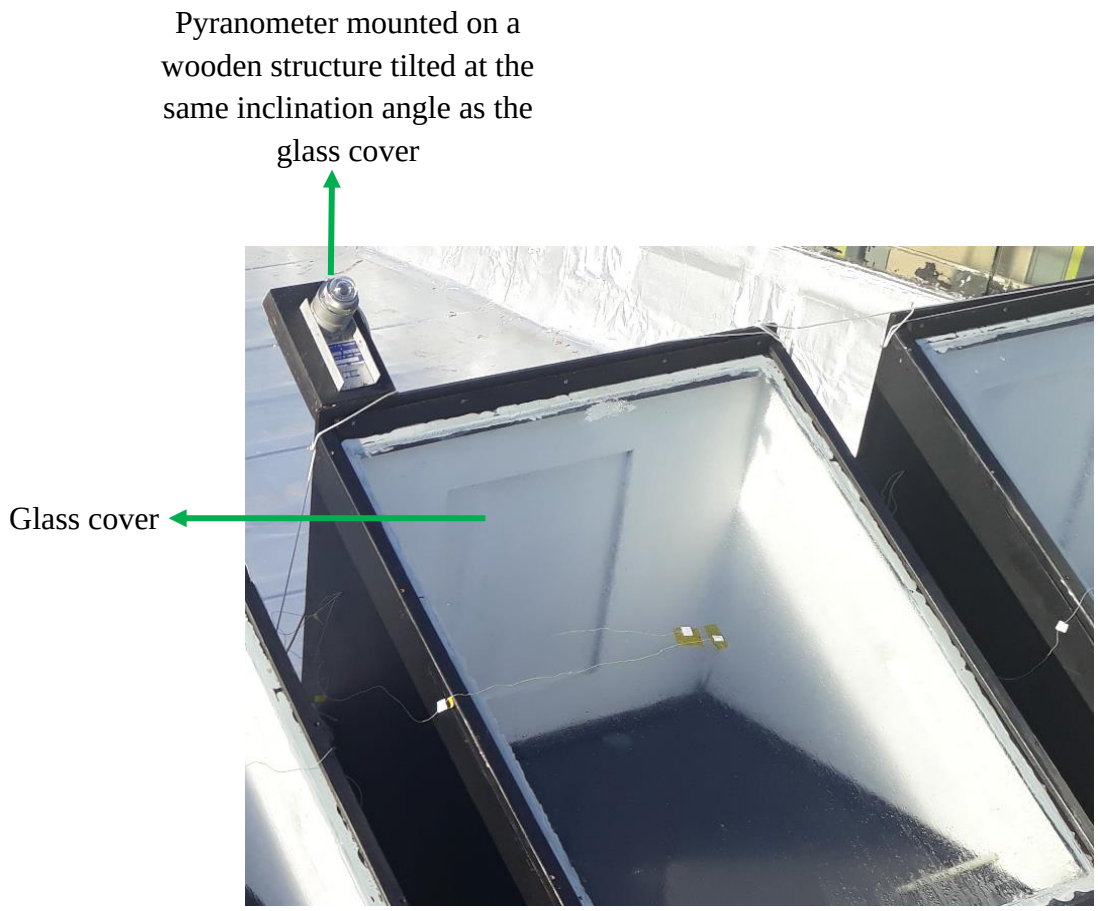

Figure 3.7: Pyranometer mounted on a wooden structure tilted at the same inclination angle as the glass cover.

The ambient temperature was measured using a K-type thermocouple (Model IEC 548-3) of accuracy ± 1.5°C, which was placed inside a white-painted Stevenson Screen. The accuracy is almost comparable to that of instruments used in previous studies on solar stills to measure ambient temperature. Elango, Kannan and Muragavel (2015) used a thermometer of accuracy ± 1°C to measure ambient temperature in their study. An anemometer (Model MCS 177) was used to measure the wind speed. The accuracy of the anemometer was ± 2% of full range and in a previous study on solar stills conducted by Tabrizi and Sharak (2010), an anemometer of lower accuracy of ± 3% of full scale was used. The anemometer was mounted on a rigid metal structure attached to a pillar, as illustrated in Figure 3.8. The pyranometer, the thermocouple and the anemometer were all connected to data loggers (Model Econ DT9812) which were in turn connected to a Central Processing Unit (CPU) to store all the climatic data, at a sampling time of 1 second and a logging interval of 10 seconds.

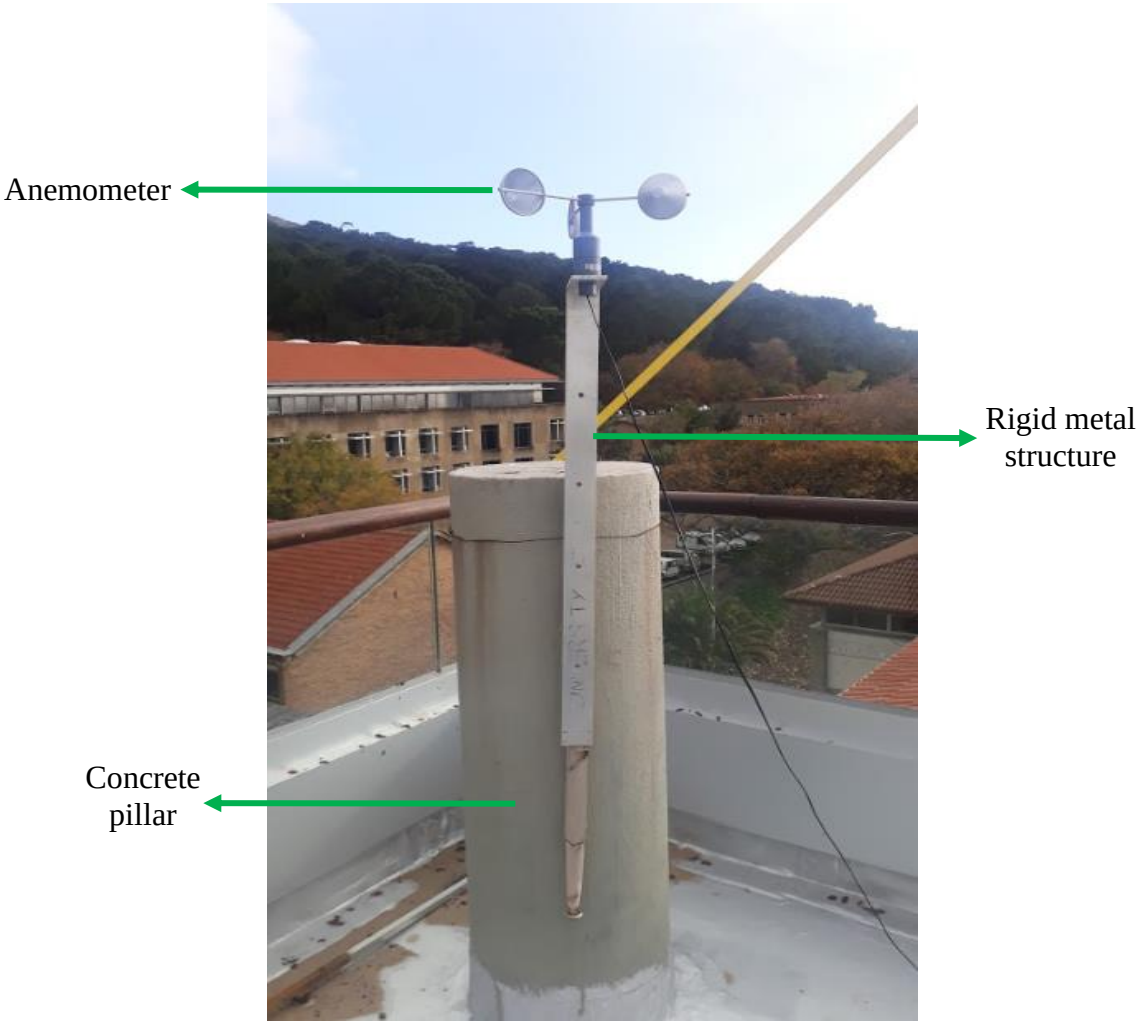

Figure 3.8: Anemometer mounted on a rigid metal structure, attached to a pillar.

Additionally, the glass of each solar still was regularly cleaned to avoid accumulation of dust particles which can lead to a reduction in the amount of solar radiation which gets transmitted through the glass. The four solar stills were placed next to each other on the roof, along with all the equipment for measuring and storing the climatic data. Additionally, since it was quite windy on the roof, sand bags were used to support the solar stills. The layout of the equipment on the roof from the front and back side is given in Figure 3.9 and Figure 3.10, respectively.

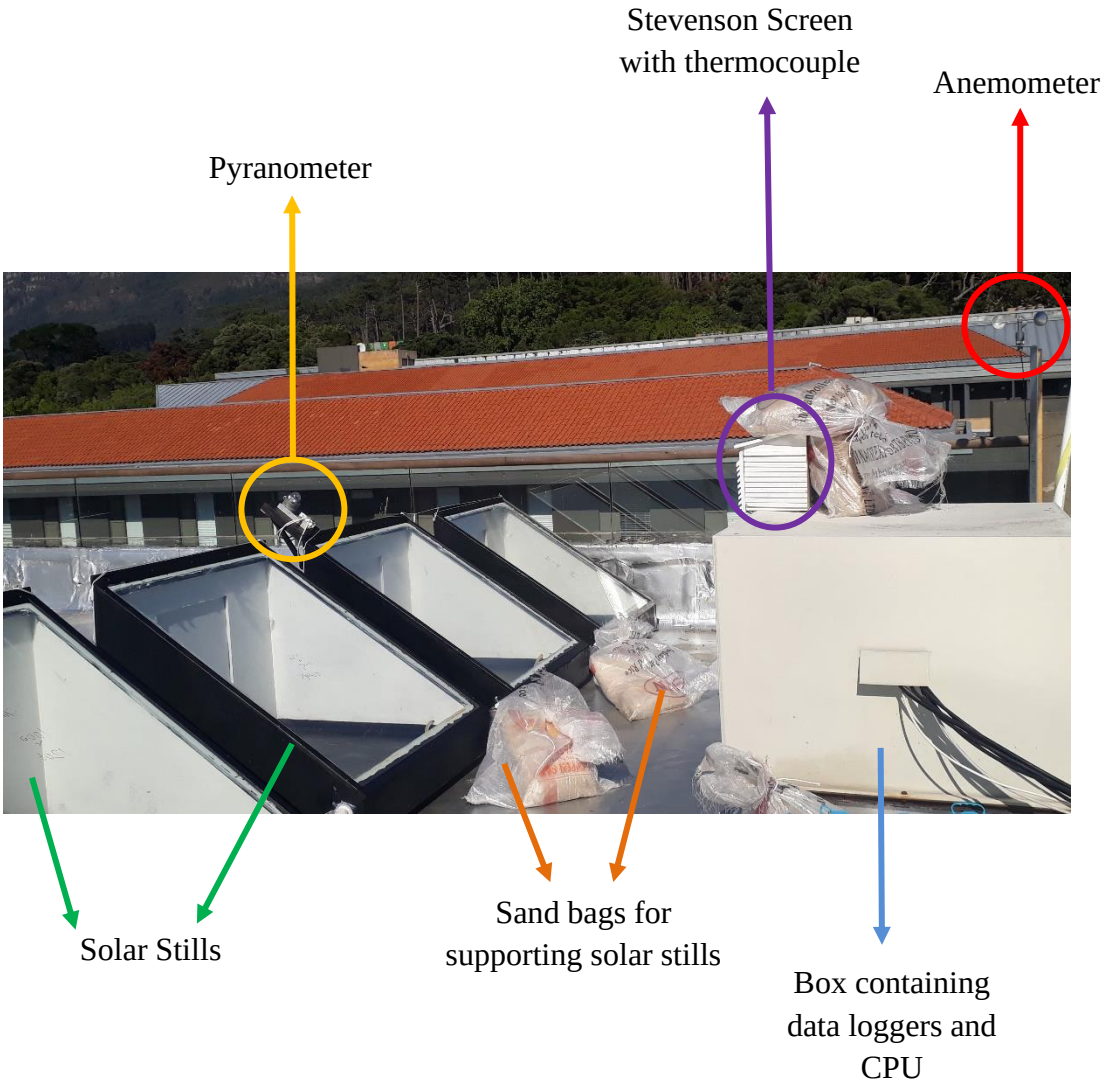

Figure 3.9: Layout of equipment on the roof – Front Side.

Figure 3.10: Layout of equipment on the roof – Back Side.

Once all the equipment were set up on the roof, 20 kg of tap water (base fluid) was placed into each of the solar still at 7 am. A small white tape was used to mark off the level of the impure water inside the basin of each solar still. The mass of the distillate collected from each solar still at 7 am the following day was measured using an electronic mass balance (Precisa XB 4200C), with an accuracy of 0.01g. This accuracy is comparable to what other researchers have used, for instance, Arunkumar et al. (2013) used a measuring jar with an accuracy of ± 10 ml (corresponding to an accuracy of ± 10 g) for measuring the mass of distillate in their study.

Top-up water was then added (each morning at 7 am) to each solar still basin up to the white tape mark. The same procedures of collecting the distillate at 7 am every morning and topping-up of water were repeated for a period of 10 days in order to verify that the performance of the four solar stills was not significantly different. Thereafter, nanofluids were placed in three of the solar stills and base fluid was again used in the remaining solar still and the mass of distillate was again measured every morning at 7 am.

3.3.3. Preparation of Al_2O_3 nanofluid

Al_2O_3 nanoparticles of size 10 nm, 50 nm, and 100 nm were purchased from Nanografi Co. Ltd, a Nanotechnology Company based in Turkey, which is involved in the development of a wide range of nanoparticles. The SDBS surfactant was also purchased from the same company. The nanoparticles were all spherical in shape and the purity was at least 99.5%.

The weight concentration of the nanoparticles was chosen as 0.2% as in the research conducted by Kabeel, Omara and Essa (2017), they found that increasing the weight concentration of the Al_2O_3 nanoparticles from 0.16% to 0.2% increased the daily efficiency of the solar still but any further increase in the concentration did not result in any significant increase in the efficiency. For stability purposes, the mass of SDBS used was one tenth of the mass of Al_2O_3 nanoparticles (Mojarrad, 2014; Prasad, Gupta & Deepak, 2015). The method of preparing nanofluids outlined by Das et al. (2017) was adapted in this study. Since this investigation deals with large volumes of nanofluids and due to the unavailability of huge equipment, the nanofluids were first prepared in small batches and then mixed together. Figure 3.11 shows a schematic for the experimental procedures for the preparation of the aluminium oxide nanofluids.

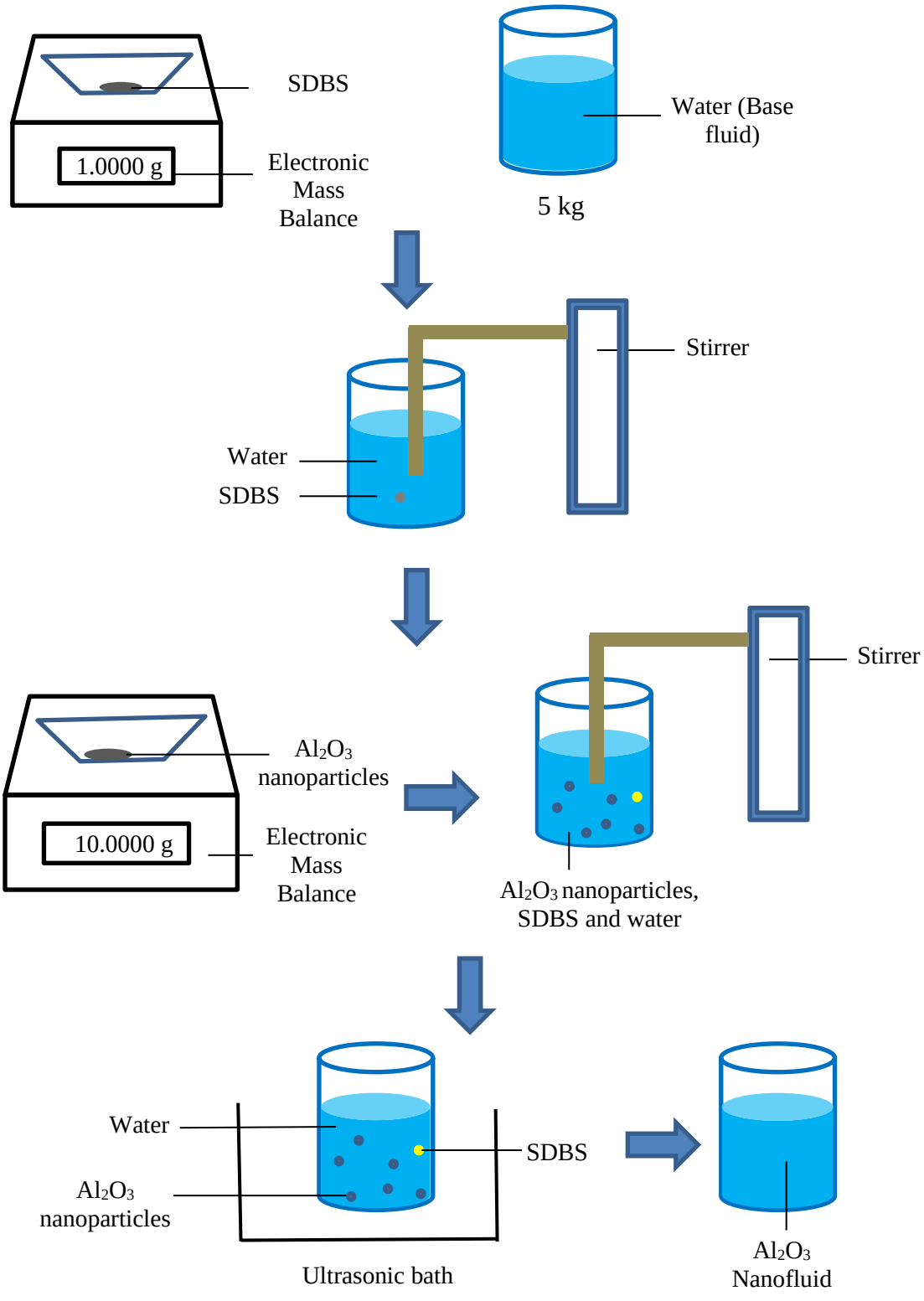

Figure 3.11: Experimental procedures for preparation of nanofluids.

1.0000 g of SDBS was measured using an electronic mass balance of model Radwag AS220/C/2, having a readability of 0.0001 g. The SDBS was added to 5 L of water, which was measured using a measuring cylinder. This mixture was then continuously stirred using a stirrer (T 25 digital ULTRA-TURRAX – IKA), for a period of one hour in order to obtain a homogenous mixture. 10.0000 g of Al_2O_3 nanoparticles, of size 10 nm, was then measured using an electronic mass balance (Radwag AS220/C/2), and this was added to the SDBS-water mixture and the resulting mixture was also stirred continuously using a stirrer (T 25 digital ULTRA-TURRAX – IKA) for one hour. This mixture was then sonicated in an ultrasonic bath (LABCON Ultrasonic UBM 22) for a period of 15 minutes to obtain the nanofluid. Three other identical batches of 5 L each were then prepared, and they were all added to one of the solar stills. Thus, this represents the solar still with nanofluids containing Al_2O_3 nanoparticles of size 10 nm. The same procedures were then repeated for nanoparticles of size 50 nm and 100 nm.

The laboratory pieces of equipment which were used in the preparation of the nanofluids are shown in Figure 3.12. By using the method outlined in the above paragraph, a homogeneous mixture of the water, nanoparticles and surfactant was obtained (nanofluid). This homogenous mixture could be observed by its cloudy appearance, as shown in the bottles from Figure 3.12.

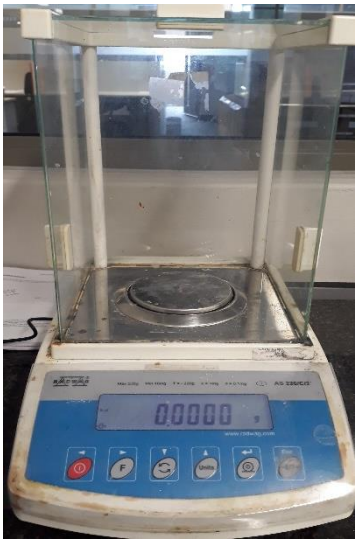

Mass balance (Radwag AS220/C/2) for measuring the mass of SDBS and Al_2O_3 nanoparticles

Stirrer (T 25 digital ULTRA-TURRAX – IKA) for mixing the base fluid, SDBS and Al_2O_3 nanoparticles

Ultrasonic bath (LABCON Ultrasonic UBM 22) for sonication

Figure 3.12: Laboratory equipment used in the preparation of Al_2O_3-water nanofluids.

3.4. Development of a clearness index correlation for Cape Town

Solar radiation data obtained from Stellenbosch comprised the global radiation on a horizonal surface ($I_{g,h}$) and the diffuse radiation on a horizontal surface ($I_{d,h}$). The approach used for the computation of the effective solar radiation inside the solar still required the beam and diffuse radiation on a horizontal surface, as given in Equations (3.60) and (3.61). For the Stellenbosch data, the diffuse and global radiation on a horizontal surface were available and to obtain the beam radiation on a horizontal surface, a simple arithmetical operation was performed by subtracting the diffuse radiation from the global radiation on a horizontal surface.

Solar radiation measured at the University of Cape Town was the radiation on an inclined surface ($I_{g,i}$), which comprised the sum of beam, diffuse and ground reflected radiation. The global radiation on a horizontal surface at this location was determined by using the circumsolar model by Iqbal (1983) which has also been used by Tuomiranta and Ghedira (2015), as given by Equation (3.104). The ground reflectance (ρ_{gr}) was taken to be 0.2 (Popoola & Burnier, 2014), β is the angle of inclination of the glass cover; and the ratio of beam radiation on an inclined surface to that on a horizontal surface (R_b) was calculated using Equation (3.105) given in Duffie and Beckman (2013), where θ_1 and θ_z are the angle of incidence and the zenith angle, respectively. The global radiation on a horizontal surface ($I_{g,h}$) was then calculated by making $I_{g,h}$ the subject of formula from Equation (3.104).

$$I_{g,i} = I_{g,h}\left[R_b + \rho_{gr}\frac{1-\cos\beta}{2}\right] \tag{3.104}$$

$$R_b = \frac{\cos\theta_1}{\cos\theta_z} \tag{3.105}$$

In order to calculate the diffuse radiation on a horizontal surface for the Cape Town location, it was essential to develop a clearness index correlation for Cape Town. The closest location to the University of Cape Town (latitude 33.96°S, longitude 18.46°E) from which solar radiation data was available was Stellenbosch (latitude 33.93°S, longitude 18.86°E). Consequently, a clearness index correlation for Stellenbosch was developed and this was also applicable to Cape Town since these two locations are very close to each other. Since hourly solar radiation data were available for Stellenbosch, an hourly clearness index (k_T) was

developed. The hourly clearness index is given in Equation (3.106) and the extraterrestrial radiation (I_o) was calculated as given in Equation (3.107) and the solar constant (I_{sc}) was taken to be 1367 Wm^{-2} (Duffie & Beckman, 2013). The zenith angle was calculated as given in Equation (3.56) and n was the n^{th} day of the year.

$$k_T = \frac{I_{g,h}}{I_o} \tag{3.106}$$

$$I_o = I_{sc}\left(1 + 0.033\cos\frac{2\pi n}{365}\right)\cos\theta_z \tag{3.107}$$

Correlations for the clearness index are typically expressed as functions of the diffuse fraction (k_D), which is the ratio of the diffuse radiation on a horizontal surface to the global radiation on a horizontal surface. The hourly data from Stellenbosch for a whole year was used in calculating hourly values for the diffuse fraction and the corresponding values for the clearness index. In order to develop the clearness index correlation, outliers were eliminated according to the approach used by Jacovides et al. (2006) for quality control purposes. Values were eliminated if (i) $I_{g,h} < 5$ Wm^{-2}; (ii) $I_{b,h} > I_o$; (iii) $I_{d,h} > 1.1\ I_{g,h}$; (iv) $I_{g,h} > 1.2\ I_o$; (v) $I_{d,h} > 0.8\ I_o$; (vi) $I_{d,h}/\ I_{g,h} < 0.9$ for $k_T < 0.2$ and (vi) $I_{d,h}/\ I_{g,h} > 0.9$ for $k_T > 0.6$. Based on these criteria, the outliers were eliminated, and the remaining data points were used in developing a clearness index correlation by plotting a graph of diffuse fraction against the clearness index, as presented in Chapter 4 in Figure 4.39.

The extraterrestrial radiation (I_o) was then calculated using geographical and astronomical parameters for the University of Cape Town location, using Equations (3.49) to (3.57) and Equation (3.107). The clearness index for the University of Cape Town was then computed using Equation (3.106), where $I_{g,h}$ was computed using Equation (3.104) and I_o was computed using Equation (3.107). The diffuse radiation on a horizontal surface at the University of Cape Town was then computed using Equation (3.108), where k_D is a function of the clearness index, which is given in Chapter 4, in Equations (4.1) to (4.3).

$$I_{d,h} = k_D\ I_{g,h} \tag{3.108}$$

The beam radiation on a horizontal surface at the University of Cape Town was then computed using Equation (3.109).

$$I_{b,h} = I_{g,h} - I_{d,h} \quad (3.109)$$

Consequently, the diffuse and beam radiation on a horizontal surface, obtained from Equations (3.108) and (3.109) were then used in the simulations in MATLAB for generating the mass of distillate obtained from each solar still at the University of Cape Town. This was done to compare numerical results with experimental results as discussed in the following section.

3.5. Model Validation

3.5.1. Analysis of variance test

Analysis of variance (ANOVA) is a statistical technique which is used to determine whether the variability as a result of experimental factors are statistically significant compared to variability caused by random factors (Pavlidis, 2003). There are two criteria which can prove that the means of given datasets are equal: (i) if the P-value from the ANOVA test is higher than the significance level and (ii) if the $F_{critical}$ value is greater than the F value (Zaiontz, 2019). In order to test the performance of the solar stills and for calibration purposes, an ANOVA test was conducted.

Experiments were conducted over a period of 10 days with base fluid only in all four solar stills, that is, with the four solar stills operating under identical climatic and experimental conditions. The mass of distillate was measured from each solar still for a period of 10 days. Office 365 Excel was used to conduct the ANOVA test, at a significance level of 0.05. This was done in order to verify that the performance of the solar stills was not significantly different from one another.

3.5.2. Statistical tools for model validation

In order to validate the mathematical models for the solar stills, theoretical results were compared against experimental results. Simulations in MALTAB were performed using climatic data including the wind speed, ambient temperature and solar radiation measured at the University of Cape Town in order to obtain the amount of distillate generated from each solar still. These numerical values were then compared with the corresponding experimental values for the mass of distillate obtained from each solar still. The accuracy of the model was tested by computing the correlation coefficient (r), the root mean square error (RMSE) and the mean bias error (MBE).

The correlation coefficient was computed using Equations (3.110) and the RMSE was computed using Equation (3.111), given in Elango, Gunasekaran and Sampathkumar (2015). Y_{sim} represents the numerical values for the distillate yield (in kgm^{-2}), obtained from the simulations in MATLAB, Y_{expt} represents the experimental values for the distillate yield (in kgm^{-2}) and N represents the number of observations. Equation (3.113) was used to compute the MBE (Kuo, Chang & Chang, 2014).

$$r = \frac{\left[N\sum Y_{sim}Y_{expt} - (\sum Y_{sim})(\sum Y_{expt})\right]}{\sqrt{N\sum Y_{sim}^2 - (\sum Y_{sim})^2}\ \sqrt{N\sum Y_{expt}^2 - \left(\sum Y_{expt}\right)^2}} \tag{3.110}$$

$$RMSE = \left[\frac{\sum (e_i)^2}{N}\right]^{0.5} \tag{3.111}$$

$$e_i = \left[\frac{Y_{sim} - Y_{expt}}{Y_{sim}}\right] \times 100 \tag{3.112}$$

$$MBE = \frac{1}{N}\sum_{i}^{N}\left(Y_{sim} - Y_{expt}\right) \times 100 \tag{3.113}$$

Similar equations for the MBE and the RMSE were also used in order to assess the performance of the clearness index correlation developed in this study.

3.5.3. Analysis of measurement uncertainty

In order to compute the measurement uncertainty, the method used by Jain and Tiwari (2004) and Gupta, Kumar and Baredar (2017) was adopted, using Equations (3.114) to (3.117). Gupta, Kumar and Baredar (2017) computed the percentage uncertainty for the most sensitive parameter for a solar still, which is the yield of fresh water. Consequently, in this study, the percentage uncertainty was also calculated for the yield of fresh water. The percentage uncertainty was computed by summing the percentage internal uncertainty and the percentage external uncertainty.

$$\sigma = \sqrt{\frac{\sum(Y_i - \bar{Y})^2}{N_0}} \tag{3.114}$$

$$U_1 = \frac{\sqrt{\sigma_1^2 + \sigma_2^2 + \cdots \sigma_N^2}}{N} \tag{3.115}$$

$$\%\ \text{internal uncertainty} = \frac{U_1}{\text{Mean of total observations}} \times 100 \tag{3.116}$$

$$\%\ \text{external uncertainty} = \left(\frac{0.01}{4200}\right) \times 100 \tag{3.117}$$

In Equations (3.114) to (3.117), $(Y_i - \overline{Y})$ represents the deviation from the mean distillate, N_0 is the number of observations in each set and N is the number of sets. In calculating the percentage external uncertainty as shown in Equation (3.117), 0.01 g was the least count of the measuring balance and 4200 g was the capacity of the measuring balance.

3.6. Summary

The design, modelling and experimentation of solar stills have been discussed in this chapter. Previous studies on solar stills with nanofluids have not incorporated the view factor in the computation of the internal radiative heat transfer coefficient; and the effects of nanoparticle size on the productivity and on the economic and environmental performance of solar stills have not been reported in any studies from the extensive literature review conducted. This chapter gave the procedures that were used to address these issues in this study.

The step-by-step procedure of developing mathematical models for solar stills with nanofluids was given, as well as the thermophysical properties of nanofluids, incorporating the nanoparticle size. The mathematical models were solved in MATLAB, using the Gauss-Seidel iterative method and the algorithm used to solve the mathematical models was also given. The experimental procedures that were followed, as well as the statistical tools which were used to validate the models, were also presented. The results obtained from the simulations in MATLAB, the experimentation, and from the model validation will be presented and discussed in Chapter 4.

CHAPTER 4
RESULTS AND DISCUSSION

A solar still is a sustainable means of generating potable water from sea water or saline water but the major drawback lies in its low productivity. Many attempts have been made by previous researchers to enhance the productivity of a solar still, and recently, the use of nanofluids is seen as an attractive technique of increasing the productivity, as discussed in Chapter 1. In Chapter 2, a comprehensive literature review on the use of nanofluids in solar stills was presented. It was observed that most of the studies so far have been experimental only and the few available numerical studies did not account for the view factor in computing the radiative heat transfer coefficient from the basin fluid to the glass cover. Furthermore, based on the extensive literature review, it was also noted that no study has investigated the effect of nanoparticle size on the productivity, and on the economic and environmental performance of solar stills. In order to address these research gaps, a detailed chapter on design, modelling and experimentation of solar stills was presented in Chapter 3. The latter gave the step-by-step procedures of how the mathematical models were developed in this study, as well as how the experiments were conducted in order to address the research gaps.

Four identical solar stills were constructed, with water only (base fluid) being used in one of them and Al_2O_3 nanoparticles of size 10 nm, 50 nm and 100 nm dispersed in the base fluid, in each of the three remaining solar stills. The performance of each solar still was evaluated in terms of its distillate output, economic and environmental performance. Comprehensive numerical and experimental results are presented in this chapter, as well as a discussion on these results. This chapter comprises three main sections, namely: a) Simulation Results, entailing the numerical results from the simulations in MATLAB based on the annual climatic data from Stellenbosch (latitude 33.93°S, longitude 18.86°E), South Africa; b) Experimental Results, comprising the results from the outdoor experiments conducted at the University of Cape Town (latitude 33.96°S, longitude 18.46°E), South Africa and c) Model Performance, involving a statistical analysis on the experimental results as well as the validation of the mathematical models which have been developed in this study.

4.1. Simulation Results

The simulations in MATLAB were carried out using the climatic data from Stellenbosch for a whole year but in order to clearly illustrate the performance of each solar still, a Sample Day was chosen and comprehensive results for the Sample Day are presented. The hourly climatic conditions, including wind speed, ambient temperature and global solar radiation on a horizontal surface for the Sample Day are first presented, followed by the annual climatic conditions in Stellenbosch.

The fluid temperature profiles, thermophysical properties, heat transfer coefficients, distillate output and efficiency of each solar still for the Sample Day are then presented and discussed. The annual distillate production and efficiency are also presented and discussed, followed by the annual economic performance and environmental performance of the solar stills.

4.1.1. Climatic conditions for Stellenbosch

As discussed in Chapter 2, in Section 2.5.1.1., environmental factors such as wind speed, ambient temperature and solar radiation greatly influence the distillate output of a solar still. In general, the higher the solar radiation level, the higher the productivity of a solar still, as demonstrated in the studies conducted by Rahbar and Esfahani (2012), Muftah et al. (2014) and Abujazar et al. (2016). A similar trend has been observed concerning the effect of ambient temperature, with the productivity increasing with increasing ambient temperature, as indicated from the studies by Nafey et al. (2000), Al-Hinai, Al-Nassri and Jubran (2002) and Danish et al. (2019). A higher solar radiation level causes more heat to be captured by the basin liner, which in turn transfer more heat to the fluid, resulting in an increase in the fluid temperature. A higher ambient temperature also causes the fluid temperature to be higher. Consequently, when the fluid temperature is higher, the evaporation process is enhanced (Xiao et al., 2013), thus resulting in a higher productivity.

On the other hand, concerning the effect of wind speed on the productivity of solar stills, conflicting results have been obtained in literature, with some studies revealing that the productivity increases with increasing wind speed (El-Sebaii, 2000; Zurigat & Abu-Arabi, 2004) while some studies indicating a decrease in productivity with increasing wind speed (Nafey et al., 2000; Al-Garni, 2012; Danish et al., 2019). El-Sebaii (2000) attributed the increase in productivity with increasing wind speed due to an increase in the temperature

difference between the basin fluid and the glass cover while Danish et al. (2019) attributed the decrease in productivity with increasing wind speed due to an increase in heat loss.

4.1.1.1. Hourly variation of global solar radiation on a horizontal surface and hourly variation of ambient temperature and wind speed on Sample Day

The hourly variation of global solar radiation on a horizontal surface, hourly variation of ambient temperature and hourly variation of wind speed for the Sample Day (from 7 am on 2nd January 2007 to 7 am on 3rd January 2007) are given in Figure 4.1, Figure 4.2 and Figure 4.3 respectively. The maximum global solar radiation on a horizontal surface was 1122 Wm^{-2} on the Sample Day. The hourly ambient temperature varied from 16.7 to 29.1 ºC and the hourly wind speed varied from 0.2 to 3.1 ms^{-1}.

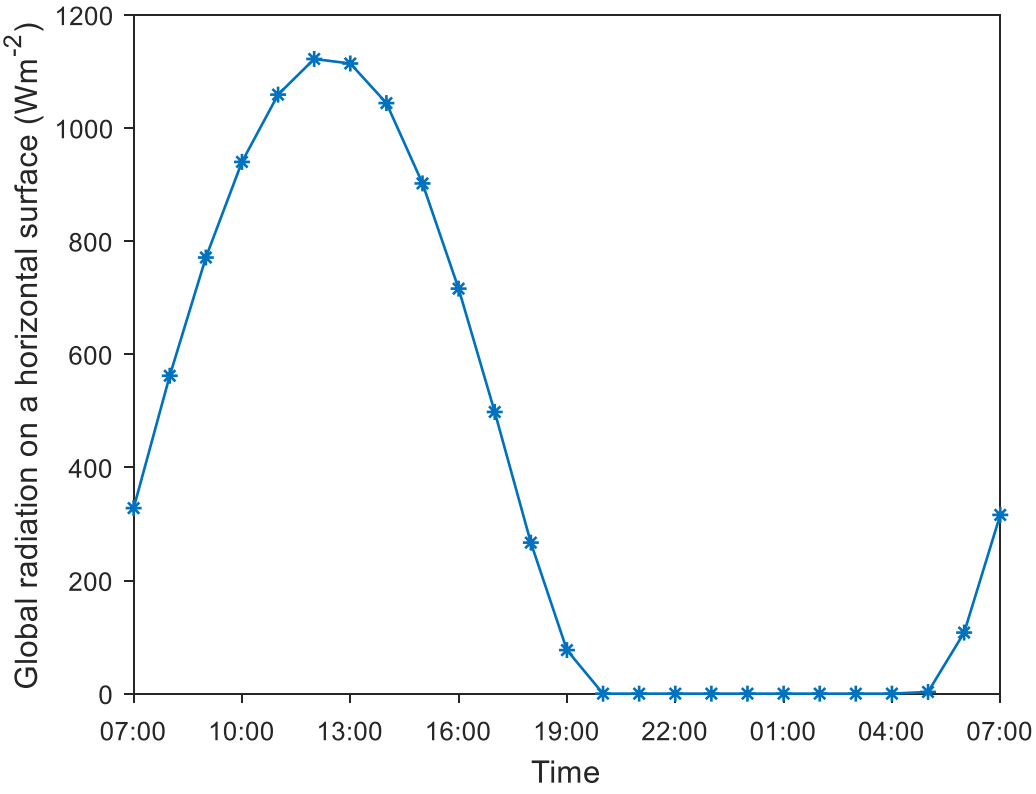

Figure 4.1: Hourly variation of global solar radiation on a horizontal surface from 2nd January 2007 at 7 am to 3rd January 2007 at 7 am.

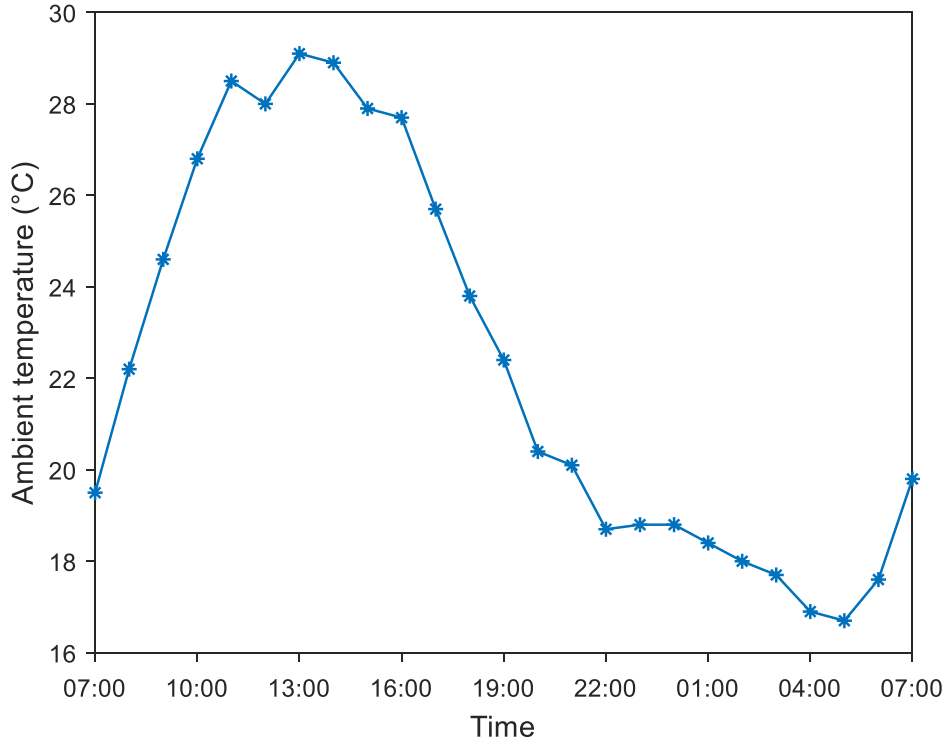

Figure 4.2: Hourly variation of ambient temperature from 2nd January 2007 at 7 am to 3rd January 2007 at 7 am.

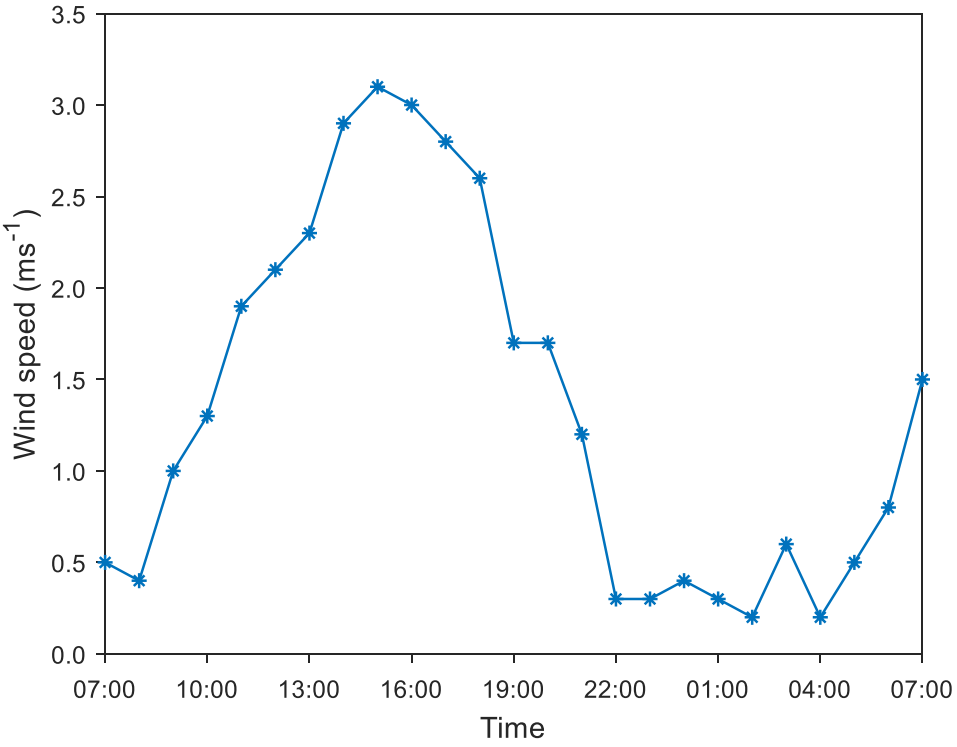

Figure 4.3: Hourly variation of wind speed from 2nd January 2007 at 7 am to 3rd January 2007 at 7 am.

4.1.1.2. Monthly hourly average global solar radiation on a horizontal surface, monthly hourly average ambient temperature and wind speed for one year

Figure 4.4, Figure 4.5 and Figure 4.6 illustrate respectively the monthly hourly average global solar radiation on a horizontal surface, the monthly hourly average ambient temperature and the monthly hourly average wind speed for Stellenbosch. The monthly hourly average global solar radiation on a horizontal surface was lowest in the month of July, at 127.2 Wm^{-2} and highest in December, at 354.4 Wm^{-2}, as shown in Figure 4.4.

Furthermore, the monthly hourly average ambient temperature was lowest during the month of July, at 11.7 ºC and highest during the month of January at 22.6 ºC, as can be depicted from Figure 4.5. On the other hand, the monthly hourly average wind speed varied from 1.4 to 2.4 ms^{-1} throughout the year, with the minimum being recorded in June and the highest recorded in September, as can be observed from Figure 4.6.

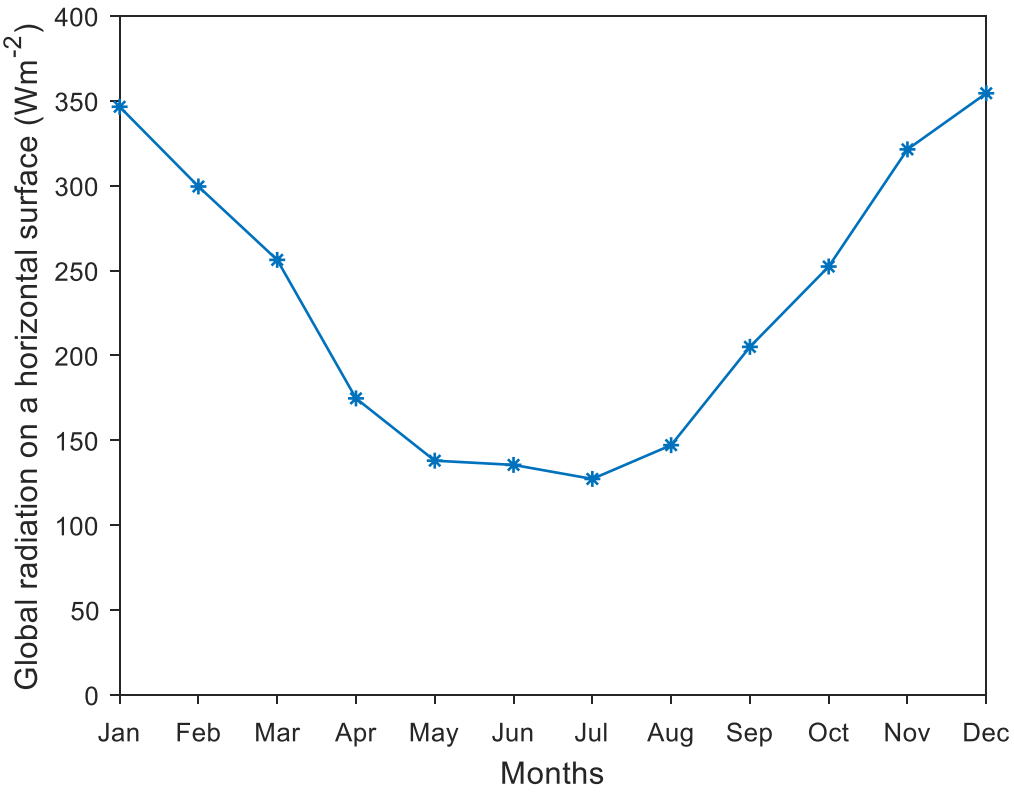

Figure 4.4: Monthly hourly average global radiation on an inclined surface in Stellenbosch, South Africa.

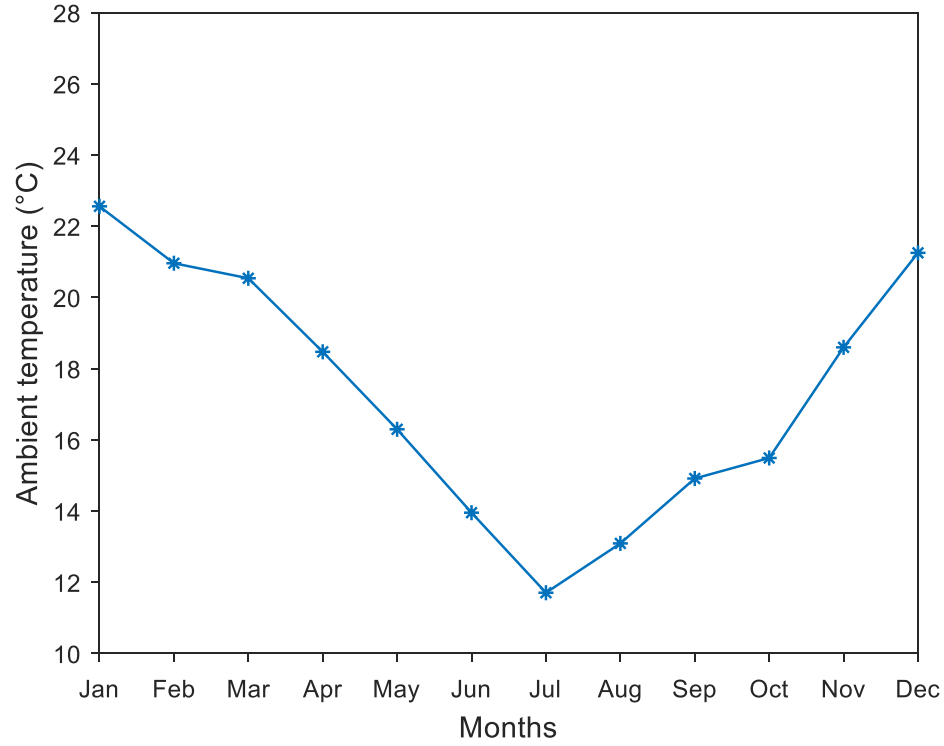

Figure 4.5: Monthly hourly average ambient temperature in Stellenbosch, South Africa.

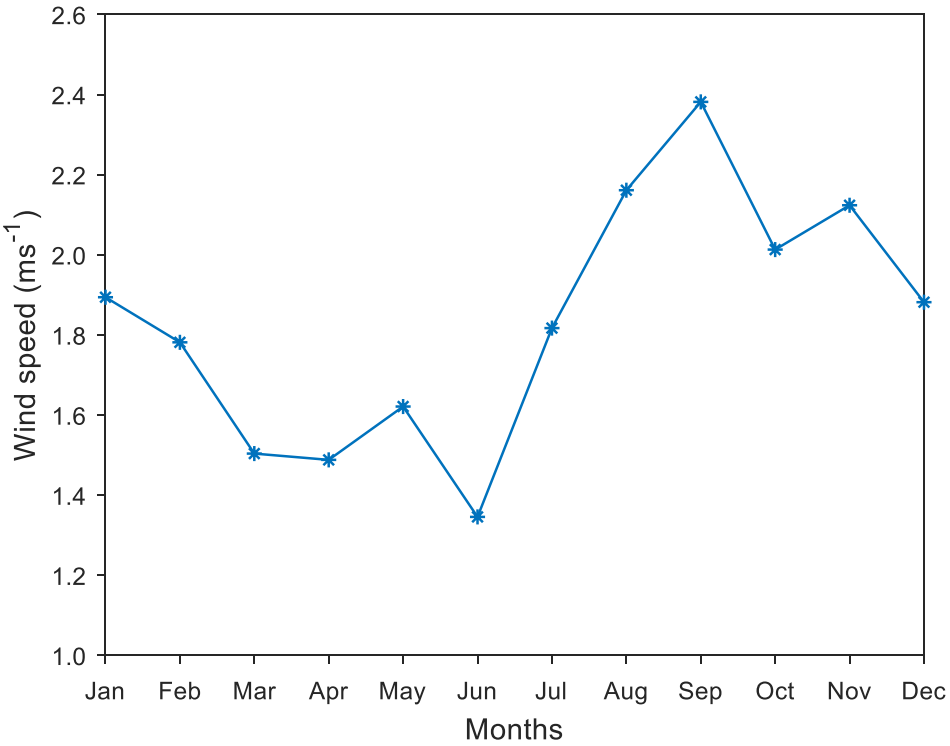

Figure 4.6: Monthly hourly average wind speed in Stellenbosch, South Africa.

4.1.2. Fluid temperature profiles for Sample Day

4.1.2.1. Comparison of hourly fluid temperature for the base fluid and the nanofluid

Figure 4.7 shows the hourly variation of the temperature of the base fluid and the nanofluid with nanoparticles of size 10 nm. The temperatures for the nanofluids with nanoparticles of other sizes have not been plotted in Figure 4.7 as the values are very close to that of the nanofluid with the 10 nm particles and they overlap. It can be observed that the fluid temperature inside the solar still with the nanoparticles was higher than the fluid temperature inside the solar still with the base fluid only. This is because nanoparticles can absorb solar radiation directly into the base fluid, causing the temperature of each discrete nanoparticle to increase, in turn causing an increase in the thermal conductivity and the temperature of the fluid (Sahota & Tiwari, 2016a). The maximum base fluid temperature was 61.91 ºC while the maximum nanofluid temperature with the 10 nm nanoparticles was 63.81 ºC.

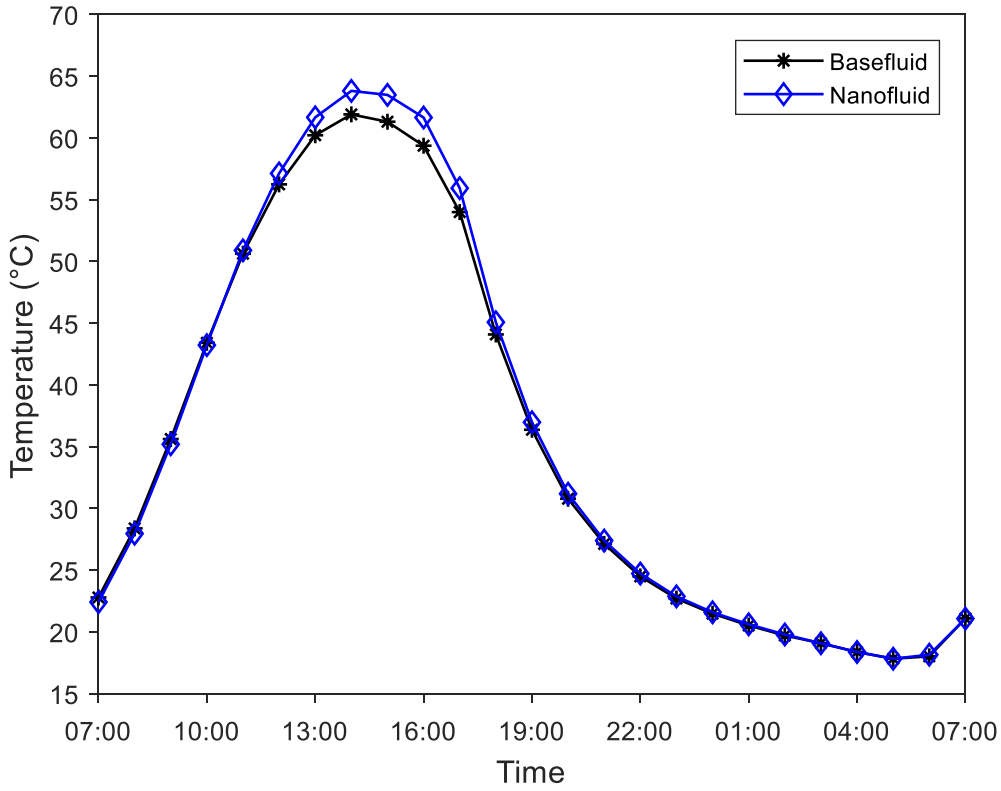

Figure 4.7: Hourly variation of fluid temperature for the base fluid and nanofluid with Al_2O_3 nanoparticles of size 10 nm, from 2nd January 2007 at 7 am to 3rd January 2007 at 7 am.

4.1.2.2. Effect of nanoparticle size on fluid temperature

Figure 4.8 illustrates the effect of nanoparticle size on fluid temperature. Only the maximum fluid temperature was plotted in order to be able to see the trend clearly. It can be observed that the maximum fluid temperature decreases as the nanoparticle size increases. The maximum fluid temperature with the 10 nm nanoparticles was 63.812 ºC while that with the 100 nm nanoparticles was 63.788 ºC. This can be attributed to the fact that the thermal conductivity of the fluid decreases with increasing nanoparticle size, as will be discussed in the next section.

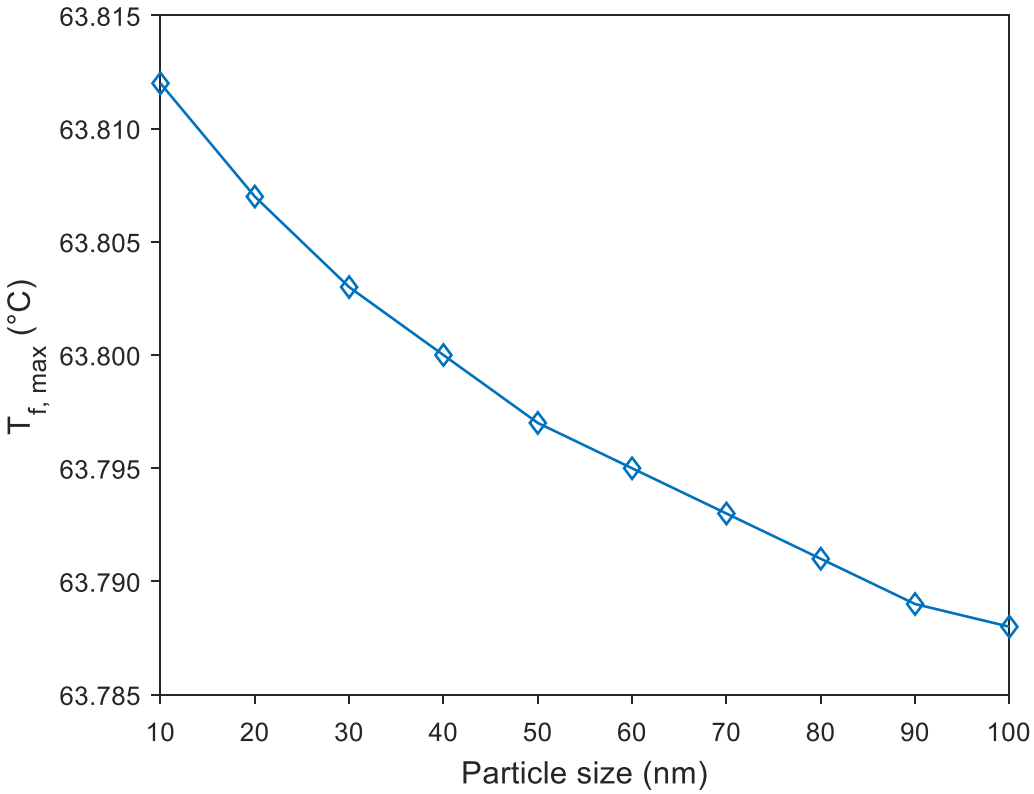

Figure 4.8: Maximum fluid temperature ($T_{f, max}$) for nanofluids with different nanoparticle sizes.

4.1.3. Thermophysical properties of fluid for Sample Day

4.1.3.1. Effect of nanoparticle size on thermal conductivity of nanofluids

Figure 4.9 gives the hourly variation of thermal conductivity of the base fluid and the nanofluid with various particle sizes for the Sample Day. It can be observed that the thermal conductivity for the nanofluids is higher than that of the base fluid and the thermal conductivity increases with decreasing nanoparticle size. The maximum thermal conductivity of the base fluid and the nanofluid with Al_2O_3 nanoparticles of size 10 nm was 0.65 $Wm^{-1}K^{-1}$ and 0.76 $Wm^{-1}K^{-1}$, respectively. Thus, a maximum increase of 16.92% could be achieved in the fluid thermal conductivity by the addition of the 10 nm Al_2O_3 nanoparticles. Moreover, it can be noted that difference in the thermal conductivity between the base fluid and the nanofluids is higher during hours of peak sunshine, which means that the effect of the nanofluids is optimum during this time.

Furthermore, the maximum thermal conductivity of the nanofluid with Al_2O_3 nanoparticles of size 100 nm was 0.74 $Wm^{-1}K^{-1}$, as can be observed from Figure 4.9. Consequently, an increase in nanoparticle size from 10 to 100 nm led to a decrease of 2.63% in the nanofluid thermal conductivity. A decrease in thermal conductivity with increasing nanoparticle size has been mentioned in previous studies (Teng et al., 2010; Khanafer & Vafai, 2011; Amin et al., 2015; Prakash et al., 2018).

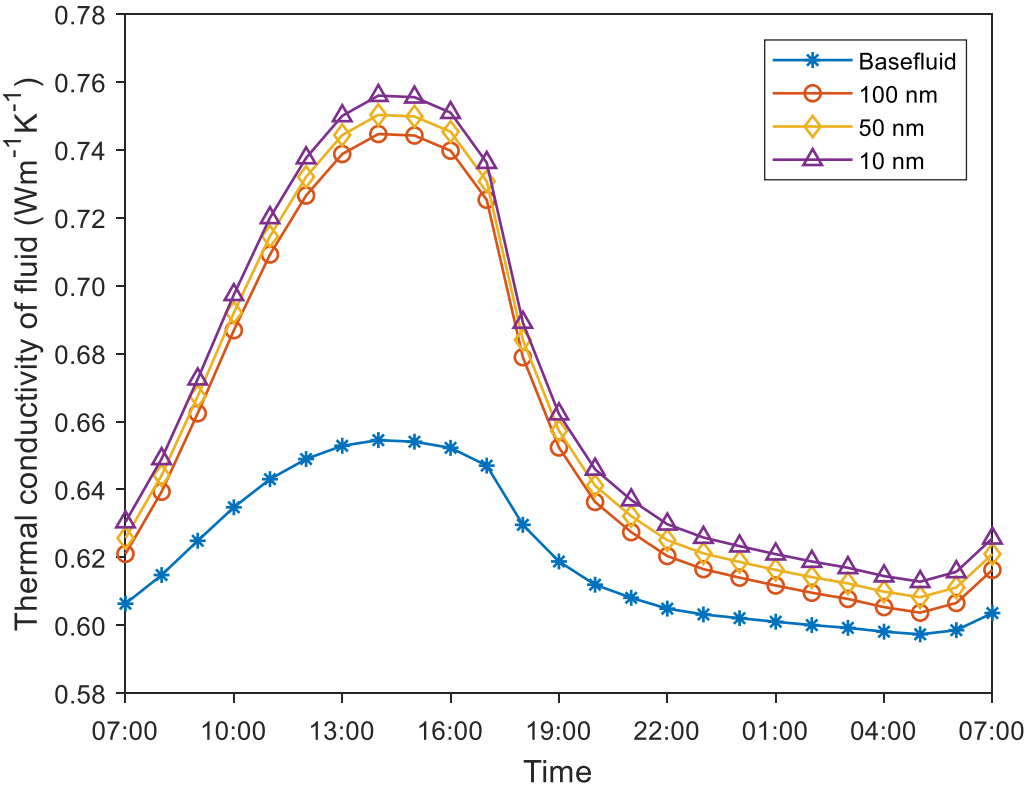

Figure 4.9: Hourly variation of thermal conductivity for the base fluid and nanofluids with Al_2O_3 nanoparticles of size 10 nm, 50 nm and 100 nm, from 2nd January 2007 at 7 am to 3rd January 2007 at 7 am.

Sezer, Atieh and Koç (2019) carried out a review on nanofluids and they reported that nanofluids with Al_2O_3 nanoparticles in the size range of 5 to 80 nm have an enhanced thermal conductivity in the range of 0.3 to 38%. Munyalo and Zhang (2018) conducted a review on the effect of nanoparticle size on the thermophysical properties of nanofluids and they indicated that the thermal conductivity of a nanofluid generally increases with a decrease in the nanoparticle size. Khanafer and Vafai (2011) reported that the increase in thermal conductivity for smaller nanoparticles is due to their larger surface area to volume ratio than bigger particles. Thus, as the nanoparticle size decreases, the surface area to volume ratio increases, which means that more heat can be transferred from the nanoparticles to the fluid, thus causing an increase in the thermal conductivity.

4.1.3.2. Effect of nanoparticle size on dynamic viscosity of nanofluids

The hourly variation of dynamic viscosity of the base fluid and the nanofluid with various particle sizes for the Sample Day are given in Figure 4.10. The addition of nanoparticles causes the viscosity of the fluid to increase. The maximum differences between the base fluid and the nanofluid viscosity occurred during hours of peak sunshine and the viscosity values were at a minimum during this time period due to the high fluid temperatures. The minimum viscosity for the base fluid and the nanofluid with Al_2O_3 nanoparticles of size 10 nm was 4.50 x 10^{-4} Pa.s and 5.91 x 10^{-4} Pa.s, respectively. This corresponds to an increase of 31.33% in the fluid viscosity. Furthermore, the viscosity model which was used in this study caused a decrease in the viscosity with increasing nanoparticle size as can be observed from Figure 4.10. During hours of peak sunshine, the minimum viscosity of the nanofluid with Al_2O_3 nanoparticles of size 100 nm was 5.68 x 10^{-4} Pa.s; hence an increase in nanoparticle size from 10 nm to 100 nm caused the viscosity of the nanofluid to decrease by 3.89%.

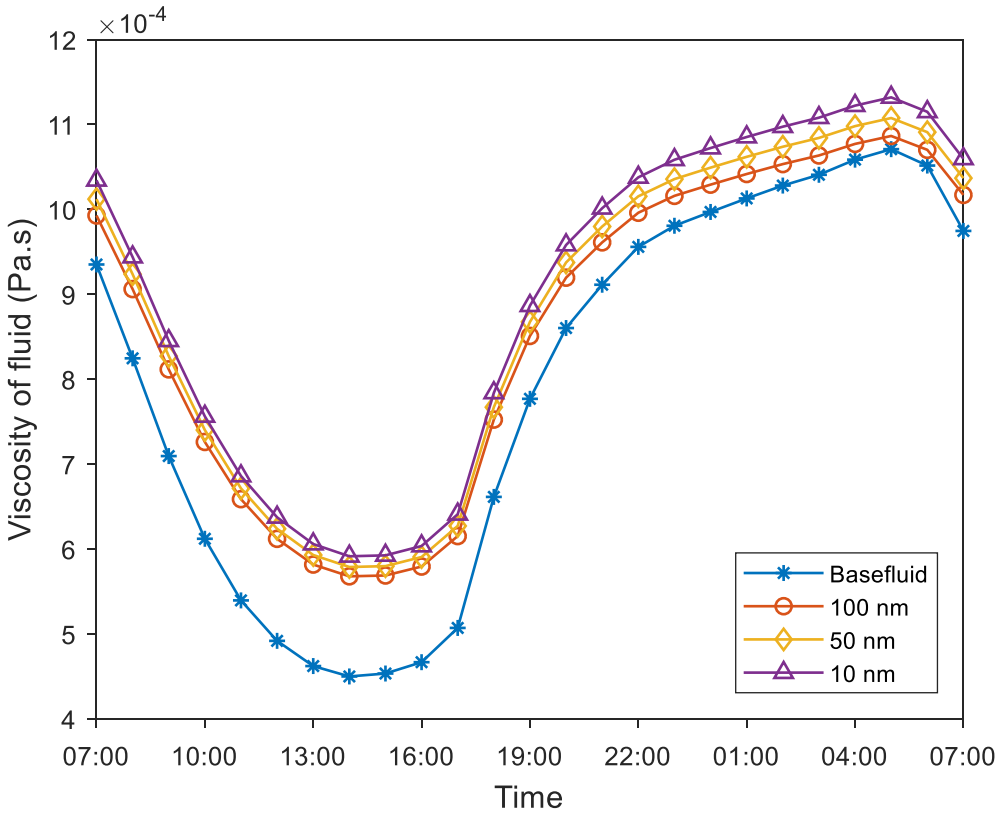

Figure 4.10: Hourly variation of dynamic viscosity for the base fluid and nanofluids with Al_2O_3 nanoparticles of size 10 nm, 50 nm and 100 nm, from 2nd January 2007 at 7 am to 3rd January 2007 at 7 am.

Nevertheless, Mahbubul, Saidur and Amalina (2012) carried out a review of the viscosity of nanofluids and they asserted that the size of the nanoparticle affects the viscosity of the nanofluid but there is no clear consensus on the effect of nanoparticle size on viscosity of nanofluids. In another review study on the viscosity of nanofluids, Mishra et al. (2014) claimed that there is no theoretical correlation which can predict accurately the viscosity of nanofluids. Munyalo and Zhang (2018) conducted a review study on the effect of nanoparticle size on thermophysical properties of nanofluids and they claimed that the effect of particle size on viscosity of nanofluids is not yet clear and more research is needed on this area. Koca et al. (2018) reviewed viscosity models for nanofluids and they also indicated that there is a discrepancy about the influence of nanoparticle size on the viscosity of nanofluids, with some studies reporting an increase in viscosity with increasing nanoparticle size while some studies reported an increase in viscosity with decreasing nanoparticle size. Consequently, it can be noted that up to now, there is no correlation incorporating the nanoparticle size which can predict accurately the viscosity of a nanofluid. The need for additional research to develop accurate correlations for predicting the thermophysical properties of nanofluids has also been emphasized in previous studies (Khanafer & Vafai, 2011; Gupta et al., 2017; Bellos & Tzivanidis, 2019).

4.1.4. Hourly variation of Nusselt Number for the Sample Day

Figure 4.11 shows the hourly variation of the Nusselt number of the base fluid and the nanofluid with various particle sizes for the Sample Day. The Nusselt number is an important parameter in the computation of the convective heat transfer coefficient from the basin liner to the fluid and thus, it is essential to illustrate its hourly variation for the Sample Day. It can be noted that the Nusselt number was higher for the nanofluids as compared to the base fluid.

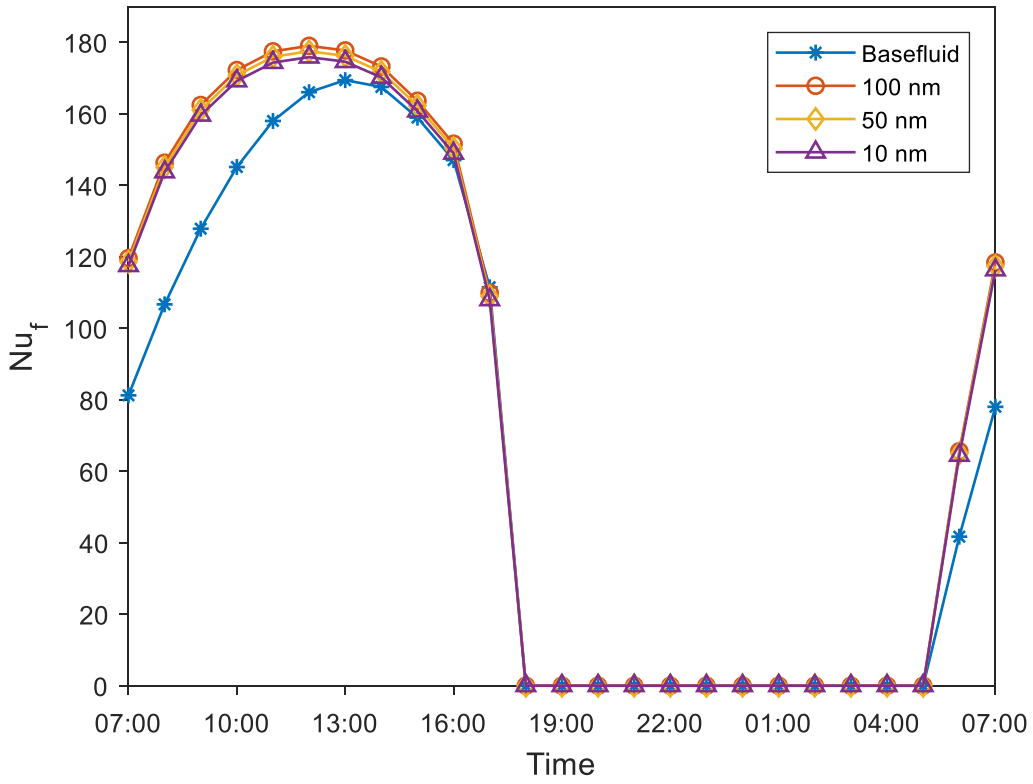

Figure 4.11: Hourly variation of the Nusselt number (Nu_f) for the base fluid and nanofluids with Al_2O_3 nanoparticles of size 10 nm, 50 nm and 100 nm, from 2nd January 2007 at 7 am to 3rd January 2007 at 7 am.

The maximum Nusselt number for the base fluid and the nanofluid with the Al_2O_3 nanoparticles of size 10 nm was 169.40 and 175.83, respectively. The Nusselt number is a function of the Rayleigh number which is in turn a function of the Grashof number and the Prandtl Number, and these two dimensionless constants are dependent on the thermophysical properties of the fluid. Due to the enhanced thermophysical properties of the nanofluid, the Nusselt number of the nanofluid was higher than that of the base fluid. It can also be seen that the nanoparticle size has some effects on the Nusselt number, as can be observed from Figure

4.11. In order to observe the trend more clearly, the maximum Nusselt Number for different nanoparticle sizes was plotted.

The variation of the maximum Nusselt Number with varying Al_2O_3 nanoparticle sizes is given in Figure 4.12. It can be seen that the Nusselt number increases with increasing nanoparticle size. The maximum Nusselt number increased from 175.83 to 178.99 as the nanoparticle size was increased from 10 to 100 nm. This can be attributed to the fact that the viscosity decreases with increasing nanoparticle size as discussed earlier. This decrease in viscosity causes the Grashof number to increase, in turn causing an increase in the Nusselt Number with increasing nanoparticle size.

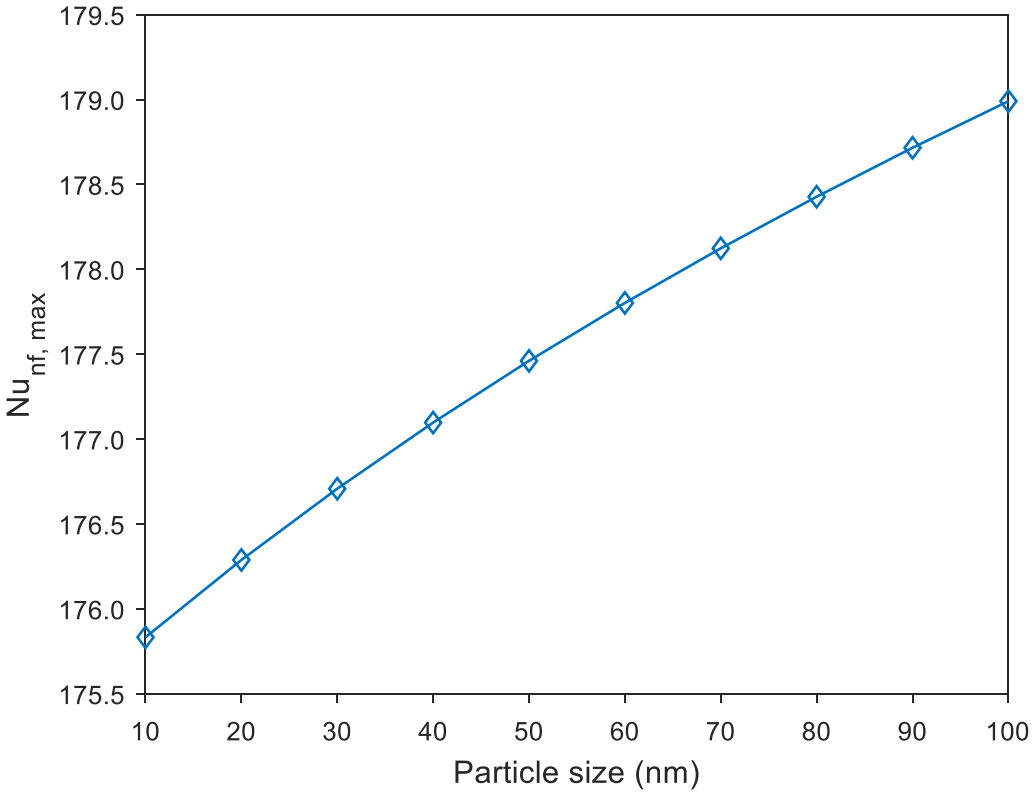

Figure 4.12: Maximum Nusselt Number for nanofluids ($Nu_{nf,\ max}$) with Al_2O_3 nanoparticles of varying sizes.

4.1.5. Heat transfer coefficients

4.1.5.1. Effect of nanoparticles on convective heat transfer coefficient from the basin liner to the fluid

Figure 4.13 illustrates the convective heat transfer coefficient from the basin liner to the fluid for the solar still with the base fluid only and for the solar still with the Al_2O_3 nanoparticles of size 10 nm. The convective heat transfer coefficient for the solar stills with other nanoparticle sizes have not been plotted in Figure 4.13 as they are so close to the values for the nanoparticles of size 10 nm that they overlap when plotted on the same graph. It can be observed that the convective heat transfer coefficient was higher for the solar still with the nanoparticles. This is attributed to the fact that the convective heat transfer coefficient is dependent on the thermal conductivity of the fluid and since the thermal conductivity of the nanofluid is higher than that of the base fluid, the convective heat transfer coefficient is higher for the nanofluid. The maximum convective heat transfer coefficient was 442.37 and 523.73 $Wm^{-2}K^{-1}$ for the base fluid and nanofluid with nanoparticles of size 10 nm, respectively.

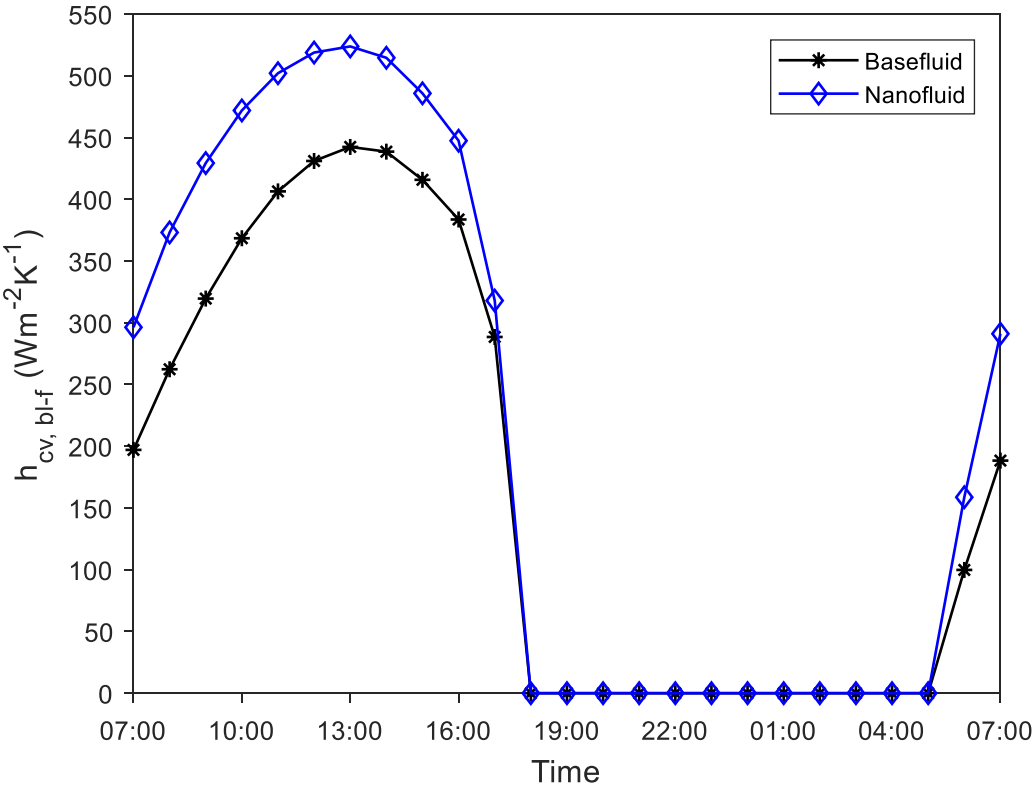

Figure 4.13: Hourly variation of convective heat transfer coefficient from the basin liner to the fluid ($h_{cv,bl-f}$) for the base fluid and the nanofluid with Al_2O_3 nanoparticles of size 10 nm, from 2nd January 2007 at 7 am to 3rd January 2007 at 7 am.

The maximum convective heat transfer coefficient from the basin liner to the nanofluid with nanoparticles of different sizes for the Sample Day is given in Figure 4.14. It is observed that the convective heat transfer increases with increasing nanoparticle size. The maximum convective heat transfer coefficient from the basin liner to the fluid increased from 523.73 to 525.14 $Wm^{-2}K^{-1}$ when the nanoparticle size was increased from 10 to 100 nm. This might be contradictory to what might be expected as it has been established that the thermal conductivity decreases with increasing nanoparticle size.

However, the convective heat transfer coefficient does not depend only on the thermal conductivity of the nanofluid, but it is also a function of the Nusselt Number which in turn depends on other thermophysical properties of the nanofluid, as given by Equations (3.39) to (3.44). The dynamic viscosity correlation which has been used for the simulations in MATLAB gives a decrease in viscosity with increasing nanoparticle size, as indicated by Figure 4.10. Consequently, this decrease in viscosity causes the Grashof number to increase,

thus causing an increase in the Nusselt number, as illustrated by Figure 4.12. Therefore, since the magnitude of the Nusselt number is higher than that of the thermal conductivity, the convective heat transfer coefficient between the basin liner and the fluid increases with increasing nanoparticle size.

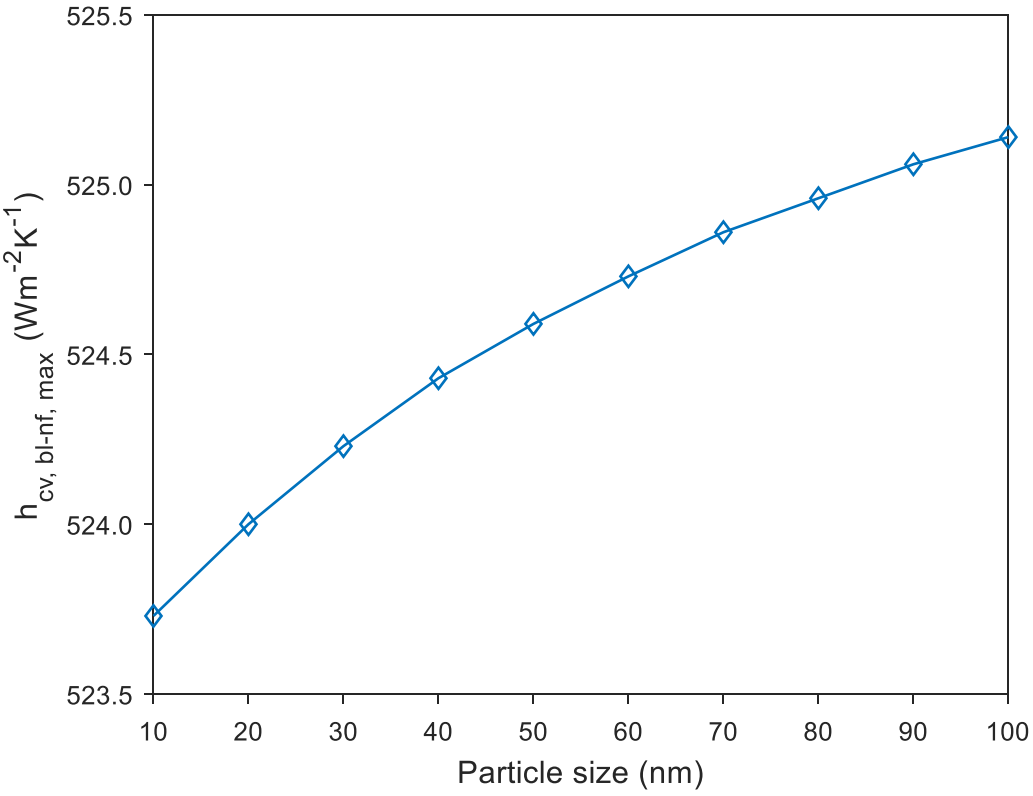

Figure 4.14: Variation of maximum convective heat transfer coefficient from basin liner to nanofluid ($h_{cv,bl\text{-}nf,\ max}$) for different particle sizes.

4.1.5.2. Effect of nanoparticles on convective heat transfer coefficient from fluid to glass cover

The variation of the convective heat transfer coefficient from the fluid to the glass cover during hours of peak sunshine for the Sample Day for the base fluid and the nanofluid with nanoparticles of size 10 nm is shown in Figure 4.15. Only the values for the peak sunshine hours and one nanoparticle size have been plotted in Figure 4.15 in order to observe the trend more clearly. It can be noted that the convective heat transfer coefficient from the fluid to the glass cover is higher for the base fluid compared to the nanofluid. The maximum convective heat transfer coefficient was 2.39 and 2.41 $Wm^{-2}K^{-1}$ for the base fluid and the nanofluid with nanoparticles of size 10 nm, respectively. The convective heat transfer coefficient was

computed using Equation (3.4) and it is dependent on the fluid temperature, vapour pressure at the fluid surface and the thermophysical properties of air-water mixture. The presence of nanoparticles causes the fluid temperature to be higher, resulting in a higher vapour pressure at the fluid surface and a higher air-water mixture density. Consequently, this leads to an enhanced convective heat transfer coefficient from the fluid to the glass cover when nanoparticles are added to the fluid.

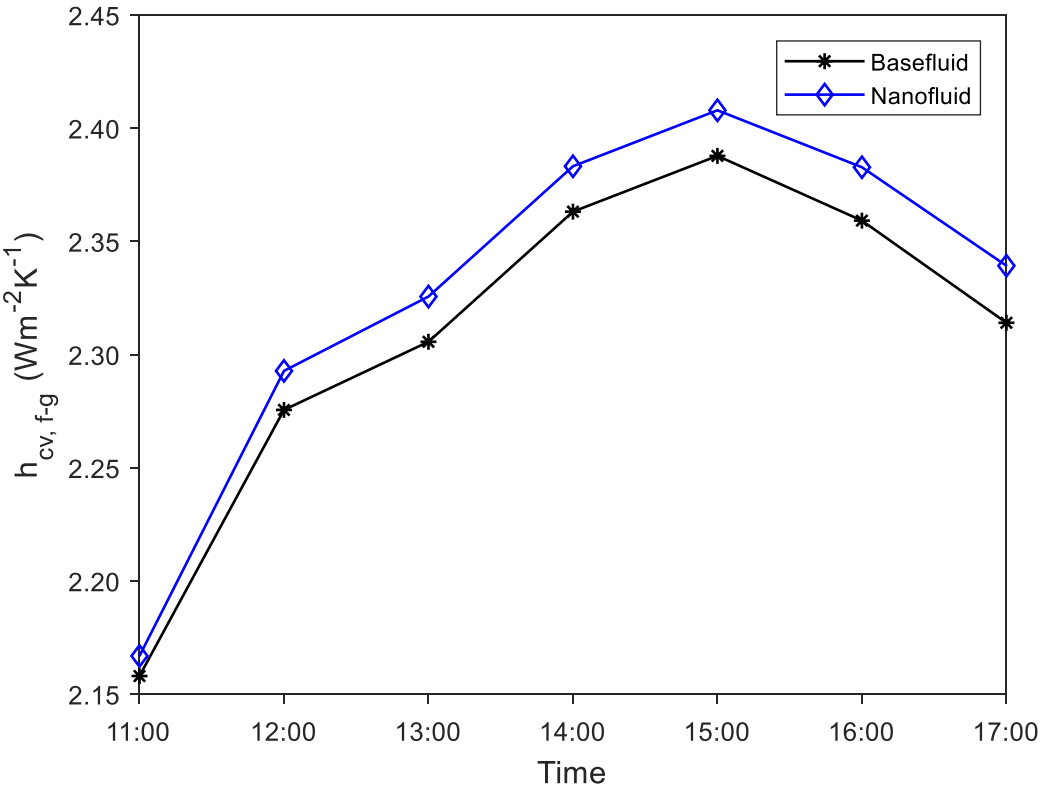

Figure 4.15: Hourly variation of convective heat transfer coefficient from the fluid to the glass cover ($h_{cv, f-g}$) for the base fluid and the nanofluid with Al_2O_3 nanoparticles of size 10 nm, from 11 am to 5 pm, on 2nd January 2007.

The maximum convective heat transfer coefficient from the fluid to the glass cover for the Sample Day for the nanofluid with different particle sizes is given in Figure 4.16. The convective heat transfer coefficient decreases with increasing nanoparticle size. This is because the thermal conductivity decreases with increasing nanoparticle size, thus causing a decrease in the fluid temperature which subsequently causes a decrease in the convective heat transfer coefficient from the fluid to the glass cover.

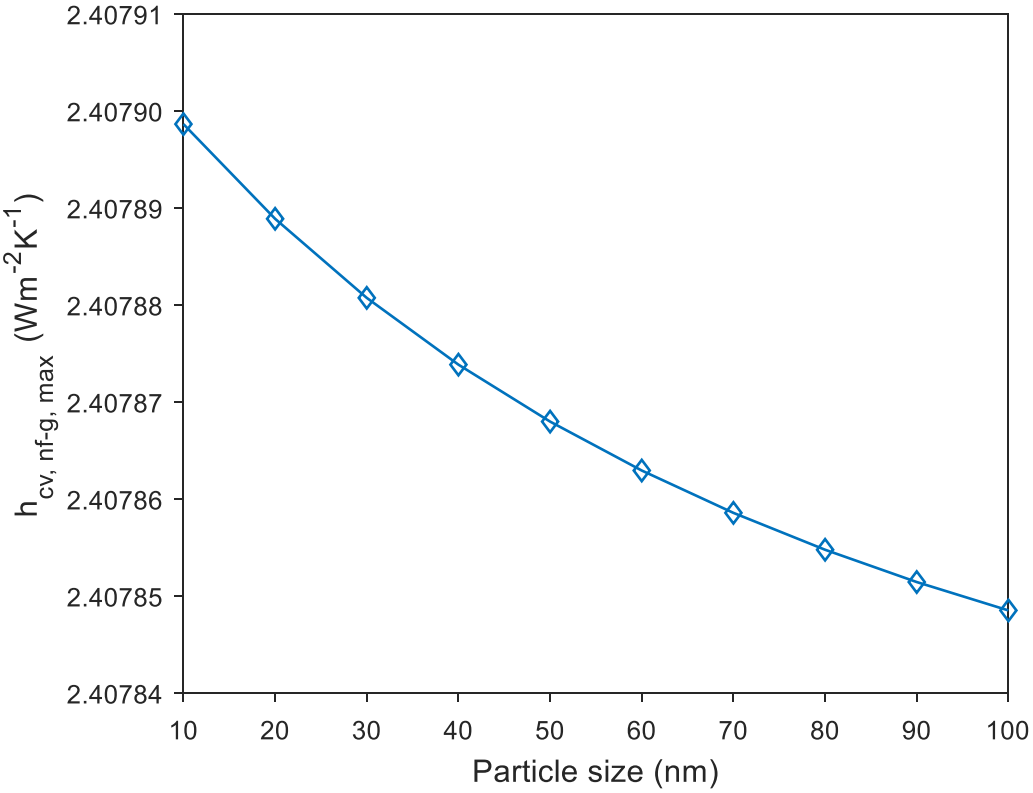

Figure 4.16: Variation of maximum convective heat transfer coefficient from nanofluid to glass cover ($h_{cv,nf\text{-}g,\ max}$) for different particle sizes.

4.1.5.3. Effect of nanoparticles on evaporative heat transfer coefficient from fluid to glass cover

The hourly variation for the evaporative heat transfer coefficient between the fluid and the glass ($h_{e,\ f\text{-}g}$) for the base fluid and the nanofluid with nanoparticles of size 10 nm is given in Figure 4.17. The graphs for the nanoparticles of other sizes have not been plotted in Figure 4.17 as they are so close to the values for the nanoparticles of 10 nm that they overlap. It is noted that the evaporative heat transfer coefficient is higher for the nanofluid as compared to the base fluid. During the Sample Day, the maximum evaporative heat transfer coefficient was 36.22 and 40.98 $Wm^{-2}K^{-1}$, for the base fluid and nanofluid with nanoparticles of size 10 nm, respectively. This corresponds to an increase in 13.14% in the evaporative heat transfer coefficient with the addition of Al_2O_3 nanoparticles of size 10 nm. This is because in a nanofluid, the presence of nanoparticles causes an increase in the temperature of the fluid, which in turn causes the vapour pressure at the surface of the fluid to increase. Furthermore, as discussed earlier, the convective heat transfer coefficient from the fluid to the glass is also

higher with the presence of nanoparticles. Since the evaporative heat transfer coefficient is a function of the fluid vapour pressure and the convective heat transfer coefficient from fluid to glass, as given by Equation (3.5), a higher fluid vapour pressure and a higher convective heat transfer coefficient from fluid to glass result in an increase in the evaporative heat transfer coefficient.

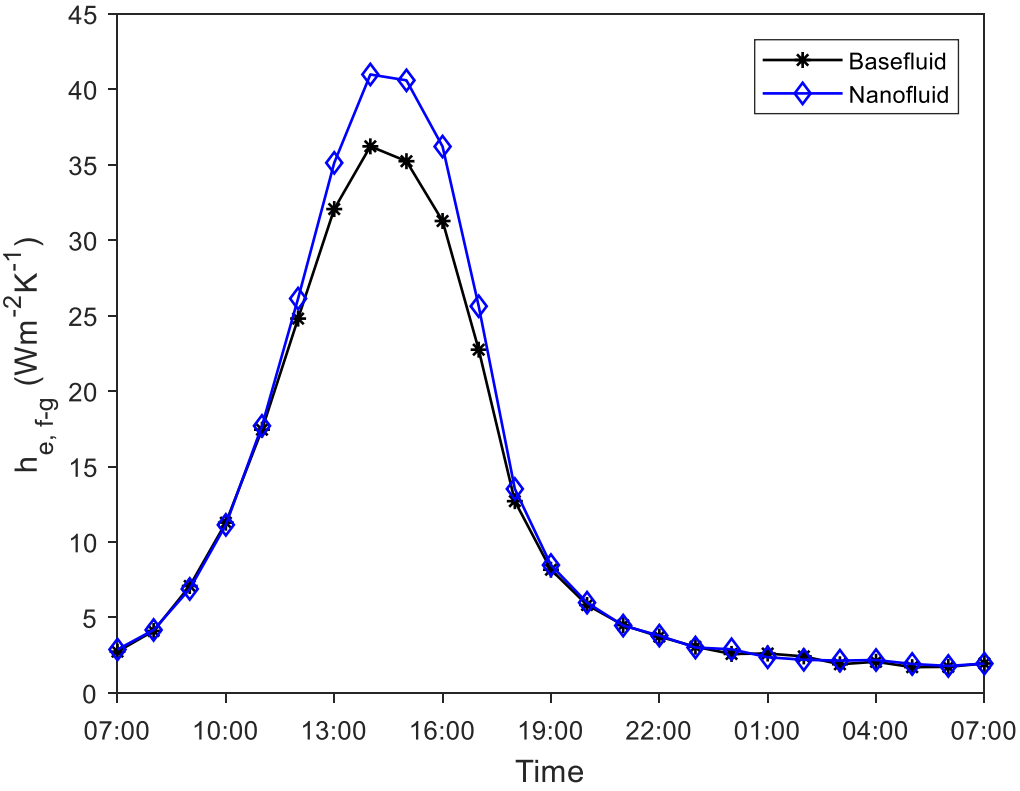

Figure 4.17: Hourly variation of evaporative heat transfer coefficient from the fluid to the glass cover ($h_{e,f-g}$) for the base fluid and the nanofluid with Al_2O_3 nanoparticles of size 10 nm, from 2nd January 2007 at 7 am to 3rd January 2007 at 7 am.

Figure 4.18 illustrates the effect of nanoparticle size on the maximum evaporative heat transfer coefficient from the nanofluid to the glass cover. It can be observed that the maximum evaporative heat transfer decreases with increasing nanoparticle size. The evaporative heat transfer coefficient decreased from 40.98 to 40.91 $Wm^{-2}K^{-1}$ when the nanoparticle size was increased from 10 to 100 nm. This is due to a decrease in the nanofluid temperature and a decrease in the convective heat transfer coefficient from fluid to glass with increasing nanoparticle size, as discussed earlier, and as exhibited by Figure 4.8 and Figure

4.16, respectively. Therefore, the evaporative heat transfer coefficient also decreases as the nanoparticle size increases.

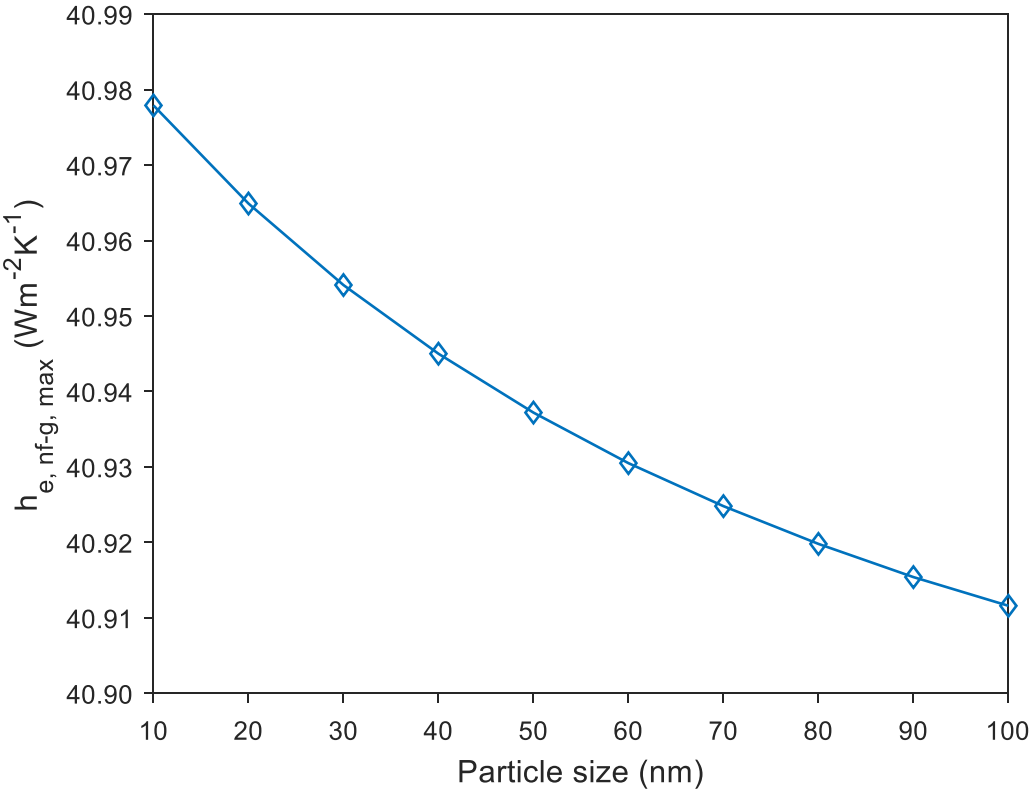

Figure 4.18: Variation of maximum evaporative heat transfer coefficient from nanofluid to glass cover ($h_{e,nf-g, max}$) for different nanoparticle sizes.

4.1.6. Distillate output

4.1.6.1. Distillate output for Sample Day

The hourly variation of the cumulative mass of distillate obtained by the solar stills with the base fluid only and with Al_2O_3 nanoparticles of size 10 nm for the Sample Day is given in Figure 4.19. The values for the cumulative mass of distillate obtained from the solar stills with other nanoparticle sizes were very close to that of the solar still with the 10 nm nanoparticles and they have not been plotted in Figure 4.19 as they would overlap.

It can be observed from Figure 4.19 that the total mass of distillate generated by the solar still with the 10 nm Al_2O_3 nanoparticles was higher than that of the solar still with the base fluid only. The addition of nanoparticles causes an increase in fluid thermal conductivity and heat transfer, thus causing an increase in the distillate production. The productivity of the solar still with the base fluid only and the solar still with the 10 nm Al_2O_3 nanoparticles was

4.23099 and 4.62342 kgm^{-2}, respectively. This corresponds to an increase of 9.28% in the productivity with the addition of nanoparticles of size 10 nm. The increase in the productivity is only 9.28% as there was not a huge difference in the temperatures of the base fluid and the nanofluid, as shown in Figure 4.7.

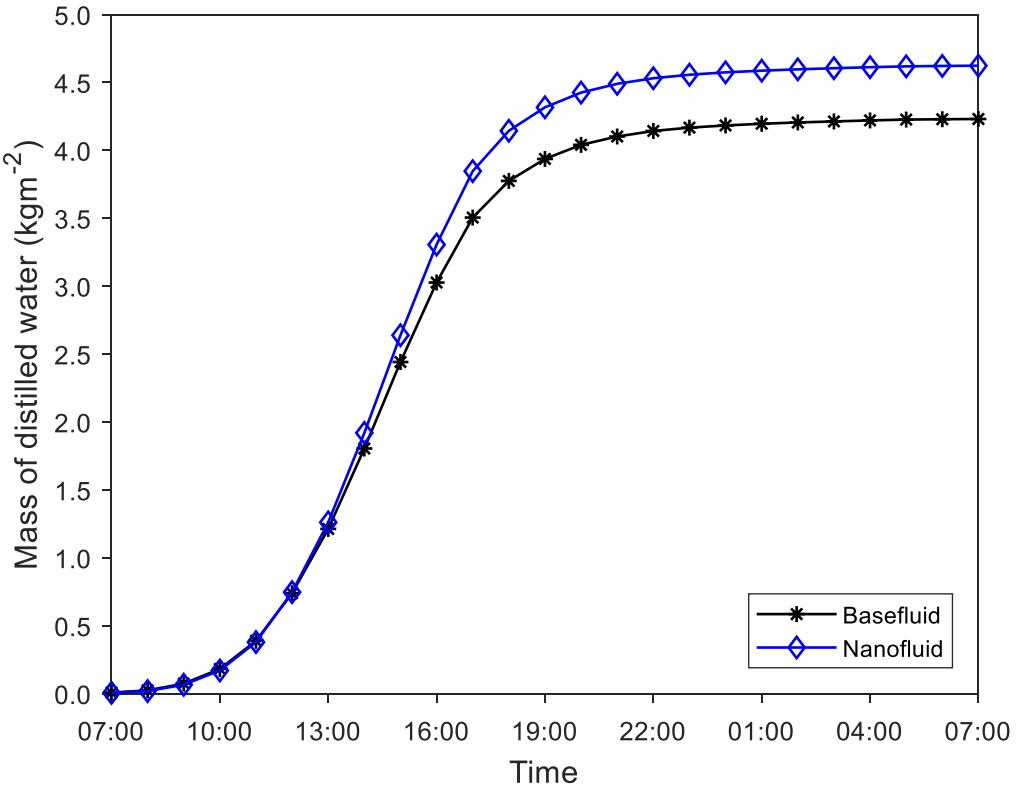

Figure 4.19: Hourly variation of cumulative mass of distillate achieved by the solar still with the base fluid only and the solar still with nanofluid containing Al_2O_3 nanoparticles of size 10 nm, from 2nd January 2007 at 7 am to 3rd January 2007 at 7 am.

The distillate production on the Sample Day from the solar stills with varying nanoparticle sizes is given in Figure 4.20. It can be observed that the productivity decreases with increasing nanoparticle size. The productivity decreased from 4.62342 to 4.61821 kgm^{-2} when the nanoparticle size was increased from 10 to 100 nm. The decrease in productivity is associated with a decrease in the fluid temperature and a decrease in the convective and evaporative heat transfer coefficients from fluid to glass with increasing nanoparticle size.

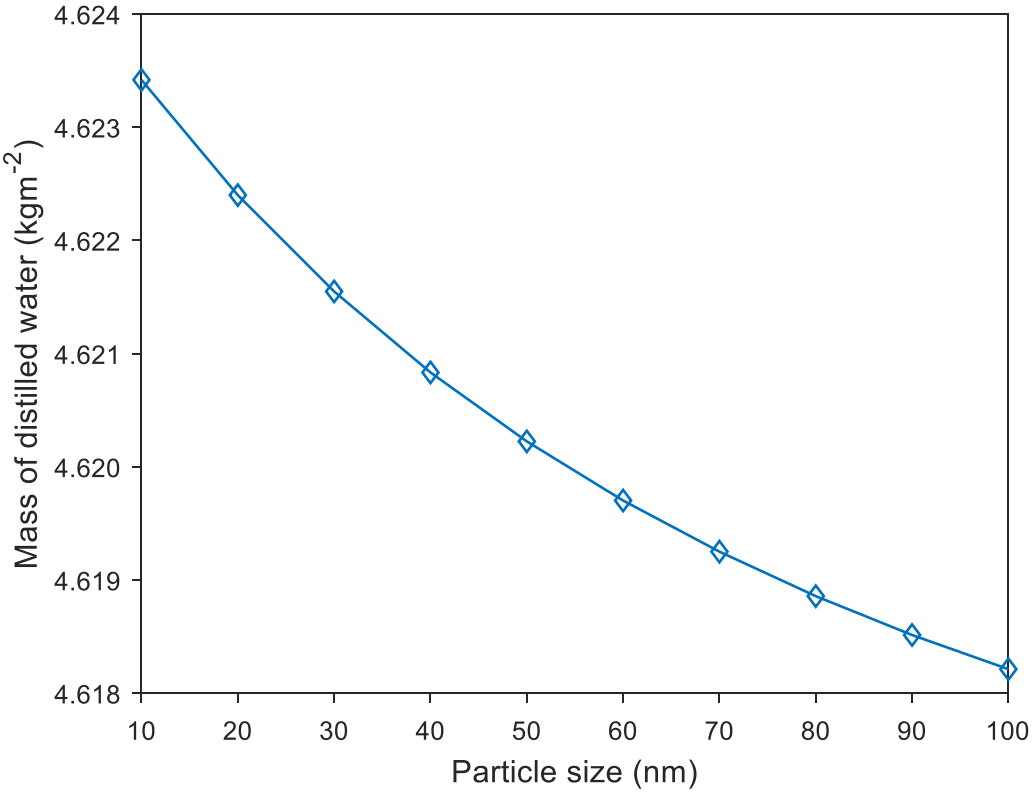

Figure 4.20: Cumulative mass of distilled water obtained from the solar stills containing nanofluids with Al_2O_3 nanoparticles of different sizes.

4.1.6.2. Mean monthly distillate production for one year

The total mass of distillate obtained from the solar stills with and without nanoparticles for each month was simulated in MATLAB and the results are given in Figure 4.21. It can be observed that the solar stills with the nanoparticles could achieve a higher distillate production than the solar still with the base fluid only. Furthermore, this difference was more significant during the months of January, February, March, October, November and December as these are the warmer months in South Africa with higher levels of solar radiation.

For instance, the total mass of distillate obtained from the solar still with the base fluid only and with nanoparticles of size 10 nm was 104.73 and 114.17 kgm^{-2}, respectively in the month of January. This translates to an increase of 9.01% in the distillate production. On the other hand, in the month of July, when solar radiation was very low, the mass of distillate was 24.62 and 24.94 kgm^{-2} for the solar still with the base fluid only and with nanoparticles of size 10 nm, respectively and this translates to an increase of only 1.31%.

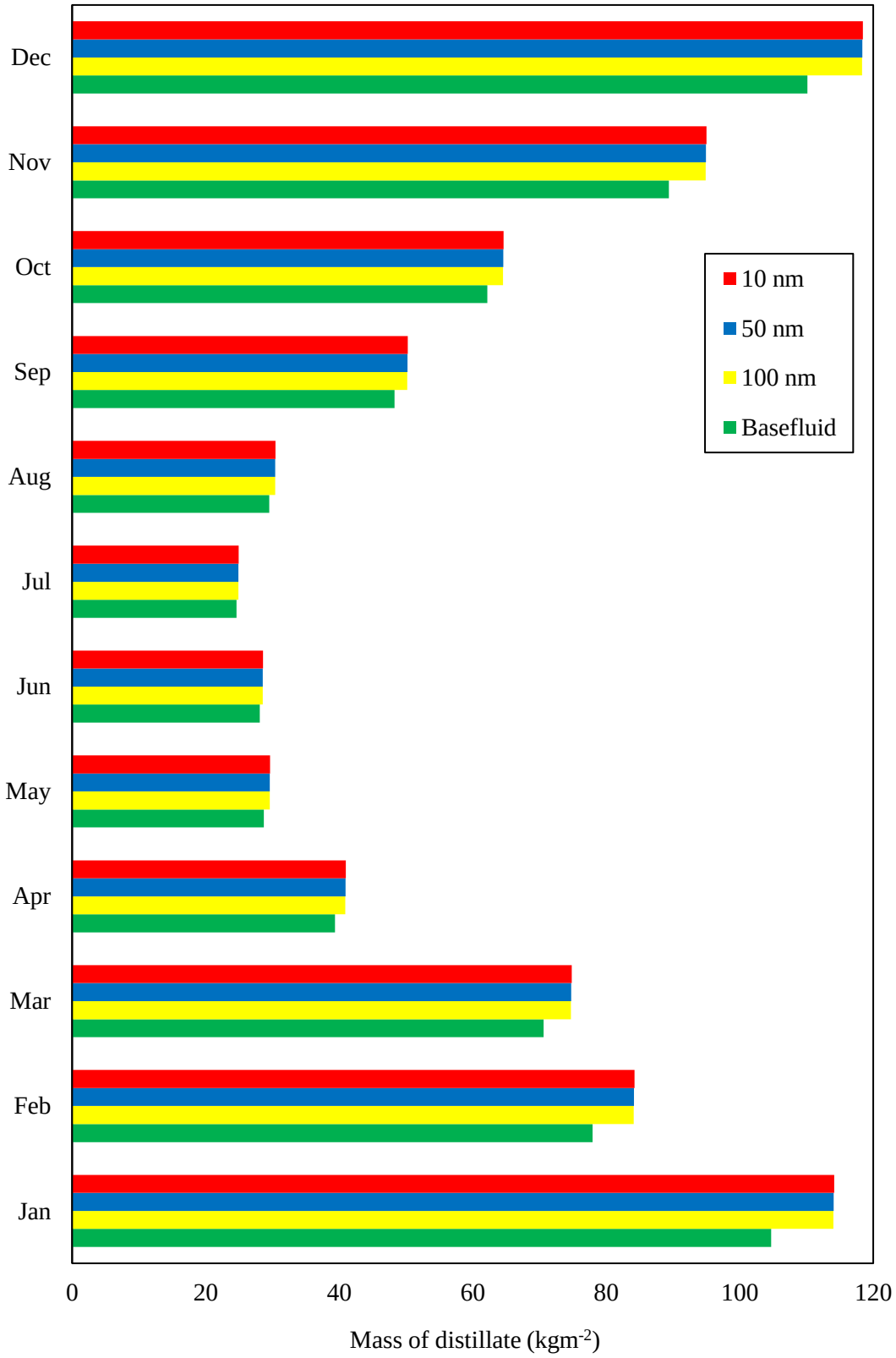

Figure 4.21: Total amount of distillate produced from the solar still with the base fluid only and with the Al_2O_3 nanoparticles of size 10, 50 and 100 nm, from January to December.

The percentage increase in the productivity of the solar stills with nanofluids compared to the productivity of the solar still with base fluid only is given in Table 4.1. It can be observed that during periods of high solar radiation, the effect of nanoparticles in solar stills is more pronounced. This can be attributed to the higher difference in the thermal conductivity of the nanofluid and the base fluid during periods of higher solar radiation levels. This results in higher differences between the base fluid and the nanofluid temperatures, in turn causing the difference in the mass of distillate generated by the solar still with the nanofluids and the solar still with the base fluid to be higher.

Table 4.1: Percentage increase in the productivity of the solar stills with nanofluids compared to the productivity of the solar still with base fluid only, for the months of January to December.

Months	**Increase in productivity %**		
	Solar still with Al_2O_3 nanoparticles of size 10 nm	Solar still with Al_2O_3 nanoparticles of size 50 nm	Solar still with Al_2O_3 nanoparticles of size 100 nm
January	9.01	8.94	8.89
February	8.05	7.98	7.93
March	5.92	5.85	5.80
April	4.08	3.99	3.93
May	3.22	3.13	3.08
June	1.65	1.57	1.52
July	1.31	1.23	1.19
August	3.08	3.00	2.95
September	4.06	3.98	3.93
October	3.92	3.84	3.79
November	6.26	6.19	6.14
December	7.55	7.48	7.43

Table 4.2 gives the annual production of distillate from the solar stills. It can be noted that the solar still with the 10 nm nanoparticles could achieve the highest annual distillate production at 756.17 kgm^{-2} and the solar still with the base fluid only generated the lowest annual amount of distillate at 713.72 kgm^{-2}. It can also be seen that the amount of distillate decreases as the nanoparticle size increases, due to decreasing fluid temperature and decreasing convective and evaporative heat transfer coefficients from the nanofluid to the glass.

Table 4.2: Annual distillate production from solar stills with and without nanoparticles.

Type of solar still	**Annual distillate production (kgm^{-2})**	**Increase in productivity (%)**
With base fluid only	713.72	0
With Al_2O_3 nanoparticles of size 10 nm	756.17	5.95
With Al_2O_3 nanoparticles of size 50 nm	755.61	5.87
With Al_2O_3 nanoparticles of size 100 nm	755.26	5.82

The annual increase in the distillate production was 5.95%, 5.87% and 5.82% for the solar still with the 10 nm, 50 nm and 100 nm nanoparticles, respectively, as compared to the solar still with the base fluid only. The differences in the annual distillate production from the solar stills with the 10, 50 and 100 nm nanoparticles were relatively lowdue to negligible differences in their heat transfer coefficients, as observed in Figure 4.16 and Figure 4.18.

4.1.7. Efficiency

4.1.7.1. Efficiency of solar stills on Sample Day

Figure 4.22 shows the efficiency of the solar stills on the Sample Day. It can be observed that the efficiency of the solar still with the base fluid only was lower than that of the solar stills with the nanoparticles. The efficiency of the solar still with the base fluid only was 35.87% while the maximum efficiency was achieved by the solar still with the Al_2O_3 nanoparticles of size 10 nm, at 39.18%. This is because the solar still with the 10 nm nanoparticles generated the highest amount of distillate for the same amount of input solar radiation.

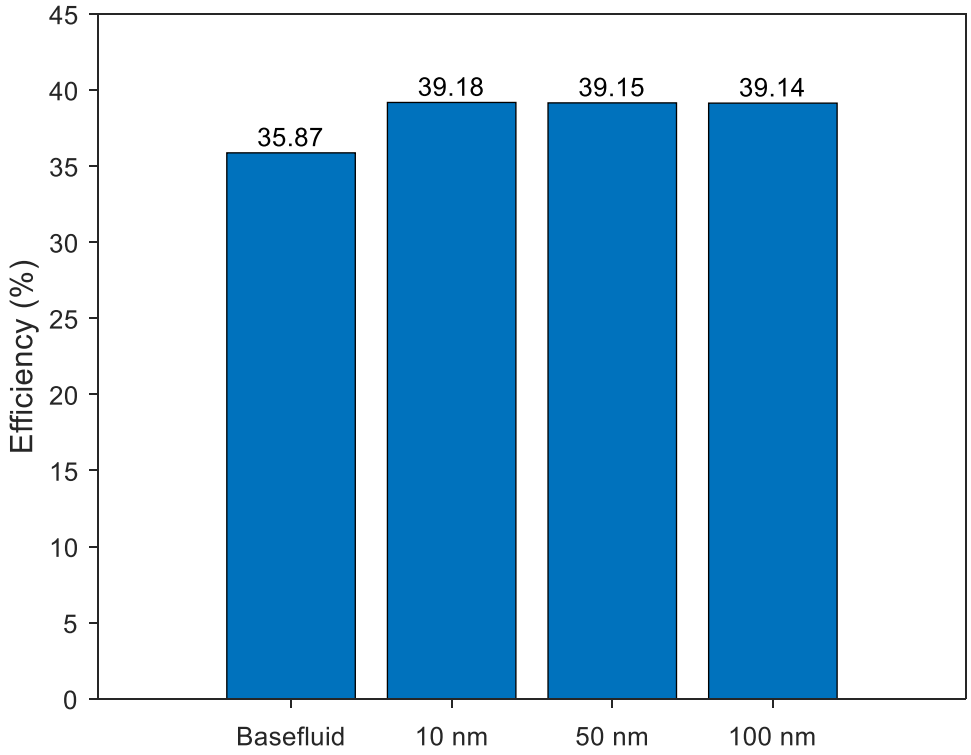

Figure 4.22: Efficiency of solar stills with base fluid only and with Al_2O_3 nanoparticles of size 10, 50 and 100 nm on Sample Day (from 2nd January 2007 at 7 am to 3rd January 2007 at 7 am).

The effect of the nanoparticle size on the daily efficiency of the solar stills with the Al_2O_3 nanoparticles for the Sample Day is given in Figure 4.23. It is observed that the efficiency decreases with increasing nanoparticle size. This is attributed to the decreasing amount of distillate generated with increasing nanoparticle size. The efficiency decreased from 39.18% to 39.14% when the nanoparticle size was increased from 10 to 100 nm.

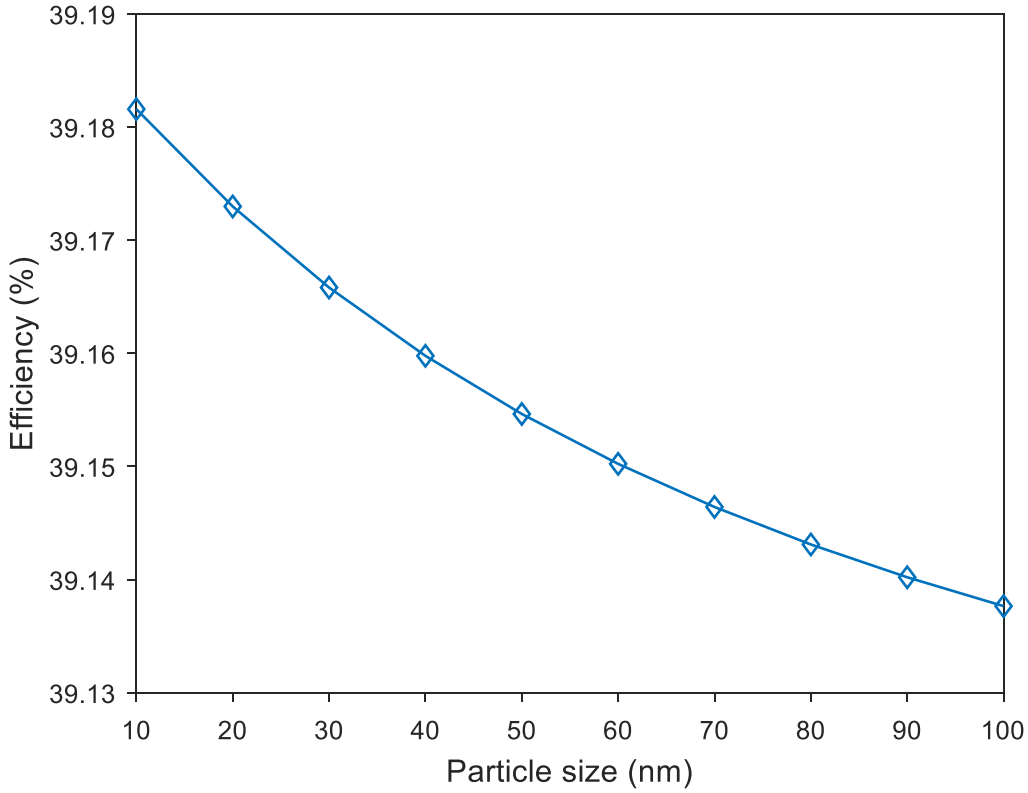

Figure 4.23: Variation of efficiency with nanoparticle size.

4.1.7.2. Mean monthly efficiency of solar stills for one year

The average monthly efficiency of the solar stills for the months of January to December is illustrated in Figure 4.24. It can be noted that the efficiency of the solar stills with the base fluid only was lower than that of the solar stills with the nanoparticles. Moreover, this difference in efficiencies was more significant during the months of January, February, March, October, November and December as these are the warmer months in South Africa, with higher levels of solar radiation. For instance, in January, the average efficiency of the solar still with the base fluid only and the solar still with the 10 nm nanoparticles was 38.38% and 41.84%, respectively, while in July, the average efficiency of the solar still with the base fluid only and the solar still with the 10 nm nanoparticles was 9.00% and 9.12%, respectively. This is due to the higher difference in the mass of distillate obtained from the solar still with the base fluid only and the solar stills with the nanoparticles during the months of higher solar radiation levels.

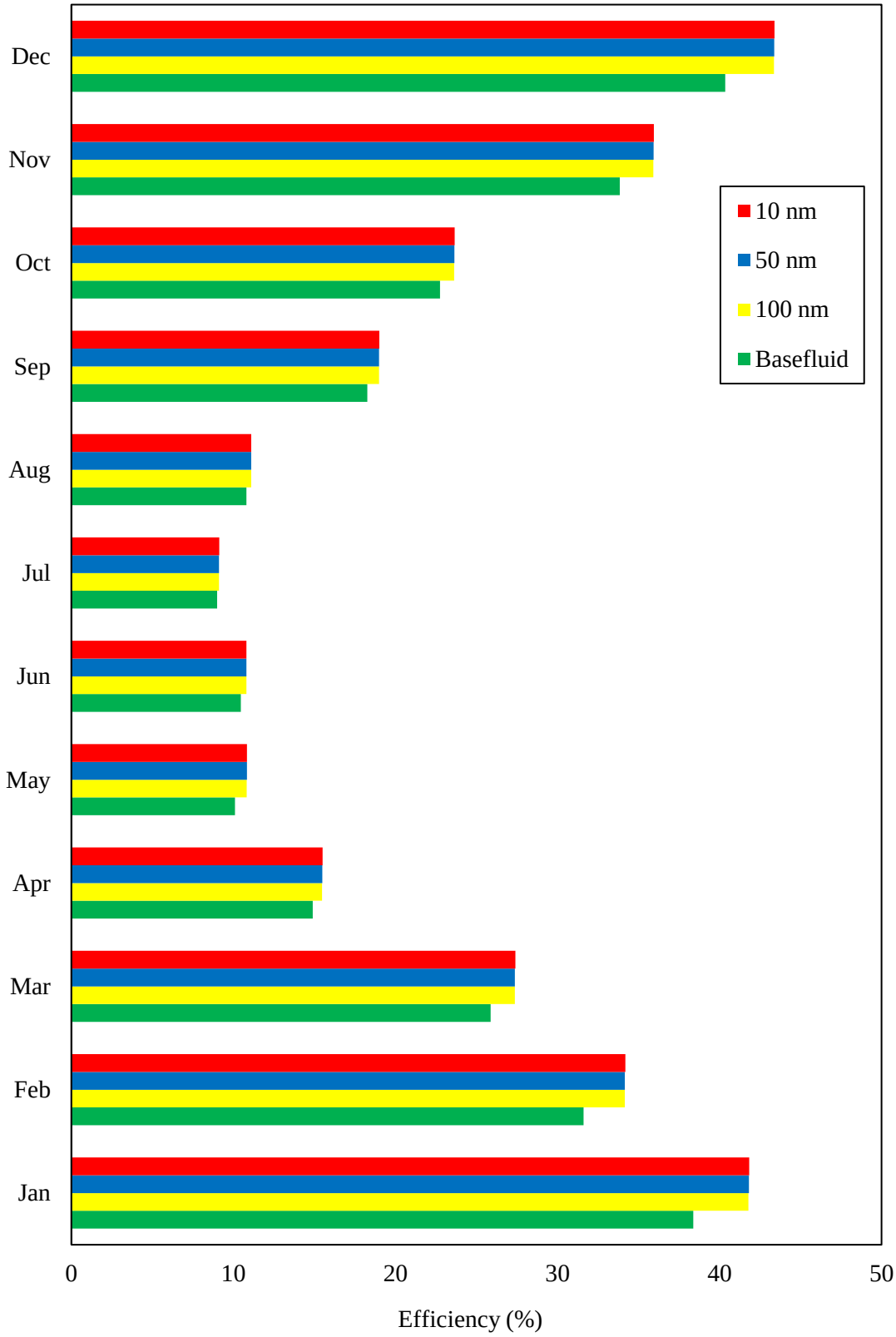

Figure 4.24: Average efficiency of solar still with the base fluid only and with Al_2O_3 nanoparticles of size 10, 50 and 100 nm, from January to December.

The mean monthly efficiencies of the solar stills were used in computing the average annual efficiencies. The mean annual efficiency of the solar still with the base fluid only was found to be 22.20% and the annual efficiencies of the solar stills with the nanoparticles are given in Figure 4.25. It can be observed that the annual efficiency decreases with increasing nanoparticle size. The annual efficiency decreased from approximately 23.57% to 23.54% when the nanoparticle size was increased from 10 to 100 nm. This is attributed to the decreasing mass of distillate with increasing nanoparticle size.

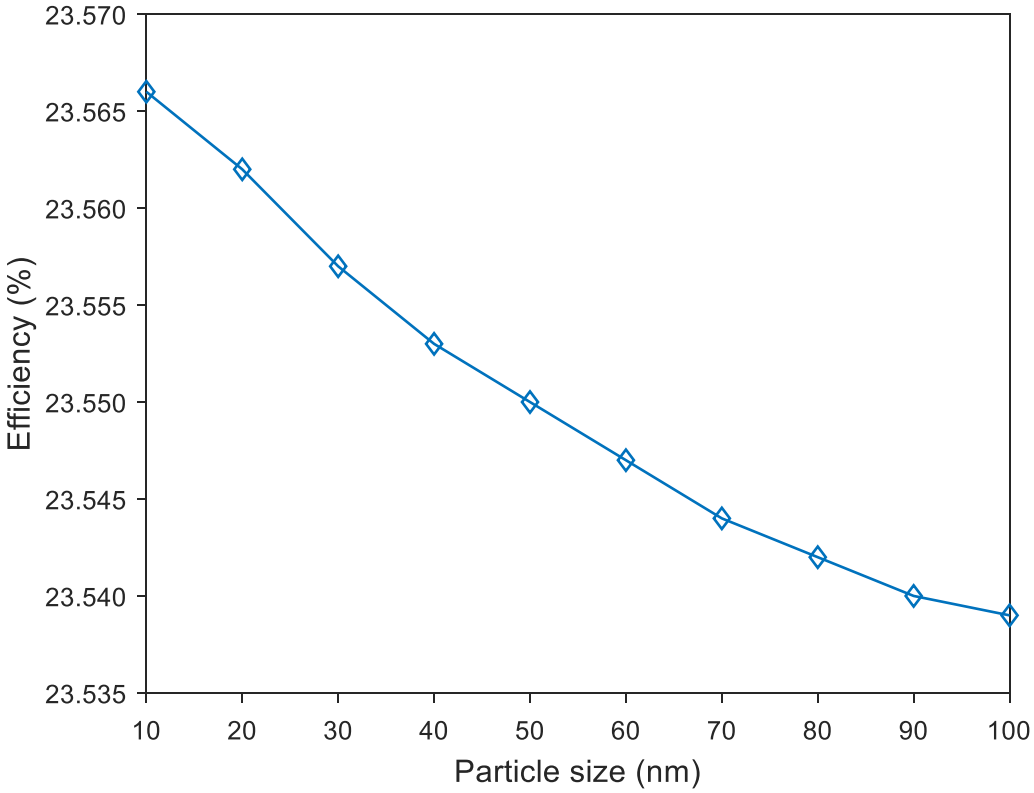

Figure 4.25: Variation of average annual efficiency of solar stills with nanofluids containing Al_2O_3 nanoparticles of different sizes.

4.1.8. Economic Performance of solar stills

Based on the costs of the raw materials given in Table 3.3 and using Equations (3.92) to (3.101) in Chapter 3, the Present Capital Cost (P) of the solar still was computed. It was found that the Present Capital Cost of the solar still with the base fluid only was 816.23 USD while that of the solar stills with Al_2O_3 nanoparticles of size 10, 50 and 100 nm were 954.94 USD, 917.79 USD and 894.15 USD, respectively. The Present Capital Cost of the solar still was thus found to decrease with increasing nanoparticle size since the cost of the nanoparticles decreased with increasing nanoparticle size, as given in Table 3.3. The Present Capital Cost of the solar still with the 10 nm Al_2O_3 nanoparticles was 17% higher than that of the solar still with the base fluid only.

4.1.8.1. Cost of distilled water

4.1.8.1.1. Cost of distilled water at an interest rate of 10%

Figure 4.26 shows the cost of distilled water for the solar still with and without nanoparticles, at an interest rate of 10%. The cost of distilled water for the solar still with the base fluid only was USD 0.1997/L. Moreover, the cost of distilled water for the solar stills with the nanoparticles was higher than that of the solar still with the base fluid only. It can also be observed that the cost of distilled water decreases with increasing nanoparticle size. This is because the capital cost decreases as the nanoparticle size increases. The cost of distilled water decreased from USD 0.2205/L to USD 0.2067/L as the nanoparticle size was increased from 10 nm to 100 nm, corresponding to a decrease of 6.26%. Furthermore, the cost of distilled water from the solar still with the 10 nm, 50 nm and 100 nm Al_2O_3 nanoparticles was 10.42%, 6.21% and 3.51%, respectively higher than the cost of distilled water from the solar still with base fluid only.

Additionally, it can be noted that the cost of distilled water obtained from all the solar stills is lower than the cost of potable water in Cape Town, which is approximately USD 0.3234 per litre, based on estimates given in BusinessTech (2018), at an exchange rate of 1 USD = 12.40 ZAR. El-Bialy et al. (2016) conducted a review of the economic analysis of solar stills and they found that the cost of distilled water from solar stills ranged from USD 0.0066 to 0.2696 per litre. In the context of this study, the cost of distilled water per litre ranged from USD 0.1997 for the solar still with base fluid only to USD 0.2205 for the solar still with the 10 nm Al_2O_3 nanoparticles. Consequently, it can be noted that the cost of distilled water obtained in

this investigation is within the range that has been obtained from previous studies on solar stills.

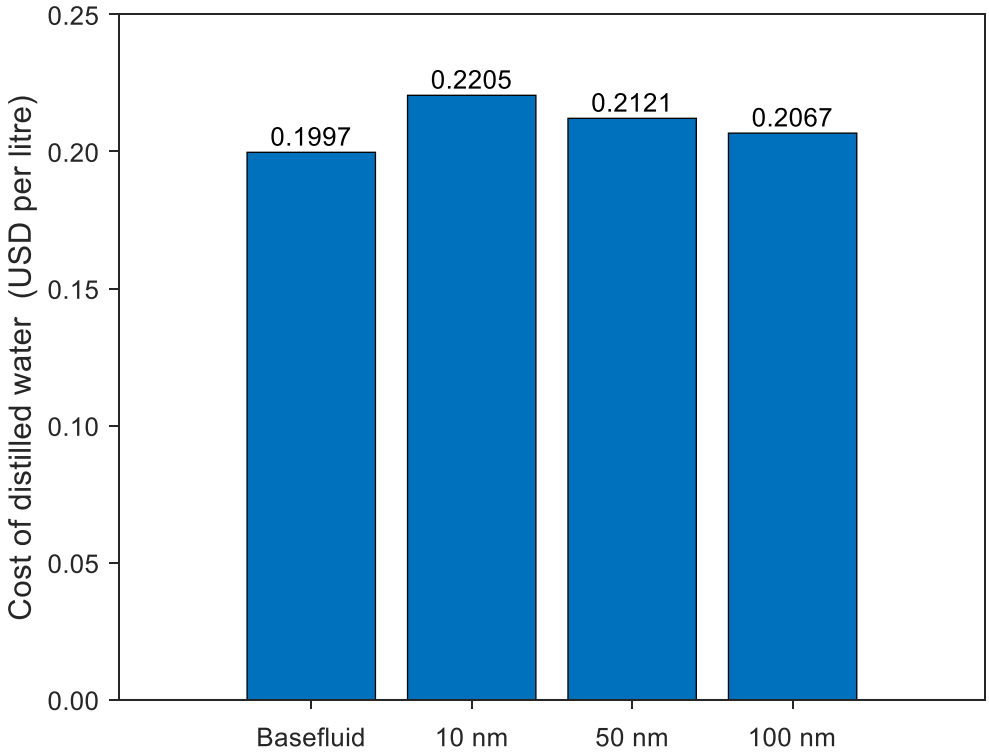

Figure 4.26: Cost of distilled water for the solar still with the base fluid only and with Al_2O_3 nanoparticles of size 10, 50 and 100 nm at an interest rate of 10%.

4.1.8.1.2. Cost of distilled water with varying interest rates

Figure 4.27 shows the cost of distilled water for each solar still with varying interest rates. It can be noted that as the interest rate increases, the cost of distilled water for each solar still increases. At an interest rate of 5%, the cost of distilled water for the solar still with the base fluid only was USD 0.1521/L while that of the solar still with the 10 nm Al_2O_3 nanoparticles was USD 0.1680/L. When the interest rate was increased to 15%, the costs were USD 0.2508/Land USD 0.2769/L for the solar still with the base fluid and the solar still with the Al_2O_3 nanoparticles of size 10 nm.

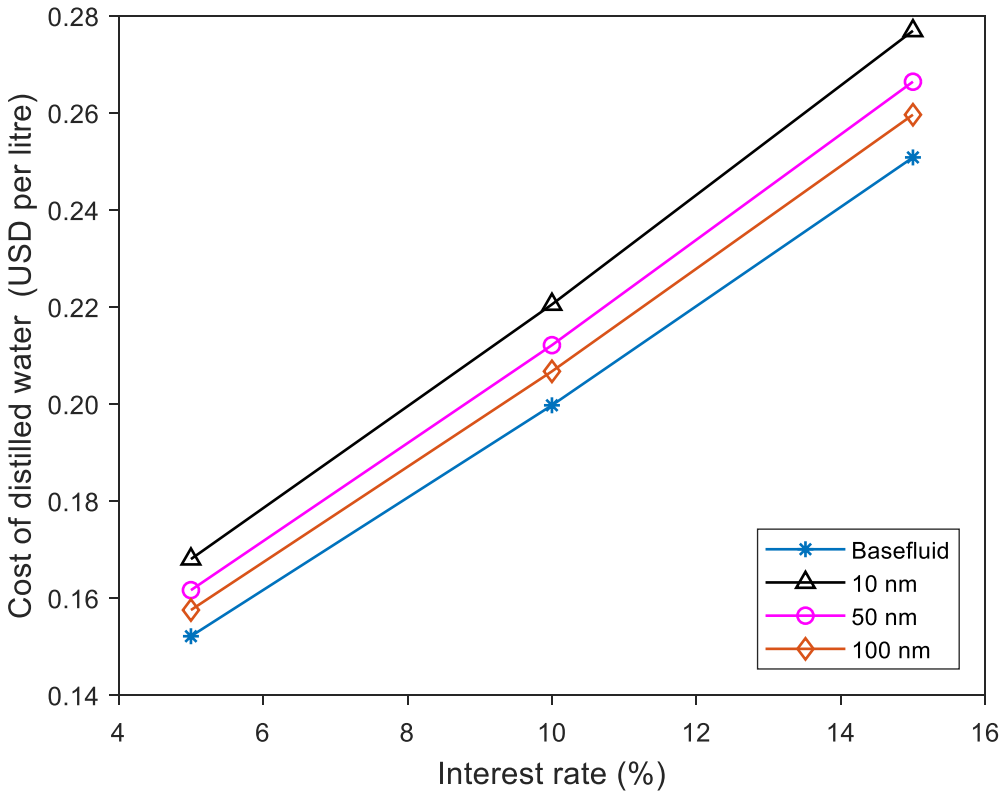

Figure 4.27: Cost of distilled water for the solar still with the base fluid only and with Al_2O_3 nanoparticles of size 10, 50 and 100 nm for various interest rates.

4.1.8.2. Payback period

4.1.8.2.1. Payback period at an interest rate of 10%

Figure 4.28 shows the payback period for each solar still at an interest rate of 10%. Equation (3.100), given in Chapter 3, was used in computing the payback period. The payback period for the solar still with the base fluid only was 4.58 years while the payback periods for the solar stills with the nanoparticles were higher. This is attributed to the additional costs of the nanoparticles and surfactant. It can also be observed that the payback period decreases with increasing nanoparticle size since the capital cost decreases with increasing nanoparticle size. The payback period was the highest for the solar still with the 10 nm nanoparticles, at 5.19 years. Additionally, the payback period for the solar still with 10 nm, 50 nm and 100 nm Al_2O_3 nanoparticles was 13.32%, 7.86% and 4.37% respectively higher than the payback period for the solar still with base fluid only.

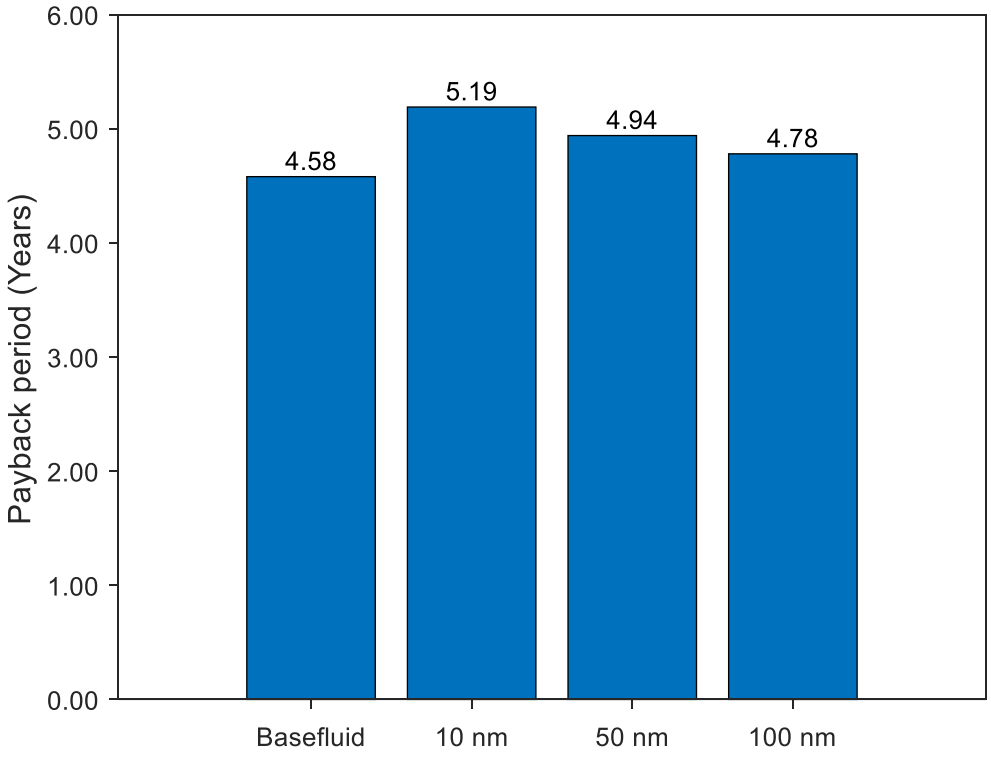

Figure 4.28: Payback period for the solar still with the base fluid only and with Al_2O_3 nanoparticles of size 10, 50 and 100 nm, at an interest rate of 10%.

4.1.8.2.2. Payback period with varying interest rates

The payback period for each solar still at varying interest rates is given in Figure 4.29. The payback period increases with an increase in the interest rate. The payback period was 3.99 and 4.45 years for the solar still with the base fluid only and for the solar still with the 10 nm Al_2O_3 nanoparticles, respectively, at an interest rate of 5%. When the interest rate was increased to 15%, the payback period was 5.41 and 6.30 years for the solar still with the base fluid only and for the solar still with the 10 nm Al_2O_3 nanoparticles, respectively. The general trend observed was a decrease in the payback period with increasing nanoparticle size due to decreasing capital costs with increasing nanoparticle size.

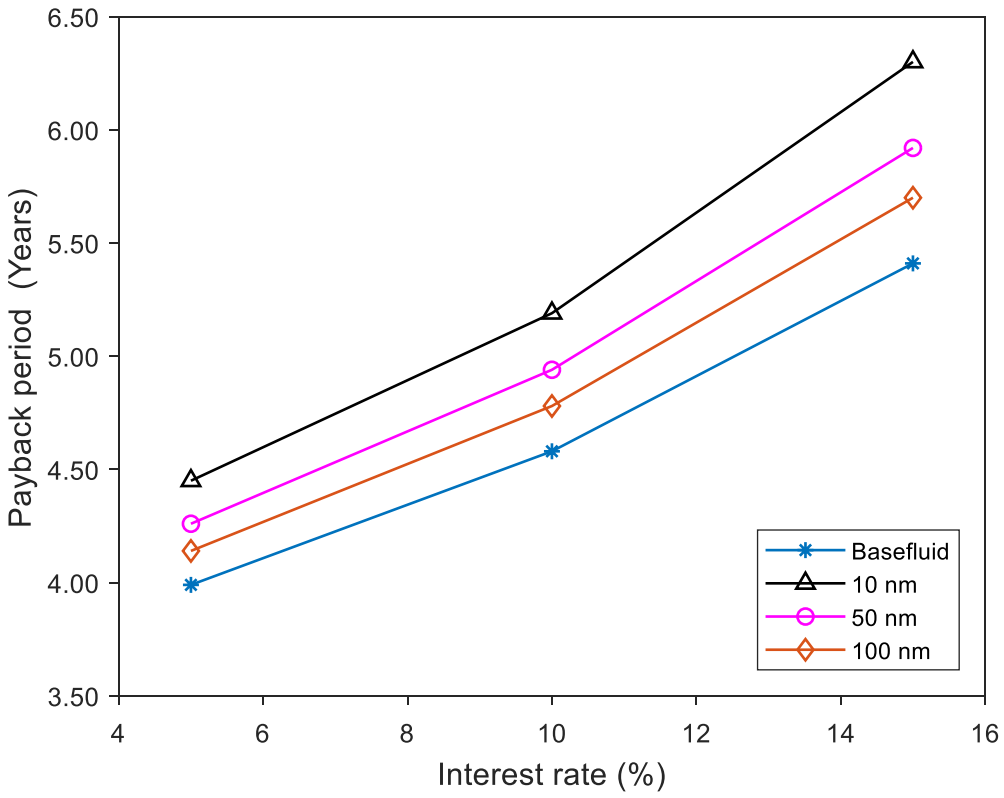

Figure 4.29: Payback period for the solar still with the base fluid only and with Al_2O_3 nanoparticles of size 10, 50 and 100 nm for various interest rates.

4.1.9. Environmental Performance of solar stills

Since one of the major advantages of using a solar still lies in its environmental benefits, the environmental performance of each solar still was evaluated in terms of the amount of CO_2 equivalent emissions mitigated per year and the environmental costs avoided per year due to a carbon tax. Figure 4.30 illustrates the annual energy output, in kWh per m^2 (of basin area) from each solar still. The annual energy output from the solar still with base fluid only was 484.02 kWh per m^2 and it was lower than the annual energy output from the solar stills with the nanofluids. The presence of Al_2O_3 nanoparticles inside the solar stills enhances the optical and heat transfer properties of the fluid, thus causing the annual energy output to increase. Moreover, the annual energy output was found to decrease with an increase in the nanoparticle size. The annual energy output decreased from 513.95 to 513.37 kWh per m^2 when the nanoparticle size was increased from 10 nm to 100 nm, as can be depicted from Figure 4.30.

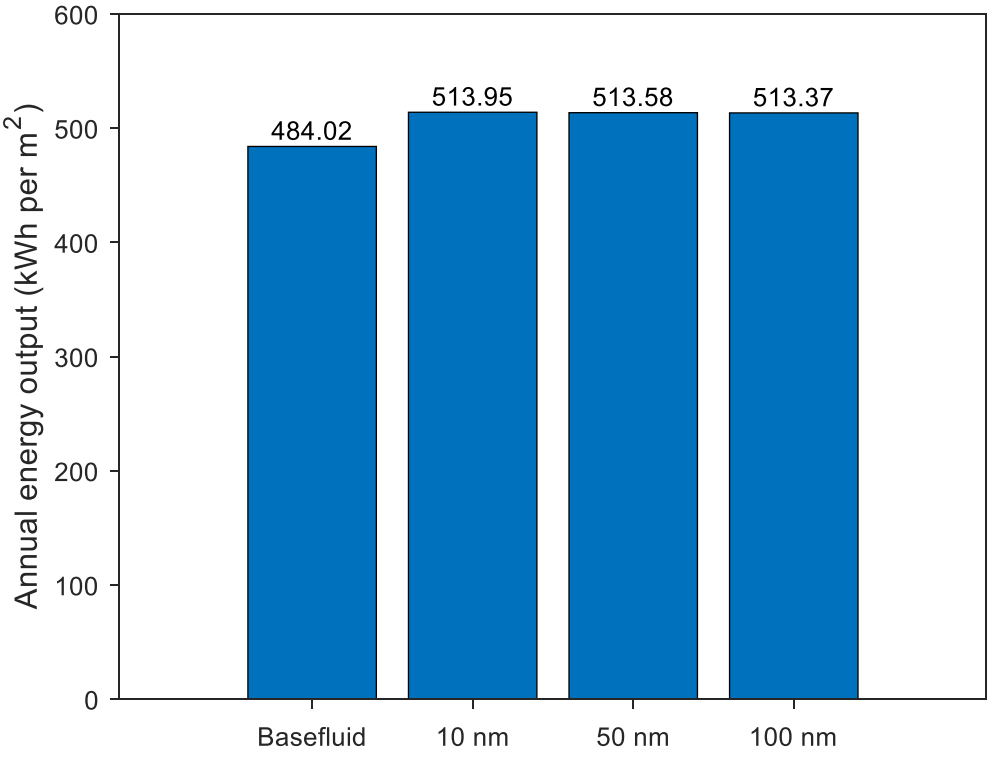

Figure 4.30: Annual energy output per m^2 (of basin area) from the solar still with the base fluid only and with Al_2O_3 nanoparticles of size 10, 50 and 100 nm.

Figure 4.31 shows the annual amount of CO_2 equivalent emissions that could be mitigated by using the energy from the solar stills instead of using energy generated from a coal powered station. The amount of CO_2 equivalent emissions mitigated per year was found to be higher for the solar stills with the nanofluids. The mitigated emissions also decreased with increasing nanoparticle size since a higher energy output could be achieved by the smaller nanoparticles. The annual amount of CO_2 equivalent emissions mitigated from the solar still with the Al_2O_3 nanoparticles of size 10 nm, 50 nm and 100 nm was 6.18%, 6.11% and 6.06%, respectively higher than the annual amount of CO_2 equivalent mitigated from the solar still with base fluid only.

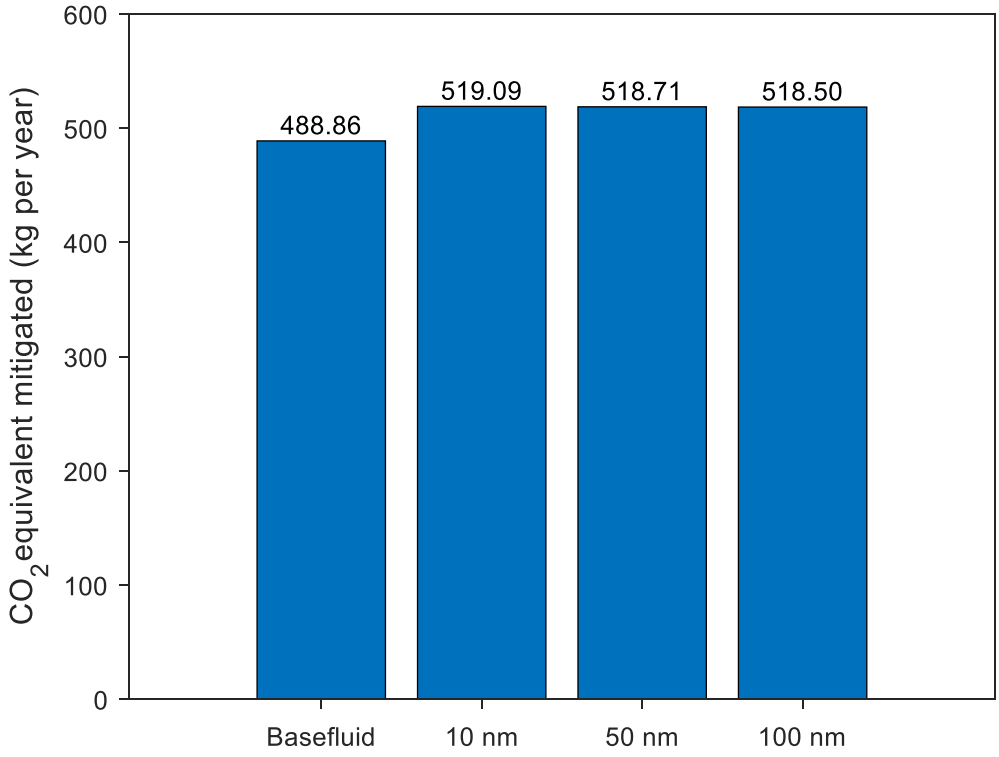

Figure 4.31: Annual CO_2 equivalent emissions mitigated from the solar still with the base fluid only and with Al_2O_3 nanoparticles of size 10, 50 and 100 nm.

Figure 4.32 illustrates the annual environmental cost that can be avoided, in USD per m^2 (of basin area) by using the solar stills. The annual environmental cost that can be avoided is higher when using a solar still with nanofluids as compared to using a solar still with base fluid only. The annual avoided environmental cost for the solar still with the base fluid only was USD 4.7309 per m^2. It was also found that the environmental costs that could be avoided decreases with increasing nanoparticle size due to decreasing energy output with increasing nanoparticle size. The annual avoided environmental cost decreased from USD 5.0235 per m^2 to USD 5.0178 per m^2 as the nanoparticle size was increased from 10 nm to 100 nm, as can be observed from Figure 4.32.

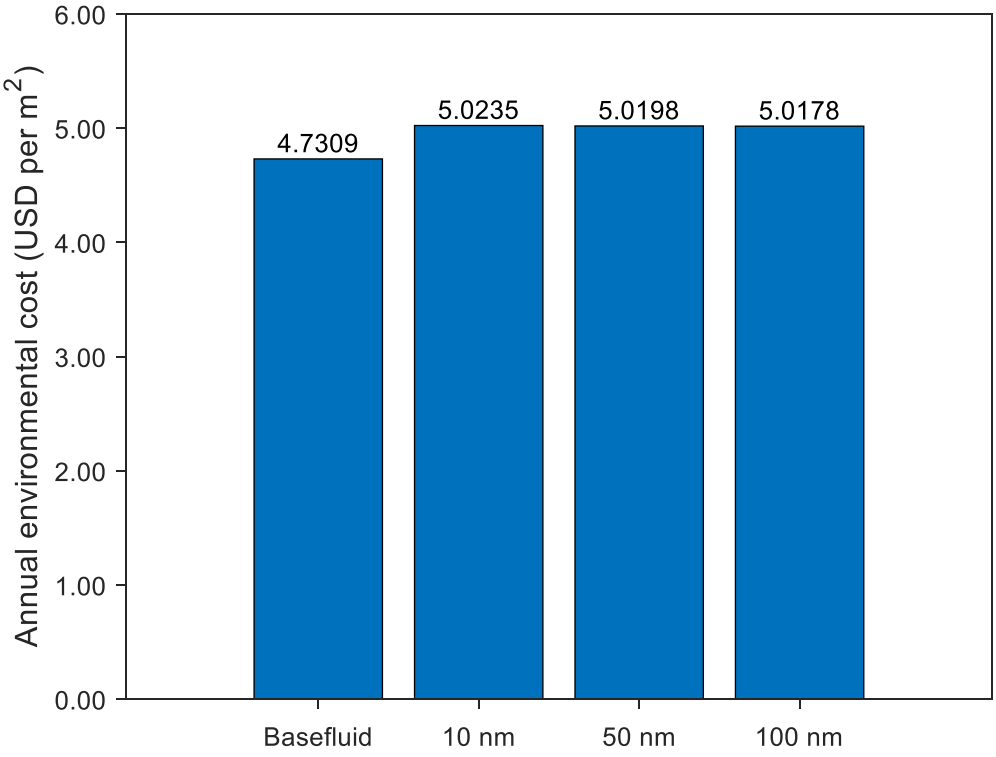

Figure 4.32: Annual environmental cost avoided per m^2 (of basin area) by using the solar still with the base fluid only and with Al_2O_3 nanoparticles of size 10, 50 and 100 nm.

4.2. Experimental Results

The results from the outdoor experiments which were conducted at the University of Cape Town, South Africa, are presented in this section. The calibration of the solar stills is first discussed, as it was essential to improve the accuracy of the results. The hourly climatic conditions, including wind speed, ambient temperature and global solar radiation on a horizontal surface for two Sample Days are then presented, followed by the hourly mass of distillate collected from each solar still on these Sample Days. The daily mass of distillate collected over 20 Test Days is then given. The effect of nanoparticle size on the experimental productivity of the solar still is also discussed in this section.

4.2.1. Calibration of solar stills

In this study, it was essential to test the performance of the four solar stills with water only (base fluid) in each of them before conducting the experiments with the nanofluids. Table 4.3 shows the experimental results collected over 10 days, with each solar still operating under identical conditions and each containing 20 kg of base fluid only.

Table 4.3: Mass of distillate, in kgm^{-2}, measured at 7 am on each day, with only base fluid in each of the four solar stills.

Day	**Mass of distillate (kgm^{-2})**			
	Solar Still 1	**Solar Still 2**	**Solar Still 3**	**Solar Still 4**
1	1.54126	1.59732	1.82583	1.93138
2	1.76858	1.67530	1.90025	1.81728
3	2.11765	2.23238	2.34252	2.36428
4	2.40280	2.47293	2.80611	2.52965
5	2.41533	2.46378	2.69204	2.90316
6	2.13626	2.21720	2.06835	2.44775
7	2.07888	2.42423	1.81268	2.52557
8	0.46757	0.65517	0.49286	0.89182
9	0.78120	1.00536	0.75729	1.15495
10	0.89852	1.02844	0.92570	1.23831

It can be observed from Table 4.3 that there are some differences between the solar stills. For instance, solar still 4 generally gives the highest amount of distillate. One of the reasons why the distillate output from each solar still was not equal is because the 4 solar stills were constructed manually, without the use of specialised machinery. This could have resulted in human error while constructing the solar stills.

Since solar still 4 gave the highest average amount of distillate over these 10 days, the three other stills were calibrated against solar still 4 in order to improve the accuracy of the measurements. Thus, the average percentage error was calculated for solar stills 1, 2 and 3. It was found that the errors were 16.14%, 10.26% and 11.01%, for solar stills 1, 2 and 3, respectively. The experimental values were then corrected for solar stills 1, 2 and 3 and these are shown in Table 4.4.

Table 4.4: Corrected mass of distillate, in kgm^{-2}, obtained from each solar still.

Day	**Mass of distillate (kgm^{-2})**			
	Solar Still 1	**Solar Still 2**	**Solar Still 3**	**Solar Still 4**
1	1.79002	1.76121	2.02685	1.93138
2	2.05403	1.84719	2.10947	1.81728
3	2.45944	2.46142	2.60043	2.36428
4	2.79061	2.72665	3.11506	2.52965
5	2.80516	2.71656	2.98843	2.90316
6	2.48105	2.44468	2.29608	2.44775
7	2.41441	2.67296	2.01226	2.52557
8	0.54304	0.72239	0.54712	0.89182
9	0.90729	1.10851	0.84067	1.15495
10	1.04354	1.13396	1.02762	1.23831

All the experimental data reported from now on have also been corrected using the percentage errors for solar stills 1, 2 and 3.

4.2.1.1. Analysis of variance test with base fluid only in all four solar stills

Office 365 Excel was used to conduct ANOVA tests in this study, at a significance level of 0.05. Table 4.5 shows the results from the ANOVA tests with a total number of 39 degrees of freedom (df = 39). Two ANOVA tests were conducted, one for the uncorrected experimental values as they were obtained (without any calibration, using the data given in Table 4.3) and one for the corrected experimental values (after calibration, using the data given in Table 4.4).

Table 4.5: ANOVA results from measurements taken over 10 days, with base fluid only in each of the four solar stills, for uncorrected and corrected experimental data.

Data	df	F	P-value	F crit
Uncorrected	39	0.3439	0.79	2.8663
Corrected	39	0.0071	1.00	2.8663

As can be observed from Table 4.5, the P-value for the uncorrected data was found to be 0.79 which is much higher than the significance level of 0.05 and the F critical value was 2.87 which is higher than the F value of 0.34. These observations show that there is not much significant difference between the performance of the solar stills. However, the ANOVA results improved further when using the corrected data after calibration of the solar stills. The P-value increased from 0.79 to 1.00, and the F critical value was 2.87 which is much higher than the F value of 0.01. Again, these ANOVA results prove that the means of the four solar stills are equal (after having calibrated solar stills 1, 2 and 3) and thus, they can be considered as identical and any variability which occurs from now on is due to experimental factors only.

4.2.2. Climatic conditions for University of Cape Town

4.2.2.1. Hourly variation of global solar radiation on a horizontal surface, and hourly variation of ambient temperature and wind speed

For two Sample Days (27 April 2019 and 06 May 2019), the mass of the distillate was measured on an hourly basis from 8 am to 6 pm at the University of Cape Town. They were chosen to represent days with low and high levels of solar radiation. The hourly variation of the climatic data for these two Sample Days are given in Figure 4.33, Figure 4.34 and Figure 4.35, which illustrate the global solar radiation on a horizontal surface, the ambient temperature and the wind speed, respectively.

The global solar radiation on a horizontal surface was higher on Sample Day 1 as compared to Sample Day 2. The maximum global solar radiation on a horizontal surface was 621 Wm^{-2} on Sample Day 1 and 543 Wm^{-2} on Sample Day 2, as can be observed from Figure 4.33. Sample Day 1 was a hotter day, with ambient temperatures ranging from 15.6 °C to 22.4 °C while the ambient temperatures for Sample Day 2 ranged from 14.1 °C to 16.5 °C, as can be depicted from Figure 4.34. Additionally, the wind speed was higher on Sample Day 2, ranging from 3.4 ms^{-1} to 6.3 ms^{-1} while on Sample Day 1, the wind speed ranged from 2.3 ms^{-1} to 3.7 ms^{-1}, as illustrated by Figure 4.35.

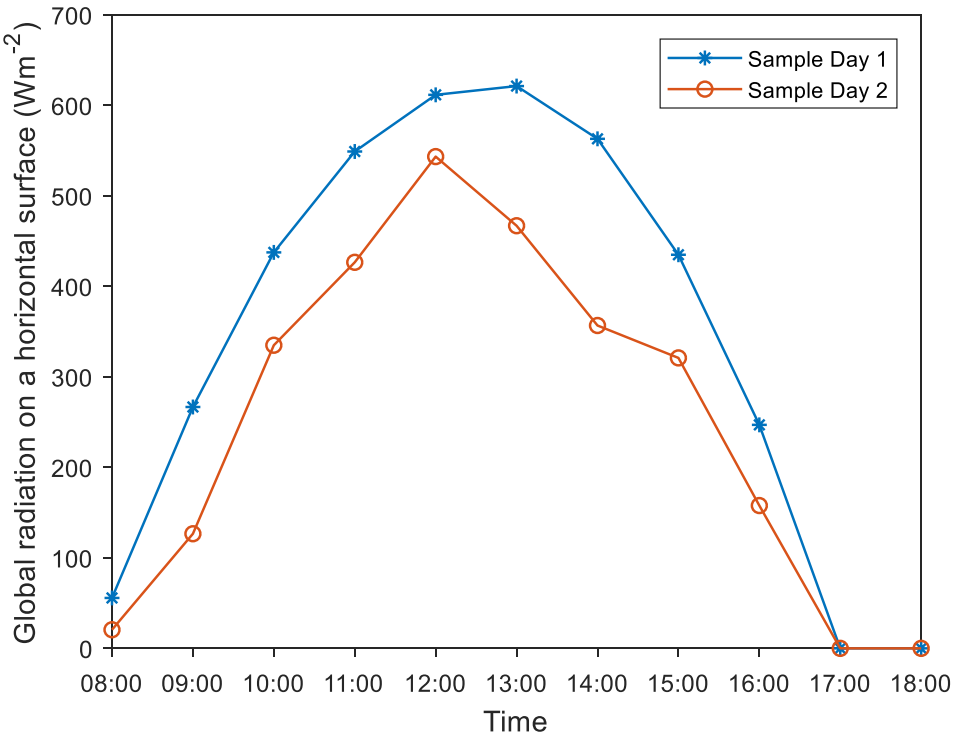

Figure 4.33: Hourly variation of global solar radiation on a horizontal surface, from 8 am to 6 pm on Sample Day 1 (27 April 2019) and Sample Day 2 (04 May 2019).

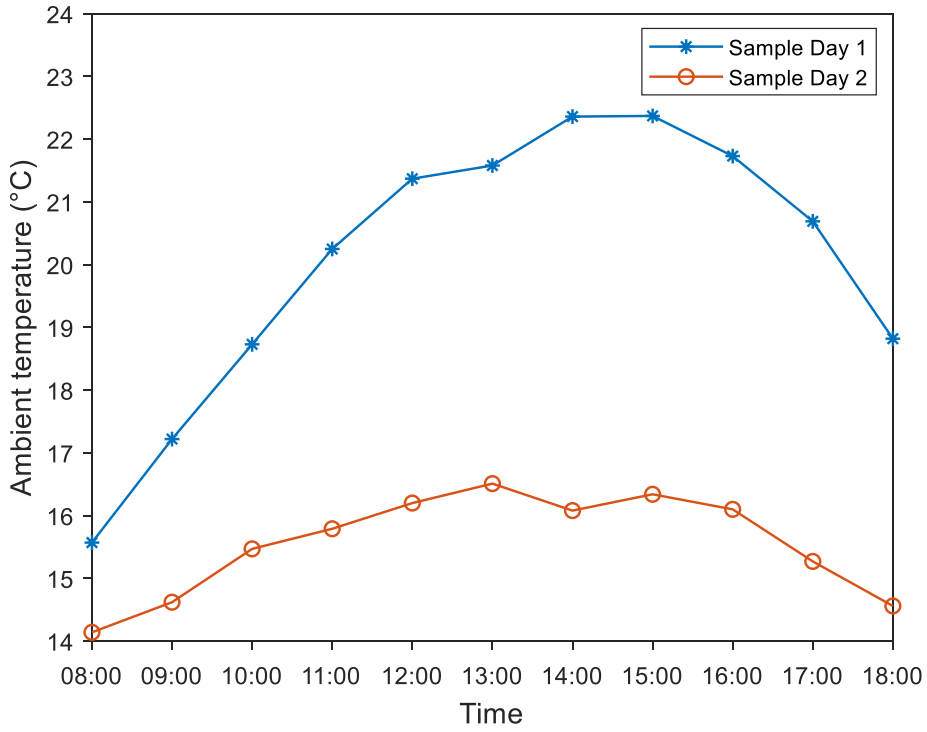

Figure 4.34: Hourly variation of ambient temperature from 8 am to 6 pm on Sample Day 1 (27 April 2019) and Sample Day 2 (04 May 2019).

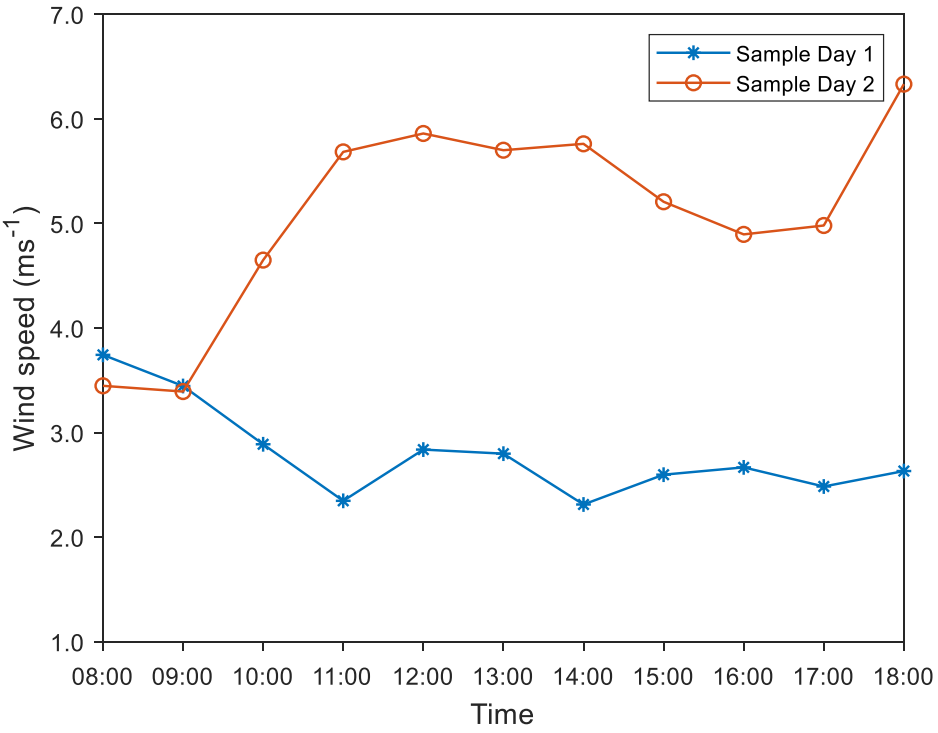

Figure 4.35: Hourly variation of wind speed from 8 am to 6 pm on Sample Day 1 (27 April 2019) and Sample Day 2 (04 May 2019).

4.2.3. Distillate Output

4.2.3.1. Hourly variation of cumulative mass of distillate obtained from the solar stills with and without nanofluids for two Sample Days

The hourly mass of distillate obtained experimentally from the solar still with the base fluid only and from the solar stills with the nanoparticles of size 10 nm, 50 nm and 100 nm for Sample Day 1 and Sample Day 2 are shown in Figure 4.36 and Figure 4.37, respectively. The mass of distillate from each solar still was collected and measured every hour from 8 am to 6 pm on both Sample Days. As can be observed from Figure 4.36 and Figure 4.37, the solar stills generated a higher amount of distillate on Sample Day 1 as compared to Sample Day 2. The highest mass of distillate collected on Sample Day 1 was 1.06997 kgm^{-2} while on Sample Day 2, the highest mass of distillate was 0.81076 kgm^{-2}. This is due to the higher solar radiation on Sample Day 1, as illustrated by Figure 4.33. Since solar radiation is the driving factor for the distillation process, a higher level of solar radiation leads to a higher distillate output.

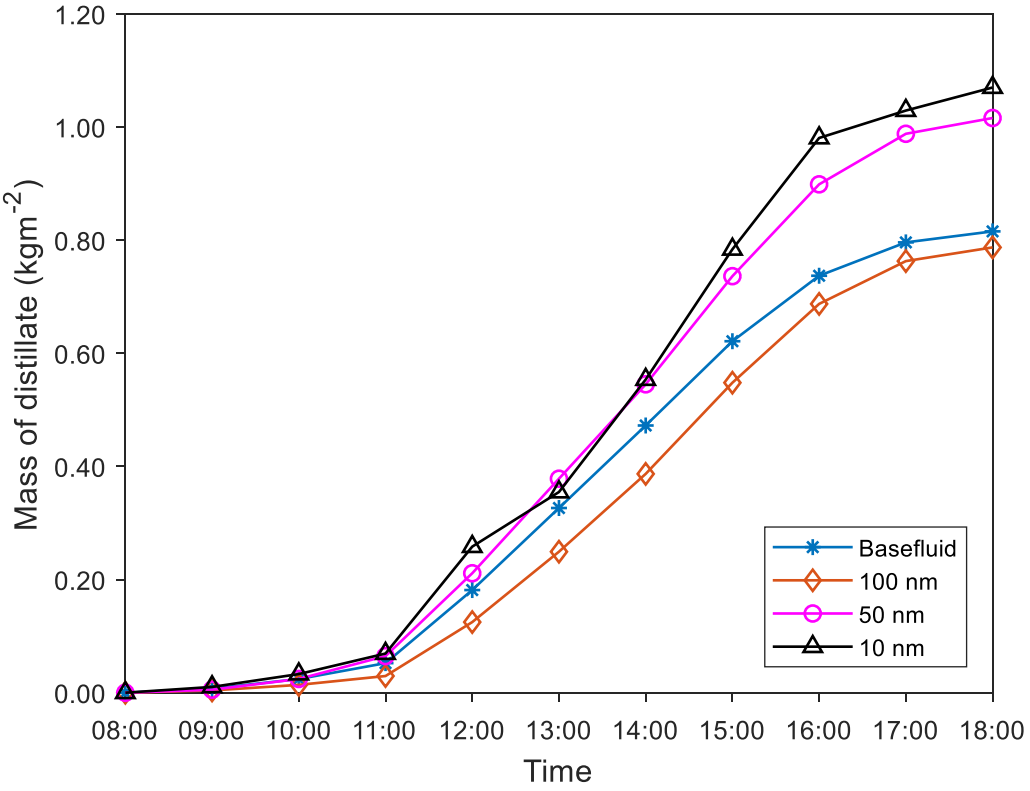

Figure 4.36: Hourly cumulative mass of distillate obtained experimentally from the solar still with base fluid only and the solar stills with Al_2O_3 nanoparticles of size 10, 50 and 100 nm, on Sample Day 1 (27 April 2019), from 8 am to 6 pm.

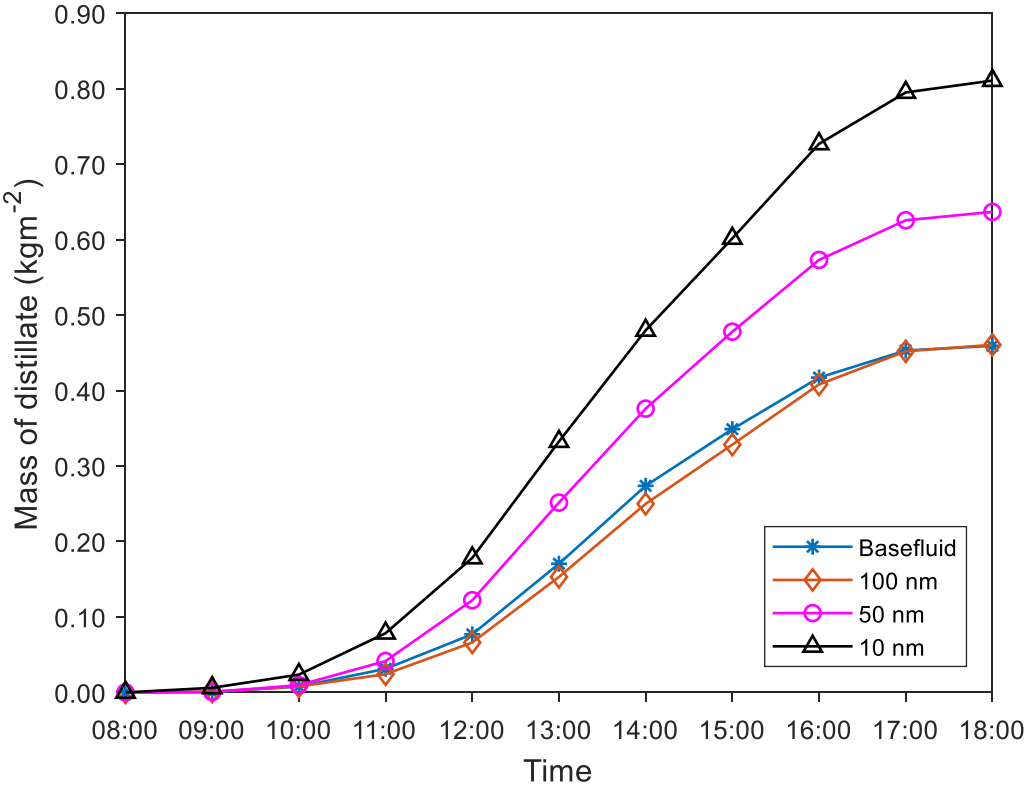

Figure 4.37: Hourly cumulative mass of distillate obtained experimentally from the solar still with base fluid only and the solar stills with Al_2O_3 nanoparticles of size 10, 50 and 100 nm, on Sample Day 2 (04 May 2019), from 8 am to 6 pm.

Furthermore, in both cases, the mass of distillate in descending order of magnitude was obtained by the solar still with the nanoparticles of size 10 nm, 50 nm and100 nm. This is because for the smaller nanoparticle size, the thermal conductivity is higher, leading to higher vapour pressure at the fluid surface, enhanced convective and evaporative heat transfer from fluid to glass, hence resulting in a higher distillate output.

On Sample Day 1, the total mass of distillate collected was 0.81562, 1.06997, 1.01609 and 0.78730kgm^{-2} from the solar still with the base fluid only and from the solar stills with the Al_2O_3 nanoparticles of size 10 nm, 50 nm and 100 nm, respectively. On Sample Day 2, the total amount of distilled water produced was 0.45929, 0.81076, 0.63675 and 0.46059 kgm^{-2} from the solar still with the base fluid only and from the solar stills with the Al_2O_3 nanoparticles of size 10 nm, 50 nm and 100 nm, respectively. It is also to be noted that on

both Sample Days, the difference in the productivities of the solar still with the base fluid only and the solar still with the 100 nm nanoparticles was the lowest.

4.2.3.2. Daily mass of distillate obtained from the solar stills with and without nanofluids for 20 Test Days

Figure 4.38 shows the daily experimental mass of distillate obtained from each of the four solar stills for 20 Test Days. These 20 Test Days were dispersed across March to May due to the occurrence of external factors such as load shedding during which there was no back up power to continuously log climatic data. The mass of distillate was measured at 7 am on each day and thus, the mass of distillate corresponds to the amount of water collected over 24 hours (from 7 am to 7 am the following day). As can be depicted from Figure 4.38, the amount of distillate produced from the solar stills with the Al_2O_3 nanoparticles is generally higher than that produced from the solar still with the base fluid only. The addition of nanoparticles to the solar still enhances the thermal characteristics of the fluid inside the basin, which in turn leads to an enhancement in the rates of evaporation and condensation, resulting in an increase in the distillate output (Kabeel, Omara & Essa, 2017).

The amount of distillate produced during these 20 Test Days ranged from 0.13671 kgm^{-2} to 2.15361 kgm^{-2}. The highest observed amount of distillate was relatively low as the 20 Test Days occurred within the months of March to May where solar radiation is not at its peak as these months fall within the autum months in Cape Town. It should also be noted that for a given set of design and operating conditions, the distillate output from a solar still is affected by environmental factors such as solar radiation, ambient temperature and wind speed. Consequently, the amount of distillate produced by solar stills with identical design and operating conditions but in different locations would not generate the same amount of distillate.

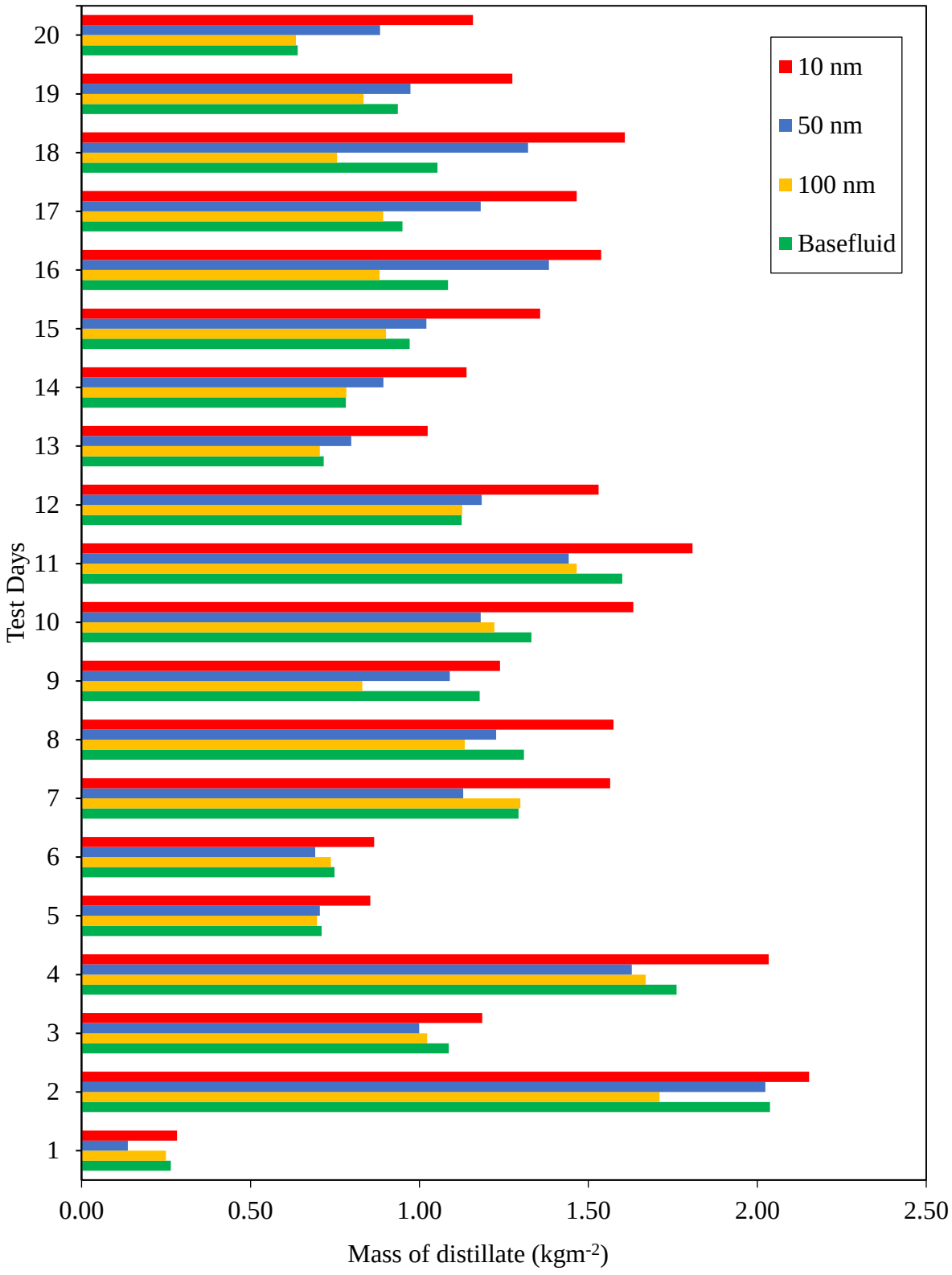

Figure 4.38: Mass of distillate obtained from the solar still with base fluid only and the solar stills with nanoparticles of size 10, 50 and 100 nm for 20 Test Days.

4.2.3.3. Effect of nanoparticle size on productivity of solar stills

The experimental results were used to compute the total distillate production from each solar still over the 20 Test Days and these are shown in Table 4.6. It can be observed that the solar still with the Al_2O_3 nanoparticles of size 10 nm and 50 nm could achieve an increase of 26.46% and 1.46% in the productivity as compared to the solar still with the base fluid only.

One anomaly which can be observed from Table 4.6 is the lower productivity of the solar still with the 100 nm Al_2O_3 nanoparticles as compared to the solar still with the base fluid only. It was found that the productivity of the solar still with the 100 nm nanoparticles was 9.38% lower than that of the solar still with the base fluid only. This can be attributed to the high nanoparticle size which results in poor stability and high agglomeration inside the solar still. The simulations in MATLAB were not able to take the instability and agglomeration effects into account and thus resulted in an increase in the distillate throughout the year.

In an experimental study conducted by Elango, Kannan and Muragavel (2015) on the use of Al_2O_3, ZnO and SnO_2 nanoparticles dispersed in the basin fluid of solar stills, it was reported that a nanofluid with smaller particle size has better stability. Liu, Wang and Liu (2015) performed an experimental investigation on the stability of Al_2O_3-water nanofluids and they claimed that for a bigger nanoparticle size, more precipitation occurs, and at a faster rate, and the stability of the nanofluid gets worse. Consequently, in this study, this means that the Al_2O_3-water nanofluid with the 100 nm particles was the least stable and caused the most agglomeration, thus resulting in a lower productivity.

Table 4.6: Total distillate production from solar stills with and without Al_2O_3 nanoparticles over a period of 20 Test Days, at the University of Cape Town.

Type of solar still	**Total distillate production over 20 Test Days (kgm^{-2})**	**Increase in productivity (%)**
With base fluid only	21.5803	0.00
With Al_2O_3 nanoparticles of size 10 nm	27.2908	26.46
With Al_2O_3 nanoparticles of size 50 nm	21.8950	1.46
With Al_2O_3 nanoparticles of size 100 nm	19.5554	-9.38

It can also be observed from Table 4.6 that the total distillate production decreased from 27.2908 to 19.5554 kgm^{-2} as the nanoparticle size was increased from 10 nm to 100 nm, corresponding to a decrease of 28.34%. This can be attributed to the higher surface area to volume ratio of the 10 nm nanoparticles, which causes the thermal conductivity of the nanofluid to be higher (Khanafer & Vafai, 2011). Furthermore, Sahota and Tiwari (2016a) indicated that nanoparticles can absorb solar radiation directly into the base fluid, causing the temperature of each discrete nanoparticle to increase. Since the 10 nm Al_2O_3 nanoparticles have the highest surface area to volume ratio, they are able to absorb more solar radiation directly into the base fluid, thus causing a higher increase in the temperature of the nanofluid, which results in a higher distillate production as compared to the solar stills with the 100 nm and 50 nm nanoparticles.

4.3. Model Performance

4.3.1. Validation of clearness index correlation for Cape Town

There was a need to develop a correlation for the clearness index (k_T) for Cape Town, South Africa, which was used in the simulations in MATLAB. After eliminating the outliers using the procedure given in Section 3.4, a total number of 3916 data points were left and these were used to plot the hourly diffuse fraction (I_d/I_g) against the hourly clearness index, as given in Figure 4.39. The shape of the graph follows a similar trend to those given in Duffie and Beckman (2013) which are also split into three different ranges for the clearness index. The correlation which was developed in this study can be expressed as given by Equations (4.1), (4.2) and (4.3).

$$\frac{I_d}{I_g} = 0.99 \qquad \text{for } k_T \leq 0.10 \tag{4.1}$$

$$\frac{I_d}{I_g} = 1.588 - 5.241k_T + 7.076k_T^2 - 3.453k_T^3 \qquad \text{for } 0.10 < k_T > 0.80 \tag{4.2}$$

(With $R^2 = 0.60$)

$$\frac{I_d}{I_g} = 0.17 \qquad \text{for } k_T \geq 0.80 \tag{4.3}$$

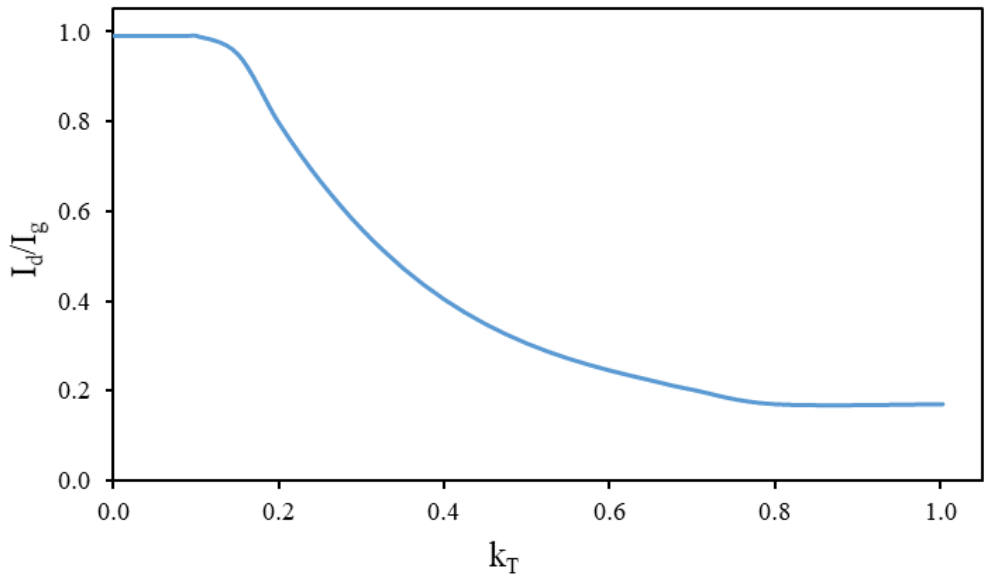

Figure 4.39: Hourly diffuse fraction (I_d/I_g) versus hourly clearness index (k_T) for Cape Town.

In order to evaluate the accuracy of the developed correlation, the MBE and the RMSE were computed. The MBE and RMSE were 0.015% and 17.58%, respectively. Kuo, Chang and Chang (2014) stated that a model performs better when the absolute values of the MBE and RMSE are low, and they reported a wide range of MBEs and RMSEs from studies on the development of clearness index correlations, with MBEs ranging from -0.07% to 11.57% and RMSEs ranging from 10.49% to 23.63%. Therefore, the model for the clearness index which has been developed in this study is valid and performs well since the values for the MBE and the RMSE are low and within the range that has been reported in previous studies. Thus, this developed correlation is valid to be used in the mathematical modelling of solar stills under the climatic conditions of Cape Town. More specifically, in this study, the developed correlation was used in the computation of the effective solar radiation inside the solar still.

4.3.2. Validation of mathematical models for solar stills containing Al_2O_3 nanoparticles of varying nanoparticle sizes

In order to validate the mathematical models for solar stills with nanofluids developed in this study, the experimental values for the mass of distillate were compared against theoretical values obtained from the simulations in MATLAB for 20 Test Days. Statistical parameters including the correlation coefficient, the root mean square error (RMSE) and the mean bias error (MBE) were used in order to validate Model 1 (with view factor) and Model 2 (without view factor). These results are shown in Table 4.7. The correlation coefficient for both Model 1 and Model 2 was found to be 0.84. On the other hand, the RMSE was 22.02% and 36.03% for Model 1 and Model 2, respectively; and the MBE was 1.49% and -17.77% for Model 1 and Model 2, respectively.

Table 4.7: Correlation coefficient, RMSE and MBE for Model 1 (with view factor) and Model 2 (without view factor).

Statistical parameter	Model 1 (with view factor)	Model 2 (without view factor)
Correlation coefficient	0.84	0.84
RMSE (%)	22.02	36.03
MBE (%)	1.49	-17.77

Until now, no author has reported correlation coefficients, RMSE or MBE for a solar still with nanofluids. However, a large range of these statistical parameters has been reported for solar stills without nanofluids. Tiwari and Tiwari (2007) conducted an investigation on the effect of water depth on the performance of a single slope solar still and they obtained RMSEs in the range of 48.47% to 93.64% and coefficients of correlation in the range of 0.6871 to 0.9778. Boutriaa and Rahmani (2017) developed a model for a solar still with a natural circulation loop and they reported RMSEs in the range of 2.7% to 26% and correlation coefficients in the range of 0.94 to 0.99. Madhlopa (2017) investigated two different correlations for evaluating the ratio between the evaporative and convective heat transfer coefficient in a single slope solar still. He obtained RMSEs of 15% and 53% for each of the two models. Abujazar et al. (2018) developed a cascaded forward neural network model to investigate the productivity of an inclined stepped solar still and they reported a RMSE of 22.48%.

Consequently, it can be deduced that the experimental results in this study are in good agreement with the numerical results obtained from the simulations in MATLAB as the correlation coefficients and the RMSEs for both Model 1 and Model 2 are within the range that has been reported in literature. Additionally, it is also noted that the RMSE for Model 1 is lower than that of Model 2 and the absolute value of the MBE for Model 1 is lower than that of Model 2, which means that the performance of Model 1 is better. Thus, the incorporation of the view factor in calculating the radiative heat transfer coefficient from the nanofluid to the glass cover improves the accuracy of modelling of solar stills with nanofluids.

4.3.3 Uncertainty Analysis

The total percentage uncertainty (sum of internal and external certainty) for the solar still with the Al_2O_3 nanoparticles was found to be 19.86%. This is within the range of uncertainties reported in literature. Shukla and Sorayan (2005) reported a total uncertainty of 20% for a single slope multiwick solar still operating under the climatic conditions of New Delhi in India. Gupta, Kumar and Baredar (2017) reported a total uncertainty of 11.04% for a solar still containing Cu_2O nanoparticles and equipped with a sprinkler for allowing water to flow across the outer surface of the glass cover, operating under the meteorological conditions of Jabalpur in India.

4.4. Summary

In this chapter, the theoretical results arising from the simulations in MATLAB were presented, as well as the experimental results and the model validation. Annual climatic data from Stellenbosch were used for the simulations in MATLAB in order to predict the annual performance of the solar stills. The experiments were conducted at the University of Cape Town and the climatic data from this location were also used in the simulations in MATLAB in order to obtain corresponding theoretical values of the productivity for each of the experimental Test Days. These experimental and theoretical values were then compared using statistical tools in order to validate the mathematical models for solar stills with nanofluids, namely Model 1 (with the view factor) and Model 2 (without the view factor).

It was found that the increase in the productivity of a solar still with nanofluids is much more distinct in summer than in winter. The productivity of a solar still was found to decrease with increasing nanoparticle size. Moreover, it was found that the cost of distilled water, the payback period and the amount of mitigated CO_2 equivalent decrease with increasing nanoparticle size. Theoretically, the productivity and the environmental performance of a solar still with nanofluids were marginally sensitive to the nanoparticle size while the cost of distilled water and the payback period were significantly affected by the nanoparticle size. The effect of nanoparticle size on productivity was found to be experimentally significant. Furthermore, it was established that the inclusion of the view factor improves the accuracy of modelling of solar stills with nanofluids. Based on the results and discussion provided in this chapter, conclusions have been made, as well as recommendations for future work. These conclusions and recommendations are presented in the next chapter.

CHAPTER 5
CONCLUSIONS AND RECOMMENDATIONS

In many parts of the world, particularly in Sub-Saharan Africa and Southern Asia, many people do not have access to safe drinking water. Desalination is increasingly becoming a crucial method of producing fresh water. However, desalination plants generally derive their energy from fossil fuels which are associated with two major negative impacts: 1) fossil fuels are non-renewable sources of energy and; 2) the combustion of fossil fuels releases greenhouse gases into the environment, in turn contributing to climate change. Consequently, it is essential to use a sustainable source of energy for driving the desalination process. A solar still is one such device which can be used to produce potable water from brackish or sea water, particularly in regions with high levels of solar radiation. It is also very convenient to use in remote locations as it can easily be constructed and maintained. The major drawback of a solar still lies in its low productivity and thus, various techniques of increasing its productivity have been investigated by previous researchers.

The addition of nanoparticles in the base fluid of a solar still has only recently been investigated, and based on the comprehensive literature review, it was noted that no study has explored the effect of nanoparticle size on the productivity of a solar still, and the effect of nanoparticle size on the economic and environmental performance of a solar still. Furthermore, most of the studies have been experimental only, and the few available numerical studies have not taken into account the view factor between the nanofluid and the glass cover in the computation of the internal radiative heat transfer coefficient. Based on these research gaps, the aim of this study was to investigate both numerically and experimentally the effect of nanoparticle size on the productivity, and on the economic and environmental performance of a solar still, taking into account the view factor in calculating the radiative heat transfer coefficient from the nanofluid to the glass cover.

To accomplish the aim of this study, the following objectives were formulated: a) to develop mathematical models for single slope solar stills; b) to design, build and test solar stills under identical climatic conditions; c) to determine the productivity of the solar stills with and without Al_2O_3 nanoparticles; d) to explore the effect of nanoparticle size on the productivity of solar stills, and on the economic and environmental performance of solar stills.; and e) to validate the mathematical models by comparing numerical results with experimental results,

as given in Chapter 1. A comprehensive literature review of previous studies conducted on solar stills with nanofluids was presented in Chapter 2. The design, modelling and experimentation of solar stills were discussed in depth in Chapter 3. The results obtained in this study were presented and discussed in Chapter 4. The conclusions which can be drawn from these results are presented in this chapter, as well as recommendations for future potential studies.

5.1. Conclusions

In this study, mathematical models for single slope solar stills were developed by formulating energy balance differential equations on each of the component of the solar still. These differential equations were discretised and solved in MATLAB by using the Gauss-Seidel iterative method. Identical solar stills were built, and experiments were conducted at the University of Cape Town, South Africa. The productivity of the solar stills with and without Al_2O_3 nanoparticles was determined. The effect of nanoparticle size on the productivity, and on the economic and environmental performance of solar stills was explored, and numerical results were compared with experimental results in order to validate the mathematical models. Thus, the aim and objectives which were formulated in this investigation have been accomplished. The conclusions which can be drawn from the numerical and experimental results are discussed below.

5.1.1. Effect of nanoparticles on the productivity of solar stills under summer and winter conditions

Simulations performed in MATLAB using climatic data from Stellenbosch showed that for the month of January, which is a summer month in South Africa, the productivity of the solar still with the 10 nm Al_2O_3 nanoparticles was 9.01% higher than the productivity of the solar still with the base fluid only. On the other hand, for the month of July, which is a winter month in South Africa, the productivity of the solar still with the 10 nm nanoparticles was only 1.31% higher than the productivity of the solar still with base fluid only. Thus, it is concluded that the solar still with the Al_2O_3 nanoparticles of the smallest size (10 nm) could achieve the highest productivity while the solar still with base fluid only gave the lowest productivity. It is also inferred that nanoparticles have a higher effect on the productivity of

solar stills in summer, attributed to the higher enhancement in the thermal conductivity of nanofluids at higher temperatures.

5.1.2. Effect of nanoparticle size on productivity of solar stills

Simulations in MATLAB using annual Stellenbosch climatic data showed that for the month of January, the productivity of the solar still with the 10 nm, 50 nm and 100 nm nanoparticles was 9.01%, 8.94% and 8.89%, respectively higher than the productivity of the solar still with the base fluid only. It is inferred that the productivity decreases with increasing nanoparticle size. On the other hand, for the month of July, the average productivity of the solar still with the 10 nm, 50 nm and 100 nm nanoparticles was 1.31%, 1.23% and 1.19%, respectively higher than the productivity of the solar still with base fluid only. Additionally, the average annual productivity of the solar stills with the 10 nm, 50 nm and 100 nm nanoparticles was 5.95%, 5.87% and 5.82%, respectively higher than the productivity of the solar still with base fluid only. It was established that the low increase in the productivity of the solar stills with nanofluids during winter months resulted in the low average annual increase.

For the experimental phase, experiments were conducted for a period of 20 days on four identical solar stills at the University of Cape (latitude 33.96°S, longitude 18.46°E), South Africa. The average daily productivity of the solar still with the 10 nm and 50 nm Al_2O_3 nanoparticles was 26.46% and 1.46%, respectively higher than the productivity of the solar still with base fluid only. On the other hand, the average daily productivity of the solar still with the 100 nm Al_2O_3 nanoparticles was 9.38% lower than the productivity of the solar still with base fluid only. This was attributed to the high nanoparticle size (100 nm) which results in poor stability and high agglomeration inside the solar still. Therefore, theoretically, the productivity was only marginally sensitive to nanoparticle size as the mathematical model for the solar still with nanofluids could not produce the same significant differences obtained experimentally.

5.1.3. Effect of nanoparticle size on the economic performance of solar stills with nanofluids

Simulations in MATLAB showed that the cost of distilled water from the solar still with the 10 nm, 50 nm and 100 nm Al_2O_3 nanoparticles was 10.42%, 6.21% and 3.51%, respectively higher than the cost of distilled water from the solar still with base fluid only. It is thus inferred that the cost of distilled water decreases with increasing nanoparticle size. Additionally, the payback period for the solar still with 10 nm, 50 nm and 100 nm Al_2O_3 nanoparticles was 13.32%, 7.86% and 4.37% respectively higher than the payback period for the solar still with base fluid only. It is concluded that the payback period decreases with increasing nanoparticle size.

Although the cost of distilled water and the payback period for the solar still with the 10 nm Al_2O_3 nanoparticles was higher than those of the solar still with base fluid only, it could achieve an increase of 26.46% in the yield of distillate, compared to the solar still with base fluid only. Moreover, knowledge is advancing in the field of nanotechnology. It is also known that technology learning plays a vital role in the reduction of the unit costs of production (Upstill & Hall, 2018). Consequently, the use of nanoparticles in solar stills may be a viable option in the future.

5.1.4. Effect of nanoparticle size on the environmental performance of solar stills with nanofluids

Simulations in MATLAB revealed that the annual energy output was 484.02 kWh per m^2 for the solar still with base fluid only, while the solar stills with the 10 nm, 50 nm and 100 nm Al_2O_3 nanoparticles achieved an annual energy output of 513.95, 513.58 and 513.37 kWh per m^2, respectively. It is inferred that the annual energy output decreases with an increase in the nanoparticle size.

The annual amount of CO_2 equivalent emissions mitigated from the solar still with the Al_2O_3 nanoparticles of size 10 nm, 50 nm and 100 nm was 6.18%, 6.11% and 6.06%, respectively higher than the annual amount of CO_2 equivalent mitigated from the solar still with base fluid only. It is thus concluded that the amount of CO_2 equivalent emissions decreases with increasing nanoparticle size.

Furthermore, the annual environmental cost that can be avoided was found to be 4.7309 USD per m^2 for the solar still with the base fluid only. On the other hand, the annual environmental cost that can be avoided was found to be 5.0235, 5.0198 and 5.0178 USD per m^2 for the solar still with the 10 nm, 50 nm and 100 nm Al_2O_3 nanoparticles, respectively. It is inferred that the environmental cost that can be avoided decreases with increasing nanoparticle size.

5.1.5. Model Validation

The ANOVA test which was conducted using experimental data collected from the University of Cape Town over a period of ten days when only base fluid was used in all four solar stills gave a P-value of 0.79 and 1.00 for uncorrected data and corrected data, respectively. This shows that the performance of the four solar stills (after calibration) was not significantly different.

Furthermore, simulations were run in MATLAB using climatic data from the University of Cape Town and the numerical results were validated against experimental results collected at the University of Cape Town. The RMSE for the solar stills with nanofluids for Model 1 (with the view factor) and Model 2 (without the view factor) was 22.02% and 36.03%, respectively. The correlation coefficient for both Model 1 and Model 2 was 0.84. Additionally, the MBE was 1.49 % and -17.77% for Model 1 and Model 2, respectively. It is thus concluded that there is good agreement between numerical and experimental results and that the mathematical models which were developed in this study are valid. It is also inferred that Model 1 overestimates the productivity while Model 2 underestimates the productivity and that the incorporation of the view factor improves the accuracy of the mathematical model for a solar still with nanofluids.

5.2. Recommendations

In this study, it was found that the productivity decreases with increasing nanoparticle size and the incorporation of the view factor improves the accuracy of the mathematical model of a solar still with nanofluids. Moreover, although there was good agreement between numerical and experimental results, there is a need for further improvements in the model as it could not give significant differences in the productivity of the solar stills with varying nanoparticle sizes, which were otherwise obtained experimentally.

Some future potential studies which could be carried out include the following:

a) Develop accurate correlations for predicting the thermophysical properties of nanofluids

As discussed in Chapter 4, there are currently no correlations incorporating the particle size which can accurately predict the thermophysical properties of nanofluids. Thus, there is a need to develop such correlations so as to be able to better predict the performance of solar stills with nanoparticles of varying sizes.

b) Investigate the effect of particle size of other nanoparticles on the productivity, and on the economic and environmental performance of solar stills with nanofluids

Based on a comprehensive literature review, it was noted that the effects of particle size of nanoparticles dispersed in the base fluid of a solar still on productivity, and on the economic and environmental performance of solar stills have not been explored so far. This study is the first one to have investigated these effects, but only Al_2O_3 nanoparticles of different sizes were used. Consequently, it would be interesting to use other nanoparticles such as CuO, Cu_2O, ZnO and TiO_2 which have previously been used in solar stills, and to explore the effects of the nanoparticle size on the productivity, and on the economic and environmental performance of solar stills.

5.3. Summary

Conclusions and recommendations were made in this chapter. The major conclusions which were drawn are: a) the effect of nanoparticles on the productivity of a solar still is much more distinct under summer weather conditions than under winter weather conditions; b) the productivity decreases with increasing nanoparticle size; c) theoretically, the productivity and the environmental performance of a solar still with nanofluids are marginally sensitive to the nanoparticle size while the cost of distilled water and the payback period are significantly affected by the nanoparticle size; d) the effect of nanoparticle size on productivity is experimentally significant and; e) the inclusion of the view factor between the nanofluid and the glass cover in the computation of the internal radiative heat transfer coefficient improves the accuracy of mathematical models for solar stills with nanofluids. The major recommendations which were made include the following: a) to develop accurate correlations for predicting the thermophysical properties of nanofluids, taking into account the nanoparticle size and; b) to explore the effect of particle size of other types of nanoparticles on the productivity, and on the economic and environmental performance of solar stills with nanofluids.

REFERENCES

Abad, H.K.S., Ghiasi, M., Mamouri, S.J. & Shaffi, M.B. 2013. A novel integrated solar desalination system with a pulsating heat pipe. *Desalination*. 311: 206-210. DOI: 10.1016/j.desal.2012.10.029.

Abderachid, T. & Abdenacer, K. 2013. Effect of orientation on the performance of a symmetric solar still with a double effect solar still (comparison study). *Desalination*. 329: 68-77. DOI: 10.1016/j.desal.2013.09.011.

Aboabboud, M.M., Mink, G. & Kudish, A. 2009. Condensation Heat Recycle in Solar Stills. *Proceedings of the World Congress on Engineering*. 1-3 July 2009. Available: https://pdfs.semanticscholar.org/8394/ce334402c429943bd6797c270d4e99c10ea5.pdf \ [2018, April 06].

Abu-Arabi, M. & Zurigat, Y. 2005. Year-round comparative study of three types of solar desalination units. *Desalination*. 172 (2): 137-143. DOI: 10.1016/j.desal.2004.05.011.

Abujazar, M.S.S., Fatihah, S., Ibrahim, I.A., Kabeel, A.E. & Sharil, S. 2018. Productivity modelling of a developed inclined stepped solar still system based on actual performance and using a cascaded forward neural network model. *Journal of Cleaner production*. 170: 147-159. DOI: 10.1016/j.jclepro.2017.09.092.

Abujazar, M.S.S., Fatihah, S., Rakmi, A.R. & Shahrom, M.Z. 2016. The effects of design parameters on productivity performance of a solar still for seawater desalination: A review. *Desalination*. 385: 178-193. DOI: 10.1016/j.desal.2016.02.025.

Al-Garni, A.Z. 2012. Enhancing the Solar Still Using Immersion Type Water Heater Productivity and the Effect of External Cooling Fan in Winter. *Applied Solar Energy*. 48 (3): 193-200. DOI: 10.3103/S0003701X12030048.

Al-Hinai, H., Al-Nassri, M.S. & Jubran, B.A. 2002. Effect of climatic, design and operational parameters on the yield of a simple solar still. *Energy Conversion & Management.* 43: 1639-1650. DOI: 10.1016/S0196-8904(01)00120-0.

Al-Karaghouli, A. & Kazmerski, L.L. 2013. Energy consumption and water production cost of conventional and renewable-energy-powered desalination processes. *Renewable and Sustainable Energy Reviews*. 24: 343-356. DOI: 10.1016/j.rser.2012.12.064.

Altarawneh, I., Rawadieh, S., Batiha, M., Al-Makhadmeh, L. Alrowwad, S. & Tarawneh, M. 2017. Experimental and numerical performance analysis and optimization of single slope, double slope and pyramidal shaped solar stills. *Desalination*. 423: 124-134. DOI: 10.1016/j.desal.2017.09.023.

Amin, T.E., Roghayeh, G., Fatemeh, R. & Fatollah, P. 2015. Evaluation of nanoparticle shape effect on a nanofluid based flat-plate solar collector efficiency. *Energy Exploration & Exploitation*. 33(5): 659-676.

Ankoliya, D.B. & Modi, K.V. 2016. Effect of nanofluid in single slope double basin solar still. *International Journal of Advance Research and Innovative Ideas in Education*. 2 (3): 1051-1057. Available: http://ijariie.com/AdminUploadPdf/Effect_of_Nanofluid_in_Single_Slope_Double_Basin_Solar_Still_ijariie2328.pdf [2017, May 23].

Annamalai, K., Puri, I.K. & Jog, M.A. 2011. *Advanced Thermodynamics Engineering*. 2nd ed. United States of America: Taylor & Francis Group.

Appadurai, M. & Velmurugan, V. 2015. Performance analysis of fin type solar still integrated with fin type mini solar pond. *Sustainable Energy Technologies and Assessments*. 9: 30-36. DOI: 10.1016/j.seta.2014.11.001.

Arunkumar, T., Denkenberger, D., Ahsan, A. & Jayaprakash, R. 2013. The augmentation of distillate yield by using concentrator coupled solar still with phase change material. *Desalination*. 314: 189-192. DOI: 10.1016/j.desal.2013.01.018.

Arunkumar, T., Velraj, R., Denkenberger, D.C., Sathyamurthy, R., Kumar, K.V. & Ahsan, A. 2016. Productivity enhancements of compound parabolic concentrator tubular solar stills. *Renewable Energy*. 88: 391-400. DOI: 10.1016/j.renene.2015.11.051.

Ashoor, B.B., Mansour, S., Giwa, A., Dufour, V. & Hasan, S.W. 2016. Principles and applications of direct contact membrane distillation (DCMD): A comprehensive review. *Desalination*. 398: 222-246. DOI: 10.1016/j.desal.2016.07.043.

Ayoub, G.M. & Malaeb, L. 2012. Developments in Solar Still Desalination Systems: A Critical Review. *Critical Reviews in Environmental Science and Technology*. 42(19): 2078-2112. DOI: 10.1080/10643389.2011.574104.

Babita., Sharma, S.K. & Gupta, S.M. 2016. Preparation and evaluation of stable nanofluids for heat transfer application: A review. *Experimental Thermal and Fluid Science*. 79: 202-212. DOI: 10.1016/j.expthermflusci.2016.06.029.

Badran, A.A., A1-Hallaq, A.A., Salman, I.A.E. & Odat, M.Z. 2005. A solar still augmented with a flat-plate collector. *Desalination*. 172(3): 227–234. DOI: 10.1016/j.desal.2004.06.203.

Bait, O. 2019. Exergy, environ-economic and economic analyses of a tubular solar water heater assisted solar still. *Journal of Cleaner Production*. 212: 630-646. DOI: 10.1016/j.jclepro.2018.12.015.

Bait, O. 2020. Direct and indirect solar–powered desalination processes loaded with nanoparticles: A review. *Sustainable Energy Technologies and Assessments*. 37: 100597. DOI: 10.1016/j.seta.2019.100597.

Baker, R.W. 2012. *Membrane Technology and Applications*. 3rd ed. Chennai, India: John Wiley and Sons Ltd.

Barrett, T.R., Robinson, S., Flinders, K., Sergis, A. & Hardalupas, Y. 2013. Investigating the use of Nanofluids to Improve High Heat Flux Cooling Systems. *Fusion Engineering and Design*. 88 (9-10): 2594-2597. DOI: 10.1016/j.fusengdes.2013.03.058.

Belessiotis, V., Kalogirou, S. & Delyannis, E. 2016. *Thermal Solar Desalination Methods and Systems*. United Kingdom: Elsevier Ltd.

Belessiotis, V., Voropoulos, K. & Delyannis, E. 1995. Experimental and theoretical method for the determination of the daily output of a solar still: input-output method. *Desalination*. 100: 99-104. DOI: 10.1016/0011-9164(96)00011-2.

Bellos, E. & Tzivanidis, C. 2019. A review of concentrating solar thermal collectors with and without nanofluids. *Journal of Thermal Analysis and Calorimetry*. 135(1): 763–786. DOI: 10.1007/s10973-018-7183-1.

Bengtsson, L. 2010. The global atmospheric water cycle. *Environmental Research Letters*. 5 (2): 1-8. DOI: 10.1088/1748-9326/5/2/025002.

Bergman, T.L., Lavine, A.S., Incropera, F.P. & Dewitt, D.P. 2011. *Fundamentals of Heat and Mass Transfer*. Rev. 7th ed. United States of America: John Wiley & Sons, Inc.

Bhardwaj, R., Kortenaar, M.V. & Mudde, R.F. 2013. Influence of condensation surface on solar distillation. *Desalination*. 326: 37-45. DOI: 10.1016/j.desal.2013.07.006.

Bhattad, A., Sarkar, J. & Ghosh, P. 2018. Improving the performance of refrigeration systems by using nanofluids: A comprehensive review. *Renewable and Sustainable Energy Reviews*. 82: 3656-3669. DOI: 10.1016/j.rser.2017.10.097.

Böckh, P.V. & Wetzel, T. 2012. *Heat Transfer Basics and Practice*. Berlin: Springer.

Bouguerra, N., Khabou, A., Poncet, S. & Elkoun, S. 2016. Thermal Conductivity of Al_2O_3/Water-Based Nanofluids: Revisiting the Influences of pH and Surfactant. *International Journal of Mechanical and Mechatronics Engineering*. 10 (12): 1919-1928.

Bourouni, K., Chaibi, M.T. & Tadrist, L. 2001. Water desalination by humidification and dehumidification of air: state of the art. *Desalination*. 137 (1-3): 167-176. DOI: 10.1016/S0011-9164(01)00215-6.

Boutriaa, A. & Rahmani, A. 2017. Thermal modeling of a basin type solar still enhanced by a natural circulation loop. *Computers and Chemical Engineering*. 101: 31-43. DOI: 10.1016/j.compchemeng.2017.02.033.

BusinessTech. 2018. *Government to step in on price of bottled water in Cape Town*. Available: https://businesstech.co.za/news/business/222305/government-to-step-in-on-price-of-bottled-water-in-cape-town/ [2019, July 01].

Camacho, L.M., Dumée, L., Zhang, J., Li, J., Duke, M., Gomez, J. & Gray, S. 2013. Advances in Membrane Distillation for Water Desalination and Purification Applications. *Water*. 5 (1): 94-196. DOI: 10.3390/w5010094.

Cappelletti, G.M. 2002. An experiment with a plastic solar still. *Desalination*. 142: 221-227.

Chaibi, M.T. 2000. An overview of solar desalination for domestic and agriculture water needs in remote arid areas. *Desalination*. 127 (2): 119-133. DOI: 10.1016/S0011-9164(99)00197-6.

Chaichan, M.T. & Kazem, H.A. 2015. Water solar distiller productivity enhancement using concentrating solar water heater and phase change material (PCM). *Case Studies in Thermal Engineering*. 5: 151-159. DOI: 10.1016/j.csite.2015.03.009.

Chapman, S.J. 2015. MALTAB Programming for Engineers. Rev. 5th ed. United States of America: Cengage Learning.

Charitar, D. 2015. Numerical study of the thermal performance of solar chimneys for ventilation in buildings. MSc Thesis. University of Cape Town.

Choi, S.U.S. & Eastman, J.A. 1995. Enhancing thermal conductivity of fluids with nanoparticles. *International mechanical engineering congress and exhibition*. 12-17 Nov 1995. San Francisco. Available: http://www.osti.gov/scitech/biblio/196525/ [2016, July 15].

Chon, C.H. & Kihm, K.D. 2005. Empirical correlation finding the role of temperature and particle size for nanofluid (Al_2O_3) thermal conductivity enhancement. *Applied Physics Letters*. 87 (15). DOI: 10.1063/1.2093936.

Choudhary, R., Khurana, D., Kumar, A. & Subudhi, S. 2017. Stability analysis of Al_2O_3/water nanofluids. *Journal of Experimental Nanoscience*. 12 (1): 140-151. DOI: 10.1080/17458080.2017.1285445.

Cisneros, J.B.E., Oki, T., Arnell, N.W., Benito, G., Cogley, J.G., Döll, P., Jiang, T. & Mwakalila, S.S. 2014. *Fresh water resources*. In: *Climate Change 2014: Impacts, Adaptation, and Vulnerability. Part A: Global and Sectoral Aspects. Contribution of Working Group II to the Fifth Assessment Report of the Intergovernmental Panel on Climate Change*. Available: https://www.ipcc.ch/pdf/assessment-report/ar5/wg2/WGIIAR5-Chap3_FINAL.pdf [2017, March 01].

Danish, S.N., El-Leathy, A., Alata, M. & Al-Ansary, H. 2019. Enhancing Solar Still Performance Using Vacuum Pump and Geothermal Energy. *Energies*. 12 (539): 1-13. DOI: 10.3390/en12030539.

Das, P.K., Islam, N., Santra, A.K. & Ganguly, R. 2017. Experimental investigation of thermophysical properties of Al_2O_3–water nanofluid: Role of surfactants. *Journal of Molecular Liquids*. 237: 304-312. DOI: 10.1016/j.molliq.2017.04.099.

Dashtban, M. & Tabrizi, F.F. 2011. Thermal analysis of a weir-type cascade solar still integrated with PCM storage. *Desalination*. 279 (1-3): 415-422. DOI: 10.1016/j.desal.2011.06.044.

Deshmukh, H.S. & Thombre, S.B. 2017. Solar distillation with single basin solar still using sensible heat storage materials. *Desalination*. 410: 91-98. DOI: 10.1016/j.desal.2017.01.030.

Devendiran, D.K. & Amirtham, V.A. 2016. A review on preparation, characterization, properties and applications of nanofluids. *Renewable and Sustainable Energy Reviews*. 60: 21-40. DOI: 10.1016/j.rser.2016.01.055.

Dey, D., Kumar, P. & Samantaray, S. 2017. A review of nanofluid preparation, stability, and thermo-physical properties. *Heat Transfer–Asian Research*. 46: 1413–1442. DOI:10.1002/htj.21282.

Du Plessis, P. 2011. The potential of solar process heat for South African industry. MSc Thesis. University of Cape Town.

Duffie, J.A. & Beckman, W.A. 2013. *Solar Energy Thermal Processes*. Rev. 4th ed. United States of America: John Wiley & Sons, Inc.

Duong, H.C., Cooper, P., Nelemans, B., Cath, T.Y. & Nghiem, L.D. 2015. Optimising thermal efficiency of direct contact membrane distillation by brine recycling for small scale seawater desalination. *Desalination*. 374: 1-9. DOI: 10.1016/j.desal.2015.07.009.

Durkaieswaran, P. & Murugavel, K.K. 2015. Various special designs of single basin passive solar still – A review. *Renewable and Sustainable Energy Reviews*. 49: 1048-1060. DOI: 10.1016/j.rser.2015.04.111.

Dwivedi, V.K. & Tiwari, G.N. 2009. Comparison of internal heat transfer coefficients in passive solar stills by different thermal models: An experimental validation. *Desalination*. 246 (1-3): 304-318. DOI: 10.1016/j.desal.2008.06.024.

Edalatpour, M., Aryana, K., Kianifar, A., Tiwari, G.N., Mahian, O. & Wongwises, S. 2016. Solar stills: A review of the latest developments in numerical simulations. *Solar Energy*. 135: 897-922. DOI: 10.1016/j.solener.2016.03.005

Elango, C., Gunasekaran, N. & Sampathkumar, K. 2015. Thermal models of solar still – A comprehensive review. *Renewable and Sustainable Energy Reviews*. 47: 856-911. DOI: 10.1016/j.rser.2015.03.054.

Elango, T. & Muragavel, K.K. 2015. The effect of the water depth on the productivity for single and double basin double slope glass solar stills. *Desalination*. 359: 82-91. DOI: 10.1016/j.desal.2014.12.036.

Elango, T., Kannan, A. & Murugavel, K. 2015. Performance study on single basin single slope solar still with different water nanofluids. *Desalination*. 360: 45-51. DOI: 10.1016/j.desal.2015.01.004.

El-Bialy, E., Shalaby, S.M., Kabeel, A.E. & Fathy, A.M. 2016. Cost analysis for several solar desalination systems. *Desalination*. 384: 12-30. DOI: 10.1016/j.desal.2016.01.028.

El-Maghlany, W.M., El-Samadony, Y.A.F. & Kabeel, A.E. 2016. Glass cover inclination angle effect on the radiation shape factor within conventional solar still. *Desalination and Water Treatment*. 57 (38): 17722-17730, DOI: 10.1080/19443994.2015.1102090.

Elminshawy, N.A.S., Siddiqui, F.R. & Sultan, G.I. 2015. Development of a desalination system driven by solar energy and low grade waste heat. *Energy Conversion and Management*. 103: 28-35. DOI: 10.1016/j.enconman.2015.06.035.

Elsahati, M.O, Richards, R.F. 2017. Effect of moisture on nanoparticle packed beds. *International Journal of Heat and Mass Transfer*. 112: 171-184. DOI: 10.1016/j.ijheatmasstransfer.2017.04.073.

El-Sebaii, A.A. & El-Bialy, E. 2015. Advanced designs of solar desalination systems: A review. *Renewable and Sustainable Energy Reviews*. 49: 1198-1212. DOI: 10.1016/j.rser.2015.04.161.

El-Sebaii, A.A. 2000. Effect of wind speed on some designs of solar stills. *Energy Conversion & Management*. 41: 523-538. DOI: 10.1016/S0196-8904(99)00119-3.

El-Sebaii, A.A. 2005. Thermal performance of a triple-basin solar still. *Desalination*. 174: 25-37. DOI: 10.1016/j.desal.2004.08.038. .1016/j.desal.2004.08.038

El-Sebaii, A.A., Al-Ghamdi, A.A., Al-Hazmi, F.S. & Faidah, A.S. 2009. Thermal performance of a single basin solar still with PCM as a storage medium. *Applied Energy*. 86(7-8): 1187–1195. DOI: 10.1016/j.apenergy.2008.10.014.

El-Sebaii, A.A., Ramadan, M.R.I., Aboul-Enein, S. & Salem, N. 2008. Thermal performance of a single-basin solar still integrated with a shallow solar pond. *Energy Conversion and Management.* 49 (10); 2839-2848. DOI: 10.1016/j.enconman.2008.03.002.

Estahbanati, M.R.K., Ahsan, A., Feilizadeh, M., Jafarpur, K., Ashrafmansouri, S. & Feilizadeh, M. 2016. Theoretical and experimental investigation on internal reflectors in a single-slope solar still. *Applied Energy*. 165: 537-547. DOI: 10.1016/j.apenergy.2015.12.047.

Esteve-Calvo, P.F. & Lloret-Clement, M. 2007. ATTRACTORS, STRUCTURAL FUNCTIONS, AND THE WATER CYCLE. *Cybernetics and Systems: An International Journal*. 38 (4): 401-409. DOI: 10.1080/01969720701291221.

Ettouney, H. 2009. Conventional Thermal Processes. In *Seawater Desalination*. A. Cipollina, G. Micale & L. Rizzuti, Eds. Heidelberg: Springer. 17-40.

European Union. 2008. ADIRA Handbook. A guide to autonomous desalination system concepts. Available: http://www.wrri.nmsu.edu/conf/conf11/2008_adira_handbook.pdf [2017, March 09].

Fath, H.E.S., El-Samanoudy, M., Fahmy, K. & Hassabou, A. 2003. Thermal-economic analysis and comparison between pyramid shaped and single-slope solar still configurations. *Desalination*. 159 (1): 69-79. DOI: 10.1016/S0011-9164(03)90046-4

Fell, J. & Winter, K. 2018. *UCT responds to City's new water tariff*. Available: http://www.alumni.uct.ac.za/news/uct-responds-to-new-water-tariff [2019, November 13].

Food and Agriculture Organisation. 2012. Coping with water scarcity – An action framework for agriculture and food security. Available: http://www.fao.org/docrep/016/i3015e/i3015e.pdf [2017, February 22].

Forgan, B.W. 2011. *Solar Radiation Measurement*. Available: https://www.wmo.int/pages/prog/www/IMOP/TrainingMat/2011-Melbourne/Doc_5_1_Solar-Radiation_BForgan.pdf [2018, May 11].

Fuskele, V. & Sarviya, R.M. 2017. Recent developments in Nanoparticles Synthesis, Preparation and Stability of Nanofluids. *Materials Today Proceedings*. 4 (2): 4049-4060. DOI: 10.1016/j.matpr.2017.02.307.

Gangadevi, R., Vinayagam, B.K. & Senthilraja, S. 2018. Effects of sonication time and temperature on thermal conductivity of CuO/water and Al_2O_3/water nanofluids with and without surfactant. *Materials Today Proceedings*. 5 (2): 9004-9011. DOI: 10.1016/j.matpr.2017.12.347.

Ganji, D.D., Sabzehmeidani, Y. & Sedighiamiri, A. 2018. *Nonlinear Systems in Heat Transfer – Mathematical Modeling and Analytical Methods*. India: Elsevier Inc.

Garg, H.P. & Prakash, J. 2000. *Solar Energy Fundamentals and Applications*. Delhi: Tata McGraw-Hill.

Ghalavand, Y., Hatamipour, M.S. & Rahimi, A. 2015. A review on energy consumption of desalination processes. *Desalination and Water Treatment*. 54 (6): 1526-1541.

Gnanadason, M.K., Kumar, P.S., Jemilda, G. & Jasper, S.S. 2012. Effect of Nanofluids in a Modified Vacuum Single Basin Solar Still. *International Journal of Scientific & Engineering Research*. 3 (1): 1-7. Available: http://www.ijser.org/researchpaper%5CEffect-of-Nanofluids-in-a-Vacuum-Single-Basin-Solar-Still.pdf [2016, July 25].

Gnanadason, M.K., Kumar, P.S., Wilson, V.H., Hariharan, G. & Vinayagamoorthi, N.S. 2013. Design and Performance Analysis of an Innovative Single Basin Solar NanoStill. *Smart Grid and Renewable Energy*. 4: 88-98. Available: http://file.scirp.org/pdf/SGRE_2013022615585338.pdf [2017, April 25].

Gorji, T.B., Ranjbar, A.A. & Mirzababaei, S.N. 2015. Optical properties of carboxyl functionalized carbon nanotube aqueous nanofluids as direct solar thermal energy absorbers. *Solar Energy*. 119: 332-342. DOI: 10.1016/j.solener.2015.07.012.

Goswami, D.Y. 2015. *Principles of Solar Engineering*. Rev. 3rd ed. United States of America: Taylor & Francis Group, LLC.

Greenlee, L.F., Lawler, D.F., Freeman, B.D., Marrot, B. & Moulin, P. 2009. Reverse osmosis desalination: Water sources, technology, and today's challenges. *Water Research*. 43 (9): 2317-2348. DOI: 10.1016/j.watres.2009.03.010.

Gu, L.D., Min, J.C. & Tang, Y.C. 2018. Effects of mass transfer on heat and mass transfer characteristics between water surface and airstream. *International Journal of Heat and Mass Transfer*. 122: 1093-1102.

Gude, V.G. 2016. Desalination and sustainability – An appraisal and current perspective. *Water Research*. 89: 87-106. DOI: 10.1016/j.watres.2015.11.012.

Gude, V.G., Nirmalakhandan, N. & Deng, S. 2010. Renewable and sustainable approaches for desalination. *Renewable and Sustainable Energy Reviews*. 14 (9): 2641–2654. DOI: 10.1016/j.rser.2010.06.008.

Gude, V.G., Nirmalakhandan, N., Deng, S. & Maganti, A. 2012. Feasibility study of a new two-stage low temperature desalination process. *Energy Conversion and Management*. 56: 192-198. DOI: 10.1016/j.enconman.2011.11.026.

Gul, M., Kotak, Y., Muneer, T. & Ivanova, S. 2018. Enhancement of Albedo for Solar Energy Gain with Particular Emphasis on Overcast Skies. *Energies*. 11, 2881. DOI: 10.3390/en11112881.

Gupta, B., Kumar, A. & Baredar, P.V. 2017. Experimental Investigation on Modified Solar Still Using Nanoparticles and Water Sprinkler Attachment. *Frontiers in Materials*. 4 (23). DOI: 10.3389/fmats.2017.00023.

Gupta, B., Shankar, P., Sharma, R. & Baredar, P. 2016. Performance enhancement using nano particles in modified passive solar still. *Procedia Technology*. 25: 1209-1216. DOI: 10.1016/j.protcy.2016.08.208.

Gupta, M., Singh, V., Kumar, R. & Said, Z. 2017. A review on thermophysical properties of nanofluids and heat transfer applications. *Renewable and Sustainable Energy Reviews*. 74: 638-670. DOI: 10.1016/j.rser.2017.02.073.

Heydari, A. & Rahbar, N. 2016. Energy and Life Cost Analysis of a Wet Wall Solar Still with Various Pump Working Conditions. *Environmental Progress & Sustainable Energy*. 36(2): 532-538. DOI: 10.1002/ep.12470.

Hitsov, I., Maere, T., De Sitter, K., Dotremont, C. & Nopens, I. 2015. Modelling approaches in membrane distillation: A critical review. *Separation and Purification Technology*. 142: 48-64. DOI: 10.1016/j.seppur.2014.12.026.

Howell, J.R., Mengüç, M.P. & Siegel, R. 2016. *Thermal Radiation Heat Transfer*. Rev. 6th ed. United States of America: Taylor & Francis Group, LLC.

Hu, X.J, Prasher, R., Lofgreen, K. 2007. Ultralow thermal conductivity of nanoparticle packed bed. *Applied Physics Letters*. 91 (203113). DOI: 10.1063/1.2814959.

Ibrahim, A.G.M. & Elshamarka, S.E. 2015. Performance study of a modified basin type solar still. *Solar Energy*. 118: 397-409. DOI: 10.1016/j.solener.2015.06.013.

IEA-ETSAP and IRENA. 2012. *Water Desalination Using Renewable Energy – Technology Brief.* Available: https://www.irena.org/DocumentDownloads/Publications/IRENA-ETSAP%20Tech%20Brief%20I12%20Water-Desalination.pdf [2016, December 07].

Ilyas, S.U., Pendyala, R. & Marneni, N. 2014. Preparation, Sedimentation, and Agglomeration of Nanofluids. *Chemical Engineering Technology*. 37 (12): 2011-2021. DOI: 10.1002/ceat.201400268.

International Desalination Association. 2017. *Desalination by the Numbers*. Available: http://idadesal.org/desalination-101/desalination-by-the-numbers/ [2017, February 22].

International Organization for Standardization. 2015. *Nanotechnologies – Vocabulary – Part 1: Core terms*. (ISO/TS 80004 – 1: 2015). Geneva: ISO.

International Renewable Energy Agency. 2012. *Water Desalination Using Renewable Energy Technology Brief.* Available: https://www.irena.org/DocumentDownloads/Publications/IRENA-ETSAP%20Tech%20Brief%20I12%20Water-Desalination.pdf [2016, July 21].

Iqbal, M. 1983. *An Introduction to Solar Radiation*. Canada: Academic Press.

Jacovides, C.P., Tymvios, F.S., Assimakopoulos, V.D. & Kaltsounides, N.A. 2006. Comparative study of various correlations in estimating hourly diffuse fraction of global solar radiation. *Renewable Energy*. 31 (15): 2492–2504. DOI: 10.1016/j.renene.2005.11.009.

Jain, D., & Tiwari, G.N. 2004. Effect of greenhouse on crop drying under natural and forced convection I: Evaluation of convective mass transfer coefficient. *Energy Conversion & Management.* 45: 765-783. DOI: 10.1016/S0196-8904(03)00178-X.

Jama, M., Singh, T., Gamaleldin, S.M., Koc, M., Samara, A., Isaifan, R.J. & Atieh, M.A. 2016. Critical Review on Nanofluids: Preparation, Characterization, and Applications. *Journal of Nanomaterials*. 1-22. DOI: 10.1155/2016/6717624.

Johnston, C. 2015. Desalination: the quest to quench the world's thirst for water. *theguardian*. 27 May. Available: http://www.theguardian.com/technology/2015/may/27/desalination-quest-quench-worlds-thirst-water [2016, March 31].

Ju, W.X. & Fang, L.X. 2009. Influence of pH on Nanofluids' Viscosity and Thermal Conductivity. *Chinese Physics Letters*. 26 (5): 1-4.

Kabeel, A.E. & Abdelgaied, M. 2016. Improving the performance of solar still by using PCM as a thermal storage medium under Egyptian conditions. *Desalination*. 383: 22-28. DOI: 10.1016/j.desal.2016.01.006.

Kabeel, A.E. & El-Agouz, S.A. 2011. Review of researches and developments on solar stills. *Desalination*. 276: 1-12. DOI: 10.1016/j.desal.2011.03.042.

Kabeel, A.E., Hamed, A.M. & El-Agouz, S.A. 2010. Cost analysis of different solar still configurations. *Energy*. 35 (7): 2901-2908. DOI: 10.1016/j.energy.2010.03.021.

Kabeel, A.E., Omara, Z.M. & Essa, F.A. 2014a. Enhancement of modified solar still integrated with external condenser using nanofluids: An experimental approach. *Energy Conversion and Management*. 78: 493-498. DOI: 10.1016/j.enconman.2013.11.013.

Kabeel, A.E., Omara, Z.M. & Essa, F.A. 2014b. Improving the performance of solar still by using nanofluids and providing vacuum. *Energy Conversion and Management*. 86: 268-274. DOI: 10.1016/j.enconman.2014.05.050.

Kabeel, A.E., Omara, Z.M. & Essa, F.A. 2017. Numerical investigation of modified solar still using nanofluids and external condenser. *Journal of the Taiwan Institute of Chemical Engineers*. 75: 77-86. DOI: 10.1016/j.jtice.2017.01.017.

Kabeel, A.E., Sathyamurthy, R., Sharshir, S.W., Muthumanokar, A., Panchal, H., Prakash, N., Prasad, C., Nandakumar, S. et al. 2019. Effect of water depth on a novel absorber plate of pyramid solar still coated with TiO_2 nano black paint. *Journal of Cleaner Production*. 213: 185-191. DOI: 10.1016/j.jclepro.2018.12.185.

Kalogirou, S.A. 2005. Seawater desalination using renewable energy sources. *Progress in Energy and Combustion Science*. 31 (3): 242-281. DOI: 10.1016/j.pecs.2005.03.001.

Kalogirou, S.A. 2009. *Solar Energy Engineering: Processes and Systems*. United Kingdom: Elsevier Inc.

Kannan, R., Selvaganesan, C., Vignesh, M., Babu, B.R., Fuentes, M., Vivar, M., Skryabin, I. & Srithar, K. 2014. Solar still with vapor adsorption basin: Performance analysis. *Renewable Energy*. 62: 258-264. DOI: 10.1016/j.renene.2013.07.018.

Kaushal, A. & Varun. 2010. Solar stills: A review. *Renewable and Sustainable Energy Reviews*. 14 (1): 446-453. DOI: 10.1016/j.rser.2009.05.011.

Kaviti, A.K., Yadav, A. & Shukla, A. 2016. Inclined solar stills design: A review. *Renewable and Sustainable Energy Reviews*. 54: 429-451. DOI: 10.1016/j.rser.2015.10.027.

Keblinski, P., Phillpot, S.R., Choi, S.U.S. & Eastman, J.A. 2002. Mechanisms of heat flow in suspensions of nano-sized particles (nanofluids). *International Journal of Heat and Mass Transfer*. 45 (4): 855-863. DOI: 10.1016/S0017-9310(01)00175-2.

Kelley, C.T. 1995. *Iterative Methods for Linear and Nonlinear Equations*. Available: https://archive.siam.org/books/textbooks/fr16_book.pdf [2019, November 08].

Khairul, M.A., Shah, K., Doroodchi, E., Azizian, R. & Moghtaderi, B. 2016. Effects of surfactant on stability and thermo-physical properties of metal oxide nanofluids. *International Journal of Heat and Mass Transfer*. 98: 778-787. DOI: 10.1016/j.ijheatmasstransfer.2016.03.079.

Khalifa, A.J.N. & Hamood, A.M. 2009a. On the verification of the effect of water depth on the performance of basin type solar stills. *Solar Energy*. 83: 1312-1321. DOI: 10.1016/j.solener.2009.04.006.

Khalifa, A.J.N. & Hamood, A.M. 2009b. Effect of insulation thickness on the productivity of basin type solar stills: An experimental verification under local climate. *Energy Conversion and Management*. 50: 2457-2461. DOI: 10.1016/j.enconman.2009.06.007.

Khalifa, A.J.N. 2011. On the effect of cover tilt angle of the simple solar still on its productivity in different seasons and latitudes. *Energy Conversion and Management*. 52: 431-436. DOI: 10.1016/j.enconman.2010.07.018.

Khan, M. & Mustafa, M. 2019. Solar Still Distillate Productivity Enhancement by Using Reflector and Design Optimization. *Innovative Energy & Research*. 8 (1). DOI: 10.4172/2576-1463.1000222.

Khan, M.A.M., Rehman, S. & Al-Sulaiman, F.A. 2018. A hybrid renewable energy system as a potential energy source for water desalination using reverse osmosis: A review. *Renewable and Sustainable Energy Reviews*. 97: 456-477. DOI: 10.1016/j.rser.2018.08.049.

Khanafer, K. & Vafai, K. 2011. A critical synthesis of thermophysical characteristics of nanofluids. *International Journal of Heat and Mass Transfer*. 54(19-20): 4410-4428. DOI: 10.1016/j.ijheatmasstransfer.2011.04.048.

Kim, H., Kim, J. & Cho, H. 2017. Experimental study on performance improvement of U-tube solar collector depending on nanoparticle size and concentration of Al_2O_3 nanofluid. *Energy*. 118: 1304-1312. DOI: 10.1016/j.energy.2016.11.009.

Koca, H.D., Doganay, S., Turgut, A., Tavman, A., Saidur, R. & Mahbubul, I.M. 2018. Effect of particle size on the viscosity of nanofluids: A review. *Renewable and Sustainable Energy Reviews.* 82: 1664-1674. DOI: 10.1016/j.rser.2017.07.016.

Kong, L., Sun, J. & Bao, Y. 2017. Preparation, characterization and tribological mechanism of nanofluids. *Royal Society of Chemistry*. 7: 12599-12609. DOI: 10.1039/c6ra28243a.

Kumar, P.V., Kaviti, A.K., Prakash, O. & Reddy, K.S. 2012. Optimisation of design and operating parameters on the year round performance of a multi-stage evacuated solar desalination system using transient mathematical analysis. *International Journal of Energy and Environment*. 3 (3): 409-434. Available: http://www.ijee.ieefoundation.org/vol3/issue3/IJEE_07_v3n3.pdf [2016, March 31].

Kumar, P.V., Kumar, A., Prakash, O. & Kaviti, A.K. 2015. Solar stills system design: A review. *Renewable and Sustainable Energy Reviews*. 51: 153-181. DOI: 10.1016/j.rser.2015.04.103.

Kumar, R.A., Esakkimuthu, G. & Murugavel, K.K. 2016. Performance enhancement of a single basin single slope solar still using agitation effect and external condenser. *Desalination*. 399: 198-202. DOI: 10.1016/j.desal.2016.09.006.

Kumar, S. & Tiwari, G.N. 2009. Life cycle cost analysis of single slope hybrid (PV/T) active solar still. *Applied Energy*. 86 (10): 1995-2004. DOI: 10.1016/j.apenergy.2009.03.005.

Kuo, C.W., Chang, W.C. & Chang, K.C. 2014. Modeling the hourly solar diffuse fraction in Taiwan. *Renewable Energy*. 66: 56-61. DOI: 10.1016/j.renene.2013.11.072.

Lee, J.H., Hwang, K.S., Jang, S.P., Lee, B.H., Kim, J.H., Choi, S.U.S. & Choi, C.J. 2008. Effective viscosities and thermal conductivities of aqueous nanofluids containing low volume concentrations of Al_2O_3 nanoparticles. *International Journal of Heat and Mass Transfer*. 51: 2651-2656. DOI: 10.1016/j.ijheatmasstransfer.2007.10.026.

Li, Y., Zhou, J., Tung, S., Schneider, E. & Xi, S. 2009. A review on development of nanofluid preparation and characterization. *Powder Technology*. 196: 89-101. DOI: 10.1016/j.powtec.2009.07.025.

Liu, L., Wang, M. & Liu, Y. 2015. Experimental Investigation on Preparation and Stability of Al_2O_3/CuO-water Nanofluids. *Asia-Pacific Energy Equipment Engineering Research Conference*.

Loong, T.T. & Salleh, H. 2017. A review on measurement techniques of apparent thermal conductivity of nanofluids. *Materials Science and Engineering*. DOI:10.1088/1757-899X/226/1/012146.

Mackay, M.E. 2015. *Solar Energy: An Introduction*. United Kingdom: Oxford University Press.

Madhlopa, A. & Johnstone, C. 2009a. Numerical study of a passive solar still with separate condenser. *Renewable Energy*. 34 (7): 1668-1677. DOI: 10.1016/j.renene.2008.12.032.

Madhlopa, A. & Johnstone, C.M. 2009b. Model for computation of solar fraction in a single-slope solar still. *Solar Energy*. 83: 873-882. DOI: 10.1016/j.solener.2008.12.002.

Madhlopa, A. & Johnstone, C.M. 2011. Computation of solar radiation distribution in a solar still with internal and external reflectors. *Solar Energy*. 85: 217-233. DOI: 10.1016/j.solener.2010.12.010.

Madhlopa, A. 2009. *Development of an advanced passive solar still with separate condenser*. Ph.D. Thesis. University of Strathclyde.

Madhlopa, A. 2014. Modelling radiative heat transfer inside a basin type solar still. *Applied Thermal Engineering.* 73: 707-711. DOI: 10.1016/j.applthermaleng.2014.07.065.

Madhlopa, A. 2017. Theoretical and empirical study of heat and mass transfer inside a basin type solar still. *Energy*. 136: 45-51. DOI: 10.1016/j.energy.2016.09.126.

Mahammed, K.Y., Kerfah, R. & Bezzina, M. 2019. Improving the Water Production of a Solar Still by Adding an Internal Condensation Chamber: A Theoretical Study. *Environmental Progress & Sustainable Energy*. 38 (5). DOI: 10.1002/ep.13198.

Mahbubul, I.M. Saidur, R. & Amalina, M.A. 2012. Latest developments on the viscosity of nanofluids. *International Journal of Heat and Mass Transfer*. 55: 874-885. DOI: 10.1016/j.ijheatmasstransfer.2011.10.021.

Mahbubul, I.M., Shahrul, I.M., Khaleduzzaman, S.S., Saidur, R., Amalina, M.A. & Turgut, A. 2015. Experimental investigation on effect of ultrasonication duration on colloidal dispersion and thermophysical properties of alumina–water nanofluid. *International Journal of Heat and Mass Transfer*. 88: 73-81. DOI: 10.1016/j.ijheatmasstransfer.2015.04.048.

Maheswari, K.S., Murugavel, K.K. & Esakkimuthu, G. 2015. Thermal desalination using diesel engine exhaust waste heat – An experimental analysis. *Desalination*. 358: 94-100. DOI: 10.1016/j.desal.2014.12.023.

Mahian, O., Kianifar, A., Heris, S.Z., Wen, D., Sahin, A.Z. & Wongwises, S. 2017. Nanofluids effects on the evaporation rate in a solar still equipped with a heat exchanger. *Nano Energy*. 36: 134-155. DOI: 10.1016/j.nanoen.2017.04.025.

Maor, T. & Appelbaum, J. 2012. View factors of photovoltaic collector systems. *Solar Energy*. 86 (6): 1701-1708. DOI: 10.1016/j.solener.2012.03.017.

Masoumi, N., Sohrabi, N. & Behzadmehr, A. 2009. A new model for calculating the effective viscosity of nanofluids. *Journal of Physics D: Applied Physics*. 42: 1-6. DOI: 10.1088/0022-3727/42/5/055501.

Matrawy, K.K., Alosaimy, A.S. & Mahrous, A.F. 2015. Modeling and experimental study of a corrugated wick type solar still: Comparative study with a simple basin type. *Energy Conversion and Management*. 105: 1261-1268. DOI: 10.1016/j.enconman.2015.09.006.

Mehta, A., Vyas, A., Bodar, N. & Lathiya, D. 2011. Design of Solar Distillation System. *International Journal of Advanced Science and Technology*. 29: 67-74.

Mishra, P.C., Mukherjee, S., Nayak, S.K. & Panda, A. 2014. A brief review on viscosity of nanofluids. *International Nano Letters*. 4: 109-120. DOI: 10.1007/s40089-014-0126-3.

Mohammed, K.A., Talib, A.R.A., Nuraini, A.A. & Ahmed, K.A. 2017. Review of forced convection nanofluids through corrugated facing step. *Renewable and Sustainable Energy Reviews*. 75: 234-241. DOI: 10.1016/j.rser.2016.10.067.

Mojarrad, M.S., Keshavarz, A., Ziabasharhagh, M. & Raznahan, M.M. 2014. Experimental investigation on heat transfer enhancement of alumina/ water and alumina/water–ethylene glycol nanofluids in thermally developing laminar flow. *Experimental Thermal and Fluid Science*. 53: 111-118. DOI: 10.1016/j.expthermflusci.2013.11.015.

Moore, H. 2012. MATLAB for Engineers. Rev. 3rd ed. United States of America: Pearson Education, Inc.

Morad, M.M, El-Maghawry, H.A.M. & Wasfy, K.I. 2015. Improving the double slope solar still performance by using flat-plate solar collector and cooling glass cover. *Desalination*. 373: 1-9. DOI: 10.1016/j.desal.2015.06.017.

Muftah, A.F., Alghoul, M.A., Fudholi, A., Abdul-Majeed, M.M. & Sopian, K. 2014. Factors affecting basin type solar still productivity: A detailed review. 32: 430-447. DOI: 10.1016/j.rser.2013.12.052.

Mukherjee, S. & Paria, S. 2013. Preparation and Stability of Nanofluids-A Review. *IOSR Journal of Mechanical and Civil Engineering*. 9 (2): 63-69.

Munyalo, J.M. & Zhang, X. 2018. Particle size effect on thermophysical properties of nanofluid and nanofluid based phase change materials: A review. *Journal of Molecular Liquids.* 265: 77-87. DOI: 10.1016/j.molliq.2018.05.129.

Murshed, S. & Estellé, P. 2017. A state of the art review on viscosity of nanofluids. *Renewable and Sustainable Energy Reviews.* 76: 1134-1152. DOI: 10.1016/j.rser.2017.03.113.

Murthy, J.Y. & Mathur, S.R. 1998. *Numerical Methods in Heat, Mass, and Momentum Transfer*. Available:

https://engineering.purdue.edu/~scalo/menu/teaching/me608/ME608_Notes_Murthy.pdf [2019, November 07].

Murugavel, K.K., Chockalingam, K.S.K. & Srithar, K. 2008. Progresses in improving the effectiveness of the single basin passive solar still. *Desalination*. 220: 677-686.

Nafey, A.S., Abdelkader, M., Abdelmotalip, A. & Mabrouk, A.A. 2000. Parameters affecting solar still productivity. *Energy Conversion & Management*. 41: 1797-1809. DOI: 10.1016/S0196-8904(99)00188-0.

Navale, V.J., Kumbhar, S.R. & Bhojawani, V.K. 2016. Experimental study of masonic solar still by using nanofluid. *International Engineering Research Journal*. 984-987. Available: http://www.ierjournal.org/pupload/mit/HP9-10%20ok.pdf [2017, May 23].

Nayi, K.H. & Modi, K.V. 2018. Pyramid solar still: A comprehensive review. *Renewable and Sustainable Energy Reviews*. 81: 136-148. DOI: 10.1016/j.rser.2017.07.004.

Nazari, S., Safarzadeh, H. & Bahiraei, M. 2019. Experimental and analytical investigations of productivity, energy and exergy efficiency of a single slope solar still enhanced with thermoelectric channel and nanofluid. *Renewable Energy*. 135: 729-744. DOI: 10.1016/j.renene.2018.12.059.

Nellis, G. & Klein, S. 2009. *Heat Transfer*. United States of America: Cambridge University Press.

Oatley-Radcliffe, D.L., Williams, S.R., Barrow, M.S. & Williams, P.M. 2014. Critical appraisal of current nanofiltration modelling strategies for seawater desalination and further insights on dielectric exclusion. *Desalination*. 343: 154-161. DOI: 10.1016/j.desal.2013.10.001.

Omara, Z.M., Kabeel, A.E. & Essa, F.A. 2015. Effect of using nanofluids and providing vacuum on the yield of corrugated wick solar still. *Energy Conversion and Management*. 103: 965-972. DOI: 10.1016/j.enconman.2015.07.035.

Omara, Z.M., Kabeel, A.E., Abdullah, A.S. & Essa, F.A. 2016. Experimental investigation of corrugated absorber solar still with wick and reflectors. *Desalination*. 381: 111-116. DOI: 10.1016/j.desal.2015.12.001.

Panchal, H. & Shah, P.K. 2011. Effect of Varying Glass cover thickness on Performance of Solar still: in a Winter Climate Conditions. *International Journal of Renewable Energy Research*. 1(4): 212-223.

Panchal, H. 2016. Performance Investigation on Variations of Glass Cover Thickness on Solar Still: Experimental and Theoretical Analysis. *Technology and Economics of Smart Grids and Sustainable Energy*. 1-7. DOI: 10.1007/s40866-016-0007-0.

Panchal, H., Patel, P., Patel, N. & Thakkar, H. 2017. Performance analysis of solar still with different energy-absorbing materials. International Journal of Ambient Energy. 38(3): 224-228. DOI: 10.1080/01430750.2015.1086683.

Panchal, H.N. & Patel, S. 2017. An extensive review on different design and climatic parameters to increase distillate output of solar still. *Renewable and Sustainable Energy Reviews*. 69: 750-758. DOI: 10.1016/j.rser.2016.09.001.

Panitapu, B., Koneru, V., Sagi, S.L.S. & Parik, A. 2014. Solar distillation using nano-material. *International Journal of Science, Engineering and Technology*. 3 (5): 583-587. Available: https://ijset.com/ijset/publication/v3s5/IJSET_2014_529.pdf [2017, May 23].

Park, C.D., Lim, B.J, Chung, K.Y., Lee, S.S. & Kim, Y.M. 2016. Experimental evaluation of hybrid solar still using waste heat. *Desalination*. 379: 1-9. DOI: 10.1016/j.desal.2015.10.004.

Park, C.D., Lim, B.J., Noh, Y.D., Lee, S.S. & Chung, K.Y. 2015. Parametric performance test of distiller utilizing solar and waste heat. *Desalination and Water Treatment*. 55 (12): 3303-3309.

Patel, H.E. & Sundararajan, T. 2010. An experimental investigation into the thermal conductivity enhancement in oxide and metallic nanofluids. Journal of Nanoparticle Research. 12 (3): 1015-1031. DOI: 10.1007/s11051-009-9658-2.

Paul, G., Chopkar, M., Manna, I. & Das, P.K. 2010. Techniques for measuring the thermal conductivity of nanofluids: A review. *Renewable and Sustainable Energy Reviews.* 14: 1913-1924. DOI: 10.1016/j.rser.2010.03.017.

Paulescu, M., Paulescu, E., Gravila, P. & Badescu, V. *Weather Modeling and Forecasting of PV Systems Operation*. 2012. London: Springer-Verlag.

Pavlidis, P. Using ANOVA for gene selection from microarraystudies of the nervous system. 2003. *Methods*. 31 (4): 282-289. DOI: 10.1016/S1046-2023(03)00157-9.

Pinto, R.V. & Fiorelli, F.A.S. 2016. Review of the mechanisms responsible for heat transfer enhancement using nanofluids. *Applied Thermal Engineering*. 108: 720-739. DOI: 10.1016/j.applthermaleng.2016.07.147.

Popiel, C.O. & Wojtkowiak, J. 1998. Simple Formulas for Thermophysical Properties of Liquid Water for Heat Transfer Calculations (from 0°C to 150°C). *Heat Transfer Engineering*. 19(3): 87-101. DOI: 10.1080/01457639808939929.

Popoola, O.M. & Burnier, C. 2014. Solar water heater contribution to energy savings in higher education institutions: Impact analysis. *Journal of Energy in Southern Africa*. 25 (1): 51-58.

Prakash, A., Satsangi, S., Mittal, S., Nigam, B., Mahto, P.K. & Swain, B.P. Investigation on Al_2O_3 Nanoparticles for Nanofluid Applications- A Review. 2018. *International Conference on Mechanical, Materials and Renewable Energy*. 377. DOI: 10.1088/1757-899X/377/1/012175.

Prakash, P. & Velmurugan, V. 2015. Parameters influencing the productivity of solar stills – A review. *Renewable and Sustainable Energy Reviews*. 49: 585-609. DOI: 10.1016/j.rser.2015.04.136.

Prasad, P.V.D., Gupta, A.V.S.S.K.S. & Deepak, K. 2015. Investigation of Trapezoidal-Cut Twisted Tape Insert in a Double Pipe U-Tube Heat Exchanger using Al_2O_3/Water Nanofluid. *Procedia Materials Science*. 10: 50-63. DOI: 10.1016/j.mspro.2015.06.025.

Pugsley, A., Zacharopoulos, A., Mondol, J.D. & Smyth, M. 2016. Global applicability of solar desalination. *Renewable Energy*. 88: 200-219. DOI: 10.1016/j.renene.2015.11.017.

Qasim, M., Darwish, N.A., Sarp, S. & Hilal, N. 2015. Water desalination by forward (direct) osmosis phenomenon: A comprehensive review. *Desalination*. 347: 47-69. DOI: 10.1016/j.desal.2015.07.016.

Rahbar, N. & Esfahani, J.A. 2012. Experimental study of a novel portable solar still by utilizing the heatpipe and thermoelectric module. *Desalination*. 284: 55-61. DOI: 10.1016/j.desal.2011.08.036.

Rajaseenivasan, T., Murugavel, K.K., Elango, T. & Hansen, R.S. 2013. A review of different methods to enhance the productivity of the multi-effect solar still. *Renewable and Sustainable Energy Reviews*. 17: 248-259. DOI: 10.1016/j.rser.2012.09.035.

Rajaseenivasan, T., Raja, P.N. & Srithar, K. 2014. An experimental investigation on a solar still with an integrated flat plate collector. *Desalination*. 347: 131-137. DOI: 10.1016/j.desal.2014.05.029.

Rajasekhar, G. & Eswaramoorthy, M. 2015. Performance evaluation on solar still integrated with nano-composite phase change materials. *Applied Solar Energy*. 51 (1): 15-21. DOI: 10.3103/S0003701X15010119.

Ranjan, K.R. & Kaushik, S.C. 2013. Energy, exergy and thermo-economic analysis of solar distillation systems: A review. *Renewable and Sustainable Energy Reviews*. 27: 709-723. DOI: 10.1016/j.rser.2013.07.025

Rao, Y.V.C. 2001. *Heat Transfer*. India: University Press Limited.

Rashidi, S., Bovand, M., Rahbar, N. & Esfahani, J.A. 2018. Steps optimization and productivity enhancement in a nanofluid cascade solar still. *Renewable Energy*. 118: 536-545. DOI: 10.1016/j.renene.2017.11.048.

Rathakrishnan, E. 2006. *Fundamentals of Engineering Thermodynamics*. 2nd ed. New Delhi, India: Prentice Hall.

Reif, J.H. & Alhalabi, W. 2015. Solar-thermal powered desalination: Its significant challenges and potential. *Renewable and Sustainable Energy Reviews*. 48: 152-165. DOI: 10.1016/j.rser.2015.03.065.

Reuters. 2019. *UPDATE 1-South African carbon tax finally becomes law*. Available: https://af.reuters.com/article/southAfricaNews/idAFL8N2320B8 [16 August 2019].

Riahi, A., Yusof, K.W., Singh, B.S.M., Olisa, E., Sapari, N. & Isa, M.H. 2015. The performance investigation of triangular solar stills having different heat storage materials. *International Journal of Energy and Environmental Engineering*. 6: 385-391. DOI: 10.1007/s40095-015-0185-x.

Robert, R.A., Kaithari, D.K., Mirza, M.M. & Bhambare, P.S. 2018. Influence of nano Al_2O_3 to improve the yield of double slope solar still. *International Journal of Students' Research in Technology & Management.* 6 (3): 1-8. DOI: 10.18510/ijsrtm.2018.631.

Rubio, E., Porta, M.A. & Fernández, J.L. 2000. Cavity geometry influence on mass flow rate for single and double slope solar stills. *Applied Thermal Engineering*. 20: 1105-1111.

Sahota, L. & Tiwari, G.N. 2016a. Effect of nanofluids on the performance of passive double slope solar still: A comparative study using characteristic curve. *Desalination*. 388: 9-21. DOI: 10.1016/j.desal.2016.02.039.

Sahota, L. & Tiwari, G.N. 2016b. Effect of Al_2O_3 nanoparticles on the performance of passive double slope solar still. *Solar Energy*. 130: 260-272. DOI: 10.1016/j.solener.2016.02.018.

Sahota, L., Shyam. & Tiwari, G.N. 2017a. Energy matrices, enviroeconomic and exergoeconomic analysis of passive double slope solar still with water based nanofluids. *Desalination*. 409: 66-79. DOI: 10.1016/j.desal.2017.01.012.

Sahota, L., Shyam. & Tiwari, G.N. 2017b. Analytical characteristic equation of nanofluid loaded active double slope solar still coupled with helically coiled heat exchanger. *Energy Conversion and Management*. 135: 308-326. DOI: 10.1016/j.enconman.2016.12.078.

Said, Z., Sajid, M.H., Alim, M.A., Saidur, R. & Rahim, N.A. 2013. Experimental investigation of the thermophysical properties of Al_2O_3-nanofluid and its effect on a flat plate solar collector. *International Communications in Heat and Mass Transfer*. 48: 99-107. DOI: 10.1016/j.icheatmasstransfer.2013.09.005.

Sampathkumar, K., Arjunan, T.V., Pitchandi, P. & Senthilkumar, P. 2010. Active solar distillation – A detailed review. *Renewable and Sustainable Energy Reviews*. 14 (6): 1503-1526. DOI: 10.1016/j.rser.2010.01.023

Sanlam, 2016. SANL*AM 2015 CARBON FOOTPRINT REPORT*. Available: http://sanlam.investoreports.com/sdr2015/pdf/Sanlam%202015%20Carbon%20Footprint%20Report.pdf [19 August 2019].

Sathyamurthy, R., Samuel, D.G.H., Nagarajan, P.K. & El-Agouz, S.A. 2015. A Review of Different Solar Still for Augmenting Fresh Water Yield. *Journal of Environmental Science and Technology*. 8 (6): 244-265. DOI: 10.3923/jest.2015.244.265.

Sekhar, Y.R. & Sharma, K.V. 2015. Study of viscosity and specific heat capacity characteristics of water-based Al_2O_3 nanofluids at low particle concentrations. *Journal of Experimental Nanoscience.* 10 (2): 86-102. DOI: 10.1080/17458080.2013.796595.

Sellami, M.H., Belkis, T., Aliouar, M.L., Meddour, S.D., Bouguettaia, H. & Loudiyi, K. 2017. Improvement of solar still performance by covering absorber with blackened layers of sponge. *Groundwater for Sustainable Development*. 5: 111-117. DOI: 10.1016/j.gsd.2017.05.004.

Sezer, N., Atieh, M.A. & Koç, M. 2019. A comprehensive review on synthesis, stability, thermophysical properties, and characterization of nanofluids. *Powder Technology*. 344: 404-431. DOI: 10.1016/j.powtec.2018.12.016.

Shankar, P., Sharma, R., Gupta, B. & Parmar, H. 2015. Effect of colour and Al_2O_3 nano particles on the efficiency of the solar still. *SSRG International Journal of Thermal Engineering*. 1 (5): 1-6. Available: http://www.internationaljournalssrg.org/IJTE/2015/Volume1-Issue5/IJTE-V1I5P101.pdf [2017, May 23].

Sharma, K.V., Sarma, P.K., Azmi, W.H., Mamat, R. & Kadirgama, K. 2012. Correlations to predict friction and forced convection heat transfer coefficients of water based nanofluids for turbulent flow in a tube. *International Journal of Microscale and Nanoscale Thermal and Fluid Transport Phenomena*. 3(4). Novia Science Publishers, Inc.

Sharma, K.V., Suleiman, A., Suhaimi, H.J., Hassan, B. & Hegde, G. 2017. Considerations on the Thermophysical Properties of Nanofluids. *Engineering Applications of Nanotechnology*. DOI: 10.1007/978-3-319-29761-3_2.

Sharon, H. & Reddy, K.S. 2015. A review of solar energy driven desalination technologies. *Renewable and Sustainable Energy Reviews*. 41: 1080–1118. DOI: 10.1016/j.rser.2014.09.002.

Sharshir, S.W., Elsheikh, A.H., Peng, G., Yang, N., El-Samadony, M.O.A. & Kabeel, A.E. 2017a. Thermal performance and exergy analysis of solar stills – A review. *Renewable and Sustainable Energy Reviews*. 73: 521-544. DOI: 10.1016/j.rser.2017.01.156.

Sharshir, S.W., Peng, G., Wu, L., Essa, F.A., Kabeel, A.E. & Yang, N. 2017b. The effects of flake graphite nanoparticles, phase change material, and film cooling on the solar still performance. *Applied Energy*. 191: 358-366. DOI: 10.1016/j.apenergy.2017.01.067.

Sharshir, S.W., Yang, N., Peng, G. & Kabeel, A.E. 2016. Factors affecting solar stills productivity and improvement techniques: A detailed review. *Applied Thermal Engineering*. 100: 267-284. DOI: 10.1016/j.applthermaleng.2015.11.041.

Shukla, K.N., Rangnekar, S. & Sudhakar, K. 2015. Comparative study of isotropic and anisotropic sky models to estimate solar radiation incident on tilted surface: A case study for Bhopal, India. *Energy Reports*. 1: 96-103. DOI: 10.1016/j.egyr.2015.03.003.

Shukla, S.K. & Sorayan, V.P.S. 2005. Thermal modeling of solar stills: an experimental validation. *Renewable Energy*. 30: 683-699. DOI: 10.1016/j.renene.2004.03.009.

Sidik, N.A.C., Mohammed, H.A., Alawi, O.A. & Samion, S. 2014. A review on preparation methods and challenges of nanofluids. *International Communications in Heat and Mass Transfer*. 54: 115-125. DOI: 10.1016/j.icheatmasstransfer.2014.03.002.

Singh, A.K.R. & Singh, H.K. 2015. Performance evaluation of solar still with and without nanofluid. *International Journal of Science, Engineering and Technology*. 3 (4): 1093-1101. DOI: 10.2348/ijset07151093.

Singh, D.B., Tiwari, G.N., Al-Helal, I.M., Dwivedi, V.K. & Yadav. J.K. 2016. Effect of energy matrices on life cost analysis of passive solar stills. *Solar Energy*. 134: 9-22. DOI: 10.1016/j.solener.2016.04.039.

Singh, D.B., Yadav, J.K., Dwivedi, V.K., Kumar, S., Tiwari, G.N. & Al-Helal, I.M. 2016. Experimental studies of active solar still integrated with two hybrid PVT collectors. *Solar Energy*. 130: 207–223. DOI: 10.1016/j.solener.2016.02.024.

Singh, H.N. & Tiwari, G.N. 2004. Monthly performance of passive and active solar stills for different Indian climatic conditions. *Desalination*. 168: 145-150. DOI: 10.1016/j. desa1.2004.06.180.

Singh, P., Singh, P., Singh, J., Singh, R.I & Kundu, K. 2012. Performance Evaluation of Low Inertia Multi-Stage Solar Still. *Proceedings of the International MultiConference of Engineers and Computer Scientists*. 14-16 March 2012. Hong-Kong.

Singh, R.V., Kumar, S., Hasan, M.M., Khan, M.E. & Tiwari, G.N. 2013. Performance of a solar still integrated with evacuated tube collector in natural mode. *Desalination*. 318. 25-33. DOI: 10.1016/j.desal.2013.03.012.

Sivakumar, V. & Sundaram, E.G. 2013. Improvement techniques of solar still efficiency: A review. *Renewable and Sustainable Energy Reviews*. 28: 246-264. DOI: 10.1016/j.desal.2015.01.004.

Skiborowski, M., Mhamdi, A., Kraemer, K. & Marquardt, W. 2012. Model-based structural optimization of seawater desalination plants. *Desalination*. 292: 30-44. DOI: 10.1016/j.desal.2012.02.007.

Sonmez, A., Budakci, M. & Bayram, M. 2009. Effect of wood moisture content on adhesion of varnish coatings. *Scientific Research and Essay*. 4(12): 1432-1437.

Srithar, K., Rajaseenivasan, T., Karthik, N., Periyannan, M. & Gowtham, M. 2016. Stand alone triple basin solar desalination system with cover cooling and parabolic dish concentrator. *Renewable Energy*. 90: 157–165. DOI: 10.1016/j.renene.2015.12.063.

Tabrizi, F.F. & Sharak, A.Z. 2010. Experimental study of an integrated basin solar still with a sandy heat reservoir. *Desalination*. 253: 195-199. DOI: 10.1016/j.desal.2009.10.003.

Tabrizi, F.F., Dashtban, M. & Moghaddam, H. 2010. Experimental investigation of a weir-type cascade solar still with built-in latent heat thermal energy storage system. *Desalination*. 260(1-3): 248–253. DOI: 10.1016/j.desal.2010.03.033.

Tanaka, H. 2009. Experimental study of a basin type solar still with internal and external reflectors in winter. *Desalination*. 249 (1): 130–134. DOI: 10.1016/j.desal.2009.02.057.

Tay, J.H., Low, S.C. & Jeyaseelan, S. 1996. Vacuum desalination for water purification using waste heat. *Desalination*. 106 (1-3): 131-135. DOI: 10.1016/S0011-9164(96)00104-X.

Teng, T.P., Hung, Y.H., Teng, T.C., Mo, H.E. Hsu, H.G. 2010. The effect of alumina/water nanofluid particle size on thermal conductivity. *Applied Thermal Engineering*. 30 (14-15): 2213-2218. DOI: 10.1016/j.applthermaleng.2010.05.036.

Tenthani, C., Madhlopa, A. & Kimambo, C.Z. 2012. Improved Solar Still for Water Purification. *Journal of Sustainable Energy & Environment*. 3: 111-113.

Tiwari, A.K. & Tiwari, G.N. 2007. Thermal modeling based on solar fraction and experimental study of the annual and seasonal performance of a single slope passive solar still: The effect of water depths. *Desalination*. 207 (1-3): 184-204. DOI: 10.1016/j.desal.2006.07.011.

Tiwari, G.N. & Dubey, S. 2010. *Fundamentals of Photovoltaic Modules and their Applications*. Royal Society of Chemistry.

Tripathi, R. & Tiwari, G.N. 2004. Performance evaluation of a solar still by using the concept of solar fractionation. *Desalination*. 169 (1): 69-80. DOI: 10.1016/j.desal.2004.08.008.

Tripathi, R. & Tiwari, G.N. 2005. Effect of water depth on internal heat and mass transfer for active solar distillation. *Desalination*. 173: 187-200. DOI: 10.1016/j.desal.2004.08.03.

Tsilingiris, P.T. 2007. The influence of binary mixture thermophysical properties in the analysis of heat and mass transfer processes in solar distillation systems. *Solar Energy*. 81(12): 1482-1491. DOI: 10.1016/j.solener.2007.02.005.

Tsilingiris, P.T. 2008. Thermophysical and transport properties of humid air at temperature range between 0 and 100°C. *Energy Conversion & Management*. 49: 1098-1110. DOI: 10.1016/j.enconman.2007.09.015.

Tsilingiris, P.T. 2009. Analysis of the heat and mass transfer processes in solar stills – The validation of a model. *Solar Energy*. 83 (3): 420–431. DOI: 10.1016/j.solener.2008.09.007.

Tuomiranta, A. & Ghedira, H. 2015. *Evaluation of Decomposition and Transposition Models for Irradiance Data Conversion under a Hot Desert Climate*.

UNICEF. 2009. *Status and trends – Drinking water and sanitation in East Asia and the Pacific*. Available: https://www.unicef.org/eapro/staus_and_trends_wes_publication.pdf [2017, March 02].

United Nations Children's Fund and World Health Organisation. 2015. *Progress on Sanitation and Drinking Water. 2015 Update and MDG Assessment*. Available: https://www.unicef.org/publications/index_82419.html [2016, February 2016].

United Nations. 2012. Report of the Human Rights Council. Available: http://www.ohchr.org/Documents/HRBodies/HRCouncil/A-67-53-Add-1_en.pdf [2017, March 02].

Upstill, G. & Hall, P. 2018. Estimating the learning rate of a technology with multiple variants: The case of carbon storage. *Energy Policy*. 121: 498–505. DOI: 10.1016/j.enpol.2018.05.017.

Velmurugan, V. & Srithar, K. 2011. Performance analysis of solar stills based on various factors affecting the productivity—A review. *Renewable and Sustainable Energy Reviews*. 15: 1294-1304. DOI: 10.1016/j.rser.2010.10.012.

Velmurugan, V., Pandiarajan, S., Guruparan, P., Subramanian, L.H., Prabaharan, C.D. & Srithar, K. 2009. Integrated performance of stepped and single basin solar stills with mini solar pond. *Desalination*. 249 (3): 902-909. DOI: 10.1016/j.desal.2009.06.070.

Welty, J.R., Rorrer, G.L. & Foster, D.G. 2015. *Fundamentals of Momentum, Heat and Mass Transfer*. Rev. 6th ed. Asia: John Wiley & Sons, Inc.

World Bank. 2016. *Renewable internal fresh water resources per capita (cubic meters).* Available: http://data.worldbank.org/indicator/ER.H2O.INTR.PC [2017, March 01].

World Health Organisation. 2017. Water sanitation hygiene. Available: http://www.who.int/water_sanitation_health/emergencies/qa/emergencies_qa5/en/ [2017, March 08].

World Health Organisation. 2019. Drinking water. Available: https://www.who.int/news-room/fact-sheets/detail/drinking-water [2019, October 15].

Xiao, G., Wang, X., Ni, M., Fei, W., Zhu, W., Luo, A. & Cen, K. 2013. A review on solar stills for brine desalination. *Applied Energy*. 103: 642-652. DOI: 10.1016/j.apenergy.2012.10.029.

Xuan, Y. & Roetzel, W. 2000. Conceptions for heat transfer correlation of nanofluids. *International Journal of Heat and Mass Transfer*. 43 (19): 3701-3707. DOI: 10.1016/S0017-9310(99)00369-5.

Yadav, S. & Sudhakar, K. 2015. Different domestic designs of solar stills: A review. *Renewable and Sustainable Energy Reviews*. 47: 718-731. DOI: 10.1016/j.rser.2015.03.064.

Yang, L., Xu, J., Du, K. & Zhang, X. 2017. Recent developments on viscosity and thermal conductivity of nanofluids. *Powder Technology*. 317: 348-369. DOI: 10.1016/j.powtec.2017.04.061.

Younos, T. 2005. Environmental Issues of Desalination. *Journal of Contemporary Water Research & Education*. 132: 11-18. DOI: 10.1111/j.1936-704X.2005.mp132001003.x.

Youssef, P.G., Al-Dadah, R.K. & Mahmoud, S.M. 2014. Comparative Analysis of Desalination Technologies. *Energy Procedia*. 61: 2604-2607. DOI: 10.1016/j.egypro.2014.12.258.

Yu, W. & Xie, H. 2012. A Review on Nanofluids: Preparation, Stability Mechanisms, and Applications. *Journal of Nanomaterials*. 1-17. DOI: 10.1155/2012/435873.

Zaiontz, C. 2019. *Basic Concepts for ANOVA*. Available: http://www.real-statistics.com/one-way-analysis-of-variance-anova/basic-concepts-anova/ [2019, July 29].

Zhou, D., Zhu, L., Fu, Y., Zhu, M. & Xue, L. 2015. Development of lower cost seawater desalination processes using nanofiltration technologies — A review. *Desalination*. 376: 109-116. DOI: 10.1016/j.desal.2015.08.020.

Zohuri, B.2018. Chapter 5 – First Law of Thermodynamics. *Physics of Cryogenics*. 119-163. DOI: 10.1016/B978-0-12-814519-7.00005-7.

Zurigat, Y.H. & Abu-Arabi, M.K. 2004. Modelling and performance analysis of a regenerative solar desalination unit. *Applied Thermal Engineering*. 24 (7): 1061-1072. DOI: 10.1016/j.applthermaleng.2003.11.010.

APPENDICES

Appendix A

Calculation of the view factor from the fluid to the glass cover

The view factor between the fluid inside the basin of the solar still and each of the 4 inner walls of the solar still was computed using the following procedures. The correlation for perpendicular rectangles with a common edge was used, obtained from Bergman et al. (2011), given in Equation (A.1).

$$
\begin{aligned}
&V_{f-wall} \\
&= \frac{1}{\pi W}\left(W\tan^{-1}\left(\frac{1}{W}\right) + H_1 \tan^{-1}\left(\frac{1}{H}\right)\right. \\
&- (H^2 + W^2)^{\frac{1}{2}} \tan^{-1}\left(\frac{1}{(H^2 + W^2)^{\frac{1}{2}}}\right) \\
&\left. + \frac{1}{4}\ln\left\{\frac{(1+W^2)(1+H^2)}{(1+W^2+H^2)}\left[\frac{W^2(1+W^2+H^2)}{(1+W^2)(W^2+H^2)}\right]^{W^2}\left[\frac{H^2(1+H^2+W^2)}{(1+H^2)(H^2+W^2)}\right]^{H^2}\right\}\right)
\end{aligned}
\tag{A.1}
$$

View factor between fluid and back wall of the solar still

Figure A.1 represents the configuration of the back wall of the solar still and the fluid inside the basin. A fraction of the radiative heat from the fluid reaches the back wall of the solar still ($V_{f\text{-}bw}$) and this was calculated using Equation (A.1), where the constants H and W were determined using Equations (A.2) and (A.3).

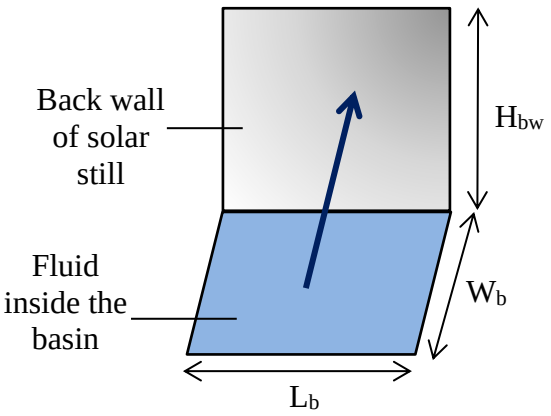

Figure A.1: View factor for the exchange of radiative heat between the fluid and the back wall of the solar still.

$$H = \frac{H_{bw}}{L_b} \tag{A.2}$$

$$W = \frac{W_b}{L_b} \tag{A.3}$$

View factor between fluid and front wall of solar still

The configuration for the fluid and the front wall of the solar still is given in Figure A.2, with the constants H and W given in Equations (A.4) and (A.5).

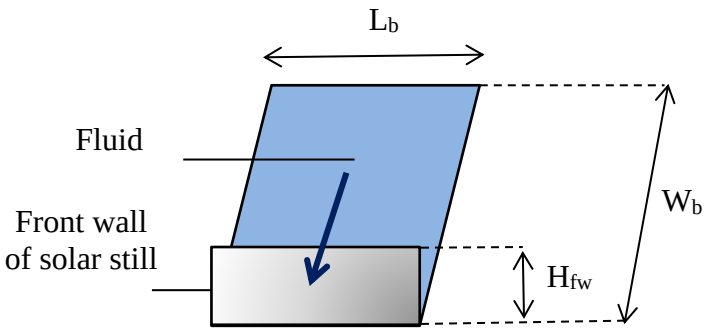

Figure A.2: View factor for the exchange of radiative heat between the fluid and the front wall of the solar still.

$$H = \frac{H_{fw}}{L_b} \quad \text{(A.4)}$$

$$W = \frac{W_b}{L_b} \quad \text{(A.5)}$$

View factor between fluid and west wall of solar still

Figure A.3 gives the configuration for the fluid and the west wall of the solar still. The parameters H and W were computed using Equations (A.6) and (A.7). The height of the west wall was calculated using Equation (A.8), obtained from Madhlopa (2014).

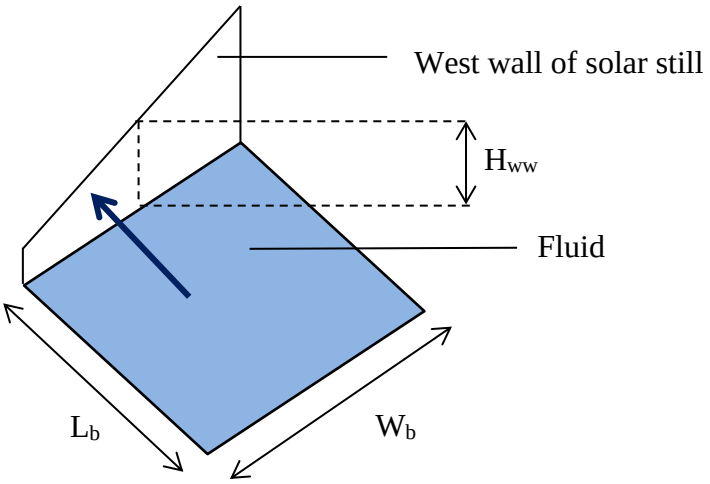

Figure A.3: View factor for the exchange of radiative heat between the fluid and the west wall of the solar still.

$$H = \frac{H_{ww}}{W_b} \quad \text{(A.6)}$$

$$W = \frac{L_b}{W_b} \quad \text{(A.7)}$$

$$H_{ww} = \frac{1}{2}\left(H_{bw} + H_{fw}\right) \quad \text{(A.8)}$$

Since the west wall and the east wall of the solar still are identical, the view factor between the fluid and the east wall is equal to the view factor between the fluid and the west wall.

$$V_{f-ew} = V_{f-ww} \tag{A.9}$$

View factor between fluid and glass cover

Since the sum of view factors is equal to 1 (Bergman et al., 2011), the view factor between the fluid and the glass cover was computed by subtracting the sum of the view factors between the fluid and the walls from 1, as given in Equations (A.10) and (A.11).

$$\sum_{j=1}^{N} V_{ij} = 1 \tag{A.10}$$

$$V_{f-g} = 1 - (V_{f-bw} + V_{f-fw} + V_{f-ww} + V_{f-ew}) \tag{A.11}$$

Calculation of the view factors between the inner walls of the solar still

The view factor from the back wall to the front wall ($V_{bw\text{-}fw}$), the view factor from the back wall to the east wall ($V_{bw\text{-}ew}$) and the view factor from the back wall to the west wall ($V_{bw\text{-}ww}$) were computed using correlations in Bergman et al. (2011). Figure A.4 shows the front, back, east and west walls of the solar still.

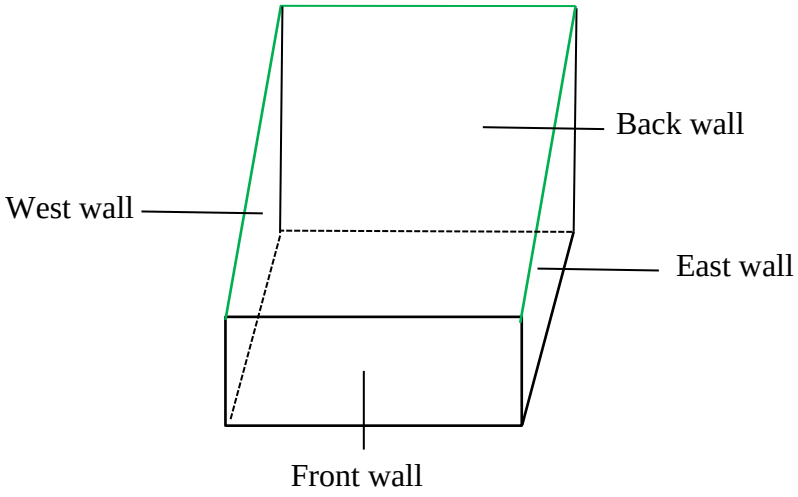

Figure A.4: Front, back, east and west walls of solar still.

View factor from back wall to front wall of solar still

The back wall and the front wall of the solar still are parallel to each other. The correlation for aligned parallel rectangles from Bergman et al. (2011), given in Equation (A.12) was used in computing the view factor from the back wall to the front wall. In Equation (A.12), V_{ij} represents the view factor from surface i to surface j; X represents the ratio of the length of surface i to the distance between surface i and surface j and Y represents the ratio of the width of surface i to the distance between surface i and surface j. However, it is to be noted that since the front wall was shorter than the back wall, an imaginary surface was added to the front wall; and the back wall was split into two surfaces, as shown in Figure A.5 in order to be able to use Equation (A.12).

$$V_{ij} = \frac{2}{\pi XY}\left\{\ln\left[\frac{(1+X^2)(1+Y^2)}{1+X^2+Y^2}\right]^{0.5} + X\,(1+Y^2)^{\frac{1}{2}}\,\tan^{-1}\frac{X}{(1+Y^2)^{0.5}} + Y\,(1+X^2)^{\frac{1}{2}}\,\tan^{-1}\frac{Y}{(1+X^2)^{0.5}} - X\tan^{-1}X - Y\tan^{-1}Y\right\} \quad \text{(A.12)}$$

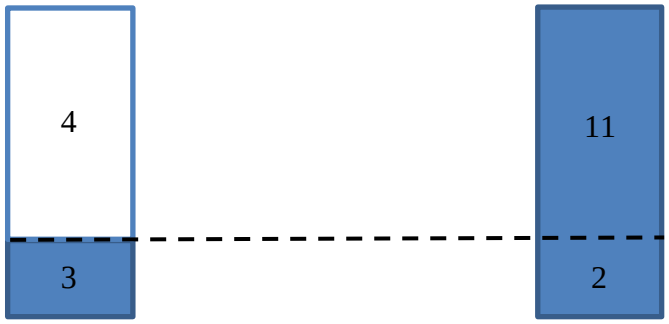

Figure A.5: Configuration of back and front walls of solar still for the computation of the view factor from the back wall to the front wall.

The view factor from the sum of surfaces 1 and 2 to the sum of surfaces 3 and 4 ($V_{12\text{-}34}$) was first computed using Equation (A.12) since the two surfaces are aligned parallel rectangles. Similarly, the view factor from surface 2 to surface 3 ($V_{2\text{-}3}$) was computed, as well as the view factor from surface 1 to surface 4 ($V_{1\text{-}4}$). Moreover, another important equation obtained from Bergman et al. (2011), as given in Equation (A.13), was used in computing the view factor from the back wall to the front wall. In Equation (A.13), j represents the originating surface which is made up of n components and A represents the area. By applying Equation (A.13), the view factor from the sum of surfaces 1 and 2 to the sum of surfaces 3 and 4 was expressed as given in Equation (A.14).

$$V_{(j)i} = \frac{\sum_{k=1}^{n} A_k V_{ki}}{\sum_{k=1}^{n} A_k} \tag{A.13}$$

$$V_{12-34} = V_{12-3} + V_{12-4} = \frac{(A_1 V_{1-3} + A_2 V_{2-3})}{A_1 + A_2} + \frac{(A_1 V_{1-4} + A_2 V_{2-4})}{A_1 + A_2} \tag{A.14}$$

By using Equation (A.14) and the reciprocity relation as expressed earlier in Equation (3.65), the view factor from the sum of surfaces 1 and 2 to the sum of surfaces 3 and 4 was reduced to Equation (A.15).

$$V_{12-34} = \frac{A_3 V_{3-1} + A_2 V_{2-3}}{A_1 + A_2} + \frac{A_1 V_{1-4} + A_2 V_{3-1}}{A_1 + A_2} \tag{A.15}$$

In Equation (A.15), only the view factor from surface 3 to surface 1 is unknown as $V_{12\text{-}34}$, $V_{2\text{-}3}$ and $V_{1\text{-}4}$ were all computed using Equation (A.12). Thus, the view factor from surface 3 to surface 1 was made the subject of formula to solve for $V_{3\text{-}1}$ and using the reciprocity relation, $V_{1\text{-}3}$ was computed as expressed by Equation (A.16). The view factor from the back wall to the front wall ($V_{bw\text{-}fw} = V_{12\text{-}3}$) was then calculated using Equation (A.17).

$$V_{1-3} = \frac{A_3 V_{3-1}}{A_1} \tag{A.16}$$

$$V_{bw-fw} = V_{12-3} = \frac{A_1 V_{1-3} + A_2 V_{2-3}}{A_1 + A_2} \tag{A.17}$$

View factor from back wall to west wall and view factor from back wall to east wall of solar still

The same procedures as above were followed in order to obtain the view factor from the back wall to the west wall of the solar still. However, in this case, the correlation for perpendicular rectangles with a common edge was used, as given in Equation (A.1). Since the height of the west wall was assumed to be the average height of the front and the back walls, as given in Equation (A.8), the height of the west wall was smaller than that of the back wall. Thus, in order to use the correlation for perpendicular rectangles with a common edge, it was important to split the back wall into two surfaces and to add an imaginary surface to the west wall in order to have a common edge.

By using Equations (A.13) to (A.17), the view factor from the back wall to the west wall was computed. Additionally, since the east and west walls are identical, the view factor from the back wall to the east wall was equal to the view factor from the back wall to the west wall, as given in Equation (A.18).

$$V_{bw-ew} = V_{bw-ww} \tag{A.18}$$

Appendix B

All the general constants needed in solving the mathematical models were written first in the MATLAB code.

```
%% Constants
%
Gsc=1367; % Solar constant (w/m2)
long_s=30; % standard meridian for local time zone (deg)
%long=18.4612; % longitude of UCT (deg)
%phi=-33.9577; % latitude of UCT (deg)
long=18.8602; % longitude of Stellenbosch (deg)
phi=-33.9321; % latitude of Stellenbosch (deg)
gamma=180; % Surface azimuth angle (deg)
sigma=5.67*10^(-8); % Stefan-Boltzmann constant
g=9.81; % acc due to gravity (m/s2)
x=pi/180; % Conversion factor from degrees to radians
beta=34; % Angle of inclination of glass cover (deg)
P0=101325; % Atmospheric Pressure in Pa
Ma=28.97; % Molecular weight of air, in kg/kmol
Mv=18.02; % Molecular weight of water vapour, in kg/kmol
Ra=(0.287*1000); % Gas constant for air, J/(kg.K)
Rv=(0.4615*1000); % Gas constant for water, J/(kg.K)
rho_gr=0.2; % Ground Reflectance
rho_iw=0.62; % Reflectance of inner wall
%
```

The various design parameters were then written for the base fluid, glass cover, basin liner, insulation and nanoparticles, in a similar format as given above for the constants. The different view factors were then calculated. The section below gives a sample calculation for computing one of the view factors. The view factor between the back wall to the front wall of the solar still was computed as follows:

```
%% View factor V(12)_(34)whole part of back wall to whole part of front wall + imaginary surface (total height = same as back wall)(2 parallel equal rectangles)
```

```
X1=(H1+H2)/Lb; Y1=Width/Lb;
V12_34a=2/(pi*X1*Y1); V12_34b=log(((1+X1^2)*(1+Y1^2)/(1+X1^2+Y1^2))^0.5);
V12_34c=X1*((1+Y1^2)^0.5)*atan(X1/((1+Y1^2)^0.5));
V12_34d=Y1*((1+X1^2)^0.5)*atan(Y1/((1+X1^2)^0.5));
V12_34e=X1*atan(X1); V12_34f=Y1*atan(Y1);
V12_34=V12_34a*(V12_34b+V12_34c+V12_34d-V12_34e-V12_34f);
%% View factor V2_3 (small part of back wall to small equal part of front wall)
X2=H2/Lb; Y2=Width/Lb;
V2_3a=2/(pi*X2*Y2); V2_3b=log(((1+X2^2)*(1+Y2^2)/(1+X2^2+Y2^2))^0.5);
V2_3c=X2*((1+Y2^2)^0.5)*atan(X2/((1+Y2^2)^0.5));
V2_3d=Y2*((1+X2^2)^0.5)*atan(Y2/((1+X2^2)^0.5));
V2_3e=X2*atan(X2); V2_3f=Y2*atan(Y2);
V2_3=V2_3a*(V2_3b+V2_3c+V2_3d-V2_3e-V2_3f);
%% View factor V1_4 (bigger part of back wall to bigger equal part of imaginary
front wall)
X3=H1/Lb;Y3=Width/Lb;
V1_4a=2/(pi*X3*Y3);V1_4b=log(((1+X3^2)*(1+Y3^2)/(1+X3^2+Y3^2))^0.5);
V1_4c=X3*((1+Y3^2)^0.5)*atan(X3/((1+Y3^2)^0.5));
V1_4d=Y3*((1+X3^2)^0.5)*atan(Y3/((1+X3^2)^0.5));
V1_4e=X3*atan(X3); V1_4f=Y3*atan(Y3);
V1_4=V1_4a*(V1_4b+V1_4c+V1_4d-V1_4e-V1_4f);
%%
V3_1=((V12_34*(A1+A2))-(A2*V2_3)-(A1*V1_4))/(A3+A2);
V1_3=(A3*V3_1)/A1;
% View factor from back wall to front wall
V12_3=((A1*V1_3)+(A2*V2_3))/(A1+A2);
```

The estimated temperatures were initialised, where *Data_stellenbosch* was the m-file containing the hourly climatic data from Stellenbosch. The initial mass of water was also 0. The symbols h0 and h represent the duration over which the simulations were carried out.

```
m_water0=0;
% Initial temperatures in K
Tg0=Data_stellenbosch(h0,5)+273.15;
```

```
Tf0=Tg0+0.0001;
Tbl0=Tg0+0.01;
tolerance=1;
```

The main *for loop* was then written, containing all the equations needed for calculating the various Earth-Sun angles, effective global radiation inside the solar still, thermophysical properties of the base fluid, nanofluid, heat transfer coefficients and the temperature equations. Once the solution converged, the mass of the distillate was computed.

```
for i=h0:h
    timecol=Data_stellenbosch(:,2);
    timetrans_all=timecol';time=timetrans_all(:,i);
    ncol=Data_stellenbosch(:,1);ntrans=ncol'; n=ntrans(:,i);% Day of the year
    B=2*pi*(n-1)/365; % radians
    E_time=229.2*(0.000075+0.001868*cos(B)-0.032077*sin(B)-0.014615*cos(2*B)-
0.04089*sin(2*B))/60;% Equation of time, in hours (Duffie, 2013:11)
    delta=0.006918-0.399912*cos(B)+0.070257*sin(B)-
0.006758*cos(2*B)+0.000907*sin(2*B)-0.002697*cos(3*B)+0.00148*sin(3*B);%
Declination angle, radians (Duffie, 2013:14)
    t_solar=time+E_time+((4*x*((long_s)-(long)))/60); % solar time, hours
    omega_1=15*x*(t_solar-12); % initial hour angle in radians
    omega_2=omega_1+(x*15); % final hour angle in radians
    omega=(omega_1+omega_2)/2; % midpoint of hour angle in radians
    omega_ss=acos(-tan(x*phi)*tan(delta));% sunset hour angle in rad
    omega_sr=-omega_ss; % sunrise hour angle
    theta_z=acos(((sin(x*phi)*sin(delta))+(cos(x*phi)*cos(delta)*cos(omega))));     %
Zenith angle in rad
    theta_1=acos((sin(delta)*sin(phi*x)*cos(beta*x))-
(sin(delta)*cos(phi*x)*sin(beta*x)*cos(gamma*x))+(cos(delta)*cos(phi*x)*cos(beta
*x)*cos(omega))+(cos(delta)*sin(phi*x)*sin(beta*x)*cos(gamma*x)*cos(omega))+(
cos(delta)*sin(beta*x)*sin(gamma*x)*sin(omega))); % angle of incidence in radians
    if omega >=0
       gamma_s=abs(acos((((cos(theta_z))*(sin(phi*x)))-
sin(delta))/((sin(theta_z))*(cos(phi*x)))));% solar azimuth angle (rad)
```

```
    else
        gamma_s=-abs(acos((((cos(theta_z))*(sin(phi*x)))-
sin(delta))/((sin(theta_z))*(cos(phi*x)))));
    end
    alpha_solar=(90*x)-theta_z ; % Solar altitude angle (rad)

    if abs(omega)< omega_ss-5*x && abs(gamma_s)> (90*x)
        Abw_p=(((Lb*Hbw)*cos(gamma_s-(gamma*x)))/tan(alpha_solar)); %
Projected area of back wall
    else
        Abw_p=0;
    end

    if abs(omega)< omega_ss-5*x && abs(gamma_s)> (90*x)
        Af_di=Lb*((Wb-((Hfw*cos(gamma_s-(gamma*x)))/tan(alpha_solar)))); % Area
of bf direcly receiving beam radiation (Madhlopa, 70)
    else
        Af_di=Lb*((Wb-((Hbw*cos(gamma_s-(gamma*x)))/tan(alpha_solar))));
    end

    Igcol=Data_stellenbosch(:,3); Igtrans=Igcol'; % global solar radiation on
horizontal surface
    Idcol=Data_stellenbosch(:,4); Idtrans=Idcol'; % diffuse radiation on horizontal
surface
    if abs(omega)< omega_ss-5*x
        Ig_h=Igtrans(:,i);
        Id_h=Idtrans(:,i);
    else
        Ig_h=0;Id_h=0;
    end

    Ib_h=Ig_h-Id_h;
```

```
Ib_eff=((Af_di+(rho_iw*Vbw_f*Abw_p))*Ib_h)/Af; % Effective beam radiation inside solar still
Qd_iw=((Abw*Vbw_f*Vbw_sky))*Id_h; % diffuse solar energy received by water

Id_eff=((Af*Vbf_sky*Id_h)+ (rho_iw*Qd_iw))/Af; % Effective diffuse radiation inside solar still
Ig_eff=Ib_eff+Id_eff; % Effective solar radiation inside solar still

%CALCULATING OPTICAL PROPERTIES OF GLASS COVER
% Angle of incidence in radians
n1=1;n2=1.526;
theta_2=asin((n1*sin(theta_1))/n2);
K_extinctioncoeff=(4+32)/2;
tau_a=exp((-K_extinctioncoeff*z_g)/cos(theta_2));

r_perpendicular=((sin(theta_2-theta_1))^2)/((sin(theta_2+theta_1))^2);
alpha_perpendicular=(1-tau_a)*((1-r_perpendicular)/(1-(r_perpendicular*tau_a)));
tau_perpendicular=(tau_a*((1-r_perpendicular)^2))/((1-((r_perpendicular*tau_a)^2)));
rho_perpendicular=r_perpendicular*(1+(tau_a*tau_perpendicular));

r_parallel=((tan(theta_2-theta_1))^2)/((tan(theta_2+theta_1))^2);
alpha_parallel=(1-tau_a)*((1-r_parallel)/(1-(r_parallel*tau_a)));
tau_parallel=(tau_a*(1-r_parallel)^2)/((1-((r_parallel*tau_a)^2)));
rho_parallel=r_parallel*(1+(tau_a*tau_parallel));

if alpha_perpendicular>0 && alpha_perpendicular<1 && alpha_parallel>0 && alpha_parallel<1
   alpha_gc=0.5*(alpha_perpendicular+alpha_parallel);
else
   alpha_gc=0;
end
```

```
if tau_perpendicular>0 && tau_perpendicular<1 && tau_parallel>0 && tau_parallel<1
    tau_gc= 0.5*(tau_perpendicular+tau_parallel); % transmittance of glass cover
else
    tau_gc=0;
end
rho_gc= 1-tau_gc-alpha_gc;

alpha_gc1=alpha_gc;
alpha_bf1=alpha_bf*tau_gc;
alpha_bl1=alpha_bl*tau_gc*(1-r_bf-alpha_bf);

Iglass=(alpha_gc1*Ig_eff);
Ifluid=alpha_bf1*Ig_eff;
Ibasin liner=alpha_bl1*Ig_eff;

for j=1:delta_t:3600
        solution=0;
        while ~solution
            Tatmcol=Data_stellenbosch(:,5);Tatmtrans_all=Tatmcol';
            Tatm_deg_C=Tatmtrans_all(:,i);
            Tatm=Tatm_deg_C+273.15;
            Ts=0.0552*(Tatm^1.5);

            Tm=(Tbl0+Tf0)/2;
            Tm_deg_C=Tm-273.15;
            Beta_volumetric_bf=(-6.8785895*(10^-5))+(2.1687942*(10^-
    5)*Tm_deg_C)+(-2.1236686*(10^-6)*(Tm_deg_C^1.5))+(7.7200882*(10^-
    8)*(Tm_deg_C^2));

            if Tbl0>Tf0
                Delta_Temp=(Tbl0-Tf0);
            else
                Delta_Temp=0;
```

```
end

%Physical Properties of Base fluid
% Base fluid density in kg/m3
rho_bf=999.79684+(0.068317355*(Tm-273.15))-(0.010740248*((Tm-273.15)^2))+(0.00082140905*((Tm-273.15)^(2.5)))-(2.3030988*(10^-5)*((Tm-273.15)^3));

% Base fluid specific heat capacity in Jkg-1K-1
cp_bf=(4.2174356-(0.0056181625*(Tm-273.15))+(0.0012992528*((Tm-273.15)^1.5))-(0.00011535353*((Tm-273.15)^2))+(4.14964*(10^-6)*((Tm-273.15)^2.5)))*1000;

% Base fluid dynamic viscosity in Pa.s  [(kg/(m.s))]
mu_bf=1/(557.82468+(19.408782*(Tm-273.15))+(0.1360459*((Tm-273.15)^2))-(3.1160832*(10^-4)*((Tm-273.15)^3)));
%Base fluid thermal conductivity in Wm-1K-1
k_bf=0.5650285+(0.0026363895*(Tm-273.15))-(0.00012516934*((Tm-273.15)^(1.5)))-(1.5154918*(10^-6)*((Tm-273.15)^2))-(0.0009412945*((Tm-273.15)^(0.5)));


Pr_bf=1/(0.074763403+(0.0029020983*Tm_deg_C)+(2.8606181*10^-5*(Tm_deg_C^2))+(-8.1395537*(10^-8)*(Tm_deg_C^3)));
thermal_alpha_bf=k_bf/(rho_bf*cp_bf);

nu_bf=mu_bf/rho_bf;% Kinematic viscosity in m2/s
Gr_bf=(g*Beta_volumetric_bf*Delta_Temp*L^3)/(nu_bf^2);
Ra_bf=Gr_bf*Pr_bf;

if Ra_bf<10^7
   Nu_bf=0.54*(Ra_bf^(1/4)); %(Incropera, 2011:610)
else
   Nu_bf=0.15*(Ra_bf^(1/3));
```

```
    end

    hcv_bl_bf=(Nu_bf*k_bf)/L;
    %% Physical Properties of mixture of air and water vapour
    Tm1=(Tf0+Tg0)/2;% Mean temperature (fluid;glass)
    Beta_volumetric1=1/Tg0; % Coeff of volumetric expansion, in K-1

    if Tf0>Tg0
       Delta_Temp1=(Tf0-Tg0); % Temperature difference
    else
       Delta_Temp1=0;
    End

%% Nanoparticles
     phi_v_np=1/(1+((((1-
phi_m_np)/(phi_m_np))*(rho_np/rho_bf))))*100; % volume fraction of np (in
percentage)  (Kabeel et al. 2017:80)

    % Kabeel, Sharma (2012: 5); Khanafer
    rho_nf=(((phi_v_np/100))*rho_np)+((1-(phi_v_np/100))*rho_bf);  %
Nanofluid density in kg/m3 (Pg 5)
    cp_nf=((((phi_v_np/100)*(rho_np*cp_np))+(((1-
(phi_v_np/100))*(rho_bf*cp_bf)))))/(rho_nf);  % Nanofluid specific heat
capacity in Jkg-1K-1 (Pg 6)
   Beta_volumetric_nf=(1/Tm);%(Kabeel, 2017)
k_nf=(((((1+(phi_v_np/100))^(1.37))*((1+(Tm_deg_C/70))^(0.2777))*((1+(d
_np/150))^(-
0.0336)))*((thermal_alpha_np/thermal_alpha_bf)^(0.01737))))*0.8938*k_bf;
% Nanofluid thermal conductivity in Wm-1K-1 (Sharma)
mu_nf=mu_bf*0.935*((1+(Tm_deg_C/70))^0.5602)*((1+(d_np/80))^-
0.05915)*((1+(phi_v_np/100))^10.51); (Sekhar)
%%
    Pr_nf=(mu_nf*cp_nf)/k_nf;
    nu_nf=mu_nf/rho_nf;% Kinematic viscosity in m2/s
```

```
thermal_alpha_nf=k_nf/(rho_nf*cp_nf);

Gr_nf=(g*Beta_volumetric_nf*Delta_Temp*L^3)/(nu_nf^2);%(Incropera, 2011:409)
Ra_nf=Gr_nf*Pr_nf;

if Ra_nf<10^7
   Nu_nf=0.54*(Ra_nf^(1/4)); %(Incropera, 2011:610)
else
   Nu_nf=0.15*(Ra_nf^(1/3));
end
hcv_bl_nf=(Nu_nf*k_nf)/L;

% TSILINGIRIS
% (0 to 100 deg C)
Tm1=(Tf0+Tg0)/2;% Mean temperature (fluid;glass)
Beta_volumetric1=1/Tg0; % Coeff of volumetric expansion, in K-1

if Tf0>Tg0
   Delta_Temp1=(Tf0-Tg0); % Temperature difference
else
   Delta_Temp1=0;
end

rho_mix=1.293393662-((5.538444326*(10^-3))*(Tm1-273.15))+(((3.860201577*(10^-5))*((Tm1-273.15)^2)))-(((5.2536065*(10^-7))*((Tm1-273.15)^3)));% Density, in kg/m3
cp_mix=1.004571427+((2.05063275*(10^-3)*(Tm1-273.15)))-(((1.631537093*(10^-4))*((Tm1-273.15)^2)))+(((6.2123003*(10^-6))*((Tm1-273.15)^3)))-(((8.830478888*(10^-8))*((Tm1-273.15)^4)))+(((5.071307038*(10^-10))*((Tm1-273.15)^5)));% Specific heat capacity, in kJ/(kg.K)
mu_mix=(1.715747771*(10^-5))+((4.722402075*(10^-8))*(Tm1-273.15))-(((3.663027156*(10^-10))*((Tm1-273.15)^2)))+(((1.873236686
```

**(10^-12))*((Tm1-273.15)^3)))-(((8.050218737*(10^-14))*((Tm1-273.15)^4)));% Viscosity, in kg/(m.s)*

k_mix=(2.40073953(10^-2))+((7.278410162*(10^-5))*(Tm1-273.15))-(((1.788037411*(10^-7))*((Tm1-273.15)^2)))-(((1.351703529*(10^-9))*((Tm1-273.15)^3)))-(((3.322412767*(10^-11))*((Tm1-273.15)^4)));% Thermal conductivity, in W/(m.K)*

alpha_mix=(1.847185729(10^-5))+((1.161914598*(10^-7))*(Tm1-273.15))+(((2.373056947*(10^-10))*((Tm1-273.15)^2)))-(((5.769352751*(10^-12))*((Tm1-273.15)^3)))-(((6.369279936*(10^-14))*((Tm1-273.15)^4)));% Thermal diffusivity in m2/s*

% (0 to 100 deg C)

P_v_f=((0.7073034146-(2.703615165(10^-2)*(Tf0-273.15))+(4.36088211*(10^-3)*((Tf0-273.15)^2))-(4.662575642*(10^-5)*((Tf0-273.15)^3))+(1.034693708*(10^-6)*((Tf0-273.15)^4))))*1000;% vapour pressure at base fluid temp, in Pa*

P_v_g=((0.7073034146-(2.703615165(10^-2)*(Tg0-273.15))+(4.36088211*(10^-3)*((Tg0-273.15)^2))-(4.662575642*(10^-5)*((Tg0-273.15)^3))+(1.034693708*(10^-6)*((Tg0-273.15)^4))))*1000;% vapour pressure at glass temp, in Pa*

% latent heat of vaporisation, in J/kg

%popiel

hv=(2500.304-(2.2521025(Tm1-273.15))-(0.021465847*((Tm1-273.15)^1.5))+(3.1750136*10^-4*((Tm1-273.15)^2.5))-(2.8607959*10^-5*((Tm1-273.15)^3)))*1000;*

%specific heat capacity of air in J/(Kg.K) (Using data from WWR)

cp_air=(-3.6693061774(10^-7)*(Tm1^3))+(8.0958732242*(10^-4)*(Tm1^2))-(3.4836762169 *(10^-1)*(Tm1))+(1.0477229221*(10^3));*

%Heat Transfer Coefficients

Vcol=Data_stellenbosch(:,6);Vtrans_all=Vcol';

V=Vtrans_all(:,i); % Wind speed in m/s

```
% Convective heat transfer coeff between glass and atm due to wind, W(m2.K)
if V<=5
   hcv_g_atm=2.8+(3*V); % (El-Sebaii, 2005: 27)
else
   hcv_g_atm=6.15*(V^0.8);
end

% Radiative heat transfer coeff between glass and sky in W/(m2K) (Duffie, 2013: 243)
if Tg0<Tatm
   hr_g_sky=0;
else
   hr_g_sky=((epsilon_gc*sigma)*(Tg0^2+Ts^2)*(Tg0+Ts));
end
% Radiative heat transfer coeff between fluid and glass, in W/(m2.K) (Duffie, 2013: 148)
hr_f_g=(sigma*(Tg0^2+Tf0^2)*(Tg0+Tf0))/(((1-epsilon_bf)/epsilon_bf)+(1/Vf_g)+(((1-epsilon_gc)*Af)/(epsilon_gc*Ag))); % with VF
%Without view factor (Sahota, 2017: 317)
%epsilon_eff=(((1/epsilon_bf)+(1/epsilon_gc))-1)^(-1);
%hr_f_g=epsilon_eff*sigma*(Tg0^2+Tf0^2)*(Tg0+Tf0);

if Tf0-Tg0>0

hcv_f_g=(0.075*k_mix)*(((g*rho_mix*Beta_volumetric1)/(mu_mix*alpha_mix))^(1/3))*(((Tf0-Tg0)+((Tf0*(P_v_f-P_v_g)*(Ma-Mv))/((Ma*P0)-(P_v_f*(Ma-Mv)))))^(1/3));
else
   hcv_f_g=0;
end
```

```
% Evaporative heat transfer coefficient in m/s, Tsilingiris 2007: 1486
hevap_f_g=(hv)*((hcv_f_g)/(cp_air))*(Ra/Rv)*(P0/((P0-P_v_f)*(P0-P_v_g)));
qevap=(hevap_f_g*(P_v_f-P_v_g)); % Evaporative heat flux, W/m2 Tsilingiris 2007: 1486
if Tf0>Tg0
   he_f_g=qevap/(Tf0-Tg0); % evaporative heat transfer coefficient in W/(m2.K)
else
   he_f_g=0;
end
ht_f_g=hr_f_g+hcv_f_g+he_f_g; % Total heat transfer coeff between fluid and g, in W/(m2.K)

% Conductive Heat trans coeff between bl and atm, through (Polystyrene and Plywood) insulation, in W/(m2.K)
hco_bl_atm=((Lins1/Kins1)+(Lins2/Kins2))^(-1);
% Overall side heat loss coeff from fluid to atm,through plywood insulation, in W/(m2.K)
Us_b_atm=(Lins2/Kins2)^(-1);

%% Calculating New Temperatures
hcv_bl_f=hcv_bl_bf;

if hcv_bl_f==hcv_bl_bf
   m_f=m_bf;
else
   m_f=m_nf;
end
if hcv_bl_f==hcv_bl_bf
   cp_f=cp_bf;
else
   cp_f=cp_nf;
end
```

```
Tg=(((m_g*cp_g*Tg0)/delta_t)+(Ag*Iglass)+(ht_f_g*Af*Tf0)+(hcv_g_atm*
Ag*Tatm)+(hr_g_sky*Ag*Ts))/(((m_g*cp_g)/delta_t)+(ht_f_g*Af)+(hcv_g_at
m*Ag)+(hr_g_sky*Ag));

Tf=(((m_f*cp_f*Tf0)/delta_t)+(Af*Ifluid)+(hcv_bl_f*Abl*Tbl0)+(ht_f_g*Af*
Tg)+(A_sf*Us_b_atm*Tatm))/(((m_f*cp_f)/delta_t)+(hcv_bl_f*Abl)+(Af*ht_f
_g)+(A_sf*Us_b_atm));
        Tbl=(((m_bl*cp_bl*Tbl0)/delta_t)+(Abl*Ibasin
liner)+(hco_bl_atm*Abl*Tatm)+(hcv_bl_f*Abl*Tf))/(((m_bl*cp_bl)/delta_t)+
(hco_bl_atm*Abl)+(hcv_bl_f*Abl));

            Tempold=[Tg0;Tf0;Tbl0];
            Tempnew=[Tg;Tf;Tbl];

            Tempdiff=abs(Tempnew-Tempold);
            if all (Tempdiff)<=tolerance
               solution=1;
            end

            temps=[Tg;Tf;Tbl];

            % Updating temperatures
            Tg0=Tg;
            Tf0=Tf;
            Tbl0=Tbl;
        end
        m_water=(delta_t*((hcv_f_g/cp_air)*(Ra/Rv))*((P0*(P_v_f-
P_v_g))/((P0-P_v_f)*(P0-P_v_g))))+m_water0;
        m_water0=m_water;
    end
end
```

In order to validate the models, the climatic data from the University of Cape Town were then put into an m-file and the same procedures as above were repeated.